

UNIVERSITÀ DEGLI STUDI DELL'INSUBRIA

Dipartimento di Scienza e Alta Tecnologia

Anno Accademico 2012-2013

Dottorato in Fisica XXVI Ciclo



*VISION: A VERSATILE AND INNOVATIVE SILICON TRACKING
SYSTEM*

Author: Daniela Lietti

ID Number: 617710

Tutor: Prof.ssa Michela Prest
Università degli Studi dell'Insubria

Co-Tutor: Dott. Erik Vallazza
INFN - Sezione di Trieste

PhD Coordinator: Prof. Philip G. Ratcliffe
Università degli Studi dell'Insubria

La differenza, signori miei, è che voi avreste
potuto farlo, io invece l'ho fatto!

Cristoforo Colombo

(*La leggenda dell'uovo*)

a Gabriele, Paolo e Tullio

Contents

Introduction	1
1 The physics case: track particles to reconstruct effects	5
1.1 Crystal physics in a nutshell	7
1.1.1 A bent crystal at work: from phenomenology to theory	7
1.1.1.1 The continuum approximation	11
1.1.1.2 Channeling	15
1.1.1.3 Dechanneling	18
1.1.1.4 Volume Effects	20
1.1.1.5 Crystal “advanced” effects	24
1.2 Bent crystals applications	25
1.2.1 Extracted beam manipulation	27
1.2.2 Beam extraction and beam collimation	29
1.2.3 Crystals as high intensity γ -ray sources	33
1.3 The role of tracking in crystal physics	38
1.3.1 From the emulsion plates to the high precision measurements: why a <i>full tracking system</i> ?	38
2 Silicon detectors & electronics for tracking	43
2.1 Semiconductors in a nutshell	44
2.1.1 The intrinsic semiconductors	44
2.1.2 The extrinsic semiconductors and the reverse-biased p-n junction	46
2.1.3 Why silicon?	49
2.2 Silicon detectors: the working principle & performance	51
2.2.1 Spatial resolution	59
2.2.1.1 Analog vs digital	62
2.2.1.2 Strip & readout pitch	64
2.2.1.3 Noise	64
2.2.2 Charge sharing	67
2.3 Electronics for silicon detectors	70

3 The INSULAB reference detector: description and commissioning	75
3.1 The CSEM+VA2 reference modules	77
3.1.1 The silicon detectors	77
3.1.2 The readout ASIC	77
3.1.3 The mechanical assembly	82
3.2 The electronics chain	82
3.2.1 The frontend electronics	84
3.2.2 The readout electronics	85
3.3 The experimental setup	90
3.3.1 The tests goals	92
3.4 The commissioning phase @ SPS H4	92
3.4.1 Pedestal and noise	92
3.4.2 Cluster analysis: the modules behavior	94
3.5 The charge sharing distribution	102
4 The INSULAB reference detector: spatial resolution measurement	109
4.1 The spatial resolution measurement	109
4.1.1 The residual method	110
4.2 Results with the standard COG method	113
4.2.1 The SPS H4 high energy beamtest	113
4.2.2 The PS T9 low energy beamtest	114
4.2.2.1 The MCS subtraction	117
4.3 Results with the eta algorithm	118
5 The VISION tracking system: moving to a high performance system	129
5.1 The VISION modules	130
5.1.1 The silicon detectors	130
5.1.2 The VA1TA ASIC	133
5.1.3 The mechanical assembly	136
5.1.4 The electronics chain	136
5.1.5 The Slow Control system	137
5.2 The commissioning phases	138
5.2.1 The tests setup and goals	138
5.2.2 Pedestal and noise	139
5.2.3 Hold scan	142
5.2.4 Cluster analysis	144
5.2.5 The spatial resolution and charge sharing measurement @ PS T9	144
5.3 The detector at work: beamtest @ MAMI	150
5.3.1 The Mainzer Mikrotron	150
5.3.2 The experimental setup: detectors & crystals	153

5.3.3	Performance of the HAMAMATSU profilometer	158
5.3.3.1	Pedestal and noise	158
5.3.3.2	Hold and DAC threshold scans	158
5.3.3.3	Analog response	162
5.3.3.4	Beam profile analysis	162
5.3.4	Some results with a Si crystal	163
5.4	Faster and general purpose: the new data transmission	166
6	Conclusions & Outlooks	173
A	Analysis procedure	179
A.1	Pedestal analysis	180
A.2	Particle position finding algorithm	183
A.3	Module alignment	184
B	The FBK-irst+VA1_prime2 UA9 modules	189
B.1	Module description	189
B.1.1	The silicon tiles and the mechanical assembly	189
B.1.2	The readout ASIC and electronics	192
B.2	The SPS H4 beamtest results	192
B.2.1	The modules behavior	193
List of acronyms		197
List of figures		203
List of tables		207
Bibliography		209
Acknowledgement		221

Introduction

The anomalous penetrating capability of charged particles interacting with straight crystals is known since at least one century (1912) when J. Stark suggested that certain directions in a crystal could be more transparent to the passage of charged particles than in an amorphous material. He realized that the motion of a particle which enters the crystal with a given alignment (which later was called the *Lindhard angle*) with respect to its lattice can be confined in the so-called *crystal channels*: this hypothesis was confirmed by several simulations and experiments in the early 1960s while its theoretical explanation by J. Lindhard dates 1964.

Two steps forward in the crystal physics were made in 1976, when E. N. Tsyganov proposed the idea to steer high energy particle beams using properly bent crystals, and in 2006, when the so-called *Volume Reflection* (VR) effect was measured for the first time by the H8RD22 Collaboration at CERN (Conseil Europeen pour la Recherche Nucleaire, Swiss). These two fundamental “discoveries” opened the way to several applications such as the manipulation, the extraction and the collimation of low/high energy charged beams, from the 7.5 GeV ones at JINR (Joint Institute for Nuclear Research, Russia) to the 980 GeV ones at FNAL (Fermi National Accelerator Laboratory, USA), or the production of high intensity/high energy γ -ray beams.

From the experimental point of view, a real breakthrough for the physics of crystals is represented by a new philosophy of testing on extracted beams: the use of a high precision tracking system capable of reconstructing the direction of each single particle. This new technique has allowed not only to identify further effects, such as the above mentioned VR, but also to improve both the knowledge on the behaviour of several crystal types (in terms of used materials and thickness along the beam direction) and the accuracy with which the samples are characterized (in terms of their deflection capability and efficiency), and to start a new research line dedicated to the study of the radiation emitted by light particles in straight/bent crystals.

This thesis work focuses on the study of the performance of different tracking and profilometry systems (the so-called *INSULAB*, *INSUbria LABoratory*, and *VISION*, Versatile and Innovative SilicON, *Telescopes*) used in the last years by the

NTA-HCCC, the COHERENT (COHERENT effects in crystals for the physics of accelerators), ICE-RAD (Interaction in Crystals for Emission of RADiation) and CHANNEL (CHanneling of NEgative Leptons) experiments, four collaborations of the INFN (Istituto Nazionale di Fisica Nucleare) dedicated to the research in the crystals physics field.

The telescopes consist in several modules equipped with $300\ \mu\text{m}$ thick silicon microstrip detectors produced by different firms (CSEM, Centre Suisse d'Electronique et Microtechnique, FBK-irst, Fondazione Bruno Kessler, and HAMAMATSU Photonics) and coupled to different types of ASICs (VA2, VA1_prime2 and VA1TA), all from IDEAS (Integrated Detector & Electronics AS). Depending on the used silicon tiles and the desired spatial resolution, all the strips or one every two (the so-called *single floating strip scheme*) have been readout. The electronics chain is based on custom ADC (Analog to Digital Converter) and memory/readout boards and have been upgraded in 2012.

The thesis is organized as follows. The first chapter is dedicated to the straight and bent crystals physics; after a brief introduction on the theoretical laws and the basic working principles of such devices, the different applications and the experimental approaches which foresee the use of a crystal, both as a clever bender in High Energy Physics (HEP) experiments or as a high intensity/high energy γ -ray source, are described in detail. The last part of the chapter focuses on the role of *tracking* in crystal physics, with particular attention on the new philosophy and techniques introduced by the H8RD22 Collaboration in this field.

The second chapter starts with a brief overview on the semiconductor materials physics to arrive to the description of the main features of silicon which is the most used material worldwide and the one on which the detectors presented in this thesis work are based. The microstrip silicon detector working principle is presented in the second part of the chapter: a general overview of the parameters (both geometrical and physical) determining the final performance of a detector, in terms of noise contribution and Signal to Noise Ratio (SNR) are described; a particular attention is also given to those factors affecting the intrinsic spatial resolution (σ_{int}) and the Charge Sharing (CS) among the strips. The chapter ends with a few hints on the modern electronic chains used to readout the charge signal in silicon microstrip detectors.

Chapters 3, 4 and 5 are the heart of this thesis work. The third chapter describes the modules of the INSULAB Telescope (also indicated as *reference modules*): both the used silicon tiles, the ASICs (Application Specific Integrated Circuits) working principle and the readout electronic chain are presented together with the results (in terms of noise response, SNR and CS) of the first commissioning phase at the CERN SPS (Super Proton Synchrotron) H4 and PS (Proton Synchrotron) T9 extracted lines.

Chapter 4 describes the two algorithms used to measure the final intrinsic spa-

tial resolution of the reference modules at different energies (10 GeV at the PS T9 beamline and 150 GeV at the SPS H4 one): both the standard Center Of Gravity (COG) method and the one based on the so-called *eta (η) distribution* correction have been used and are compared. Dedicated analysis, used to estimate and correct both the Multiple Coulomb Scattering contribution and the tilt angle introduced during the detector positiong along the beamline, are also described.

The first part of chapter 5 contains the description of a new tracking system (the VISION Telescope) based on a different type of silicon tiles and ASICs; in particular the focus is pointed on the need to develop a more compact and faster system which is at the same time general purpose. The commissioning of the VISION Telescope at the CERN PS T9 beamline in presented in terms of the same figures of merit used for the reference modules (noise, SNR, σ_{int} and CS). One of the VISION modules has also been used by the ICE-RAD and CHANNEL Collaborations at the Mainzer Mikrotron (MAMI) accelerator to study a set of new generation crystals (with a thickness down to 50 nm along the beam direction) with a low energy electron beam. The last part of the chapter deals with the description of a new data transmission system developed to further increase the acquisition rate of the whole system.

Chapter 1

The physics case: track particles to reconstruct effects

Bent crystals [1, 2] are devices developed to deflect relativistic charged particles working as the traditional bending magnets (heavy and bulky objects able to produce huge magnetic fields); thanks to the coherent interaction of the particles with the ordered crystalline structure, a 0.5 mm (x) \times 7 cm (y) \times 2 mm (z, beam direction) silicon strip crystal has the same effect of a 72 T magnetic field [2].

The physics of straight crystals was born in 1912 when the German physicist Johannes Stark proposed for the first time the idea that certain directions in a crystal¹ could be more transparent to the passage of charged particles [4] (figure 1.1), an effect which later was called *Channeling (CH)*. However, it took more than 50 years for its experimental demonstration with ion beams and computer simulations (1963 [5, 6]) and its theoretical explanation by the Danish theoretical physicist Jens Lindhard (1964 [7, 8]). The following decade was dedicated to the study of the crystal channeling properties both in the low (\sim MeV) and high (\sim GeV) energy region [2].

In 1976 the Russian physicist Edouard N. Tsyanov proposed to bend a crystal and to use it to deflect charged particles [9]; his pioneering idea was experimentally confirmed in 1979 [10] at JINR² and opened the way to many theoretical, analytical and experimental studies in the following years. Among these studies there is one which plays a fundamental role both for the physics of crystals and the high energy physics: the discovery, first in computer simulations (1987 [11])

¹The crystal used by Stark, in experiments performed at the RWTH (Rheinisch-Westfälische Technische Hochschule) University in Aachen (Germany) and primarily dedicated to the study of the X-ray diffraction by crystals [3], was a \sim 1 mm thick plate.

²Joint Institute for Nuclear Research, Dubna (Russia), <http://www.jinr.ru/>.

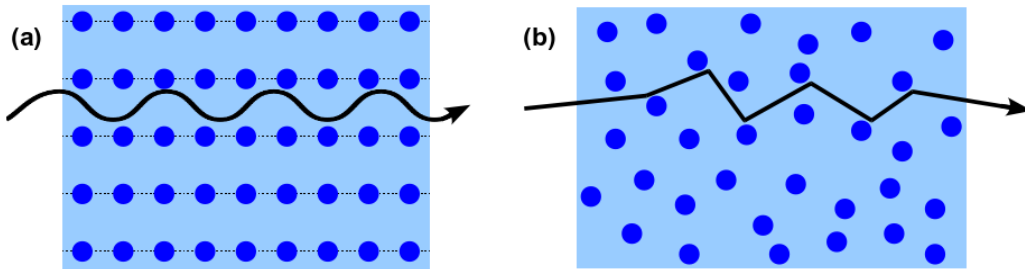


Figure 1.1: Stark's idea: the motion of a charged particle through a crystal (a) is different from the one in non ordered structures (b) (the so-called *amorphous materials*); the suppression of both the Multiple Coulomb Scattering (MCS) effect and of the energy loss via ionization in the so-called *crystal channel* is able to confine the particle motion in the average continuum potential wells formed by the subsequent atoms distribution.

and then in experiments at IHEP³ (2006 [12]) and at CERN⁴ (2006 [13]), of the so-called *Volume Reflection (VR)* effect. A new era for the high energy beam collimation (and not only) was starting.

In parallel, the pioneering researches of Bruno Ferretti [14], Mikael L. Ter-Mikaelian [15], Freeman J. Dyson and Herbert Uberall [16] on the influence of the crystalline lattice on the electromagnetic radiation produced by light charged particles crossing a crystal led to the discovery of the so-called *coherent radiation*. The possibility to generate intense radiation sources by electrons/positrons captured in the CH or VR regime in straight/bent crystals became soon of large interest and stimulated a large number of experiments in the following years [17–24].

This chapter begins with the description of the bent crystal physics, starting from the phenomenological point of view, going through the crystal working principle, to arrive to the microscopic properties and the theoretical laws behind the experimentally observed macroscopic phenomena. A brief review of the possible applications is also given (more details can be found in [1, 2]). The second part of the chapter focuses on the state of the art of the experimental and analysis techniques used for testing crystals; in particular the new innovative test philosophy [13, 25] (the so-called *2006-breakthrough*), based on real time single particle track reconstruction, is presented.

³Institute for High Energy Physics, Protvino (Russia), <http://www.ihep.ru/>.

⁴Conseil Europeen pour la Recherche Nucleaire (European Organization for Nuclear Research), Geneve (Switzerland), <http://www.cern.ch>.

1.1 Crystal physics in a nutshell

The aim of the following sections is to give to the reader some notions about the crystals physics, without going too deep on the analytical aspects and calculations of the laws governing the particle motion in a crystal channel. A complete overview of the straight/bent crystal physics, both from the theoretical, analytical and experimental point of view, can be found in [1, 2, 26].

1.1.1 A bent crystal at work: from phenomenology to theory

Figure 1.2 shows the bent crystal working principle: the schematic views of the different processes occurring in a bent crystal depending on its mutual orientation with respect to the incoming particle are shown in figure 1.2(a) while figure 1.2(b) presents the scatter plot⁵ obtained with a 400 GeV/c proton beam impinging on a Si strip crystal, 1.94 mm thick along the beam direction and 0.5 mm wide, bent along the (110) plane.

Thanks to the very high spatial resolution (better than $4.2 \mu\text{m}$ in the direction measuring the crystal effects [27]) of the detectors (the topic of this thesis work, presented in chapters 3 and 4), the different regions corresponding to the different phenomena are clearly visible in figure 1.2(b) and can be described with the following figures of merit [1, 28]:

- the *deflection angle*, defined as the difference between the incoming and the outgoing particle angle measured before and after the crystal, respectively: in other words it defines the angular deflection (ϕ) imparted by the crystal. Both the crystal physical properties and the particle energy and type affect the value of the ϕ angle;
- the *angular acceptance*, which corresponds to the angular interval ($\Delta\alpha$) of the incoming particles in which the deflection can take place; as for the deflection angle, $\Delta\alpha$ depends both on the particle and the crystal characteristics;
- the *deflection efficiency* defined as

$$\xi = \frac{N}{N_{TOT}} \quad (1.1)$$

⁵A scatter plot is a 2D histogram where on the horizontal axis there is the crystal misalignment with respect to the beam direction (α) while on the vertical one the deflection angle produced by the crystal itself (ϕ). In this coordinate system, $\alpha = 0$ means a perfect alignment between the crystal planes/axes and the beam, while $\phi = 0$ indicates that there is no deflection.

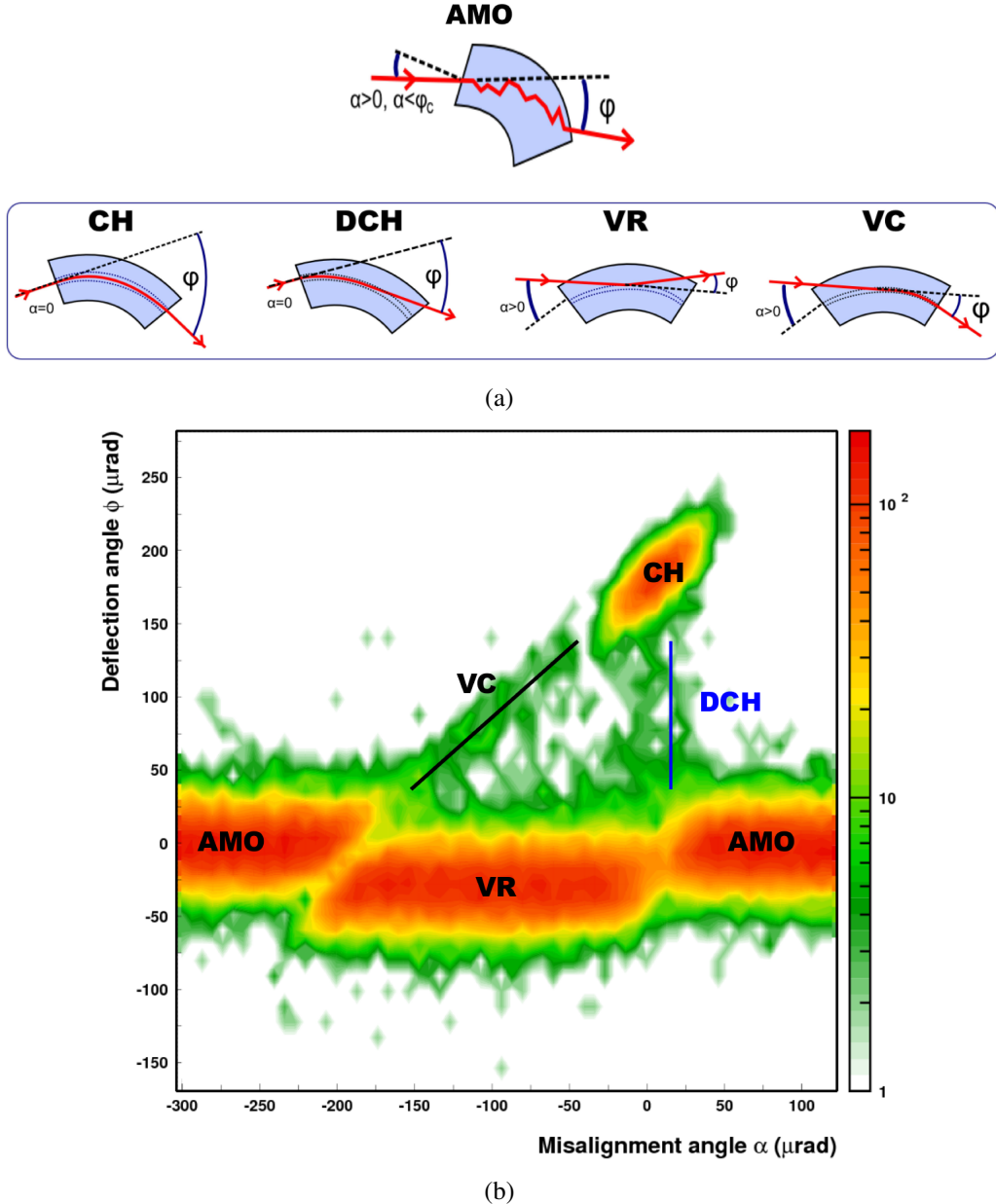


Figure 1.2: The bent crystals working principle (adapted from [1]). (a) Schemes of the different phenomena occurring in a bent crystal as a function of the crystal planes orientation with respect to the incoming particle beam. (b) The scatter plot obtained rotating the crystal with a dedicated goniometric system: the deflection angle (ϕ) as a function of the alignment (α) between the crystal and the incoming particles is presented; the acronyms indicate the different regions, *Amorphous-AMO*, *Volume Reflection-VR* and *Channeling-CH*, while the lines represent the *DeChanneling-DCH* and the *Volume Capture-VC* conditions (in blue and black, respectively).

where N is the number of particles “captured” in a given regime (CH, VR, etc.) and N_{TOT} the total number of particles impinging on the crystal. As will be discussed in the following, there are many factors that contribute to the efficiency (and to the corresponding inefficiency) of a given effect, including the crystal length, type, material and quality [29]. For this reason several new innovative manufacturing techniques, both for the crystals and the supporting systems (the so-called *holders*), have been developed in the last years⁶ [25, 30, 31].

The scatter plot in figure 1.2(b) thus allows to characterize a bent crystal as follows (both in a qualitative and a quantitative way⁷):

- in the external regions of the plot ($\alpha < -230 \mu\text{rad}, \alpha > 30 \mu\text{rad}$) the distribution of the particles is centered around $\phi = 0$ because the crystal is misaligned: this situation (top sketch in figure 1.2(a)) corresponds to the so-called *Amorphous-AMO* condition where a particle “sees” the crystal as a non ordered structure, *i.e.* an amorphous material. In this case the width of the particle distribution is given by the MCS contribution of the crystal itself and of the material budget along the beamline (a certain amount of air + the silicon detectors used for the measurement);
- the so-called best *Channeling-CH* condition is reached when $\alpha = 0$: an incoming particle is perfectly aligned with the crystal planes and is captured in the channel being deflected as schematically shown in the first sketch in the bottom row of figure 1.2(a). In particular [1, 2]:
 - * the channeling deflection angle (ϕ_{CH}) depends on the physical properties of the used crystal as follows:

$$\phi_{CH} = l/R \quad (1.2)$$

where l is the crystal thickness along the beam direction and R the circular curvature provided by the mechanical support. For the crystal used in figure 1.2(b) the deflection angle is $\phi_{CH} = 181.9 \pm 0.7 \mu\text{rad}$, which corresponds to a curvature radius R of 10.65 ± 0.01 m, while a 75% efficiency value has been obtained applying the procedure described in [1] for the correction of the crystal torsion effect;

⁶Moreover, ξ represents a crucial aspect for the crystal-based beam manipulation; in fact, it gives the estimation of the performance and of the quality of the used technique. For instance, only high efficiency allows a good enough cleaning performance in a crystal-based collimation system [28].

⁷For a complete description of the analysis procedure (which includes the crystal pre-alignment, the calculation of the interesting angles and the study of the torsion effect [32]) see [1].

- * on the other hand the channeling angular acceptance (α_{CH}) strongly depends on the incoming particle energy through the following equation (the so-called *Lindhard or critical angle* [2]):

$$\alpha_L = \alpha_C = \sqrt{\frac{2 \cdot U_{max}}{pv}} \quad (1.3)$$

where U_{max} is the height of the potential well in a straight crystal⁸ while p and v are the particle momentum and velocity, respectively;

- for a large interval of α values ($-182 \mu\text{rad} \leq \alpha \leq 0 \mu\text{rad}$), almost the whole beam is slightly deflected, in a direction opposite to the channeling one, in the so-called *Volume Reflection-VR* regime. It consists in the reversal of the transverse momentum of the incoming particle when it becomes parallel to the crystal planes inside the crystal volume (third sketch in the bottom row of figure 1.2(a)). As shown in figure 1.2(b), both the VR angular acceptance (being determined by the bending angle of the atomic plane [12]) and the deflection efficiency are very large compared to the ones for CH while the VR deflection angle is small and can be expressed with the following equation [33]:

$$\phi_{VR} \sim 1.5 \cdot \alpha_C \quad (1.4)$$

For the crystal used in figure 1.2(b) an angular deflection $\phi_{VR} = -29.7 \pm 0.8 \mu\text{rad}$ and a deflection efficiency larger than 97% have been measured;

- given a crystal is not an empty region, the fluctuations in the particle trajectories could take the particle out or bring it into the channeling condition, contributing to the inefficiency of the CH and VR conditions, respectively:

- * the so-called *DeChanneling-DCH* regime (second sketch in the bottom row of figure 1.2(a)) affects the particles which are initially captured in CH and, after a given path (the so-called *dechanneling length* L_D), are expelled from the channel due to the scattering with the crystalline medium. In figure 1.2(b) the dechanneled particles are those at $\alpha = 0$ and located in the vertical region between the channeling peak and the amorphous one;
- * on the other hand the particles which are brought in the channel in the so-called *Volume Capture-VC* regime, fill the diagonal region in figure 1.2(b) connecting the end of the VR zone with the CH peak.

⁸As will be shown later, the potential well in bent crystals is different from the one in straight crystals; the U_{max} value is thus smaller, corresponding to a smaller critical angle [1].

As for VR, VC takes place when the particle becomes tangent to the crystal channel inside the lattice volume but, instead of being reflected, it is captured in the channel behaving like a channeled particle. Since the α angle differs from 0, in this case the deflection angle is smaller than the one for CH (fourth sketch in the bottom row of figure 1.2(a)).

1.1.1.1 The continuum approximation

A crucial aspect for the theoretical treatment of the bent crystal physics is the so-called *continuum approximation* [2] which is schematically represented in figure 1.3: a charged particle travelling with a small angle ($\alpha \ll 1$) with respect to the crystallographic planes experiences a series of correlated collisions with the crystal lattice atoms; in this condition the transversal component of the particle momentum p is very small compared to the longitudinal one (figure 1.3(a)).

The net result is a long path along the longitudinal direction and the interaction with a large number of atoms: the electric potential $V(x, y, z)$ of each atom could be thus replaced with an average potential generated by the whole plane, as if the charge inside the crystal had a continuum distribution (figure 1.3(b)).

The *average continuum potential* is defined as [2]:

$$U_{pl}(x) = Nd_p \int_{-\infty}^{\infty} \int_{-\infty}^{\infty} V(x, y, z) dy dz \quad (1.5)$$

where Nd_p represents the planar atom density being N the number of atoms per unit volume and d_p the interplanar spacing. Assuming Lindhard's parametrization [7] for the single atom potential:

$$\begin{aligned} V(r) &= \frac{Z_i Ze^2}{r} \Phi\left(\frac{r}{a_{TF}}\right) \\ \Phi\left(\frac{r}{a_{TF}}\right) &= 1 - \left(1 + \frac{3(a_{TF})^2}{r^2}\right)^{-1/2} \end{aligned} \quad (1.6)$$

(where Z_i is the atomic number, Ze the charge of the incoming particle, r the particle-atom distance and $\Phi(r/a_{TF})$ the screening function taking into account the crystal charge distribution⁹) equation 1.5 becomes:

$$U_{pl}(x) = 2\pi Z_i Ze^2 Nd_p \left(\sqrt{x^2 + 3a_{TF}^2} - x \right) \quad (1.7)$$

where x is the distance from the plane.

⁹ a_{TF} is the Thomas-Fermi screening radius $a_{TF} = 0.8853 \cdot a_B \cdot Z^{-1/3}$ with $a_B = 0.529 \text{ \AA}$ [1].

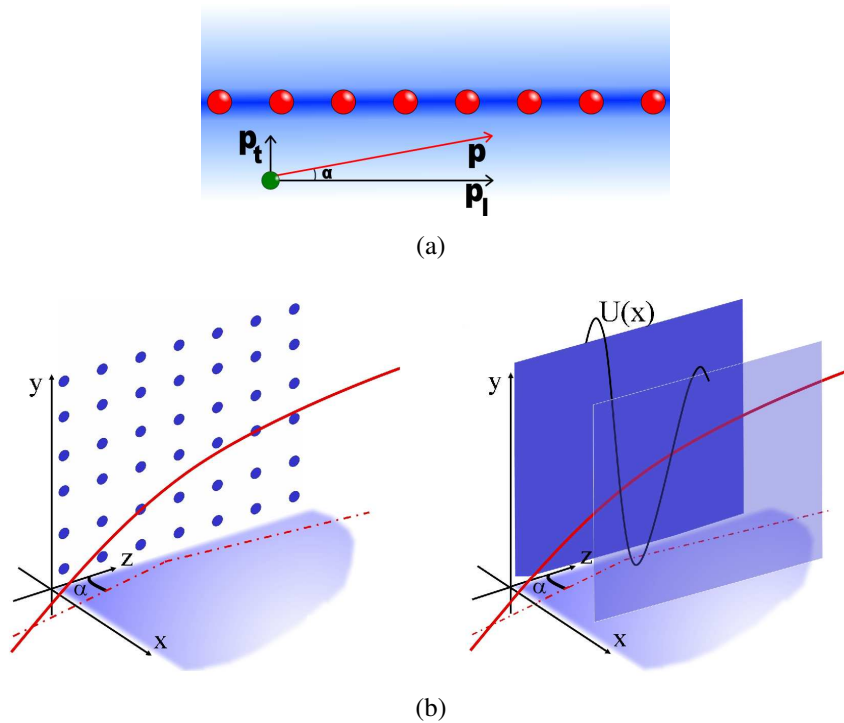


Figure 1.3: (a) Schematic description of the motion of a particle (green dot) quasi aligned with a series of atoms inside a crystal (red dots) [1]; the parallel and transversal components of the particle momentum p are also shown. (b) Representation of the average potential well $U_{pl}(x)$ experienced by a particle trapped in the crystal channel [1].

As shown in figure 1.3(b), a particle moving in a crystal channel “feels” the average potential generated by the sum of the single atoms electric potential; however the contribution of the two nearest ones is dominant so that the average potential $U(x)$ can be written as [2]:

$$U(x) \simeq U_{pl} \left(\frac{d_p}{2} - x \right) + U_{pl} \left(\frac{d_p}{2} + x \right) - 2U_{pl} \left(\frac{d_p}{2} \right) \quad (1.8)$$

where $x = 0$ corresponds to the middle position between the two planes and $U(0) = 0$. The $U(x)$ value in turn, being proportional to Z_i and N (equation 1.7), depends on the crystal material and, for a given crystal, changes as a function of the interplanar distance d_p : the wider the channel the greater its confinement strength. Table 1.1 summarizes the main channel parameter values for silicon, germanium and tungsten [2], the typical materials used to build crystals in high energy physics experiments¹⁰.

	Channel	L_c [Å]	d_p [Å]	a_{TF} [Å]	ρ [Å]	Z_i	$U(x_c)$ [eV]
Si	110	5.43	1.92	0.194	0.075	14	16
	111L		2.35				19
	111S		0.78				4.2
Ge	110	5.65	2.00	0.148	0.085	32	27
	111L		2.45				30
	111S		0.81				7.2
W	10	3.16	1.58	0.112	0.050	74	63
	110		2.24				105

Table 1.1: Main parameters of the crystal channel for Si, Ge and W [2]: the channels typically used to deflect particle beams are listed (L_c indicates the crystal lattice constant).

¹⁰In this case the average continuum potential has been computed in the so-called *Molière approximation*

$$\Phi \left(\frac{r}{a_{TF}} \right) = \sum_{i=1}^3 \alpha_i \cdot \exp \left[\frac{\beta_i}{a_{TF}} \right] \quad (1.9)$$

(where $\alpha=(0.1, 0.55, 0.35)$ and $\beta=(6.0, 1.2, 0.3)$ [2]) and with $x_c = d_p/2 - 2/\rho$ being ρ the rms (Root Mean Square) amplitude of the atomic thermal vibration, which for silicon at room temperature is 0.075 Å [28].

As shown in the top part of figure 1.4, representing the average continuum potentials computed with the ECHARM software¹¹ both for positive (left) and negative (right) 150 GeV/c pions in a silicon (110) crystal, $x = 0$ corresponds to the minimum (maximum) value of the potential for positive (negative) particles.

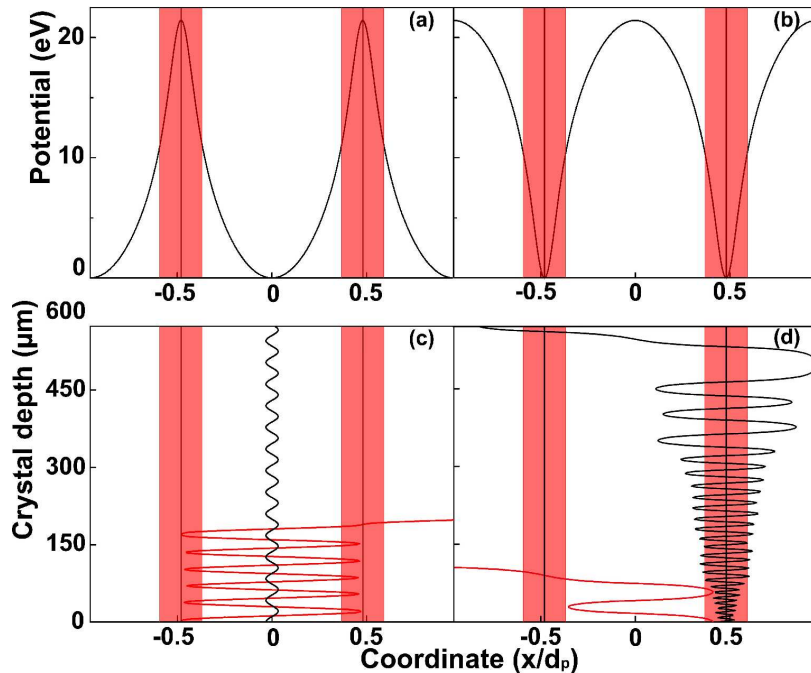


Figure 1.4: Planar potential (top) and particle trajectories (bottom) (simulated, respectively, with the ECHARM and DYNECHARM++ softwares) in a (110) silicon crystal [35]. The red shaded areas represent the nuclear corridors while the vertical black lines indicate the positions of the atomic planes; particles with different impact parameters (red/black trajectories) have been considered.

The bottom part of figure 1.4 shows the simulated pions trajectories inside the crystal¹²: as will be discussed in section 1.1.1.3, the larger is the particle impact parameter (red lines), the larger is the probability for a particle to be dechanneled by the regions with the high nuclear density (the so-called *nuclear corridors* [26]).

¹¹Electrical CHARacteristics of Monocrystals [26, 34] is a software, written in C++, to calculate the one- and two-dimensional averaged physical quantities along the main planes/axes of any orthorhombic or tetragonal crystal structure [2].

¹²In this case the DYNECHARM++ (DYNAMIC ECHARM++ [26, 36]) software has been used: it is a toolkit to simulate the trajectories of the charged particles interacting with complex crystal structures. The core of the code (which is written in C++) is based on the integration of the equation of motion for the charged particles under the continuum approximation while the electrical characteristics of the crystals are computed with the ECHARM software.

Moreover, negative particles, which are “captured” around the crystal planes (as their potential well minima correspond to the nuclei positions) are more subjected to the DCH effect, even if they are initially aligned with the plane with a small impact parameter (black lines); this results in a shorter dechanneling length L_D for negative particles with respect to the one for positive particles in the same conditions (beam energy and used crystal [1]).

1.1.1.2 Channeling

According to equation 1.3, the CH effect occurs when a particle impinges on the crystal with the “correct” angle, *i.e.* when the misalignment angle is $-\alpha_c < \alpha < \alpha_c$ in the coordinate system given in figure 1.2(b). In terms of energy, this condition corresponds to a particle transversal energy which does not exceed the maximum value of the potential well formed by the atomic nuclei.

In the continuum approximation $\alpha \sim p_t/p_l \ll 1$ which in turn gives $p_l \sim p$; the total energy of the system can be thus written as follows [2]:

$$\begin{aligned} E &= \sqrt{p_t^2 + p_l^2 + m^2 c^4} + U(x) \simeq \frac{p_t^2 c^2}{2E_l} + E_l + U(x) \\ E_l &= \sqrt{p_l^2 c^2 + m^2 c^4} \\ E_t &= \frac{p_t^2 c^2}{2E_l} + U(x) \\ E_t &= \frac{p_l^2 c^2}{2E_l} \alpha^2 + U(x) \simeq \frac{p^2 c^2}{2E} \alpha^2 + U(x) = \text{const.} \end{aligned} \tag{1.10}$$

where E_l and E_t indicate, respectively, the longitudinal and the transversal energy while the last two equalities derive from the energy conservation principle. The particle transversal energy is thus a function of its alignment (α) with the crystal plane and of its position (x) inside the channel (figure 1.5).

As already mentioned, the particle remains trapped in the channel until its transversal energy $E_t \leq U_{max}$ (critical value of the transverse energy), *i.e.*:

$$E_t = \frac{p^2 c^2}{2E} \alpha^2 + U(x) \leq U_{max} \tag{1.11}$$

Equation 1.11 thus defines the possible values of α and x for a channeled particle; in particular [2]:

- a particle approaching the crystal close to the atomic planes is rapidly removed from the CH condition; thus the maximum potential value U_{max} does

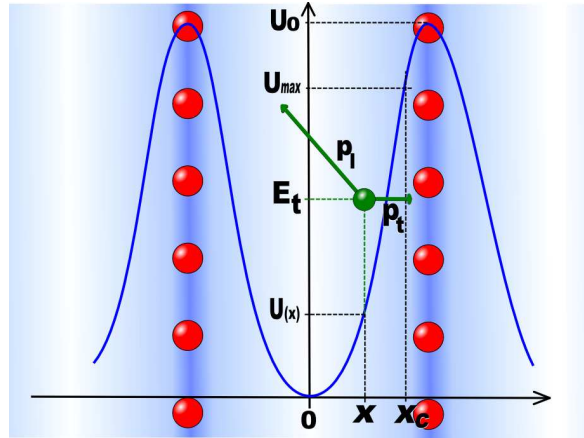


Figure 1.5: Schematic view of the interplanar potential [1]: the red dots represent the atomic nuclei while the blue line is the potential shape $U(x)$; the green dot represents a particle with a transversal energy $E_t \leq U_{max} = U(x_c)$.

not correspond to the top of the potential barrier (U_0) and the following equation holds:

$$U_{max} = U(x_c); x_c = d_p/2 - a_{TF} - 2\rho \quad (1.12)$$

where x_c is the so-called *critical transverse coordinate* and takes into account the effect of the atomic thermal vibration [2];

- taking into account the relation $pc^2 = vE$ the transverse particle energy becomes:

$$E_t = \frac{p^2}{2} + U(x) \quad (1.13)$$

for which the conditions $E_t = U_{max}$ and $x = 0$ correspond to particles which enter the channel in its center, thus giving the maximum misalignment angle (equation 1.3). For a straight Si crystal $U_{max} \approx 20$ eV (table 1.1), thus α_c is 280 μ rad at 500 MeV, 9.42 μ rad at 450 GeV and 2.39 μ rad at 7 TeV [1];

- the particle trajectory for an arbitrary $U(x)$ can be directly obtained from equation 1.11: taking into account that $\alpha = dx/dz$ (where dx and dz are the infinitesimal increases in the transversal and longitudinal spatial directions, respectively) and differentiating with respect to z , one obtains a sinusoidal oscillation (as shown in figure 1.4):

$$\begin{aligned} x &= \frac{d_p}{2} \sqrt{\frac{E_t}{U_0}} \sin\left(\frac{2\pi \cdot z}{\lambda} + \phi\right) \\ \lambda &= \pi d_p \sqrt{\frac{p^2}{2U_0}} \end{aligned} \quad (1.14)$$

where λ is the oscillation period which for instance is $\sim 25.5 \mu\text{m}$ for 400 GeV/c protons in silicon [1].

As far as bent crystals are concerned, the previous treatment of the CH effect is still valid since a macroscopic curvature radius of several meters has negligible effects on the crystalline microscopic structure in the Å range [2]. However it causes the particle to feel a centrifugal force in the non-inertial frame which rotates with the particle itself¹³. Taking into account the centrifugal force (defined as $pv/R(z)$, with $R(z)$ the local curvature radius), the transversal energy and the equation of motion given by the expressions 1.13 and 1.14 remain valid with the substitution of the *effective* interplanar potential $U_{eff}(x)$ [2]:

$$\begin{aligned} E_t &= \frac{pv}{2}\alpha^2 + U_{eff}(x) \\ pv\frac{d^2x}{dz^2} + U_{eff}(x) &= 0 \\ U_{eff}(x) &= U(x) + \frac{pv}{R}x \end{aligned} \quad (1.15)$$

where the dependence of the curvature from the local position in z has been removed since the crystal curvature can be considered constant ($R(z) = R$) along the whole crystal thickness. Figure 1.6 shows the effective interplanar potential for a Si (110) crystal bent with 2 different curvature radii: the larger pv/R , the smaller the potential depth (and thus the confinement capability of the crystal) and the minimum of the barrier is shifted toward the atomic plane.

At some critical $(pv/R)_c = R_c$ value (the so-called *Tsyganov critical radius*), the well disappears and channeling is no longer possible; this in turn affects both the value of the critical angle (equation 1.3) and the expression of the particle motion (equation 1.14) which become:

$$\begin{aligned} x &= -x_c \frac{R_c}{R} + x_c \sqrt{\frac{E_t}{U_0^b}} \sin\left(\frac{2\pi \cdot z}{\lambda} + \phi\right) \\ \alpha_L^b &= \sqrt{\frac{2 \cdot U_{max}^b(R)}{pv}} = \alpha_L \left(1 - \frac{R_c}{R}\right) \end{aligned} \quad (1.16)$$

where $U_{max}^b(R)$ indicates the transversal energy limit for channeling in a bent crystal and $U_0^b = U_{eff}(x_c) - U_{eff}(x_{min})$. $x_{min} = -x_c R_c / R$ corresponds to the “new” equilibrium point in the channel, *i.e.* the “new” position of the potential well minimum [1, 2]; on the other hand, the last equality for the Lindhard angle has been obtained considering $U_0^b = U_0 \left(1 - \frac{R_c}{R}\right)^2$ [1].

¹³In this reference system, the z coordinate follows the direction of the bent atomic planes while the x and α coordinates are defined with respect to the local atomic plane at a given z position [2]; see [1] for more details.

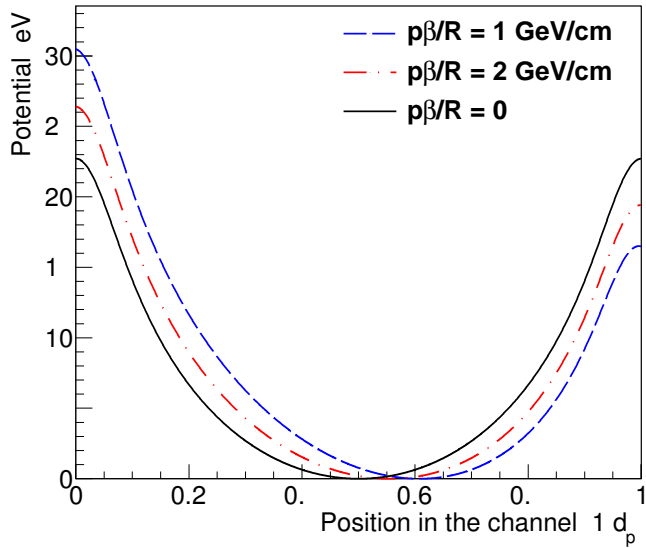


Figure 1.6: The interplanar potential for a Si (110) crystal bent with 2 different curvature radii (expressed in terms of pv/R) [26]; the potential computed in the Moliére approximation (solid black line) is shown for comparison.

1.1.1.3 Dechanneling

As mentioned in section 1.1.1, not all the particles captured in the CH regime remain in this condition travelling across the crystal along its whole thickness; moreover, the assumption that E_t is conserved during the motion inside the crystalline lattice is no more valid in a real crystal [2]. The scattering processes at the basis of the DCH effect produce, in fact, an increase in the transversal energy which, overcoming the interplanar potential barrier, causes the release of the particle from the CH condition (figure 1.7).

In particular, two main categories of scattering events, both described by an exponential law with a characteristic decay length¹⁴, can be recognised:

- the Multiple Coulomb Scattering on Nuclei (MSN) in which an instant change in E_t occurs for those particles crossing the crystal with a initial large value of the transversal energy, *i.e.* $E_t \sim U_0$: these particles are quickly removed from the CH condition and the corresponding dechanneling length

¹⁴According to [2], the following exponential decay can be used:

$$N(z) = N_0 \cdot e^{-\frac{z}{L_D}} \quad (1.17)$$

where $N(z)$ is the number of channeled particles at the z position along the crystal ($z \leq$ crystal length) and N_0 is the number of channeled particles at the crystal entry face.

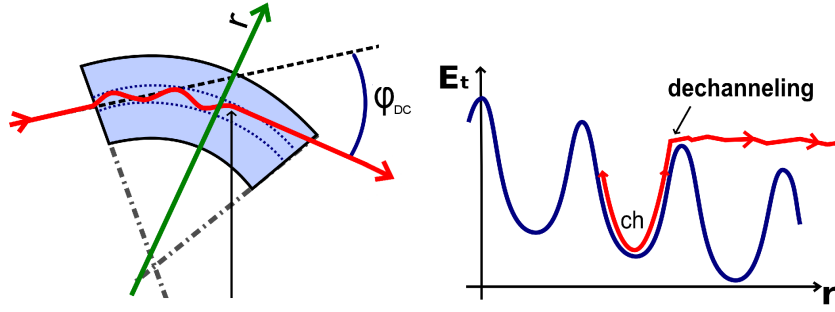


Figure 1.7: Schematic views of the DeChanneling process in a bent crystal [1]; the particle trajectory in the non inertial frame which rotates with the channel (left) and in the phase space (right) are shown.

can be defined as [1]:

$$L_D^n = E_{gap} \cdot pv \cdot \frac{2X_0}{E_c^2} \quad (1.18)$$

where X_0 is the radiation length, $E_c = 13.6$ MeV [37] and $E_{gap} = U_0 - U_{max}$;

- the Multiple Coulomb Scattering on Electrons (MSE) where a progressive growth of E_t occurs for particles with $E_t < U_{max}$; with respect to MSN, this phenomenon is “slower” and affects the particles along their whole path inside the crystal. The corresponding dechanneling length is given by [2]:

$$L_D^e = \frac{256}{9\pi^2} \cdot \frac{pv}{\ln(2m_e c^2 \gamma / I) - 1} \cdot \frac{a_{TF} d_p}{Z r_e m_e c^2} \quad (1.19)$$

where $I = 16 \cdot Z_i^{0.9}$ is the ionization potential, m_e and r_e are, respectively, the electron mass at rest and the classical radius and γ is the Lorentz factor.

Considering silicon crystals and 400 GeV positive charged particles, $L_D^n \simeq 2$ mm while $L_D^e \simeq 22$ cm [1] which means the MSE effect is negligible in short crystals (the last generation ones with a thickness smaller than 1 mm) while the MSN effect represents the main source of dechanneling.

It can be noted that both L_D^n and L_D^e are proportional to the incoming particle energy (pv) which means the probability to remain in the CH condition linearly increases with the particle energy as expected given the scattering angle $\theta_{MCS} \propto E^{-1}$ [38]; therefore, the effects due to multiple scattering, which reduce the channeling efficiency, become less important at high energy.

The situation becomes slightly worse when the crystal is bent: considering equation 1.16 for the particle motion, in fact, the channeled particles are shifted towards the atomic plane and thus are more subjected to the scattering with the

large nuclear density region. As for the Lindhard angle (equation 1.16), the expression for the dechanneling length in bent crystals becomes:

$$L_D^b = L_D \left(1 - \frac{R_c}{R} \right)^2 \quad (1.20)$$

1.1.1.4 Volume Effects

As already discussed in section 1.1.1, in a bent crystal CH is not the only phenomenon able to deflect particles; as shown in figure 1.2(b), the so-called *volume effects* play a crucial role in the particles deflection. In particular the change in the potential well shape (figure 1.6) allows the particles misaligned with the crystal planes at its entry face (those with $\alpha \geq \alpha_c$ which cannot enter the CH regime) to arrive at a tangency point with the bent crystallographic planes while crossing the crystal volume. In terms of energy this corresponds to an initial large transversal component ($E_t \geq U_0$); in turn, being E_t a motion constant [1], a progressive alignment of the particle with respect to the channel in the non inertial frame comoving with the crystal channel is possible¹⁵. Here two effects may take place:

- the particle loses its transversal energy and gets trapped into the channel in the VC condition (figure 1.8); it is the inverse of the DCH process (figure 1.7). According to the so-called *Lindhard reversibility rules* [7], in fact, these two processes require the same amount of transversal energy: a decrease for the VC effect and an increase for the DCH one (as discussed in section 1.1.1.3).

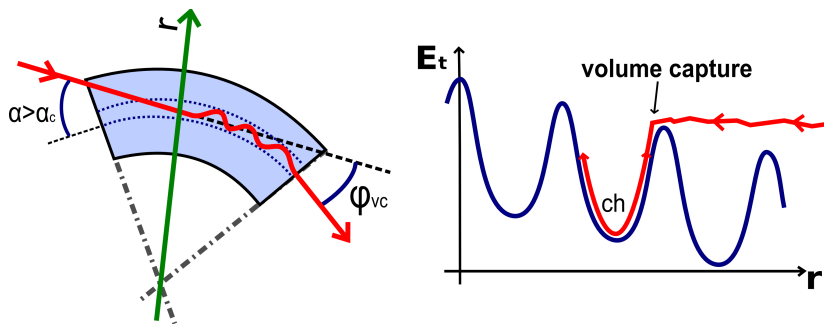


Figure 1.8: Schematic views of the Volume Capture regime in a bent crystal [1]; the particle trajectory in the non inertial frame which rotates with the channel (left) and in the phase space (right) are shown.

The number of particles undergoing this process (which contributes to the VR inefficiency) can be computed considering the $\delta_z = R\alpha_c$ distance, along

¹⁵Thanks to equation 1.15, at a certain radial coordinate r_t , $U_{eff}(r_t) = E_t$ and thus $\alpha = 0$.

which the particle is almost aligned with the crystal planes and could be captured into the channel, and the fact that α_c gives the angular scale allowing channeling; the following estimation for the VC probability holds [2]:

$$P_{VC} = \frac{\delta z}{L_D} = \frac{R\alpha_c}{L_D} \propto \frac{R}{(pv)^{3/2}} \quad (1.21)$$

where L_D derives from the fact that the DCH probability (P_{DCH}) is equal to the VC probability (P_{VC}), thanks to the reversibility rules, while the last proportionality is given by the dependence of both α_C (equation 1.3) and L_D (section 1.1.1.3) from the particle energy¹⁶;

- the particle transversal direction is elastically reversed by the interaction with the potential barrier resulting in the VR condition (figure 1.9).

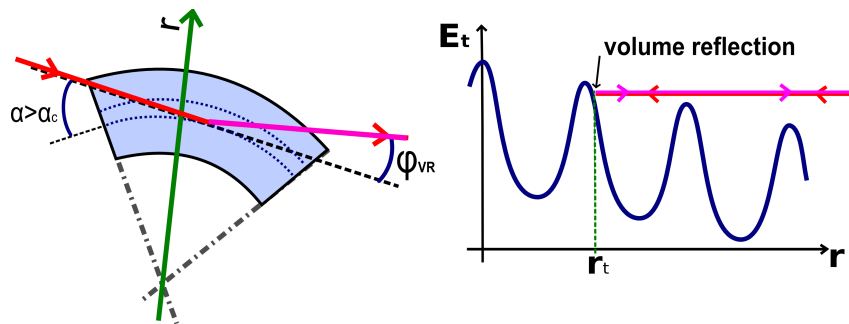


Figure 1.9: Schematic views of the Volume Reflection regime [1]: the particle trajectory in the non inertial frame which rotates with the channel (left) and in the phase space (right) are shown.

As shown in the left part of figure 1.9, VR takes place, as well as VC, when a particle enters the crystal misaligned with its planes so that the transversal energy overcomes the potential barrier; the particle is not channeled and crosses the crystal approaching the tangency point r_t with the channel with a trajectory similar to the VC one (red lines in the right part of figures 1.8 and 1.9). However, with respect to the VC case, the transversal energy fluctuations in the VR regime are not able to cause the particle confinement in the CH condition: in this point the particle has no longer a transversal

¹⁶A more rigorous expression for the VC probability is given by [2] which introduces a numerical correction factor:

$$P_{VC} = \frac{\pi}{2} \frac{R\alpha_c}{L_D} \quad (1.22)$$

This formula has been confirmed in [39] with a 10-20% accuracy [2].

kinetic energy thus it reverses the motion under the influence of the interplanar potential (pink line in the right part of figure 1.9). In other words the reflection can be described in two steps: the particle is first stopped by the potential barrier and then re-accelerated in the opposite direction; moreover, from figure 1.9-right, it is clear that the transversal energy of the reflected particle is too large to trap the particle into the CH regime so that it follows the direction assumed after the reflection.

According to equation 1.4, the VR deflection angle is proportional to the CH critical angle through the factor 1.5 which includes both the effective position in the channel in which the particle enters and leaves the crystal and the bending of this latter which deforms the effective potential [33]. In particular, a study of the VR features in terms of deflection angle and inefficiency as a function of the crystal curvature [1, 40] has shown that:

- * the VR deflection angle ϕ_{VR} (black dots and red squares in figure 1.10) linearly increases with R until it reaches a *plateau*; as shown in figure 1.6, since the deformation of the interplanar potential is larger for a small curvature radius, the effective planar potential tends to a straight line (which means a smaller depth of the potential wells which reduces the crystal confinement strength);
- * for the same reasons, the VR angle rms σ_{VR} (pink and blue triangles in figure 1.10) becomes smaller; moreover the increase in the spread of the electric field strength near the turning points in the effective potential is responsible of the larger σ_{VR} values for small curvature radii;
- * the VR inefficiency ϵ_1 (black dots and red squares in figure 1.11) linearly increases with the crystal curvature radius in agreement with equation 1.21; the other analytical curve ϵ_2 represents the percentage of the volume captured particles.

Summarizing, the larger R , the larger ϕ_{VR} ; the larger R , the smaller ξ_{VR} and $\Delta\alpha_{VR}$. Thus, to obtain the same acceptance, the crystal length should be increased but the particle loss in inelastic interactions with the crystal nuclei should be kept under control. The optimal bending radius for short Si crystals could be thus defined as $10R_c$ [33] which maximizes both the deflection angle, the VR efficiency and the angular acceptance.

As mentioned above, the VC and VR effects are very similar: the particle becomes aligned with the crystal planes while crossing its volume and its energy transversal component equals the $U_{eff}(r_t)$ value. Nevertheless, as stated by equation 1.21, the VC effect scales with the particle energy approximately as $E^{3/2}$ and

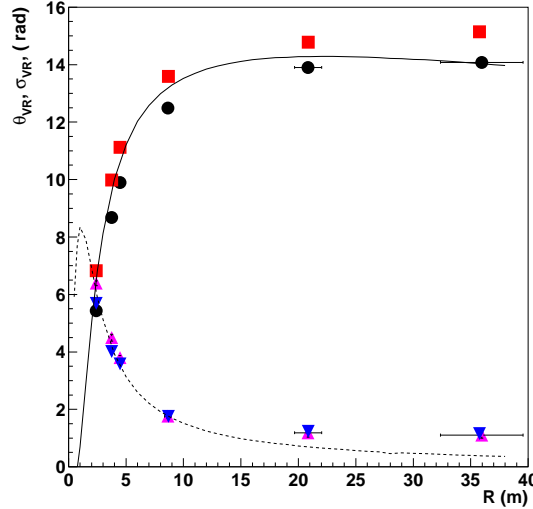


Figure 1.10: The mean VR angle ϕ_{VR} and its rms σ_{VR} as a function the crystal curvature radius [1]; the experimental data (black dots and pink triangles for the mean and the rms, respectively), the simulation data (red squares and blue triangles) and the analytical curves (continuous and dashed) are shown for comparison.

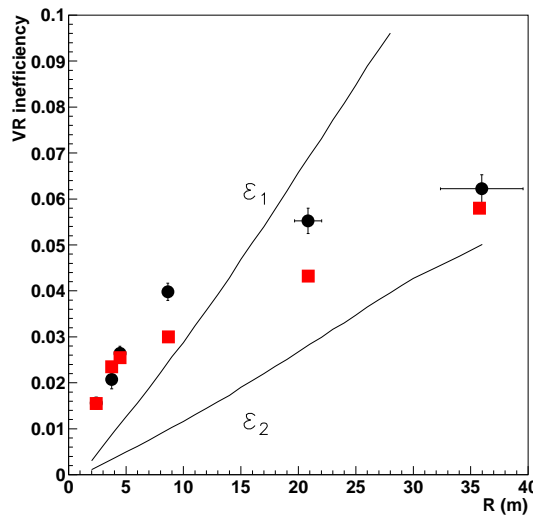


Figure 1.11: The VR inefficiency ϵ_1 as a function the crystal curvature radius [1]; the experimental data (black dots), the simulation data (red squares) and the analytical curve (continuous) are shown for comparison. ϵ_2 represents the probability to enter in the stable channeling condition (VC regime).

thus it is less probable at high energies; on the other hand VR becomes the dominant effect and almost all the particles are subject to VR as experimentally proved at 400 GeV/c [1] with the crystal used in figure 1.2(b).

1.1.1.5 Crystal “advanced” effects

As shown in the previous section, the VR effect allows to deflect high energy particle beams with a very high efficiency and offers a larger angular acceptance than the one for CH; on the other hand its smaller deflection angle, together with the dependence of this latter on the intrinsic crystal properties, strongly limit the VR capabilities.

For these reasons, in recent years different solutions to increase the VR deflection angle (while maintaining a large enough deflection efficiency) have been studied in computer simulations and experimentally tested:

- the **Multi VR in a sequence of crystals (MVR)** (figure 1.12(a)) consists in the use of a series of many crystals aligned between each other; in this way a particle, crossing the sequence of crystals, is subjected to a series of reflections, resulting in a larger deflection angle.

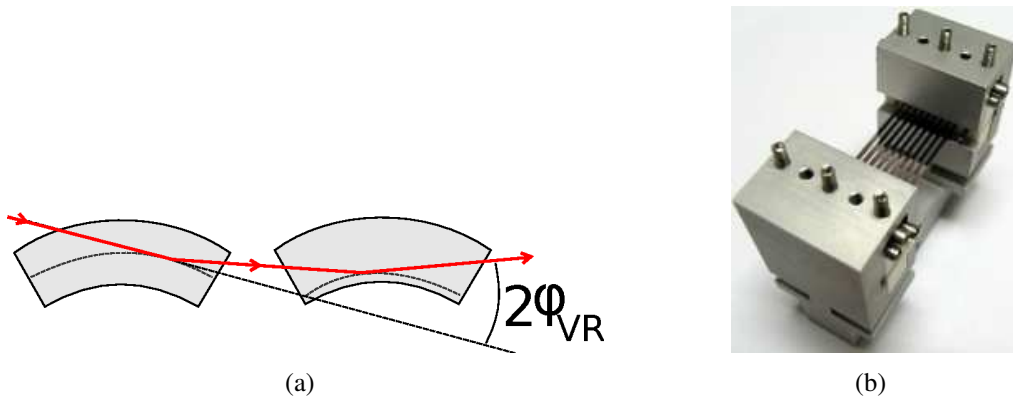


Figure 1.12: (a) Schematic view of the Multiple Volume Reflection in a couple of bent crystals [1]; (b) photo of an array of 9 silicon strip crystals [1].

The feasibility of this technique, both with positive and negative particles, has been tested and experimentally proven in 2008 [1, 41] using a series of multi-strip crystals (like the one shown in figure 1.12(b)): 400 GeV/c protons have been deflected of a $67.5 \pm 0.5 \mu\text{rad}$ angle with 92% efficiency while a $79.5 \pm 1.0 \mu\text{rad}$ deflection angle and a 87% efficiency have been measured with 150 GeV/c electrons at the CERN H8 and H4 beamlines, respectively; in both cases only 5 strips of the whole crystal array were properly aligned to exploit the MVR effect [1];

- on the other hand, going to the “second crystal dimension” (*i.e.* rotating it along the vertical direction), the so-called **axial effects** offer the possibility to drive particles that are spinning around the axes or to reflect them in several planes inside a single crystal. In particular, two main effects have been studied up to now:
 - * the *Axial Channeling (ACH)* in which the particle is aligned with respect to the planes and is moving at a small angle with respect to the crystal atomic string (left part of figure 1.13(a)); in this condition the particle feels an electric field with a cylindrical symmetry distribution (right part of figure 1.13(a)). The interesting feature of ACH is twofold:
 - the critical angle is larger (of a factor 2-3) than the one for the planar case [2] which means a larger angular acceptance; nevertheless it increases the probability for dechanneling for negative particles;
 - the undeflected component of the beam is practically absent as experimentally demonstrated in [42] where the results are compared with a Montecarlo simulation.
 - * the *Multi VR in One Crystal (MVROC)* where deflection angles up to 5 times larger than ϕ_{VR} could be reached [1]. It is based on the possibility that, under specific alignment conditions and using properly designed crystals, the volume reflections due to the main vertical plane and the corresponding skew ones take place subsequently during a single crystal crossing thus increasing the final value of the deflection as shown in figure 1.13(b). This effect has been theoretically described in 2007 [43] and experimentally demonstrated in 2009 [44] on the H8 beamline with 400 GeV protons.

1.2 Bent crystals applications

The intention of the following sections is to give to the reader a few hints on the possible applications of the bent crystals physics, focusing the attention on the high energy beam manipulation¹⁷. Crystals are, in fact, easy to use and compact,

¹⁷For completeness, bent crystals are also used in medicine and biology; in particular, the so-called *microbeams* (very small size particle beams in the mm²-nm² scale) can be produced, exploiting the CH effect in bent crystals, to study the effects of a low radiation dose on single cells (or small group of cells) or to characterize a sample in terms of its composing elements through the so-called *Particle Induced X-ray Emission (PIXE)* technique (more details can be found in [1] and the literature therein).

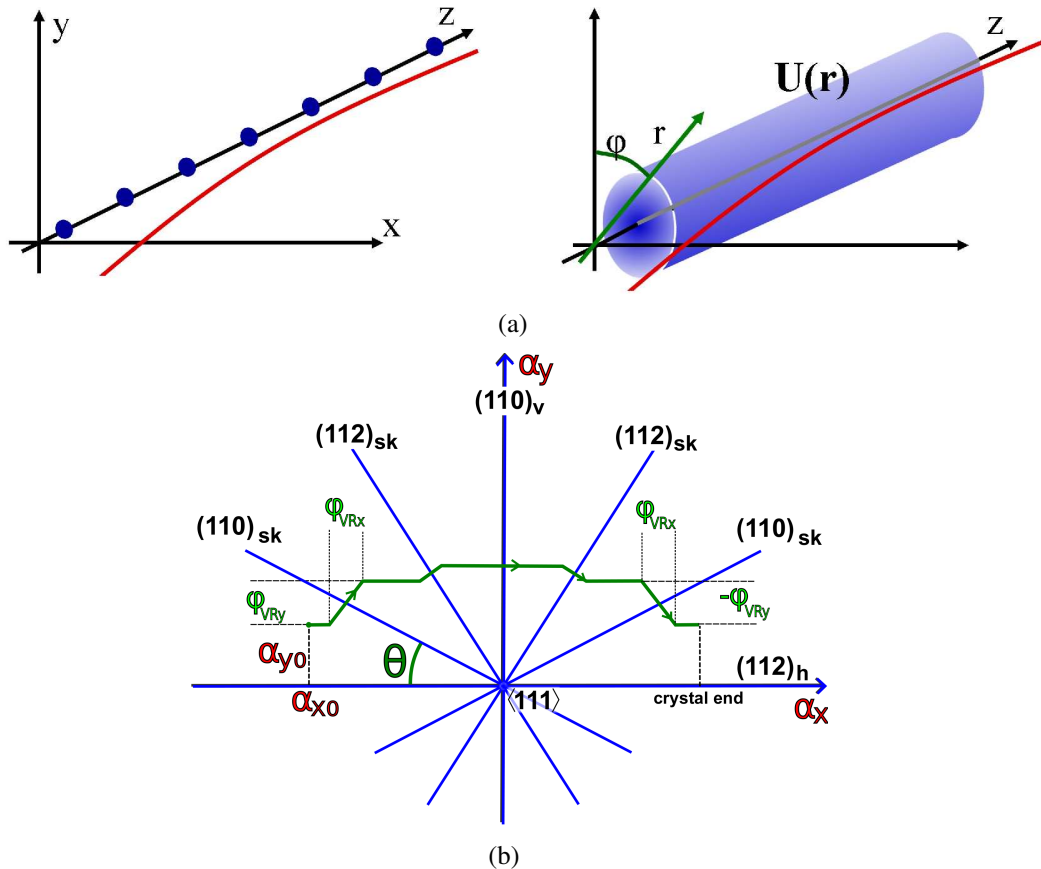


Figure 1.13: (a) A particle (right) aligned with the crystallographic axis and trapped in the Axial CHanneling regime by the corresponding continuous potential (left) [1]. (b) The Multi VR in One Crystal principle (shown in the phase space of the horizontal and vertical misalignment) [1]: the blue lines represent the crystalline planes (the main and the skew ones) while the green arrow is the trajectory of a particle initially misaligned with respect to the axis (of α_{x0} and α_{y0}) and subject to MVROC.

their behaviour is predictable and reliable and they have been demonstrated to be radhard [29, 45, 46].

Starting from the techniques commonly used for the manipulation of the extracted beams (*beam splitting* and *focusing*, section 1.2.1), the attention will be focused on the current hot topic in high energy particle physics (the *crystal-based extraction/collimation systems*, section 1.2.2) to arrive to the possibility to produce *intense photon beams* (section 1.2.3) thanks to the coherent radiation generated by light charged leptons crossing bent crystals [19–24].

1.2.1 Extracted beam manipulation

Since Tsyganov's idea in 1976, the bent crystals promising properties, together with their very small sizes and compactness (compared to the magnet dipoles ones), were rapidly exploited to manage extracted particle beams [2]. In particular, bent crystals are used in two main fields:

- the crystal *beam splitting* technique¹⁸ has been used since 1988 at the IHEP laboratory to share the 70 GeV proton beam between several experimental areas (where different experiments can be carried out simultaneously [2]). Figure 1.14(a) shows the layout of the IHEP crystal beam splitting station: the crystal splitter, placed in a pre-existing bending magnet (M4) and aligned in the CH regime, is able to deflect the proton beam up to 59 mrad [2] and divide it between two experimental zones (channel 21 and 23);
- on the other hand, bent crystals are efficiently used since 1985 as *beam focusing* devices [47]: a crystal bent in such a way that the directions of the crystalline planes converge towards a focal point (figure 1.14(b)) allows not only to deflect a particle at a given angle but also to focus it. For instance, as shown in figure 1.14(c), the Full Width Half Maximum (FWHM) of the 1 GeV proton beam at the synchrocyclotron of LINP¹⁹ has been reduced from 15 ± 0.1 mm down to 0.65 ± 0.05 mm using a 44 mm thick bent silicon crystal [47].

¹⁸Typically, a beam splitter consists in electrostatic or magnetic splitters which require a considerable space [2].

¹⁹Leningrad Institute of Nuclear Physics, now Petersburg Nuclear Physics Institute (PNPI), Gatchina (Russia), <http://www.pnpi.spb.ru/index.html.en>.

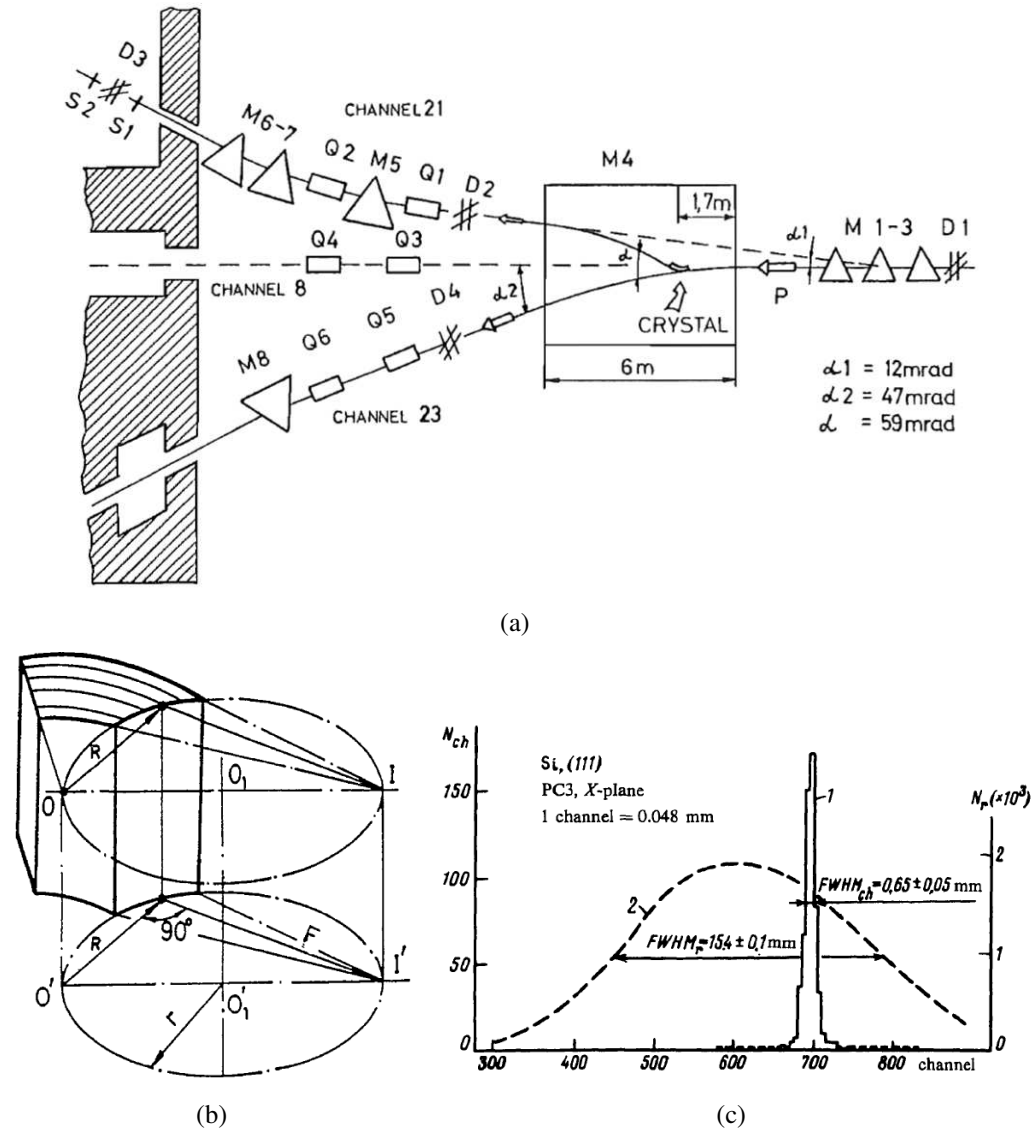


Figure 1.14: (a) Schematic view of the beam splitting station installed at the IHEP laboratory [2]: M1-8 are bending magnets, Q1-6 are quadrupoles, D1-4 are beam profilometers and S1-2 are scintillator counters. (b) The principle of beam focusing with a bent crystal [2] and (c) the 1 GeV proton beam at LINP focused by a 44 mm thick silicon bent crystal [47].

1.2.2 Beam extraction and beam collimation

Among the bent crystals applications, the most attractive one is the possibility to extract or collimate high energy particle beams²⁰. In both cases, the basic principle is the same (as shown in figure 1.15): a crystal (oriented in different regimes) intercepts the beam halo deviating it from the circular trajectory. At this point:

- the deflected beam is lost on an absorber (collimation case); typically the so-called *Target Aperture Limitation (TAL)* secondary collimators²¹ are used for this purpose;
- the extracted beam is sent to a Bending Magnet (BM) that brings it to the experimental areas (extraction case).

In both cases, the crystal acts as a *clever kicker* without spreading the beam halo over the whole solid angle (which is the main limit of the standard multi-stage collimation systems²²) but directing it towards a given direction (*i.e.* on the TAL absorber or on the BM that serves an experimental area). Moreover, crystal assisted extraction and collimation present several benefits with respect to the classic methods [45]:

- they can work in *parasitic mode*, *i.e.* they allow at the same time the operation of a collider and the production of an extracted beam;
- since the extraction mechanism does not use a resonant method, the extracted beam has an almost flat time structure;
- very small beam sizes and regular beam shapes can be obtained;
- polarized beams can be extracted without affecting the polarization of the main circulating beam;
- several different design schemes can be used to obtain the required beam deflection and efficiency; for instance:

²⁰The collimation system is an essential apparatus in particle accelerators and, in particular, for the Large Hadron Collider (LHC) one [29]. Its role is to reduce the so-called *beam halo*, *i.e.* the external region of the beam populated by those particles which are leaving the nominal orbit because of the scattering on the residual gas or the beam-beam interaction. The halo reduction thus represents a crucial aspect for modern accelerators since halo particles cause equipment damages, residual radiation and large experimental backgrounds [1].

²¹At LHC \sim 1 m long tungsten absorbing blocks are used; at the low energy of the U-70 IHEP ring, stainless steel 250 cm long absorbers are exploited [46].

²²They are based on amorphous targets which spread the primary halo; the resulting secondary halo is in turn directed to a secondary collimator [28].

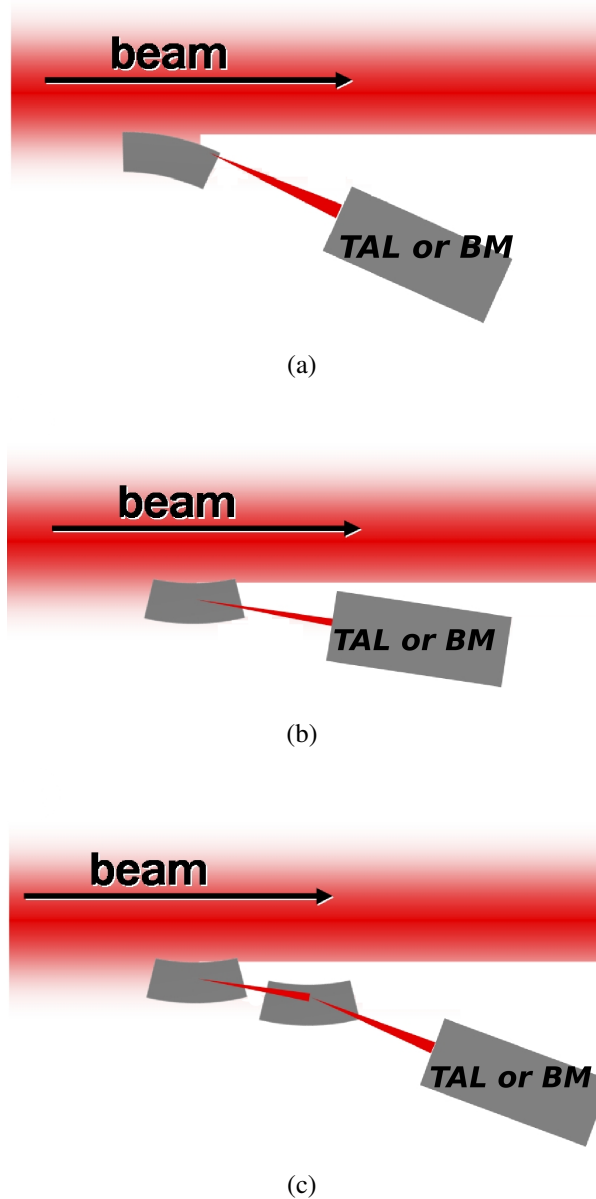


Figure 1.15: Schematic views of three possible beam extraction/collimation systems (adapted from [1]): (a) the CH, (b) the VR and (c) the MVR regimes are considered.

- * crystals oriented in the CH condition (figure 1.15(a)) are used to deflect the halo very far from the circulating beam and with a large enough efficiency;
- * on the other hand the systems based on crystals aligned in VR or MVR regimes (figures 1.15(b) and 1.15(c)) allow to obtain larger extraction efficiency values;
- both the extraction and the halo collimation can be exploited in a broad range of energies, from the sub-GeV cases (*i.e.* for medical accelerators) to the multi-TeV machines.

Given these advantages, crystal-based extraction and collimation have rapidly progressed thanks to the effort of several worldwide research centers [48]: JINR [49], FNAL²³ [50–52], IHEP [46, 53], CERN [54–58] and BNL²⁴ [59]. As summarized in table 1.2, a very large energy range has been investigated across the last three decades with the aim to increase the extraction/collimation efficiency ξ_{coll} (defined as the ratio of the beam intensity measured in the external beamline or at the TAL station over the total beam loss as measured in the entire ring [45]) and test the crystal lifetime eventually reduced by the particle power deposit.

Research center	Year	Energy range [GeV]	Particle type	ξ_{coll} [%]	Reference
JINR	1984	4.2 - 7.5	p ⁺	10^{-4}	[49]
FNAL	1985	up to 400	p ⁺	10	[50]
IHEP	1989	up to 70	p ⁺	1	[53]
CERN	1990-2000	up to 270	p ⁺ , Pb ions	0.55-50	[54–56]
FNAL	1994-1996	900	p ⁺	25	[51]
IHEP	1997-2000	up to 70	p ⁺	60-85	[46]
BNL	2001-2003	900	p ⁺ , Au ions	25	[59]
FNAL	2005-2011	980	p ⁺	70	[52]
CERN	2009-2015	120	p⁺, Pb ions	75-85	[57, 58]

Table 1.2: Experiments performed in the last 30 years to prove and investigate the crystal-based extraction/collimation technique. The CERN-UA9 experiment [57, 58] (which is the last frontier in this field) is shown in red.

Efficiency values up to 85% have been obtained mainly thanks to:

²³Fermi National Accelerator Laboratory, Batavia (USA), <http://www.fnal.gov/>.

²⁴Brookhaven National Laboratory, Upton (USA), <http://www.bnl.gov/world/>.

- the discovery and the subsequent study of the so-called *multipass mechanism* [46, 55]. It takes place in a circular accelerator where the particles stay on the same orbit for many turns; when a crystal is put in the beam halo with the correct orientation for CH or VR and a particle crosses it without being channeled, the particle has anyway a new possibility of being channeled the next turn and so on; the net result is an increase of ξ_{coll} ;
- the improvement in the fabrication and the following tests²⁵ of a *new generation* of bent crystals and holders [46, 52]:
 - * on one side, the so-called *STrip-like (ST)* crystals (figure 1.16(a)), which have a small thickness along the beam direction, have allowed to reduce both the MCS and the nuclear interactions in the crystal itself; in this way the average number of particles crossings in many turns and ξ_{coll} increase;
 - * on the other hand, the so-called *O-Shaped (OS)* crystals (figure 1.16(b)) have provided a further increase of ξ_{coll} thanks to the reduction of the crystal torsion;
 - * finally, the so-called *QuasiMosaic (QM)* crystals (figure 1.16(c)) have opened the way to the manipulation of low energy particle beams [60].

As far as the crystal lifetime is concerned, several experimental tests have been performed both at IHEP and at CERN together with computer simulations²⁶:

- IHEP crystals [45] with a different thickness along the beam direction were exposed to particle fluxes up to 10^{13} - 10^{14} proton hits/s for a time interval between 0.5-1 s and several minutes without significant changes in the CH efficiency nor a clear presence of radiation damages. Moreover one of the crystals has served for extraction for 10 years (from 1989 to 1999) without replacement [46];
- at CERN with 450 GeV/c protons and fluxes up to 10^{20} protons/cm² [56, 61] the crystal lost only 30% of its deflection efficiency, which means ~ 100 years lifetime in the so-called *H8 microbeam* environment before the crystal needs replacement;

²⁵Moreover, Monte Carlo simulations were performed to study the crystal extraction/collimation at the CERN SPS (Super Proton Synchrotron), FNAL, BNL and IHEP: ξ_{coll} could be raised up to 90% mainly thanks to the shortening of the crystals (more details can be found in [46] and the literature therein).

²⁶Moreover, different materials (W, Mo and diamond), together with the typically used ones (Si and Ge), have been considered and tested both from the mechanical (ease in bending) and purity point of view (low mosaic spread and low dislocation density) together with their radiation hardness [29, 48, 56].

- proper scaling of the IHEP results showed that a Si crystal would meet operations in the strict LHC environment with a considerably large safety margin, considering a LHC bunch of 10^{11} protons and the fact that the IHEP crystals showed to withstand to an instant dump of 1000 bunches [29].

1.2.3 Crystals as high intensity γ -ray sources

This section briefly summarizes some applications of the coherent radiation emitted by bent crystals oriented in the CH or VR condition, without analyzing its theoretical aspects which can be found in more detail in [1, 62].

As already mentioned, bent crystals offer great advantages not only thanks to their very promising deflecting properties but also as high intensity sources of γ -rays. The coherent aspects characterizing the interaction of a particle crossing a straight/bent crystal, in fact, do not affect only the particle trajectory but also the way it loses energy while travelling through the crystalline medium [2, 62].

Since 1950 many experimental and theoretical studies have been dedicated to the investigation of the photon emission by relativistic light leptons crossing straight crystals (see [14–18] and the literature therein); these studies have demonstrated the strong difference of the electromagnetic processes in crystals with respect to the ones in amorphous media [62]. Nevertheless this phenomenon and the resulting applications, in particular in bent crystals, are still under investigation [19–24].

As mentioned in section 1.1, CH and VR phenomena are very different from the deflection point of view: the small deflection angle of VR is compensated by its excellent deflection efficiency and angular acceptance; CH offers larger and adjustable deflection angles at the expense of a smaller efficiency. Nevertheless, when the coherent radiation emission is taken into account, their description becomes similar. In both cases the microscopic interaction with the interplanar potential plays the main role producing an oscillation in the transversal direction with respect to the motion [1, 20, 62]:

- in the CH regime the particle transversal energy is smaller than the potential barrier and the particle performs a quasi harmonic oscillation (figure 1.17 left) whose amplitude depends on the initial transversal energy value [26]; moreover, the particle energy loss via ionization (MCS with the nuclei) is strongly suppressed with respect to the one given by radiation emission;
- in the VR condition the transversal energy exceeds the potential barrier so that the particle crosses the crystalline planes in an almost regular sequence (figure 1.17 right).

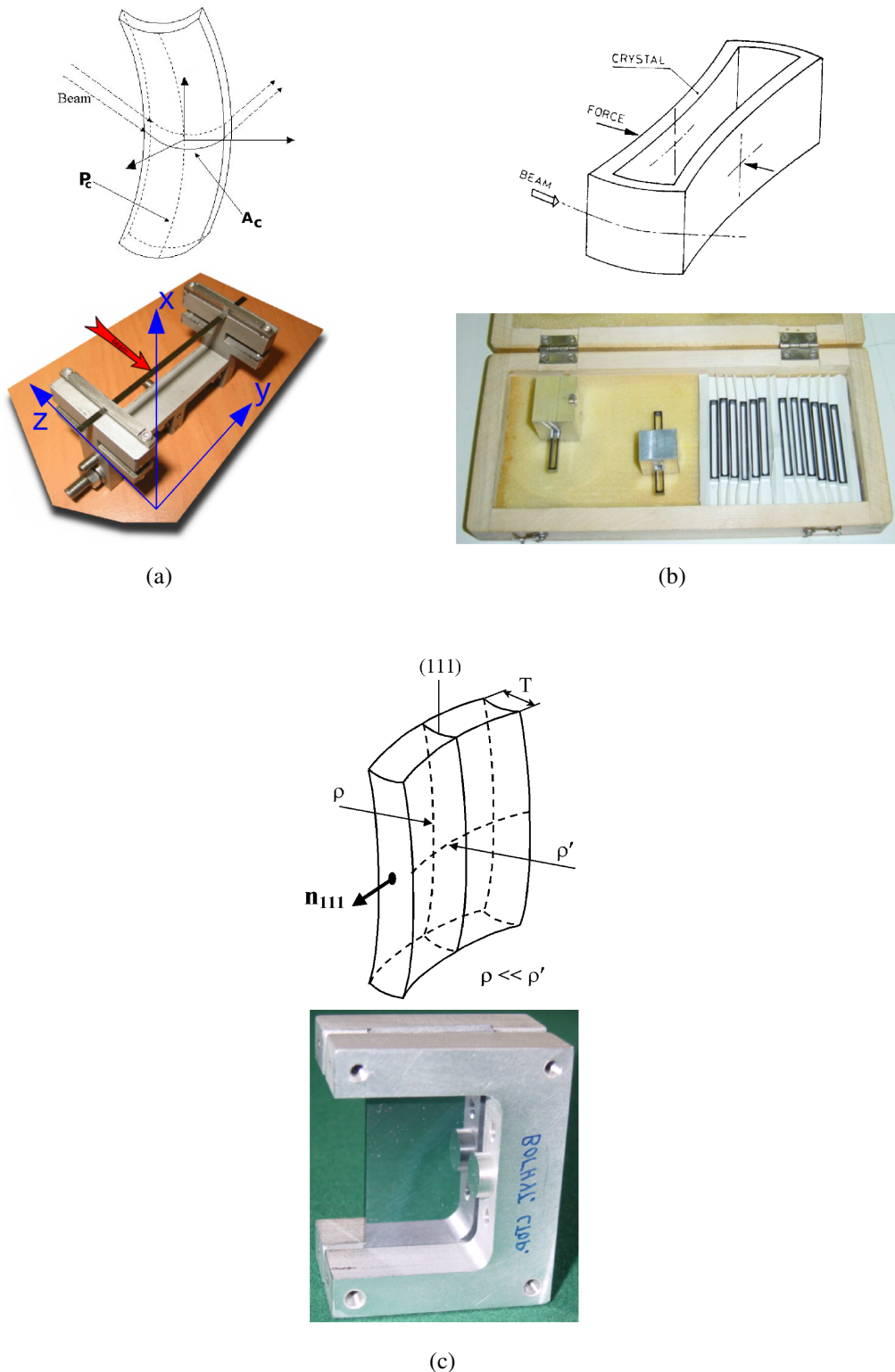


Figure 1.16: Schematic views and photos of three different bent crystals designs: (a) the *Strip-like* (*ST*), (b) the *O-Shaped* (*OS*) and (c) the *QuasiMosaic* (*QM*) one.

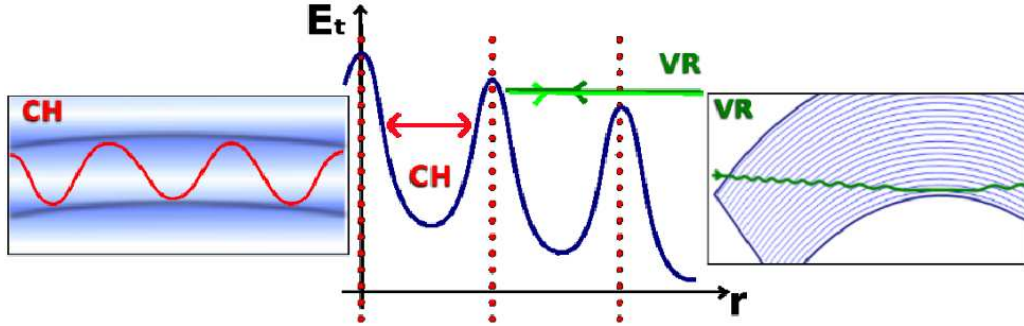


Figure 1.17: Trajectories of a channeled (left) and a volume reflected (right) particle inside a bent crystal; also the quasi harmonic interplanar potential is shown (center) [20].

In both cases the net result is the emission of an intense radiation whose spectrum, depending on the particle energy, can present several peaks which correspond to the different harmonics of the oscillation [1, 62].

As far as the applications are concerned, there are many proposals to exploit the enhancement of the radiation emission in straight/bent crystals properly aligned in the CH or VR condition [1]:

- the most attractive is certainly the possibility to produce *high intensity/high energy photons* through the coherent interactions both in straight and bent crystals. With respect to the standard γ -ray beam production methods, in fact, crystals offer the possibility to generate much more intense beams of γ -rays²⁷ and cover a wider energy range. In addition to that, a peaked structure spectrum and highly polarized γ -ray beams can be obtained;
- at the same time also the $\gamma \rightarrow e^+ + e^-$ conversion in crystals is enhanced, resulting in a “compact” electromagnetic shower that allows to increase the number of emitted positrons without depositing too much energy in the medium. This idea represents a great advantage for the next e^+/e^- colliders (*e.g.* the future ILC²⁸ and B factories) which will require an increased beam intensity that in turn corresponds to the development of a more powerful positron source. Tests on the crystal-based positron source have been successfully performed at the KEKB injector linac²⁹ showing a $\sim 25\%$ in-

²⁷Typically the standard way to produce high energy γ -ray beams is the use of bending magnets where high energy electrons lose their energy via bremsstrahlung; even if high energy end-point spectra can be produced, this technique does not allow to generate high intensity beams [1].

²⁸International Linear Collider, <https://www.linearcollider.org/ILC>.

²⁹Kō Enerugi Kasokuki Kenkyū Kikō, High Energy Accelerator Research Organization, Tsukuba (Japan), <http://www.kek.jp/en/>.

crease in the positron yield and a $\sim 20\%$ reduction of the heat load on the target [63] compared to that for a conventional tungsten plate (figure 1.18);

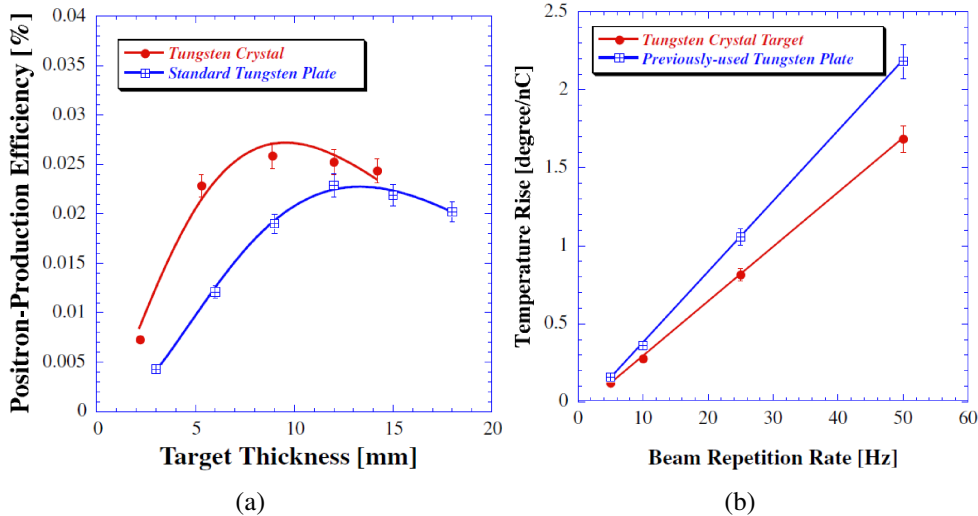


Figure 1.18: The crystalline positron source used at KEKB compared with a standard one based on a tungsten plate [63]: (a) the e^+ production efficiency as a function of the crystal/plate thickness and (b) the normalized targets temperature rise as a function of the beam repetition rate.

- on the other hand, the strong dependence of the CH radiation emission from the incoming particle mass can be exploited for Particle IDentification (PID) at very high energy where the standard methods (Cherenkov counters or Transition Radiation Detectors - TRDs) cannot be used; the PICH³⁰ program [64] at CERN has recently proven this technique (figure 1.19);
- the use of bent crystals opened new ways for the photon production: the increased angular acceptance in the VR condition, the possibility to control the number of particles undergoing a certain effect (the so-called *tagging capabilities*) and the development of new crystal types (the so-called *Crystalline Undulators (CU)* [65], figure 1.20) allow, on one side, to apply the above described techniques to low energy/low collimated beams and, on the other hand, to further increase the emitted radiation intensity.

³⁰Particle Identification with CHanneling radiation.

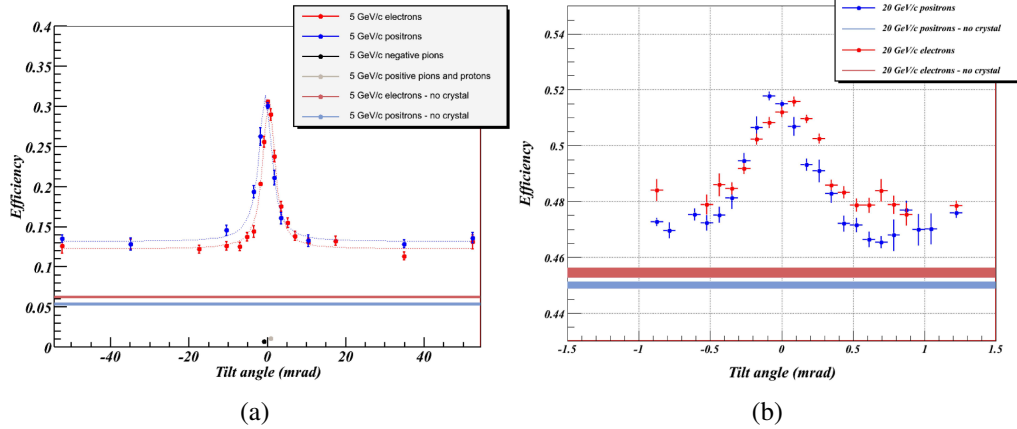


Figure 1.19: Experimental results of the PICH program [64]: the photon efficiency (defined as the number of particles emitting a detected radiation, over the total acquired ones) as a function of the misalignment between the crystal and the incoming beam. At small angles a clear enhancement in the emitted radiation can be seen for electrons and positrons of (a) 5 GeV/c and (b) 20 GeV/c momentum.

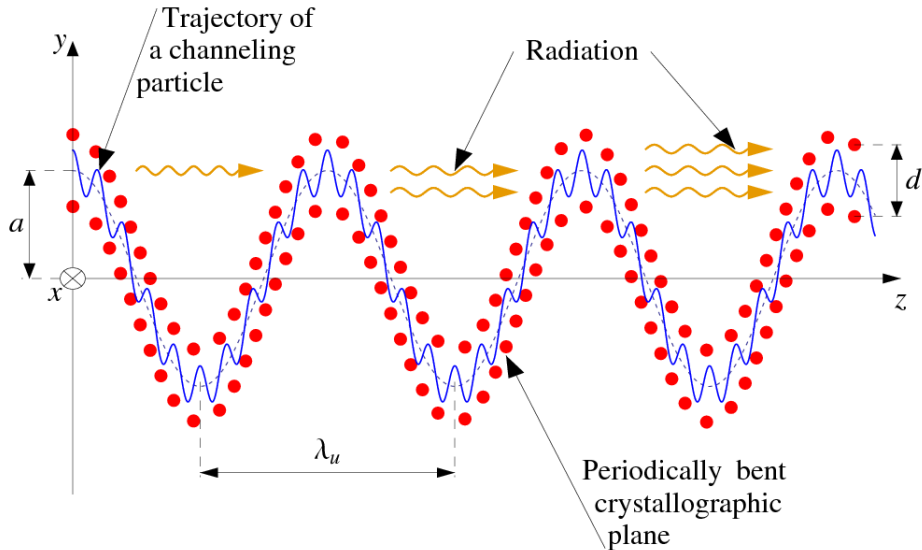


Figure 1.20: The *Crystalline Undulators (CU)* working principle [1]. The nuclei forming the bent crystalline planes are shown in red, the blue line is the channeled particle trajectory, d is the interplanar distance while a and λ_u are the oscillation amplitude and period, respectively: the radiation emitted at each oscillation adds coherently.

1.3 The role of tracking in crystal physics

As can be seen from section 1.1, the investigation of the bent crystal effects requires high precision measurements: CH and VR are, in fact, identified by relatively small deflection angles and occur for small angular acceptances (both of the order of hundreds of μrad). To provide a complete and high precision characterization of a sample (straight or bent) the whole setup must comply with two main requirements [2]:

- to have a large enough *repeatability*; for this reason high precision goniometric systems are used to rotate the crystals with an angular translation comparable to the CH critical angle (few μrad in the GeV energy range [2]); for instance the ones described in [1, 25] or in this thesis work (section 5.3.2) allow to align the samples with a 2-5 μrad precision;
- to measure the particle distribution with very high *angular precision* that in turn corresponds to have a particle position reconstruction system with a very high *spatial resolution*, close to the physical limit of the bent crystal effects; for instance the ones presented in chapters 3 and 5 have a 4-8 μm spatial resolution [27, 66].

The setups typically used nowadays in bent crystal physics studies [1, 57, 60] completely meet the two above mentioned requirements; nevertheless, to achieve a good enough performance, it took more than 30 years and a multi-stage process, that has registered a turning point in 2006 when, for the first time, real time position sensitive detectors were used to reconstruct the *single particle track* [25].

1.3.1 From the emulsion plates to the high precision measurements: why a *full tracking system*?

As described in [2, 67], the first channeling experiments were typically based on integrated measurements to estimate the deflection angles and the efficiency values of the various crystal effects. During the last three decades, special methods for the identification of the channeled, reflected and non-channelled particles have been tested and improved:

- on one side, the anomalous ionization loss (up to \sim 60% less [2] with respect to an amorphous material) has been used to study the CH effect in straight crystals (where the non channelled particles overlap the channelled ones). In this case the crystals themselves have served for the identification of the different crystal regimes: as described in [68], Ge or Si crystals were doped with B ions, a 200 \AA Al layer was deposited as a back contact for the biasing and the crystals were used as solid state ionization detectors;

- on the other hand, in bent crystals (where the CH portion is clearly separated from the non channeled and the VR ones) the angular dependence of the different regimes has been used (and nowadays is the most used technique) to study the crystals properties. For these purposes different strategies (whose pros - red - and cons - green - are summarized in table 1.3) have been tested with the aim to increase the measurement precision at the same time minimizing the time needed to collect the required statistics and to perform the data analysis [2]:
 - * at first, sets of *Drift Chambers (DCs)*, together with a system of coincidence/anticoincidence counters and/or crystals operating as dE/dx detectors, were used soon after the bent crystal physics birth (in 1976) allowing a spatial resolution up to $\sim 100 \mu\text{m}$;
 - * later, thanks to their very high spatial resolution (up to $\sim 1 \mu\text{m}$), *Nuclear Emulsions (NEs)* were used both for the investigation of the crystals imperfections and to disentangle the different crystal effects; for instance, the first experimental evidence of the VR effect in 2006 [12] has been measured with 2 R-100 emulsions placed downstream the crystal and exposed to an integrated flux of 5 particles/ μm^2 (figure 1.21);

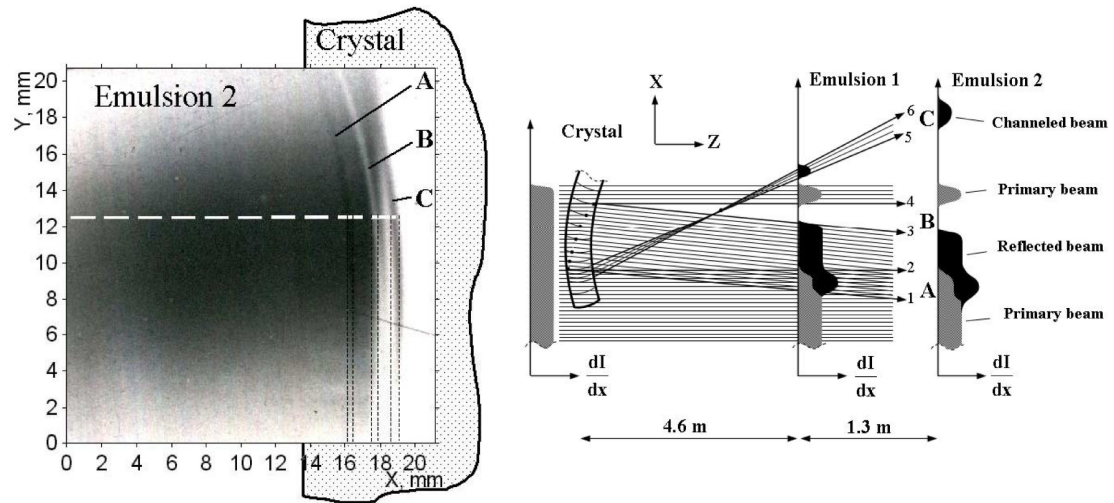


Figure 1.21: The 70 GeV IHEP proton beam reconstructed with a nuclear emulsion as described in [12]: the three different regions, named A, B and C correspond, respectively, to the reflected, the primary and the channeled portion of the beam (as schematically reported in the right part).

- * at last, as already mentioned above, the real breakthrough is represented by the use of tracking/profilometry systems based on high spa-

tial resolution *Silicon Detectors (SiDs)*. They allowed, in fact, to reach the desired spatial accuracy (see for instance figure 1.2(b) or [1, 25, 60, 66]) and, at the same time, a strong reduction of the time needed for both the measurement and the data analysis phases together with a greater compactness of the whole system. For these reasons, the real time systems have completely replaced the previous integrated measurements, making the crystal physics more precise and fast.

System	Resolution	Device & DAQ	Data analysis
DCs	Good ($\sim 100 \mu\text{m}$)	Very complex	Time consuming
NEs	Very High ($\sim 1 \mu\text{m}$)	Easy	Time consuming
SiDs	High ($\sim 5 \mu\text{m}$)	Compact	Real time

Table 1.3: Comparative table between the three data taking systems typically used in crystal physics: green and red indicate the pros and cons, respectively.

Going in detail on the systems based on real time silicon detectors, depending on the beam conditions (energy, dimensions and divergence) and on the available space in the experimental area two more considerations can be made³¹:

- beam profile integrated measurements (figure 1.22(a)), where the beam impinges on a crystal placed on a goniometer and the different components are detected downstream by SiDs [60, 66], are the ideal ones to study the crystal effect in the sub-GeV energy range. However, in this case, the reduction of the MCS contribution represents a crucial aspect imposing stringent requirements both on the beam characteristics (the beam has to be very narrow and highly collimated [1]) and on the beam collimation and alignment systems (which have to guarantee the above mentioned requirements on the beam shape and, at the same time, provide high enough beam intensity to characterize the crystals in a short time [67]);
- on the other side the capability to reconstruct the single particle track before and after the crystal (figure 1.22(b)) offers, especially at high energy, clear advantages with respect to the previous one: a larger versatility with respect to the beam conditions together with the possibility to correlate the angular information with the impact point on the crystal make this strategy the ideal one for many crystal experiments in the hundred-GeV energy range. However, even if this scheme allows to select the interesting portion of the beam (*i.e.* CH, VR, etc.) with special offline analysis methods (see for instance [1]), a low divergent and enough collimated beam is still desiderable

³¹More detailed considerations can be found in [1].

to maximize the *good* statistics, *i.e.* the number of particles that actually cross the crystal.

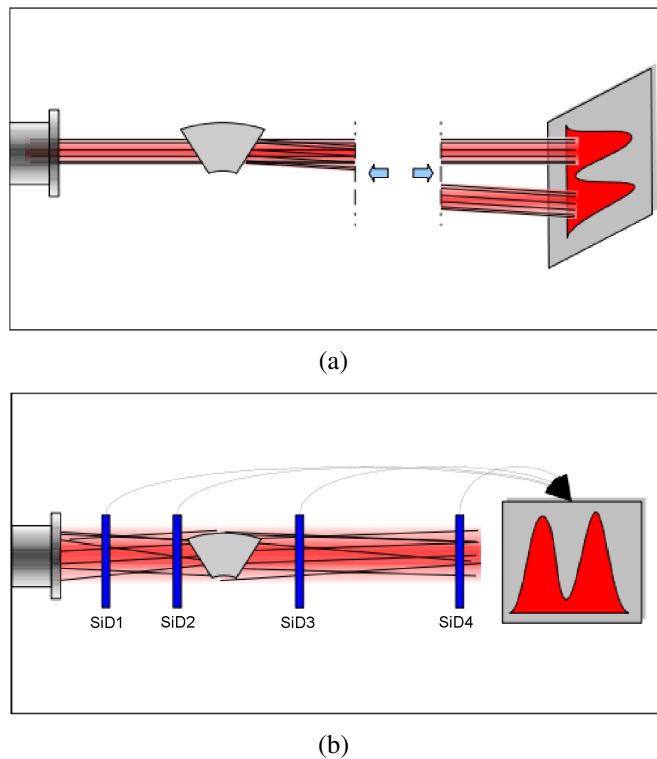


Figure 1.22: Schematic views of two strategies to perform a crystal channeling test [1]: (a) beam profile integrated measurements or (b) single particle track reconstruction (SiD1-4 are silicon detectors).

Chapter 2

Silicon detectors & electronics for tracking

Since 1980, when the German physicist Josef Kemmer introduced the planar technology¹ for the silicon detector production [71] (which in turn allowed the segmentation of the tiles themselves), high performance semiconductor based tracking systems have become essential as precise position sensitive detectors, both in fixed target or collider experiments and in space and medical physics. For instance, the modern LHC experiments exploit several m² of silicon for their tracking/vertexing detectors [72, 73]. On the other hand, in standard data taking silicon based tracking systems are extensively used to test the performances of many other types of detectors (for example calorimeters [74–76]) or more complex systems as in the bent crystal physics presented in chapter 1 [1, 20, 32, 66].

From the technology point of view, the present panorama is very wide [70, 77] and several different strategies are applied nowadays to develop very high spatial resolution (down to submicron values [78]) devices: from single and double side microstrip and pixel silicon detectors, to the high purity germanium, GaAs and diamond sensors and the ultra-thin 3D systems [70, 77, 79].

The first part of this chapter gives a brief overview of the basic properties of semiconductors and of the techniques used to improve the material quality (in terms of number of free charge carriers and conductivity). After a comparison between the most common semiconductor materials used in particle physics, the attention will be focused on the working principle and performance of the silicon based position sensitive detectors. In particular, the effect of the various technical parameters (such as the physical and the readout pitch or the charge sharing among the strips) on the detector performance (especially in terms of spatial resolution)

¹Kemmer's idea was to systematically apply the “planar” MOS (Metal Oxide Semiconductor) technology developed in microelectronics, *i.e.* the application of successive processing steps on the surface of a silicon wafer [69, 70], also in detector construction [71].

will be discussed.

The last part of the chapter is dedicated to the state of the art of the electronics used for the readout of modern silicon detectors.

2.1 Semiconductors in a nutshell

The following sections briefly review the basic properties of semiconductor materials and their electrical characteristics that make them the most important materials for electronics applications and widely used as particle detectors. A more detailed analysis can be found in [69, 70, 77, 80].

2.1.1 The intrinsic semiconductors

The key point that makes semiconductor materials so important for many different applications is their characteristic energy band structure (figure 2.1). In particular, the semiconductors peculiarity is to behave as insulators or as conductors depending on the temperature: *e.g.* they are insulators at 0 K while they are conductors at 300 K [69]. The energy band gap between the valence and the conduction bands in semiconductors has, in fact, intermediate values (table 2.1) with respect to the ones for insulators and conductors: 1.12 eV for Si, 0.66 eV for Ge and 1.43 eV for GaAs are just a few examples.

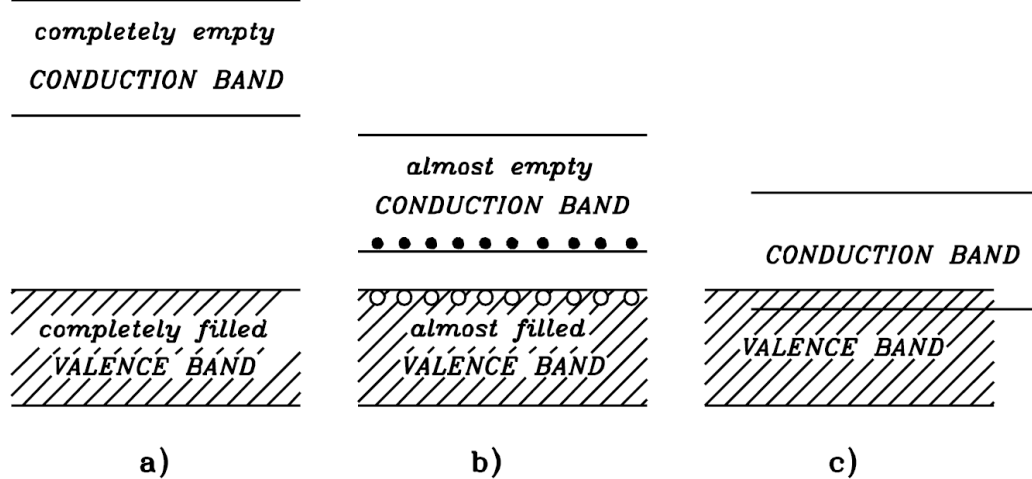


Figure 2.1: Schematic view of the energy bands structure of a) an insulator, b) a semiconductor and c) a conductor [70].

As a consequence, at room temperature, few electrons can be thermally excited into the conduction band; as a net result the semiconductor material has a

Material	Si	Ge	GaAs	diamond
Atomic number Z	14	32	31+33	6
Atomic weight A	28.08	72.60	144.63	12.01
Atomic density [cm $^{-3}$]	5.00·10 22	4.42·10 22	2.21·10 22	-
Lattice structure	diamond	diamond	zincblende	diamond
Lattice constant a [\mathring{A}]	5.43	5.66	5.65	3.57
Density ρ [g/cm 3]	2.33	5.33	5.32	3.52
Relative dielectric constant ϵ_r	11.8	16.0	10.9	5.5
Energy gap [eV]				
E_g	1.12	0.66	1.43	5.47
E_g (at 0 K)	1.16	0.75	1.52	5.51
Ionization energy [eV]	3.60	2.96	4.20	13.00
Effective density of states [cm $^{-3}$]				
in the conduction band N_C	2.80·10 19	1.04·10 19	4.70·10 17	-
in the valence band N_V	1.02·10 19	6.10·10 18	7.00·10 18	-
Mobility [cm 2 /V·s]				
electron μ_e	1500	3900	8500	1800
hole μ_h	600	1900	400	1600
Intrinsic carrier density n_i [cm $^{-3}$]	1.45·10 10	2.40·10 13	1.10·10 7	≤10 3
Minority carriers lifetime [s]	2.50·10 $^{-3}$	10 $^{-3}$	~10 $^{-8}$	-
Intrinsic resistivity ρ_c [Ω ·cm]	2.3·10 5	47.0	~10 8	≥10 12
Conductivity σ [S/cm]	5.38·10 $^{-6}$	0.0223	1.56·10 $^{-9}$	-
Breakdown field [V/ μ m]	30	10	40	2000
Fano factor F	0.12	0.13	0.10	0.08
Radiation length [cm]	9.36	2.30	2.30	12.15
[g/cm 2]	21.82	12.25	12.25	42.70
Hygroscopic	no	yes	-	no
Earth crust abundance [mg/kg]	2.82·10 5	1.5	1.90·10 1 (Ga) 1.80·10 1 (As)	2.00·10 2 (C)

Table 2.1: General properties of the most commonly used semiconductors and compound. All the values are from [69] and are at T=300 K (unless otherwise stated); the red values are from [70], the blue ones from [77], the orange ones from [81] and the green one from [82]; the conductivity has been computed as $\sigma = e \cdot n_i \cdot (\mu_e + \mu_h)$, where e is the electron charge [38].

conductivity in the 10^{-8} - 10^4 S/cm range [82]. However, these values for the conductivity are far from being ideal for particle physics applications; for this reason, the so-called *doping* procedure (section 2.1.2) is used since the '50ies both to improve and to control the semiconductor conductivity².

2.1.2 The extrinsic semiconductors and the reverse-biased p-n junction

As shown in figure 2.2, the key element of the doping procedure is to move, by introducing a minimal amount of special impurities (~ 1 - 100 ppm [82]), the Fermi energy level³ close to the conduction or the valence band obtaining the so-called *n-type* and *p-type* materials, respectively. Let's consider for instance a silicon atom⁴:

- by adding pentavalent 15th group elements, the so-called *donors* (P, As, etc), only four electrons of the dopants form a covalent bond with the Si atoms leaving the fifth weakly bound (figure 2.2(a)-left). At room temperature this excess of negative charge increases the conductivity of the semiconductor: a current flow mainly due to the movement of these *free* electrons appears and, as shown in figure 2.2(a)-right, the Fermi level moves close to the conduction band;
- viceversa, by adding trivalent 13th group elements, the so-called *acceptors* (B, Ga, etc), three covalent bonds are formed while the fourth remains incomplete (figure 2.2(b)-left). This vacancy (*hole*) is filled by an adjacent electron and so on: as a net result the holes become the majority charge carriers producing a measurable current; in this case the Fermi level shifts close to the valence band (figure 2.2(b)-right).

²The effects of semiconductor doping were long known empirically but the process was formally developed by the American engineer John R. Woodyard working at the Sperry Gyroscope Company during World War II [83].

³The Fermi level E_F , which for the intrinsic semiconductors lies in the middle of the energy band gap, is defined as the energy level with an occupation probability of 50% [69]; taking into account the dynamic equilibrium and the neutrality condition the following equation holds [69]:

$$E_F = \frac{E_C + E_V}{2} + \frac{kT}{2} \cdot \ln \left(\frac{N_V}{N_C} \right) \quad (2.1)$$

where k is the Boltzmann constant while E_C (E_V) and N_C (N_V) are the minimum (maximum) available energy and the density of states in the conduction (valence) band (table 2.1).

⁴Silicon is a semiconductor element belonging to the 14th group of the periodic table, according to the modern IUPAC (International Union of Pure and Applied Chemistry, <http://www.iupac.org/>) classification; Si atoms have a tetrahedron crystalline structure with 4 valence electrons which form covalent bonds with the neighbouring atoms.

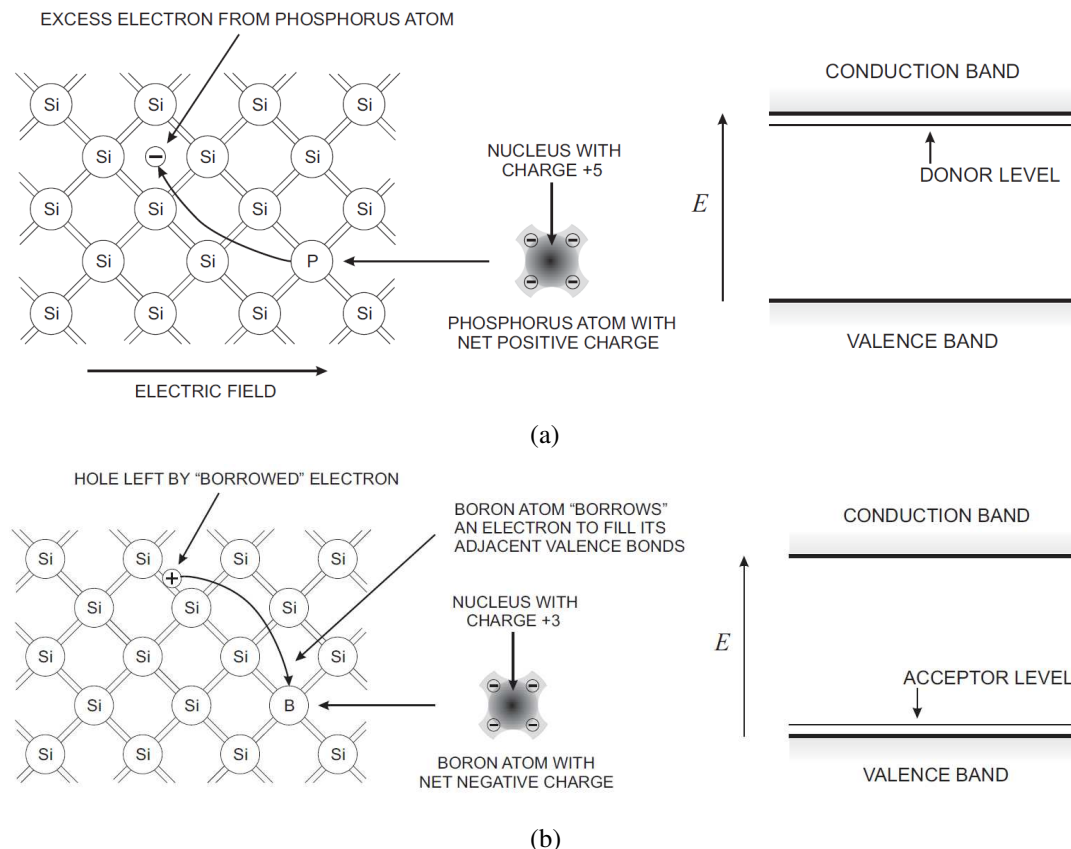


Figure 2.2: The impurities (left) and the Fermi level (right) in a doped semiconductor: (a) a n-type material and (b) a p-type one; the Fermi level is close to the conduction or the valence band, respectively.

A crucial aspect of this procedure is that, by substituting a small amount of dopant atoms, the number of charge carriers in the semiconductor strongly increases (acting in turn on the value of the conductivity): *weakly doped* silicon crystals contain only 1 impurity per 1 billion of Si atoms while *highly doped* semiconductors contain 1 dopant atom per 1 thousand of Si atoms.

The basic idea to use doped semiconductors as particle detectors is to create a carrier-free active volume, where the particles deposit their energy, and to read the signal at the edges of such a volume: the solution is to build the so-called *p-n junction* (*i.e.* a single crystal doped with both acceptor and donor atoms) and to apply a reverse bias voltage.

Figure 2.3 shows a planar reverse-biased p-n junction at the dynamic equilibrium:

- at first, when the p- and n-type materials get in touch, the initial charge carriers gradients in the contact zone cause the electrons to diffuse toward

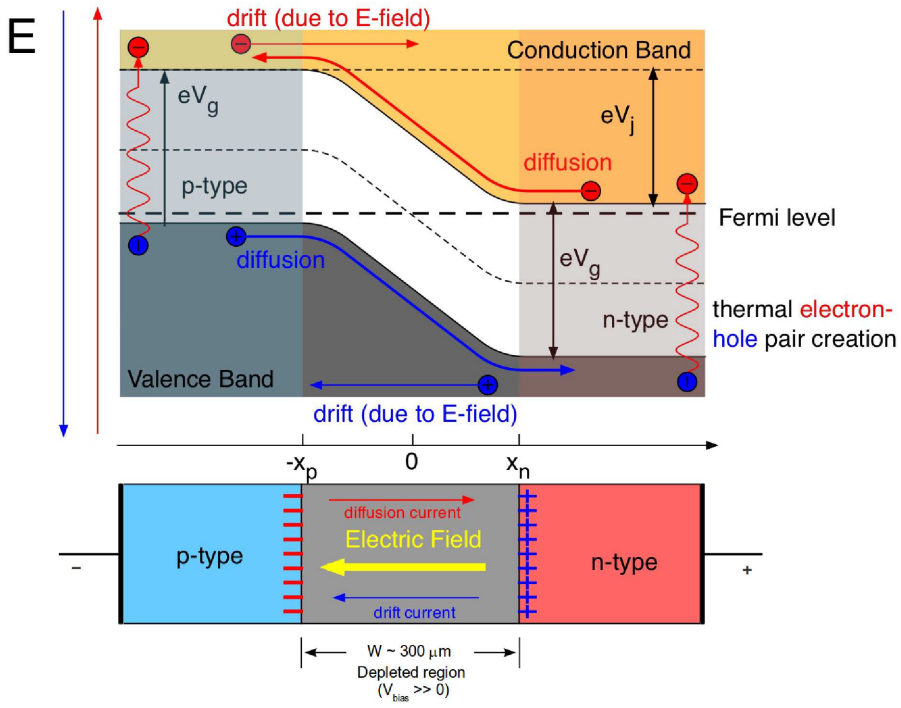


Figure 2.3: Schematic view of a planar reverse-biased p-n junction.

the p-type region and the holes to migrate in the opposite direction: positive donor ions and negative acceptor ones remain uncompensated in the n-type and in the p-type zones, respectively, forming the so-called *space charge region* or *depleted region*;

- at the same time, the carriers migration creates a potential barrier that contrasts the holes/electrons diffusion until the dynamic equilibrium is reached. The so-called *built-in potential*, i.e. the electrostatic potential corresponding to the potential barrier, is given by

$$V_{bi} = \frac{kT}{q} \ln \frac{N_A N_D}{n_i^2} \quad (2.2)$$

where n_i is the intrinsic carrier density, q is the electronic charge while N_A (N_D) is the acceptor (donor) concentration; in other words, the built-in potential strongly depends on the doping concentration. For instance [70]

$$\begin{aligned} N_A &= 10^{16} \text{ cm}^{-3}; N_D = 10^{12} \text{ cm}^{-3} \\ V_{bi} &= 0.0259 \cdot \ln \frac{10^{16} \cdot 10^{12}}{(1.45 \times 10^{10})^2} = 0.458 \text{ V} \end{aligned} \quad (2.3)$$

- for a non-biased p-n junction the width of the depleted region is generally small ($25.3 \mu\text{m}$ for the example given in equation 2.3) and can be determined using the Poisson equation [69]:

$$W = \sqrt{\frac{2\epsilon_{Si}}{q} \cdot \left(\frac{N_A + N_D}{N_A N_D} \right) \cdot V_{bi}} \quad (2.4)$$

$$W \approx \sqrt{\frac{2\epsilon_{Si} V_{bi}}{q N_D}}$$

where ϵ_{Si} is the absolute dielectric constant of silicon⁵ while the second expression is the approximation for a p⁺n junction ($N_A \gg N_D$) where the depletion region is almost entirely on the n-side of the junction;

- applying an external potential difference V_{bias} of the same sign of V_{bi} (*i.e.* applying a reverse bias voltage) the height of the barrier becomes $V_B = V_{bias} + V_{bi}$: thus the width of the space charge region and, in turn, the signal collected by the external electrodes increase. In this case, assuming the same concentration of equation 2.3 and $V_{bias} = 40 \text{ V}$, the width of the depletion layer is $\sim 230 \mu\text{m}$ and $2.3 \mu\text{m}$ on the n-side and p-side, respectively;
- under equilibrium conditions, minority charge carries (electrons in the p-type material and holes in the n-type one) are thermally generated everywhere inside the crystal volume and are free to drift and diffuse under the influence of the electric field: the net effect is an increase of the current at the edges of the crystal volume, known as *leakage current* (I_L)⁶. To keep I_L as low as possible, in order to reduce the intrinsic background of the detector itself, the purity of the crystal must be controlled with a special care; moreover it must be noticed that I_L proportionally depends on W (which in turn linearly increases with $\sqrt{V_{bias}}$) and reaches a stable value when the detector is fully depleted [80].

2.1.3 Why silicon?

A variety of criteria may be applied in choosing the detector material and can be classified in two main categories [70]:

⁵The absolute dielectric constant for silicon is defined as $\epsilon_{Si} = \epsilon_r \cdot \epsilon_0$, where ϵ_r is the relative dielectric constant (reported in table 2.1) and ϵ_0 is the vacuum permittivity ($8.85 \cdot 10^{-14} \text{ F/cm}$ [70]).

⁶It depends on the point where the electron-hole pairs are generated and it consists of two elements: the generation current, given by the charge produced in the depletion region, and the diffusion one, coming from the electron-hole pairs generated in the proximity of the space charge region and which have had a chance to diffuse in it before their recombination [80].

- the *intrinsic properties* of the used material, such as the energy needed to create an electron-hole pair, the density and the atomic number;
- the *technological feasibility* both from the costs point of view and the maturity of the used technology in producing high purity/low defects concentration materials; at the same time the possibility to integrate the readout electronics on the same detector substrate is becoming a fundamental task in particular in the present experiments such as the LHC ones [72, 84].

Compared with other materials, semiconductors are the preferred ones for high precision tracking devices, as well as for a wide range of radiation detectors, thanks to their unique physical properties [80, 84]:

- with respect to gaseous and scintillating materials, the semiconductors require the smallest amount of energy to create an electron-hole pair; considering for instance Si, Ne and plastic scintillator, the average required energy (w_i) per pair/photon production is 3.6 eV, 37 eV and 300 eV, respectively [37]. As a consequence, semiconductor based detectors have an excellent intrinsic energy resolution and the smallest value of the Fano factor⁷, in the 0.08-0.13 range (table 2.1);
- they are high density low Z materials with excellent mechanical properties: very compact and thin (down to $\sim 150 \mu\text{m}$ along the beam direction [85]) tracking devices can be built with a large enough output signal⁸, limiting at the same time the MCS contribution; moreover they can be assembled in complex geometries without a deterioration of their bulk characteristics;
- even if in semiconductors there is no multiplication of the primary charge deposited by the incident particles and the output signal is a function of the detector thickness only, they allow to reach unique and very high spatial resolution values (down to $0.7 \mu\text{m}$ [78]). The capability to measure the particle position is in fact connected both to the shape and the time structure of the charge clouds and to the design of the detector itself, *i.e.* the

⁷The Fano factor (F) includes all the fundamental processes which lead to energy loss inside the detectors material and it is related to the energy resolution through the following expression:

$$R = 2.35 \sqrt{\frac{F w_i}{E}} \quad (2.5)$$

where E is the energy of the incident particle.

⁸Considering a typical thickness of $300 \mu\text{m}$ and an average energy loss of $390 \text{ eV}/\mu\text{m}$ in a silicon $\langle 111 \rangle$ lattice, one obtains $\sim 3.2 \times 10^4$ e-h pairs, a signal that can be measured with a low noise electronics chain [80].

choice of the physical (p) and the readout (p_{RO}) pitch as will be described in section 2.2.1.

Three more considerations can be made, in particular, for silicon which is the most used and preferred material for high precision tracking purposes [77, 84]:

- it has a *small* enough and at the same time *large* enough value of the energy band gap E_g . In fact, even if Ge has a smaller E_g value with respect to the Si one (table 2.1) which means a larger signal, on the other hand a too small E_g value greatly increases the dark current requiring Ge based detectors to be operated at the liquid N temperature (77 K);
- thanks to the Integrated Circuits (ICs) technology developed on silicon substrates, very large crystals of unprecedent purity can be built and segmented using the microlithographic techniques; this allows, in turn, to develop devices which feature very small sizes and an associated precision of $1 \mu\text{m}$. Moreover the possibility of the selective growth of highly insulating layers with very good chemical stability (SiO_2 and Si_3N_4), makes silicon the *top player* both in the mass market of ICs and, as a consequence, in the one for the detectors frontend and readout electronics chain production;
- it is the second most abundant element on the Earth crust (it is present in the sand); moreover, with respect to Ge, Si is not hygroscopic and can be exposed to the atmosphere without particular care, it has a larger temperature range of stability and it is cheaper.

2.2 Silicon detectors: the working principle & performance

Figure 2.4 shows the schematic cross section and a top view photo of an AC coupled double side silicon microstrip detector: the p-n junction is reverse biased and both the p- and n- sides are segmented in smaller regions, the so-called *microstrips*, each acting as a charge collecting element. As shown in the insert of figure 2.4(a), a metal layer (typically a 50-200 nm thick aluminum coating [86]) is deposited on each strip to provide a low-resistance path for the signal readout while intermediate $\text{SiO}_2/\text{Si}_3\text{N}_4$ layers protect the detector surface and act as noise filters. Each strip has its own bias circuit and is coupled to a readout channel through dedicated $\sim 20 \mu\text{m}$ diameter Al wires (the so-called *bondings*).

The detector working principle is the following:

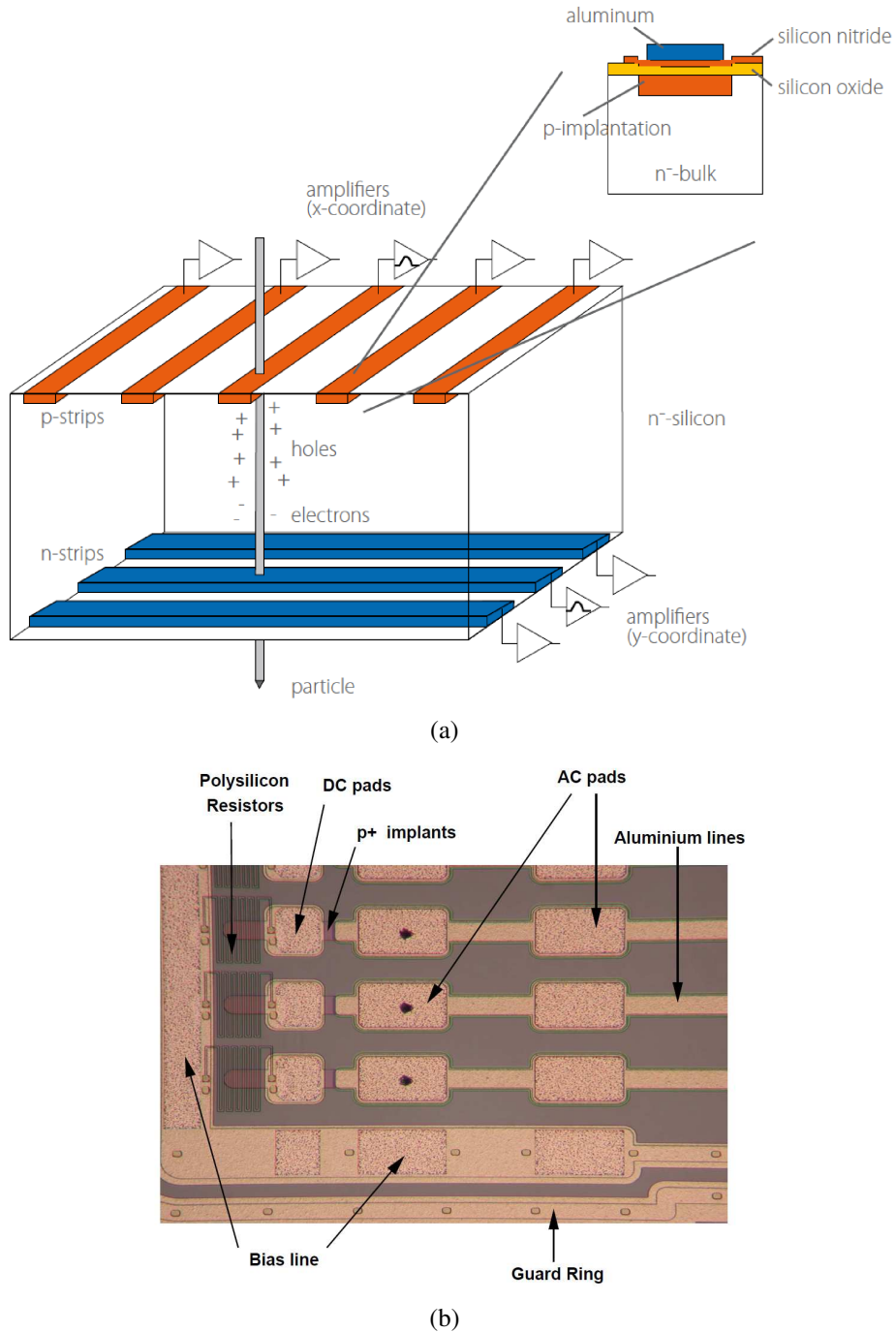


Figure 2.4: (a) Schematic view of an AC coupled double side silicon microstrip detector [86]: both the p- and the n-type regions are segmented in separated microstrips which in turn are connected to one channel of the readout electronics (amplifiers). (b) Top view microscope photo of the p-side of an AC coupled microstrip detector [73]: the different elements are indicated with the arrows.

- when a particle crosses the active volume (in this case a weakly doped n-type material), the produced holes and electrons drift toward the p- and the n-side, respectively;
- each strip implant acts as an independent electrode and collects the charge (positive for the holes and negative for the electrons) produced by the ionizing incident particle;
- the signal at the end of each strip is readout and conditioned by a channel of the readout electronics (amplifiers in figure 2.4(a)).

From the design point of view, a series of geometrical and physical parameters should be optimized depending on the desired performance of the final system [73, 77, 79, 84, 86, 87]:

- *electronics coupling*: two different approaches can be implemented depending on the detector geometry and the available space, *i.e.* directly connecting the strips to the readout channels (*DC-coupling*) or through coupling capacitors. In particular, to keep the detector noise under control and filter the leakage current, both external or integrated⁹ (*AC-coupling*, figure 2.5) capacitors can be used. From a practical point of view, these latter are the preferred ones since the number of bondings halves, the noise is less and are able to withstand drops of up to 100 V;

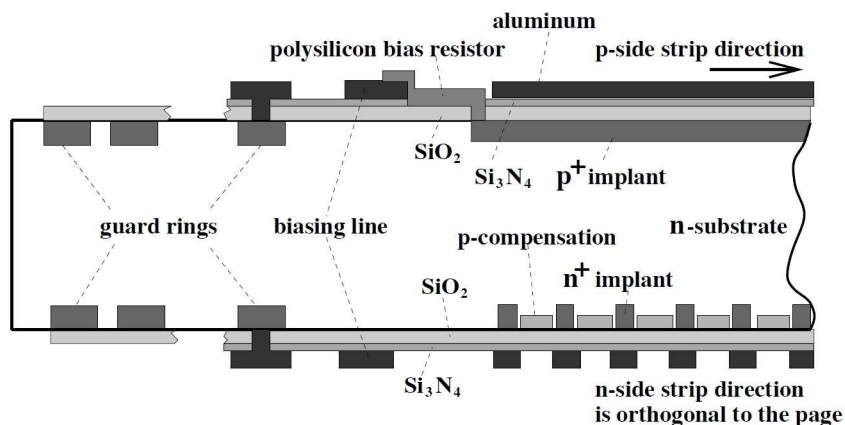


Figure 2.5: Cross section of a double side microstrip detector with integrated coupling capacitors and polysilicon biasing resistors [87].

⁹They are built inserting an insulating SiO_2 layer (50-200 nm thick) between the strip implant and the metallization; in some cases, an additional Si_3N_4 layer (50-100 nm thick) can provide extra security [77].

- *biasing*: to deplete the detector, the strips are connected to a bias line surrounding the whole sensor through dedicated resistors (figures 2.4(b) and 2.5). The value of the resistors has to be large (a few $M\Omega$) to limit the strip current in case of breaks of the coupling capacitors: the CMS (Compact Muon Solenoid) silicon devices use, for instance, 1-2 $M\Omega$ resistors. Three different choices are available at present: the integrated polysilicon resistors (figure 2.5), the punch-through structures and the implanted resistors¹⁰;
- *protection*: one or several “guard rings” (figures 2.4(b) and 2.5) define the active volume of the detector and are typically unbiased or floating structures; they isolate the sensor from field border effects (like the charge accumulation at the silicon edges) and prevent the leakage current from being absorbed by the edge strips forming a well-defined electrical boundary for the detector itself;
- *n-type segmentation*: with respect to the p-side, additional isolation structures are introduced on the n-side to avoid the formation of a layer of electrons (attracted by the fixed positive charge at the SiO_2 interface) which would short circuit the n^+ strips. Several solutions¹¹ have been explored and implemented from the technological point of view (figure 2.6);
- *thickness & pitch*: both these parameters determine the output signal value (which in turn affects the Signal to Noise Ratio - SNR) and the spatial resolution of the system. Depending on the application, the experimental conditions, the used readout electronics and costs they have to be optimized:
 - * thicknesses between 250 and 500 μm are typically used: larger values in fact require a larger bias voltage which would cause problems in the charge collection and a worsening of the SNR; on the other hand thinning the sensor improves the radiation tolerance (especially at high fluences where the type inversion is important [85]); however, for thinner detectors the loss of the signal results in a poorer SNR;
 - * since the charge produced by the ionizing particle spreads during the drift to the electrodes with a 20 μm FWHM Gaussian-like distribution, the typical physical pitches (p) are in the 25-200 μm range;
 - * readout pitches (p_{RO}) are around 20-200 μm since the modern frontend electronics (Application Specific Integrated Circuits - ASICs) has a physical pitch in the 20-50 μm range; moreover, depending on the

¹⁰More details can be found in [70, 87].

¹¹More details can be found in [70, 88].

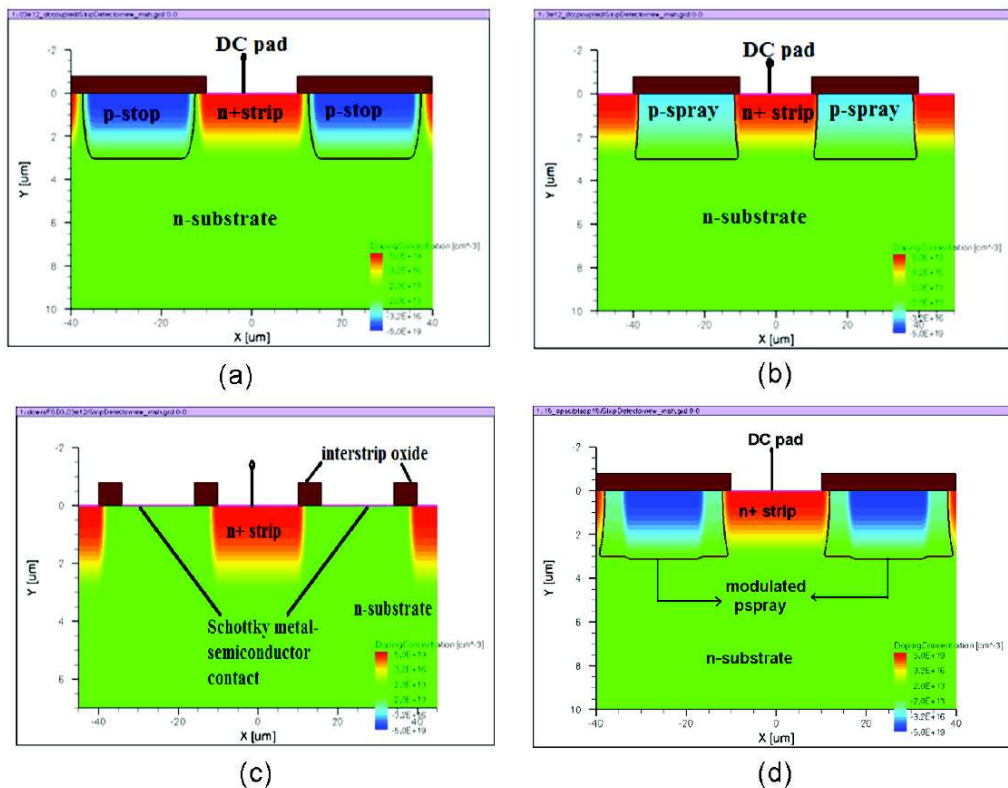


Figure 2.6: Simulated isolation techniques used to avoid the strip short circuit on the n-side layer in a double side silicon detector [88]: (a) the conventional intermediate *p-stops* technique, (b) the standard and (d) modulated *p-spray* ones and (c) the innovative *Schottky barrier* method.

technological choices (such as the number of the readout channels) and the needed spatial resolution, a detector may have one or more intermediate (*floating*) strips (figure 2.7).

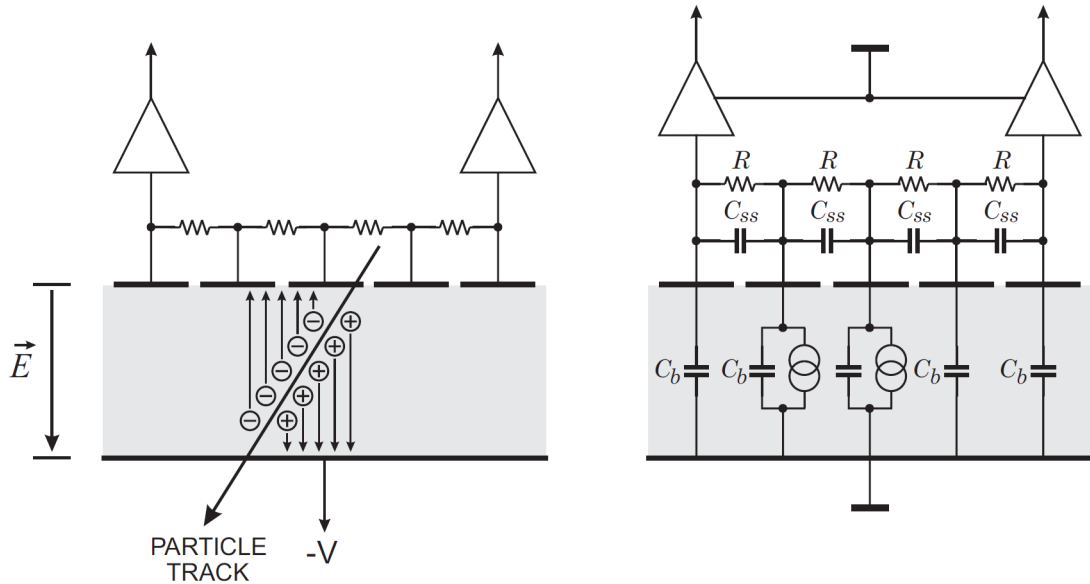


Figure 2.7: Schematic view of the intermediate (*floating*) strip readout method and of its equivalent circuit [77]: in this case only one every 4 strips is read out and the coordinate is found via interpolation.

- *detector capacitance*: figure 2.8(a) presents the schematic diagram of the capacitive connections of a microstrip detector:

- * C_c is the coupling capacitance between the detector and the readout electronics and affects the amplitude of the output signal; its value is strongly related to the strip geometry (both the length and width) and adds in series; thus for large C_c values, its contribution can be neglected;
- * C_b is the intrinsic capacitance of the bulk material, *i.e.* the one between the strip and the backside and depends on the applied bias voltage. As shown in figure 2.8(b), the larger the bias voltage, the larger $1/C_b^2$ which in turn means the intrinsic capacitance is proportional to the inverse of the square root of the applied voltage:

$$C_b = A \cdot \sqrt{\frac{q\epsilon_{Si}N_D}{2(V_{bi} + V_{bias})}} \approx \frac{1}{\sqrt{V_{bias}}} \quad (2.6)$$

where the detector has been approximated to a standard parallel-plate capacitor of area A and dimension W equal to the depletion region width (equation 2.4), thus $C_b = \epsilon_{Si} \cdot A / W$;

- * C_i is the interstrip capacitance, *i.e.* the one between adjacent couples of strips; its value depends both on the metallization layer of the strip and on the width of the strip implant.

In order to obtain a high performance detector (limiting the noise contribution as shown in section 2.2.1.3), the value of all these capacitances must be controlled with care; in particular, when the charge sharing among the strips is used to improve the detector spatial resolution (section 2.2.1), C_i should greatly exceed C_b to avoid a large loss of signal and, at the same time, C_c should greatly exceed C_i to ensure a good charge collection;

- *detector resistivity*: it is defined as the capability of a given material to oppose to an electric current flow¹²; considering for instance a p⁺n junction, it can be expressed in terms of the majority carrier mobility (μ_n) and the donor concentration (N_D) as follows:

$$\begin{aligned}\rho_c &= \frac{1}{q\mu_n N_D} \\ V_{bias} &= \frac{W^2}{2\epsilon_{Si}\rho_c\mu_n}\end{aligned}\tag{2.7}$$

where the second equality directly comes from equation 2.4. As shown in figure 2.9, the larger ρ_c (*i.e.* for a lower doping concentration), the smaller the reverse bias voltage: for instance, a 300 μm thick detector with $\rho_c \sim 10$ kΩ·cm is depleted at ∼32 V;

- *single vs double side*: the 2D particle position reconstruction capability together with the requirement of a low material budget along the beam direction can be reached using double side devices. Moreover the correlation between the signals recorded by each side of the detector can be used to disentangle the ambiguities in the multihit events [80]. On the other hand, as already said, the segmentation of the n-side and the complexity of its readout electronics, together with larger fabrication costs, represent the main drawback in producing double side silicon devices;
- *radiation damage*: the silicon devices used in the present High Energy Physics (HEP) experiments suffer serious radiation damages; very large

¹²In other words, it is the reciprocal of the conductivity σ which defines the material ability to conduct an electric current [69].

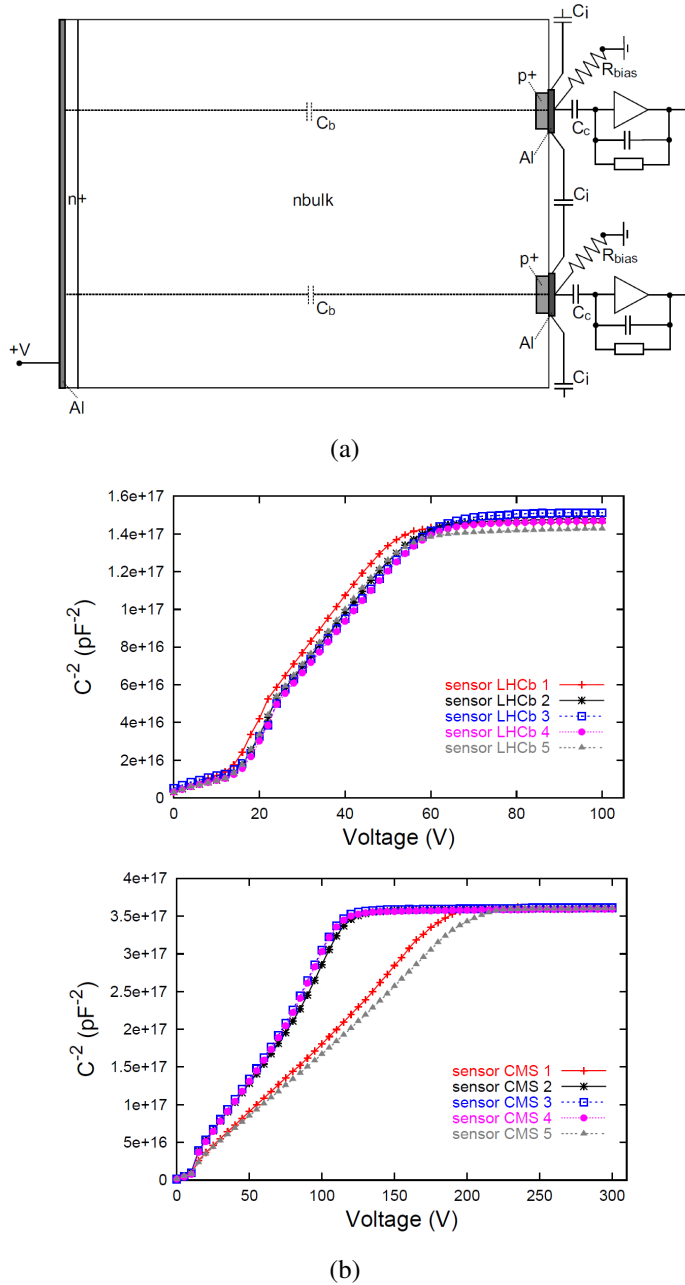


Figure 2.8: (a) Schematic view of the capacitive connections in a single side microstrip silicon detector [89]; (b) the intrinsic capacitance as a function of the bias voltage measured with (top) 5 $320\ \mu\text{m}$ thick LHCb Multi-Geometry sensors and (bottom) 5 $500\ \mu\text{m}$ thick OB2-type CMS detectors (adapted from [73]).

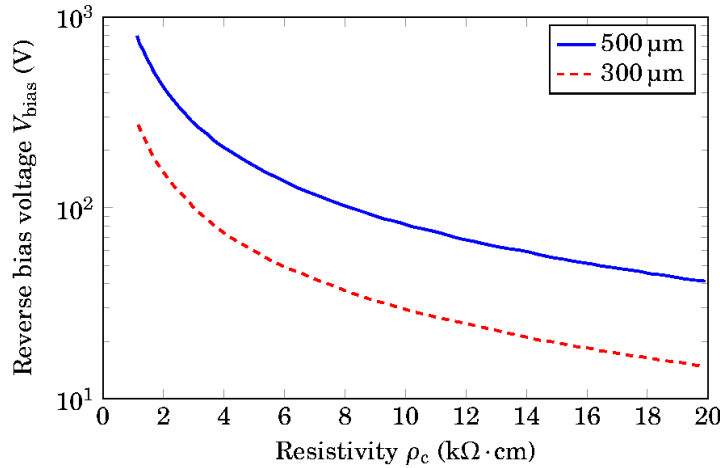


Figure 2.9: The bias voltage V_{bias} as a function of the bulk material resistivity for two different detector thicknesses.

doses of radiation¹³, mainly given by neutrons and gammas, induce microscopic defects both in the $\text{SiO}_2/\text{Si}_3\text{N}_4$ interfaces, altering the electric properties of the sensor (such as the overall noise and the interstrip capacitance), and in the bulk volume, causing the atoms displacement from their original position. The main consequences of these defects reflect in macroscopic effects like¹⁴:

- * the change of the effective doping concentration (N_{eff}) which in turn affects the operating voltage ($U_{dep} = V_{bias}$) needed for the full depletion (figure 2.10);
- * an increase in the reverse current due to the creation of “additional” generation/recombination centers;
- * the deterioration of the charge collection efficiency due to the trapping of the charge carriers which reduces their effective drift length.

2.2.1 Spatial resolution

The hot topic of this thesis work is the measurement of the intrinsic spatial resolution (σ_{int}) of various types of silicon tracking and beam monitoring systems (presented in chapters 3 and 5). It is defined as the detector capability to compute the particle position and thus to distinguish the position of two separate particles

¹³For instance, the expected yearly radiation dose at LHC is $\sim 10^{14}$ hadrons per cm^2 [90].

¹⁴More details can be found in [79, 85, 90].

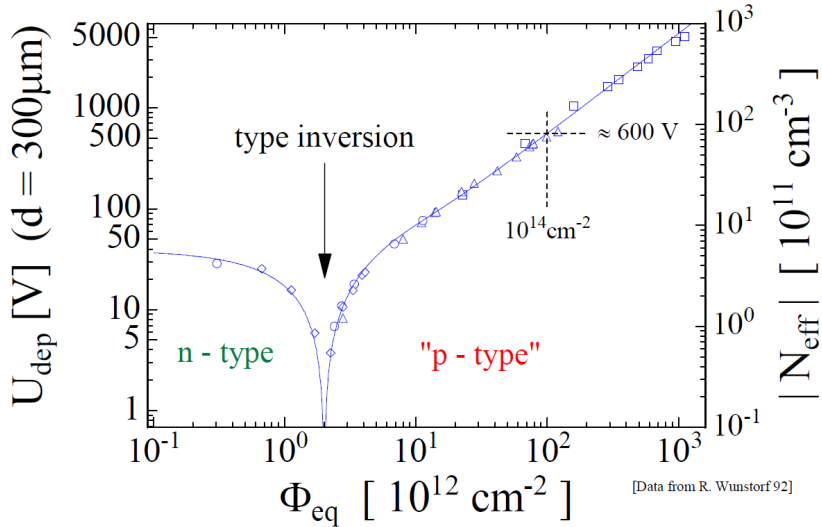


Figure 2.10: Change of the full depletion voltage $U_{dep} = V_{bias}$ of a $300 \mu\text{m}$ thick n-type silicon sensor and of its absolute effective doping concentration N_{eff} as a function of the normalized neutron fluence [90].

hitting the detector volume: in other words it corresponds to the uncertainty in the reconstructed coordinates.

The value of the intrinsic spatial resolution¹⁵ is affected by many effects which can be divided in two main categories [80, 86]:

- the first group contains the so-called *intrinsic processes*, *i.e.* all the physical laws ruling the detector working principle; it includes:

* the *drift* of the charge carriers (figure 2.11 left), which in turn affects the time response of the detector; in particular the drift time ($t_{e,h}$ defined as the time taken by the charge to reach the electrodes) can be expressed in terms of the carriers mobilities $\mu_{e,h}$ through the following equation

$$t_{e,h} = \frac{d}{v_{e,h}} = \frac{d}{\mu_{e,h} E} \quad (2.8)$$

where d is the detector thickness, $v_{e,h}$ is the drift speed and E the electric field intensity. The smaller $t_{e,h}$ (*i.e.* the larger E which in turn means a larger depletion voltage), the worse the spatial resolution since the number of single-strip events increases (see section 2.2.1.1 for details);

¹⁵The offline analysis method used to extract the final intrinsic spatial resolution value from the

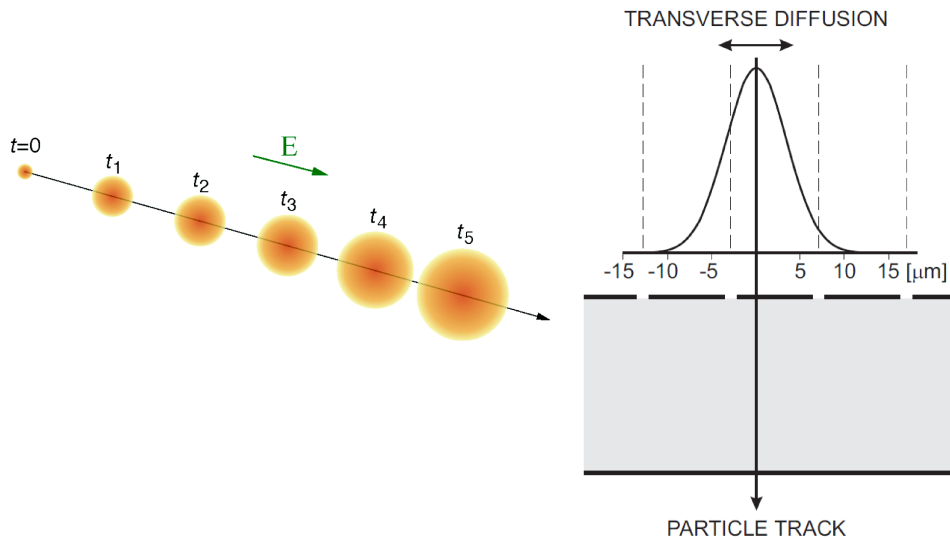


Figure 2.11: Schematic representation of the drift and diffusion processes in a silicon microstrip detector [77].

- * the *diffusion* of the charge carriers given by the multiple collisions with the atoms of the bulk material; as already mentioned the diffusion follows a Gaussian-like law (figure 2.11 right) and is connected to the charge carriers mobility through the following equations:

$$\frac{dN}{N} = \frac{1}{\sqrt{4\pi Dt}} \cdot e^{\left(-\frac{x^2}{4Dt}\right)} dx$$

$$D = \frac{kT}{q}\mu \quad (2.9)$$

where D is the diffusion coefficient;

- * the *statistical fluctuations* of the energy loss: since silicon detectors are thin, the dE/dx energy loss follows an asymmetric Landau-like distribution (figure 2.12 and equation 3.3) with a long tail toward the large energy values due to δ -electrons (which are characterized by a large energy transfer in a single collision). Even if the δ -electrons production probability is small, their range in silicon can be quite large causing a displacement of the measured tracks up to $\sim 3\text{-}4 \mu\text{m}$ ¹⁶;

experimental data is presented in chapter 4.

¹⁶For instance in a $280 \mu\text{m}$ thick microstrip detector the emission probability of a 50 keV energy δ -electron is 11%; assuming that $N_p = 20000$ electrons are released around the primary track and a 50 keV electron is produced and drifts perpendicularly to the track generating $N_\delta = 14000$

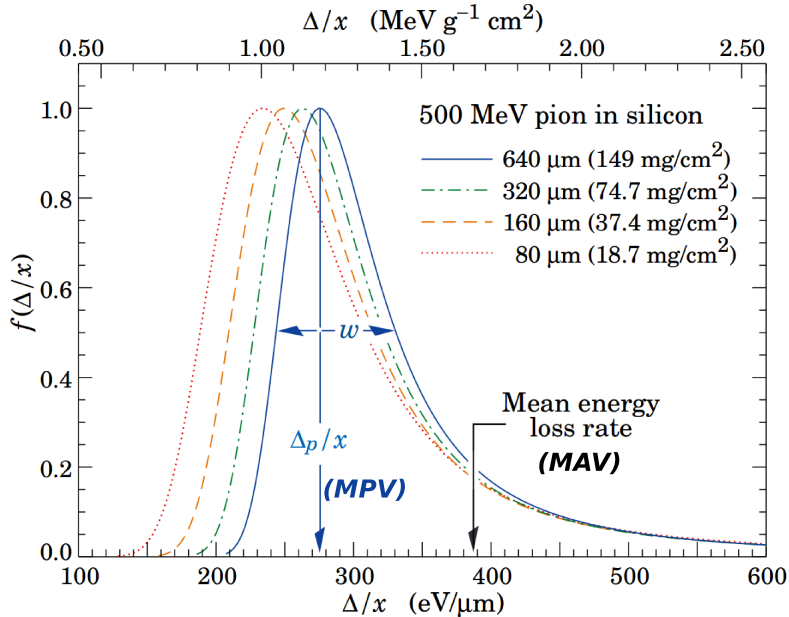


Figure 2.12: The energy loss distribution of 500 MeV pions in silicon detectors of different thickness (adapted from [37]): in all the cases the Mean Average Value (MAV) is about 50% larger than the Most Probable Value (MPV).

- the second one comprises the so-called *design parameters*, such as the choice of the readout method (digital or analog sampling, physical/readout pitch and noise), and are discussed in detail in the following sections.

2.2.1.1 Analog vs digital

Depending on the choice of the readout method two classes of events can be identified and affect the final value of the intrinsic spatial resolution:

- in the so-called *digital* readout mode, only the strips with a signal over a given threshold (red line in figure 2.13(a)) are stored and only the binary information is recorded: in most of the events the *cluster*¹⁷ is composed of one strip. In this case, for tracks crossing the detector perpendicularly or

electrons along its path (which is $r_\delta \sim 16 \mu\text{m}$), the track displacement (Δx) can be computed as follows [80]:

$$\Delta x = \frac{N_\delta \cdot \frac{r_\delta}{2}}{N_\delta + N_p} = \frac{14000 \cdot 8 [\mu\text{m}]}{34000} = 3.3 \mu\text{m} \quad (2.10)$$

¹⁷A cluster represents the group of neighbouring strips where the particle deposits its charge; see section 3.4.2 and appendix A for more details.

with a small angle of incidence (which is the typical case studied in this thesis work), the spatial resolution is defined as:

$$\sigma_{digi} \approx \frac{p}{\sqrt{12}} \quad (2.11)$$

known as the *digital* spatial resolution; considering for instance a physical strip pitch of $25 \mu\text{m}$ and $50 \mu\text{m}$, σ_{digi} results $7.22 \mu\text{m}$ and $14.45 \mu\text{m}$, respectively;

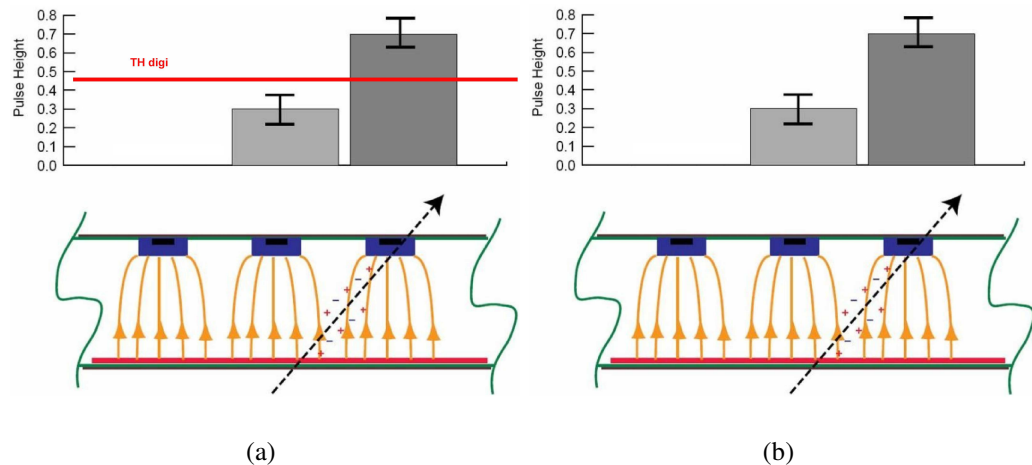


Figure 2.13: Schematic view of a cluster composed of (a) one or (b) two strips (adapted from [86]): both the digital and analog readout method have been considered, respectively.

- on the other hand, using the so-called *analog* readout mode the signal of all the strips is saved recording the effective charge detected by each strip (figure 2.13(b)) and the particle position can be measured using offline interpolation algorithms¹⁸. The number of events with a cluster composed of more than one strip increases improving the spatial resolution which in this case is defined as:

$$\sigma_{analog} \approx \frac{p}{SNR} = \frac{p}{S/N} = p \cdot \frac{N}{S} \quad (2.12)$$

where S is the total signal of the cluster and N its noise rms: therefore, the larger the SNR, the better the spatial resolution.

¹⁸More details can be found in chapter 4.

2.2.1.2 Strip & readout pitch

The most important external parameters affecting the intrinsic value of the spatial resolution in a silicon microstrip detector are the physical (p) and readout (PRO) pitch; considering again the two above mentioned classes of events (single/multiple strips events), the following considerations hold:

- as already mentioned, the typical width of the charge cloud originated by the particle interaction is $\sim 20 \mu\text{m}$; as a consequence, a physical pitch larger than $50 \mu\text{m}$ strongly reduces the spatial resolution since most of the events are single-strip cluster ones: the obtained value for σ_{int} is thus close to the σ_{digi} one. Using a smaller physical pitch improves the spatial resolution value but requires a larger number of readout channels and thus an increase of both the overall system power consumption and of the production costs;
- a possible solution to improve the resolution without reducing the physical pitch is the implementation of intermediate strips, biased at the same depletion voltage of the others but not connected to a readout channel, located between couples of readout strips (figure 2.7). This method is known as *floating strips readout* and allows to limit the number of electronics channels maintaining at the same time a high enough spatial resolution. In this case the capacitive coupling among contiguous strips allows the charge sharing between them increasing the number of events with a multi-strip cluster: the obtained value for σ_{int} is thus close to the σ_{analog} one or even better. Table 2.2 summarizes the expected spatial resolution for a detector with a $60 \mu\text{m}$ PRO and different physical strip pitches (a $20 \mu\text{m}$ FWHM Gaussian-like charge cloud distribution has been considered).

p pitch [μm]	PRO pitch [μm]	1-strip cluster [%]	2-strip cluster [%]	σ_{int} [μm]
60	60	66	33	8.4
20	60	33	66	3.4

Table 2.2: Intrinsic spatial resolution for a $60 \mu\text{m}$ PRO silicon detector with different p [80].

2.2.1.3 Noise

Since in semiconductor detectors there is no multiplication of the charge signal, one of the main limiting factors for the spatial resolution is represented by the noise contribution. From equation 2.12 it can be noted in fact that a larger noise

means a poorer spatial resolution; moreover, in double side detectors where the correlation between the signals on the two sides is used for the multi-track events and ghosts rejection/identification [80], the reduction of the noise is a fundamental task.

The schematic views of the typical frontend chain used for silicon detectors and of its equivalent circuit are shown in figures 2.14(a) and 2.14(b): both the silicon electrical characteristics (in particular the capacitance C_d and the leakage current I_L) and the features of the readout chain affect the global noise of a detector in different ways.

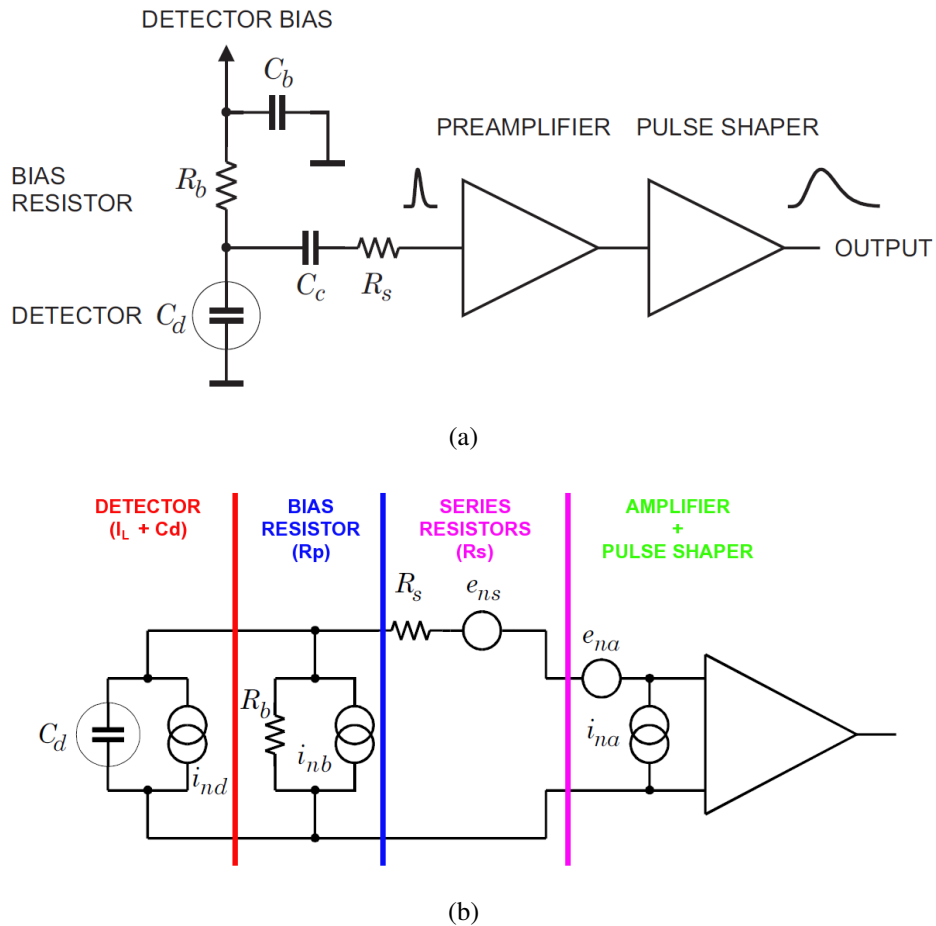


Figure 2.14: Schematic views of (a) the detector typical frontend and (b) its equivalent circuit (adapted from [77]): both the current (i_n) and voltage (e_n) sources of noise are indicated (see text for details).

Since the particle passage in the detector is measured through the charge deposit, the system noise is generally expressed in terms of the so-called *Equivalent*

Noise Charge (ENC), defined as the detector signal corresponding to a unitary SNR [77]. In particular, referring to figure 2.14(b), the noise sources can be modeled as parallel/series voltage or current generators [77, 86]:

- the leakage current I_L is represented by a current noise generator (i_{nd}) which contributes to the ENC through the following equation:

$$\text{ENC}_{\text{leak}} = \frac{e}{q} \sqrt{\frac{qI_L t_p}{4}} \quad (2.13)$$

where e is the Euler number and t_p is the shaping time¹⁹ of the readout amplifier;

- the detector capacitance C_d at the input of the charge sensitive amplifier is the dominant noise source and its effect on the noise can be parametrized as:

$$\text{ENC}_{\text{ele}} = A + B \cdot C_d \quad (2.14)$$

where A and B are constants and are defined by the preamplifier design;

- the contribution of the parallel (bias) resistor R_p (modeled as a current generator i_{nb}) can be written as:

$$\text{ENC}_{R_p} = \frac{e}{q} \sqrt{\frac{t_p kT}{2R_p}} \quad (2.15)$$

- the series resistor R_s , given both by the strip itself and the bondings, acts as a voltage generator (e_{ns}) and adds to the noise with the following term:

$$\text{ENC}_{R_s} = C_d \frac{e}{q} \sqrt{\frac{kTR_s}{6t_p}} \quad (2.16)$$

- finally, the amplifier noise is described by a combination of voltage (e_{na}) and current (i_{na}) at its input; it adds in series with the other sources and mainly contributes through a $1/f$ noise to the total ENC value²⁰.

Since the above mentioned noise contributions are random and uncorrelated, they add in quadrature and the total ENC at the output of the pulse shaper is obtained integrating over the full bandwidth of the system; for instance, the total ENC for the DELPHI (DEtector with Lepton, Photon and Hadron Identification)

¹⁹It defines the time interval needed by the pulse to reach its maximum [77].

²⁰For the $1/f$ noise definition see [77].

MVD (Micro Vertex Detector) and of the CMS tracker are, respectively, 552 e^- and 760 e^- [86].

From the above mentioned list, it must be clear that, to achieve a large enough SNR (which in turn means to improve the final value of the intrinsic spatial resolution), a particular care should be taken in the choice of the shaping time of the readout amplifier. For instance, the SNR at room temperature of an undamaged detector is $\sim 15\text{-}20$ for a fast electronics ($t_p \approx 50\text{ ns}$) and $\sim 50\text{-}100$ for a slower one ($t_p \gg 50\text{ ns}$) [87]. As shown in figure 2.15, at small shaping times the total ENC is dominated by the voltage noise sources while at long shaping times the current noise contributions are the most important; the total ENC shows a minimum where the two contributions are equal and it is flattened by the $1/f$ component (which is time independent): increasing the voltage or current noise contribution shifts the noise minimum at a longer shaping time.

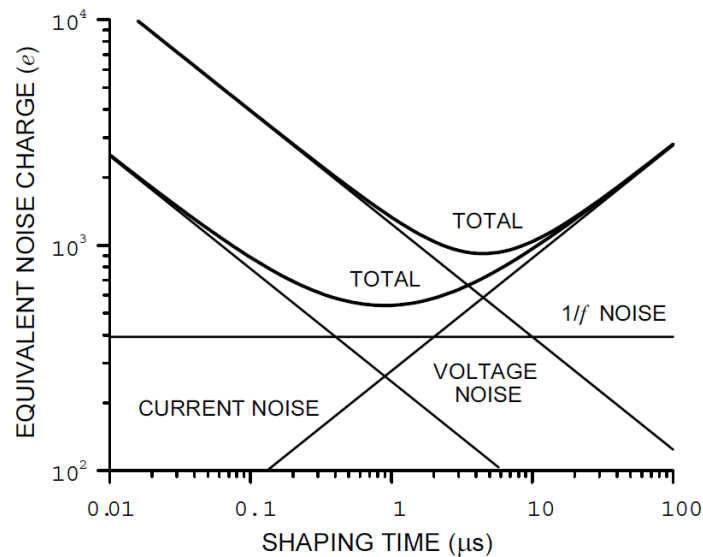


Figure 2.15: The ENC as a function of the amplifier shaping time [77].

2.2.2 Charge sharing

As mentioned in section 2.2.1.2 the position reconstruction capability of a microstrip silicon detector can be improved with the floating strip readout method. The physical principle at the basis of this technique is the so-called *Charge Sharing* (CS) among neighbouring strips. In fact, thanks to the capacitive coupling

between contiguous strips, when an intermediate strip is hit, the charge is equally shared between the closest neighbouring readout strips.

A way to study the charge sharing among the strips is the use of the so-called *eta distribution* (η) [80]; for single cluster events in which the cluster is composed of two contiguous strips, it is defined as the non-linear interpolation between the pulse height of the strip with the largest signal in the event (PH_{high}) and the one of the neighbouring strip (PH_{right} or PH_{left}):

$$\begin{aligned}\eta_{right} &= \frac{-PH_{high} + PH_{right}}{PH_{high} + PH_{right}} \\ \eta_{left} &= \frac{PH_{high} - PH_{left}}{PH_{high} + PH_{left}}\end{aligned}\quad (2.17)$$

Figure 2.16 shows the eta distribution of a double side silicon microstrip detector with a 50 μm readout pitch and 50 μm (left) and 25 μm (right) physical pitch²¹: the presence of peaks means that the charge division is far from being linear (otherwise the distribution should be flat [91]) and their symmetric position reflects the fact that the signal sampling is the correct one²².

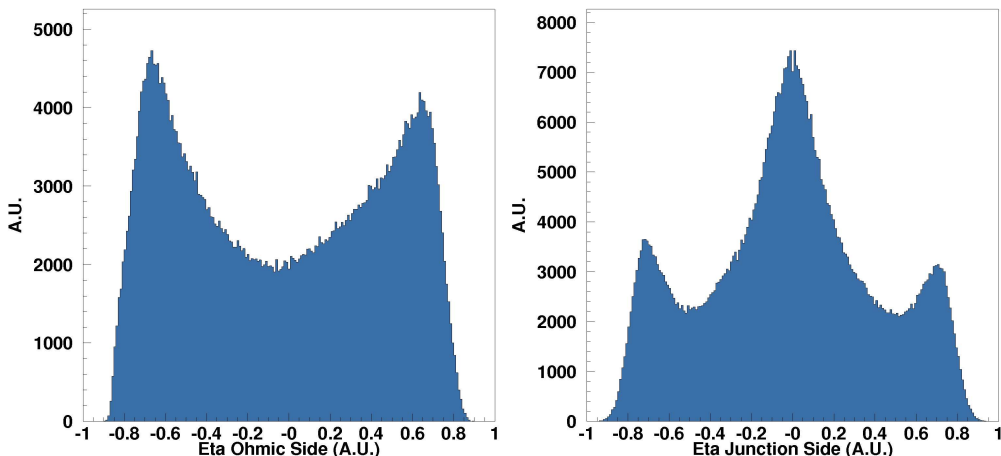


Figure 2.16: The eta distribution of two sides of a silicon microstrip detector with (left) 50 μm physical and readout pitch and (right) 25 μm physical and 50 μm readout pitch.

The peculiar non-linear shape of the η distribution is due both to the width of

²¹One module of the INSULAB Telescope (presented in chapter 3) has been used.

²²More details on the asymmetries given by an uncorrect sampling of the signal can be found in appendix A and in [86].

the diffusion cloud and to the detector characteristics (such as the thickness, the resistivity and the applied bias voltage) [86, 91]:

- referring to figure 2.17 and considering a physical pitch equal to the readout one, two different regions can be distinguished: the region where the strip is implanted (*A*) and the one between two neighbouring strips (*B*). Depending on the point where the particle hits the detector, different situations can be identified and correspond to different values of η (figure 2.16-left):
 - * for a particle crossing the detector perpendicularly in the middle of the *B* region (dashed line) the charge is equally shared between the two strips and the charge division is roughly linear: $PH_{right} \simeq PH_{left}$ and therefore η equals 0;
 - * on the other hand, if a particle crosses the detector in the *A* region, most of the charge is collected by one strip: $PH_{right} \gg$ or $\ll PH_{left}$ and the η -value is close to -1 or +1;
 - * finally, the diffusion of the charge cloud and the noise contribution fill up the region between the two outermost peaks;

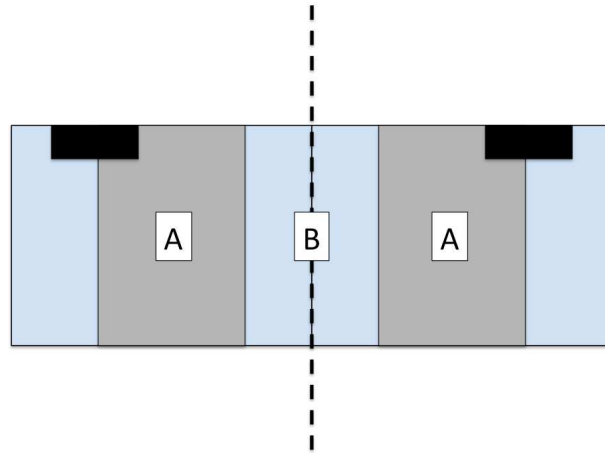


Figure 2.17: Schematic view of two readout strips in a silicon detectors [86]: the *A* and *B* regions represent, respectively, the zone nearby to the strip implant and the one close to the border between the two strips (dashed line).

- if a floating strip is introduced, the peaks at $\eta=-1$ and $\eta=+1$ remain unchanged and a new peak at $\eta=0$ appears which corresponds to the intermediate floating strip (figure 2.16-right). Moreover, the larger the number

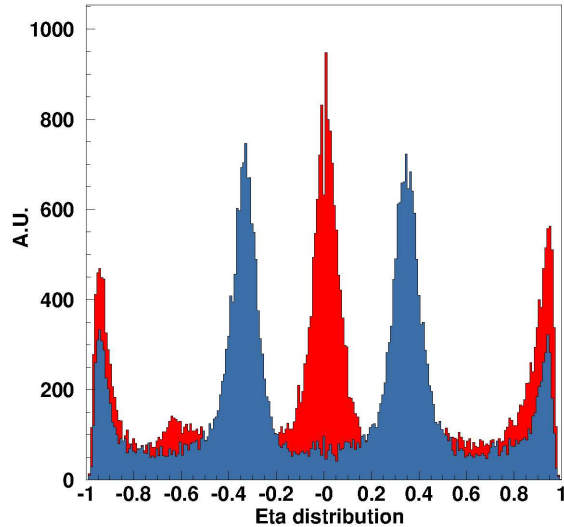


Figure 2.18: Comparison of the η distribution of a silicon microstrip detector with (red) a single floating strip scheme and (blue) a double floating strip one.

of intermediate strips, the larger the number of new peaks in the region between the two outermost ones (figure 2.18).

The positions of the most lateral peaks in the η distribution thus give an estimation of the capacitive coupling of a strip with the adjacent ones: a more precise procedure to estimate the effective value of the CS is presented in chapter 3 and in [86].

2.3 Electronics for silicon detectors

In the last 70 years (from the construction in 1947 of the first transistor by the American physicists John Bardeen, Walter Brattain and William Shockley) the electronics for semiconductor detectors has been strongly improved. In particular, since the silicon detectors have no internal multiplication of the charge signal, the main goal was the development of low noise and low power systems which had at the same time very small dimensions (down to a few tens of mm^2 which comprised thousands of elements²³) and were able to manage several parallel channels at once (typically ranging from 32 to 128). A very large variety of approaches and technologies were explored: from the bipolar technology of the 1960s to the MOS Large Scale Integration (LSI) logic in the 1970s and the Very Large Scale Integration (VLSI) one in the 1980s based on the Complementary MOS (CMOS)

²³See for instance the dimensions of the integrated circuits used in this thesis work [92–94].

technology. This latter proved to be superior [84] and rapidly became the most used one and the basis of the modern readout ASICs.

Figure 2.19(a) presents a schematic view of the electronic chain used with silicon microstrip detectors; it can be divided in two main blocks:

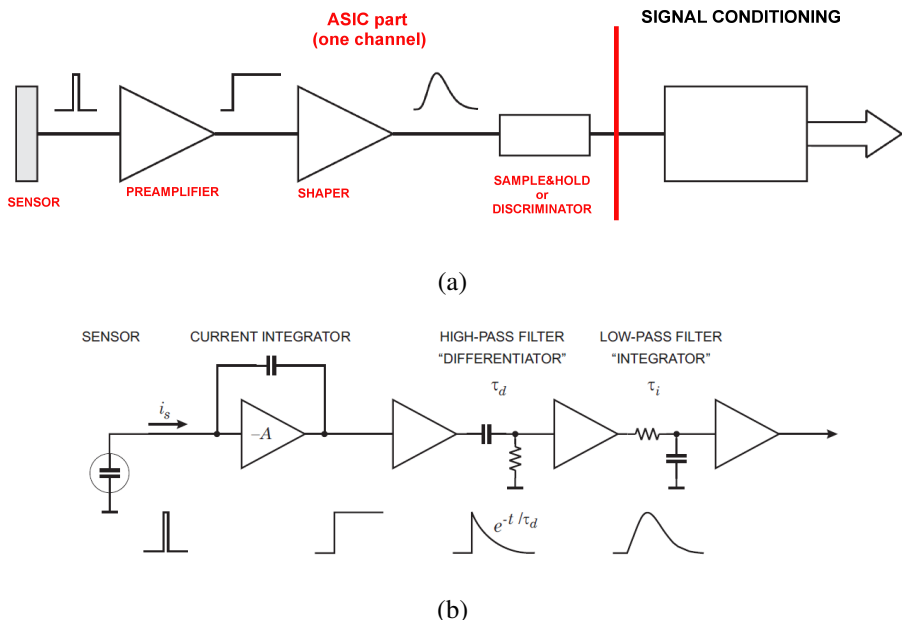


Figure 2.19: (a) The schematic diagram of a typical readout chain for silicon microstrip detectors (adapted from [77]): the ASICs main blocks are shown in red while the part responsible of the signal conditioning (frontend+readout) in black. (b) Details of the electrical circuits used for the signal amplification and shaping [77].

- the **ASICs part**: it is responsible of the first signal amplification, its formation and its sampling; the ASICs are typically housed on dedicated hybrid boards and, as shown in figure 2.19(a), a single channel is composed of:
 - * a *preamplifier* (figure 2.19(b)-left), based on the Charge Sensitive Amplifier (CSA), which integrates the total charge (Q) on a feedback capacitor (C_f) and produces a voltage step with an amplitude $-Q/C_f$;
 - * a *CR-RCⁿ shaper* consisting of a differentiator followed by n integrators (figure 2.19(b)-right); it has to filter the noise contribution and to “shape” the signal. The peaking time of the shaped signal depends on the number of RC steps: for example a fast shaper configuration is used in the so-called *self-triggering* ASICs [94] to generate the trigger

for the signal sampling; on the other hand, for the signal formation and its effective sampling, shapers with a slower peaking time can be used;

- * a *Sample&Hold (S&H)*, in case of the analog readout: the shaper output is usually stored in a capacitor, which in turn is driven by a dedicated digital signal (the *hold* one²⁴), and readout afterwards. On the other hand if a digital output is foreseen, each channel has a *discriminator* which is directly fed with the shaper output.

It must be noted that in the large HEP experiments (such as the LHC ones), given the very large amount of data ($O(10^7)$) which means $\approx 20\text{-}25$ interactions every 25 ns), the shaped signals are temporarily stored in dedicated readout buffers on the frontend boards waiting ($\sim 3 \mu\text{s}$) for the so-called *Level 1 Trigger (LvL1T)* decision²⁵ [72]. In particular the so-called *analog or digital pipelines* are used; for instance, the CMS Silicon Strip Tracker (SST) readout is accomplished by the APV25 ASIC [95] which contains 192 cells analog pipelines per channel (figure 2.20) to accomodate for latencies up to $4 \mu\text{s}$ ²⁶;

- the **conditioning part**: it is typically based on external custom electronics boards connected to the ASICs hybrids with standard coaxial cables or optical fibers; this part includes:

- * the *frontend* electronics which typically handles the signals for the detectors and the ASICs biasing together with their configuration settings (for instance the threshold for the discriminator, the value of the hold signal or, if a configuration register is needed for the ASICs, the values of the ASICs mask); in some cases a further amplification stage is also present. Morevoer, for double side silicon detectors, the frontend electronics also includes a separate stage for the handling of the n-side signals;

²⁴See sections 3.1.2 and 5.2.3 for more details.

²⁵Depending on the experiment, two or three trigger levels are foreseen to reject the background and provide a first decision on whether to keep the event or not; the LvL1T selection rate is 100 kHz and the decisions are based on the identification of high p_T electrons, muons, jets or missing E_T in the calorimetry and muon systems [72].

²⁶For completeness, the LHCb experiment uses the BEETLE and the SALT (Silicon ASIC for LHCb Tracker) ASICs for the readout of the VErtex LOcator (VELO) telescope and the Upstream Tracker (UT), respectively [96]. The ALICE Silicon Strip Detector (SSD) is readout with the mixed analog-digital very large dynamic range HAL25 ASIC [97] while in the ATLAS Semiconductor Tracker (SCT) a 132 cells digital pipeline is implemented in the ABDC ASIC [98].

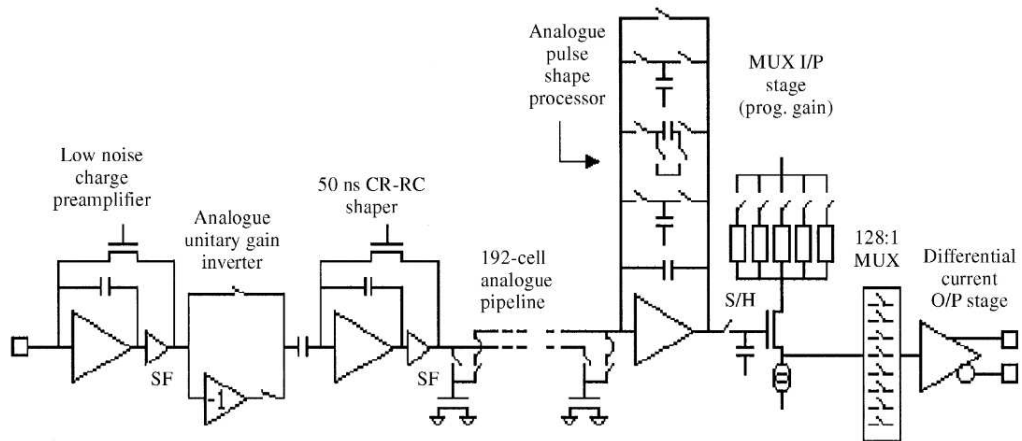


Figure 2.20: The architecture of one channel of the APV25 ASIC [95].

- * the *readout* electronics which is responsible of the digitization of the multiplexed shaper analog output, through dedicated ADC (Analog to Digital Converter) stages, the data storage, the communication with the PC and, if it is not directly included in the ASICs themselves, the generation of the trigger for the sampling of the data.

Further details and a complete overview of the electronics chains used for silicon microstrip detectors together with their main features can be found in [69, 70, 77].

Chapter 3

The INSULAB reference detector: description and commissioning

A very high precision tracking system represents a key element in many physics fields ranging from space physics to medical physics and particle physics. Testing new detectors (or detector components) is in fact fundamental to investigate and characterize such detectors in terms of efficiency, signal and time response, linearity and so on. In several cases the required angular precision is of the order of a few μrad corresponding to a spatial resolution in the 5-10 μm range. For example, as mentioned in chapter 1, a very high particle position reconstruction capability is a fundamental task in crystal physics where the typical effects given by the interaction of the particles with the crystallographic planes (or axes) are of the order of hundreds of μrad [1] (see section 1.3 for more details).

Since 2007 the INSULAB Research Group¹ has provided the tracking system for several INFN² research and R&D projects:

- the characterization of several bent crystals of a large variety of materials (Si, Ge, SiGe graded, LiNbO₃, etc. [99, 100]), types (quasimosaic, single- or multi-strip [1, 101]) and dimensions (from hundreds of μm down to tens of nm along the beam direction [102]) for the NTA-HCCC³, COHERENT⁴ and ICE-RAD⁵ experiments [1, 20–22, 60];
- the study of large area and large dynamic range Silicon PhotoMultipliers (SiPMs) coupled to shashlik or LYSO/PbWO₄ crystal based electromag-

¹INSUbria LABoratory Research Group (Università degli Studi dell’Insubria - section of Como), <http://insulab.dfm.uninsubria.it/index.php>.

²Istituto Nazionale di Fisica Nucleare, <http://www.infn.it/index.php?lang=en>.

³INFN experiment dedicated to the crystal physics [1, 28, 103].

⁴COHERENT effects in crystals for the physics of accelerators.

⁵Interaction in Crystals for Emission of RADiation.

netic calorimeters for high energy and space physics (the FACTOR⁶ and TWICE⁷ projects [74–76, 104]). In this case the tracking system is based on the so-called *Silicon Beam Chambers* (SiBCs [105, 106]) developed in the AGILE (Astro-rivelatore Gamma a Immagini LEggero) satellite framework⁸ in 1999 and completely upgraded last year with the electronics developed for the COHERENT experiment and presented in this thesis work.

The tracking system used for the crystals tests, the so-called *INSULAB Telescope* [27, 86], is based on microstrip silicon detectors. It has been developed in collaboration with INFN-Ts⁹ and during the past years several modules have been assembled both to test different solutions (in terms of ASICs and detectors) and to develop a high performance system (both in terms of spatial resolution and time response) limiting the material along the beamline. Silicon detectors from three different manufacturers (single side ones by HAMAMATSU¹⁰ and double side ones by FBK-irst¹¹ and CSEM¹²) and different readout ASICs (VA2 [92], VA1_prime2 [93] and VA1TA [94] by IDEAS¹³) have been used to improve the telescope performance and assemble a very compact silicon-only system [27].

This chapter describes the design and construction of the first *INSULAB Telescope* modules featuring double side silicon detectors produced by CSEM and the VA2 ASICs¹⁴. The first part of the chapter presents a complete description of the detector characteristics (the silicon tiles and the readout ASICs), the assembly and the mechanics while the second part describes the new readout electronics developed in 2012 to replace the old one based on commercial ADCs. The performance of the telescope modules is defined in terms of noise, Signal to Noise Ratio (SNR) and Charge Sharing (CS) among the strips as obtained in dedicated beamtests at the CERN SPS H4 and PS (Proton Synchrotron) T9 beamlines.

⁶Fiber Apparatus for Calorimetry and Tracking with Optoelectronic Read-out.

⁷Techniques for Wide-range Instrumentation in Calorimetry Experiments.

⁸AGILE Official Website, <http://agile.rm.iasf.cnr.it/>

⁹INFN Sezione di Trieste, <http://www.ts.infn.it/>.

¹⁰HAMAMATSU Photonics, <http://www.hamamatsu.com>.

¹¹Fondazione Bruno Kessler, <http://www.fbk.eu>.

¹²Centre Suisse d’Electronique et Microtechnique, <http://www.csem.ch>.

¹³Integrated Detector & Electronics AS, <http://www.ideas.no>.

¹⁴The description and the results obtained with the modules built with the HAMAMATSU and FBK-irst silicon tiles + the VA1TA ASIC (indicated in the following as the *VISION Telescope*) are presented in chapter 5 while the ones for the FBK-irst+VA1_prime2 modules (named the *UA9 modules*) are given in appendix B.

3.1 The CSEM+VA2 reference modules

The so-called *INSULAB Telescope* [27, 86] consists in several independent elements, called *modules*, equipped with microstrip silicon detectors, the readout ASICs and the frontend and readout electronics. The following sections describe the first version of the telescope which used the modules described in [107] and developed to test the BaBar Silicon Vertex Detector (SVT) prototype [108].

Four modules (indicated in the following as *reference modules*) have been assembled in 1994 with the CSEM silicon tiles and the VA2 ASICs at INFN-Ts and tested in the last five years at the CERN PS and SPS beamlines with charged particles in the 1-150 GeV/c momentum range [27, 86]. In 2012 the readout electronics has been upgraded (section 3.2); three reference modules have been successfully used at the CERN SPS H8 beamline for the COHERENT experiment to characterize several new generation crystals [99, 100, 109].

3.1.1 The silicon detectors

Table 3.1 summarizes the general features of the CSEM+VA2 reference modules while figure 3.1 presents a photo of an assembled detector. Each module houses a high resistivity 300 μm thick double side silicon microstrip detector with a sensitive area of $1.92 \times 1.92 \text{ cm}^2$ for a total of 384 strips [27, 107]. The so-called *one floating strip* scheme has been adopted for the readout of the p-side (the *junction side*) i.e. the detector has a p⁺ implantation strip every 25 μm and a readout pitch of 50 μm . The n-side (the *ohmic side*), with the strips perpendicular to the p-side ones, has a n⁺ implantation every 50 μm separated by p+ blocking strips; also in this case the readout pitch is 50 μm .

The silicon tile is fully depleted with a bias voltage in the 36-54 V range and the average leakage current is of the order of 1.5-2.0 nA per strip.

3.1.2 The readout ASIC

Three VA2 ASICs [92] per side are needed to readout the whole detector. The VA2 ASIC, whose technical features are listed in table 3.2, is a 128 channel radiation tolerant integrated circuit built with the 1.2 μm N-well CMOS technology. A top view photo and the ASIC architecture are shown in figure 3.2: each channel contains a folded cascode low-noise/low-power preamplifier (CSA), a CR-RC slow shaper and a Sample&Hold (S&H) circuit. The output information is a multiplexed analog one with a maximum clock frequency of 10 MHz¹⁵.

¹⁵A multiplexed readout is the one in which the sampled signals are sent out one after the other thanks to a clock signal; the typical clock values used with the reference modules are 1.25, 2.5 and 5 MHz.

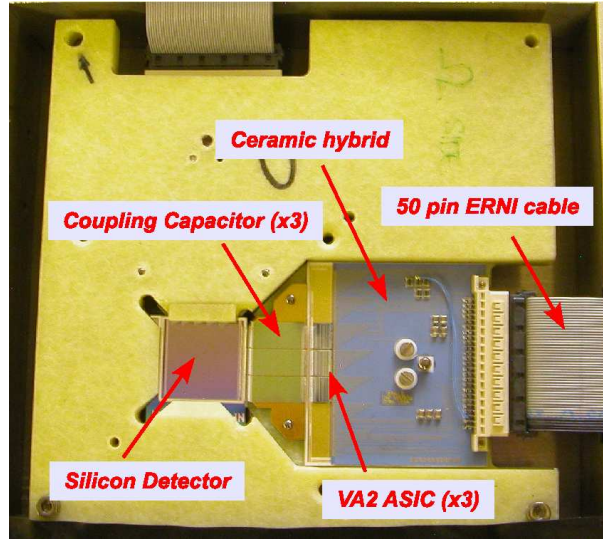


Figure 3.1: Photo of the CSEM+VA2 reference detector assembled on the fiber-glass frame together with the readout ASICs and the ceramic hybrid.

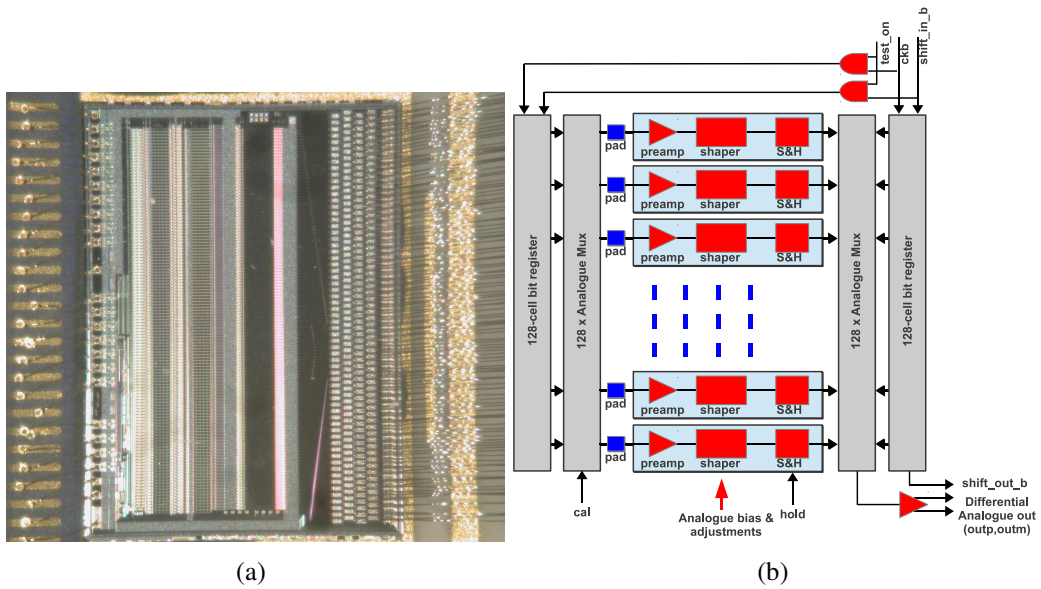


Figure 3.2: The VA2 ASIC [92]: (a) a top view photo and (b) the architecture of the ASIC (S&H stands for Sample&Hold).

Detector	Double
Produced by	CSEM
ASIC	VA2
Detector dimensions [cm ²]	1.92×1.92
Number of readout channels	384
Bulk thickness [μm]	300
Resistivity [kΩ·cm]	> 4
Leakage current [nA/strip]	1.5-2.0
Full depletion bias voltage [V]	36-54
AC coupling	no (150 pF ext. cap.)
p-side - <i>junction</i>	
physical pitch [μm]	25
readout pitch [μm]	50
floating scheme	yes
n-side - <i>ohmic</i>	
physical pitch [μm]	50
readout pitch [μm]	50
floating scheme	no
Fiberglass support	
shape	square
dimensions [cm ²]	12.5×12.5
thickness [cm]	1.0
ASIC connection	direct bonding

Table 3.1: General features of the CSEM+VA2 reference modules.

ASIC name	VA2
Process (N-well CMOS)	$1.2 \mu\text{m}$
Die surface [mm ²]	6.18×4.51
Die thickness [μm]	~ 600
Number of channels	128
Input pad size [μm^2]	50×90
Output pad size [μm^2]	90×90
ENC at 1 μs of peaking time [e ⁻ rms]	$80 + 15 \cdot C_d$
Power consumption [mW]	170
Slow shaper peaking time [μs]	1-3
Fast shaper peaking time [μs]	not present
Dynamic range [# MIPs]	± 4
Current gain [$\mu\text{A}/\text{fC}$]	~ 25

Table 3.2: Technical features of the VA2 ASIC [92]; C_d stands for the overall input capacitance of the silicon tile.

Several adjustable parameters can be tuned to properly operate the shaper and the preamplifier to obtain a proper output signal (in terms of shaping time and amplitude) [92]. Figure 3.3 shows the output signals of the junction (black squares) and ohmic (red triangles) side with a different setting of the configuration parameters (in particular the *delay* bit¹⁶ was turned OFF/ON only for the ohmic side). To study the analog output signal shape an automatic procedure has been used:

- the *test on* bit of the ASIC has been enabled via software; only 1 channel at a time out of 384 is enabled; the channel is selected via a 128-bit input shift register [92];
- a calibration signal (that is a single square signal of variable amplitude and time width generated by an Agilent 33220A Waveform Generator¹⁷) has been fed into the ASIC input lines;
- the value of the hold (that is the time at which the signal is sampled¹⁸) has been automatically varied by the DAQ (Data AcQuisition) system in the 0-5750 ns range with a step of 100 ns; 100 events per step have been acquired. The readout sequence is started by the *sync* signal of the pulse generator;

¹⁶It acts on the input signal to the ASIC and delays the signal itself of a given quantity.

¹⁷Agilent Technologies, <http://www.agilent.com>.

¹⁸The *hold* is defined as the interval between the trigger signal which in this case is generated by the *sync* signal of the pulse generator) and the sampling of the shaper output signal (see section 5.2.3 for more details about the hold scan working principle).

- for each hold value the output signal of the selected channel has been recorded by a dedicated readout board (see section 3.2.2) and saved as a PAW¹⁹ ntuple; this information allows to study the output signal value as a function of the hold one (figure 3.3).

The peaking time for the junction side (black squares) is ~ 1500 ns while for the ohmic one (red triangles) is ~ 2000 ns when the *delay* bit is disabled (figure 3.3(a)) and ~ 1000 ns less when the *delay* bit is ON (figure 3.3(b)); the difference in the signal amplitude of the two sides in both cases is given by the different gain of the complete electronics chain.

Moreover, as explained in [86], the signal sampled by the ADC readout boards (section 3.2.2) is affected not only by a different setting of the ASIC parameters but also by a different length of the cables connecting the ADC boards to the VME (Versa Module Eurocard) electronics and the crate itself (section 3.2.2). The cables length in fact depends on the experimental area conditions and could vary from 1 up to some tens of meters.

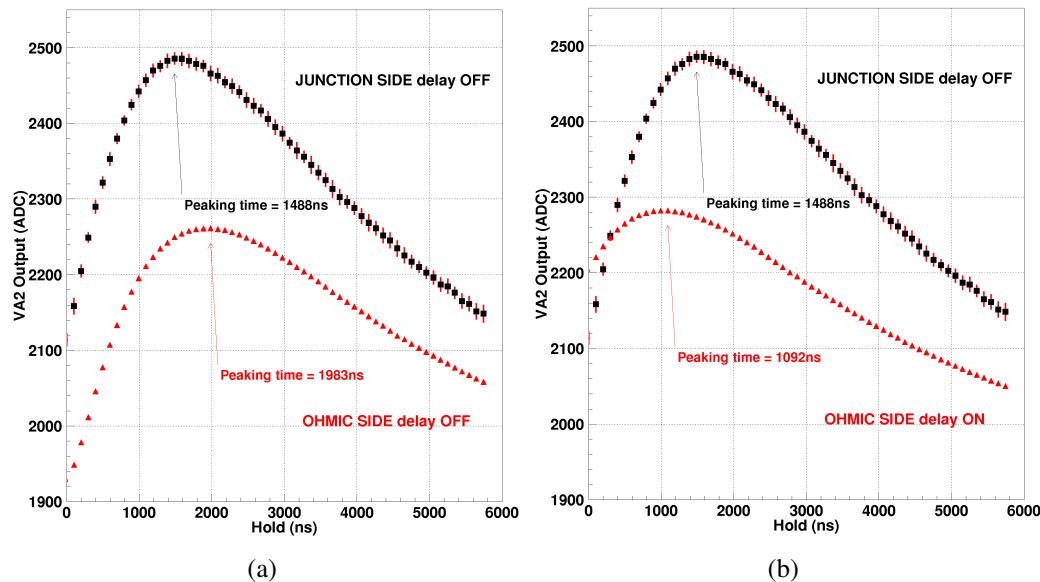


Figure 3.3: The junction (black squares) and ohmic (red triangles) side output signals of a single channel measured with the calibration input: the *delay* bit was always disabled for the junction side and (a) disabled and (b) enabled for the ohmic one.

¹⁹Physics Analysis Workstation, <http://wwwasd.web.cern.ch/wwwasd/paw/>.

3.1.3 The mechanical assembly

The silicon tile and the ceramic hybrid (hosting the ASICs) are assembled on a $12.5 \times 12.5 \text{ cm}^2$ 1 cm thick fiberglass support (figure 3.1). The ASICs have been glued with conductive epoxy glue (H20E by Epotek²⁰) and their control and output pads are bonded with $17 \mu\text{m}$ diameter Al wires (figure 3.4(a)). The strips are capacitively coupled to the input of the amplifier-multiplexer ASICs using custom 128 channel capacitor chips built on a quartz substrate (figure 3.4(b)); each capacitor chip channel comprises a 150 pF capacitor and protection diodes against the capacitor breakdown [107]. The fiberglass frame and the first part of the readout electronics are housed in an aluminum box ($12 \times 50 \text{ cm}^2$ and 4 cm thick) that protects the detectors from the light and possible damages and makes the entire module very easy to handle and transport (figure 3.4(c)).

3.2 The electronics chain

Up to 2011 the readout electronics for the CSEM+VA2 reference modules was based on standard ADC boards, the V550 ones by CAEN²¹ operating in the zero suppression mode [103]. In particular during the readout sequence the data were transferred from the ASICs to the ADCs and written on the disk on an event by event basis. If 4 modules were used and the overall noise of each module allowed a large enough cut for the zero suppression in order to have less than 5 strips per module above threshold, the readout sequence required:

- $384 \times 0.2 \mu\text{s} = 76.8 \mu\text{s}$ for the analog to digital conversion (the so-called *multiplexing time*);
- $5 \text{ strips} \times 8 \text{ sides} \times 5 \mu\text{s}$ (VME cycle) = $200 \mu\text{s}$ for the transfer from the ADCs to the PC.

Adding these values together one obtains a total readout time of $\sim 300 \mu\text{s}$, allowing a maximum DAQ rate of $\sim 3 \text{ kHz}$ [103]. To increase this value, in 2012 the readout electronics has been changed exploiting a completely different phylosophy (as discussed in the following).

A schematic view of the new electronics chain is shown in figure 3.5: it is designed to minimize the dead time and to work with pulsed beams such as the CERN extracted ones or the continuous wave ones such as the electron beam at MAMI²². The dead time reduction allows to acquire a large enough statistics in

²⁰Epoxy Technology Inc, <http://www.epotek.com>.

²¹Costruzioni Apparecchiature Elettroniche Nucleari S.p.A., <http://www.caen.it/>

²²More details about the CERN beamlines are given in section 3.3 while the one of the MAMI accelerator is presented in chapter 5 (section 5.3.1).

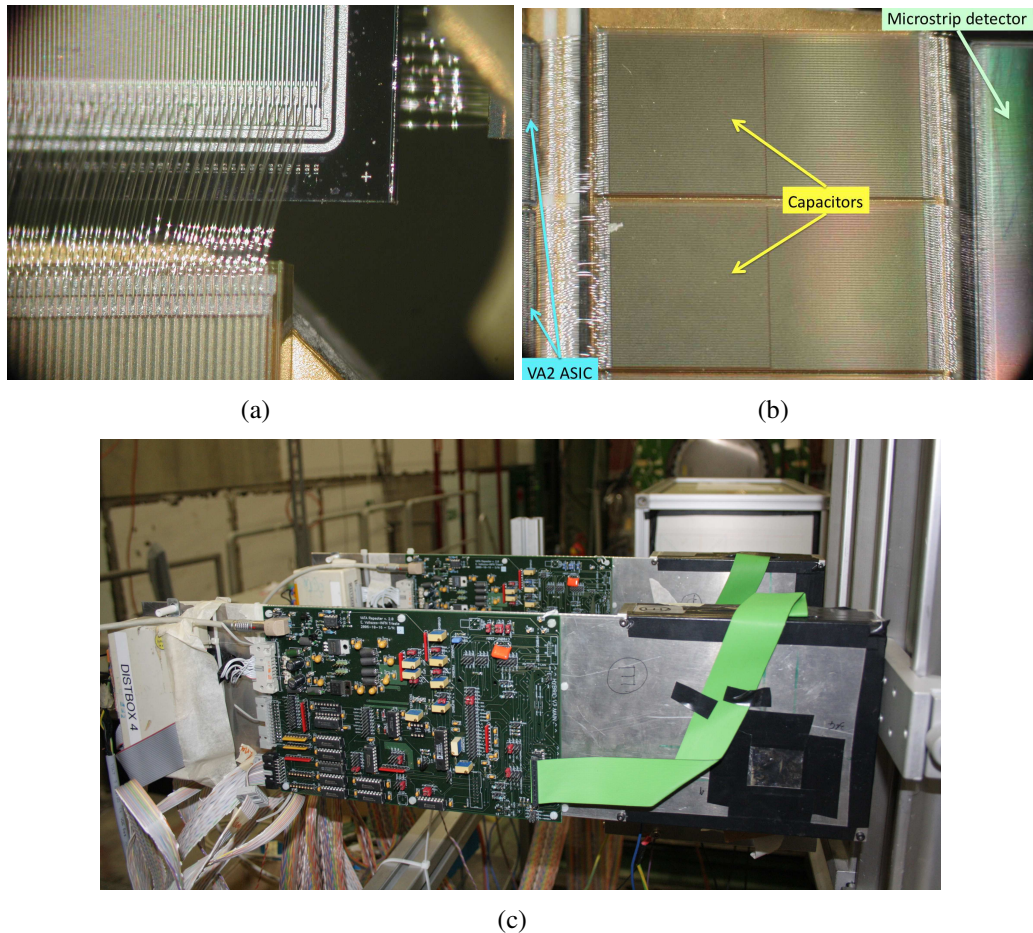


Figure 3.4: Details of the CSEM+VA2 reference module assembly: (a) the Al bonding wires and (b) the coupling capacitors connecting the silicon tile to the VA2 ASICs. (c) The module mounted on the CERN PS T9 beamline with its frontend electronics.

a short time, that is a key element in many experiments and is fundamental, for example, when studying very small effects (in terms of deflection angle) like the ones in bent crystals.

The interface between the detector+ASIC hybrids and the readout electronics is presented in section 3.2.1 and is provided by the so-called *frontend electronics* (pink dashed box in the top right part of figure 3.5); this part has not been changed since 2007 [86, 103]. The *readout electronics* is a VME (Versa Module Eurocard) custom one with three main elements for the output signals sampling, the data storage and the trigger generation; its description is given in section 3.2.2.

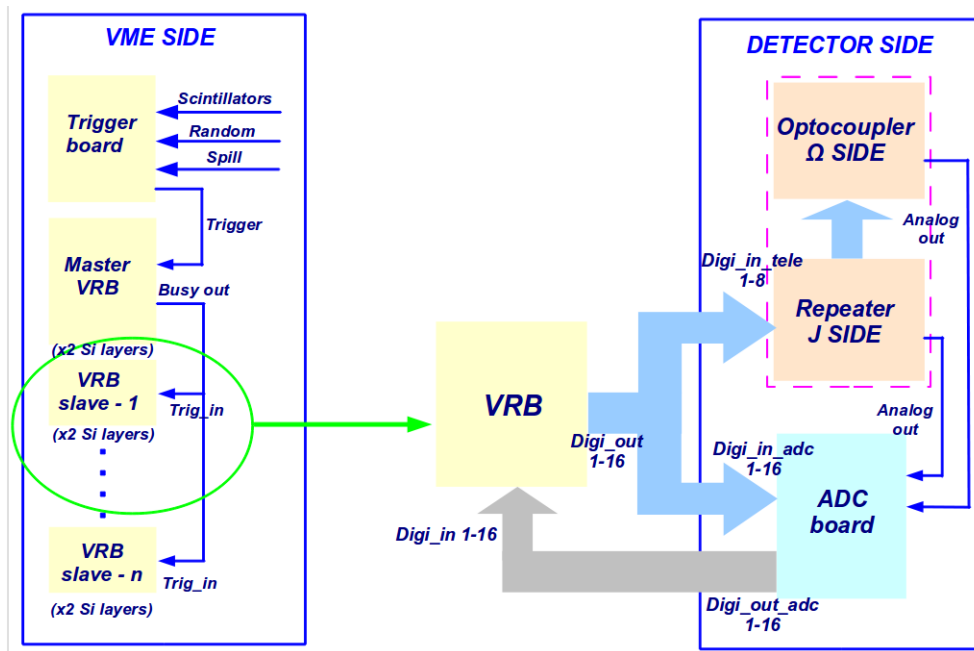


Figure 3.5: Schematic view of the complete electronics chain [27]: its main parts, the *frontend* (pink dashed box) and the *readout* one, are shown.

3.2.1 The frontend electronics

The frontend electronics is based on the so-called *repeater* and *optocoupler boards* [27]. Each repeater board (figure 3.6(a)) is a 4 layer Printed Circuit Board (PCB) responsible of the first part of the signal conditioning and the biasing of the detector and the ASICs. Each board performs the following tasks:

- it provides the configuration digital signals to the ASICs through 50 pin ERNI²³ cables; since the signals are differential in order to transport them

²³ERNI Electronics Inc., Richmond (USA), <http://www.erni.com>.

to long distances²⁴ without being affected by noise, the board transforms the RS422 differential signals²⁵ to single ended ones as requested by the ASICs;

- it provides the bias to the detector and the ASICs themselves. The ASICs power rails (± 2 V) are generated starting from ± 6 V power regulators on the repeater itself while the biasing for the silicon tiles is provided by a dedicated battery box (in the range 18-54 V with 9 V steps). The digital and analog supplies are filtered separately;
- it amplifies with a NE592²⁶ the multiplexed analog output of the hybrid; the current-voltage conversion takes place on the hybrid itself;
- it allows to choose the configuration settings (threshold and trigger mask) for the VATA ASIC family as will be discussed in chapter 5.

Since the modules house a double side silicon tile, the n-sides of each module have a “zero” level which is not ground (0 V) but the bias voltage (18-54 V). For this reason both the digital and analog signals from and to the ohmic side are level shifted by the optocoupler board (figure 3.6(b)) with the ADUM 2400²⁷ for the digital signals and the HCPL 4562²⁸ for the analog ones.

3.2.2 The readout electronics

The Data AcQuisition (DAQ) system is a VME one controlled by a SBS Bit3 620 board²⁹ optically linked to a PC running the Linux operating system. The DAQ software is written in C with Tcl/Tk³⁰ for the user graphical interface (figure 3.7). For the experiments with crystals the DAQ system is also able to remotely control the goniometric system to align the crystal with respect to the incoming beam [1]. On the other hand, for the new modules based on the self-triggering VATA ASICs, a configuration window (figure 3.7 right) is available and allows the setting of the trigger mask of the ASICs.

²⁴For instance, the setup used by the COHERENT experiment at CERN features a typical distance between each module of ~ 10 m to be able to distinguish the different effects induced by the interaction of the particles with the crystallographic lattice [1, 20].

²⁵RS422 (also EIA-422) is a technical standard that specifies the electrical characteristics of a digital signaling transmission.

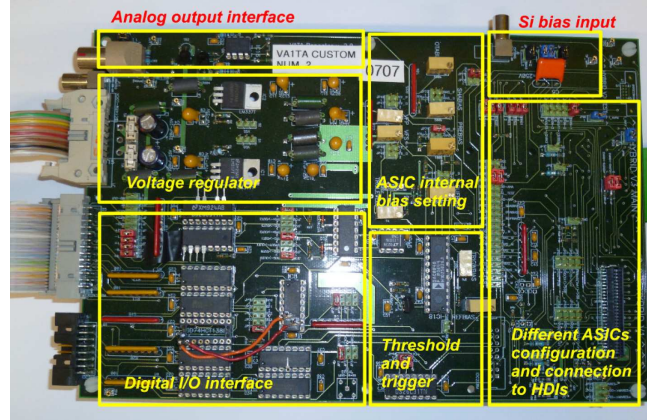
²⁶ON Semiconductors, <http://www.onsemi.com>.

²⁷Analog Devices, <http://www.analog.com>.

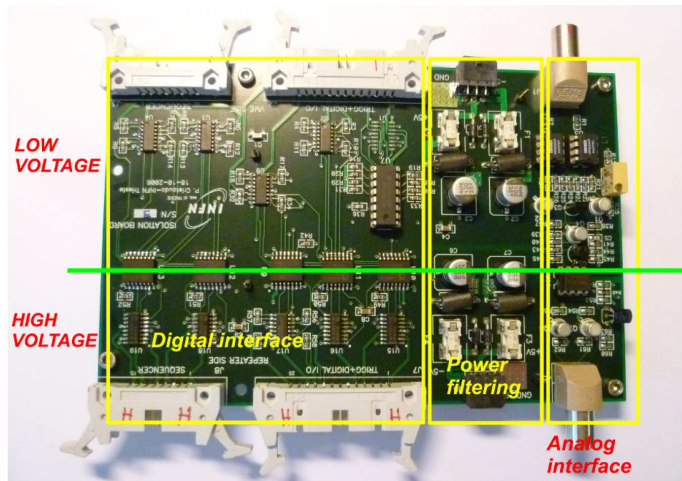
²⁸AVAGO Technologies, <http://www.avagotech.com>.

²⁹SBS Technologies Inc., now acquired by GE Intelligent Platforms, Virginia (USA), <http://www.geautomation.com>.

³⁰Tcl (Tool Command Language) is a dynamic programming language and Tk is its graphical user interface toolkit, <http://www.tcl.tk>.



(a)



(b)

Figure 3.6: Photos of the frontend electronics [27]: (a) the *repeater board* and (b) the *optocoupler* one; the main blocks performing the different tasks listed in the text are shown.

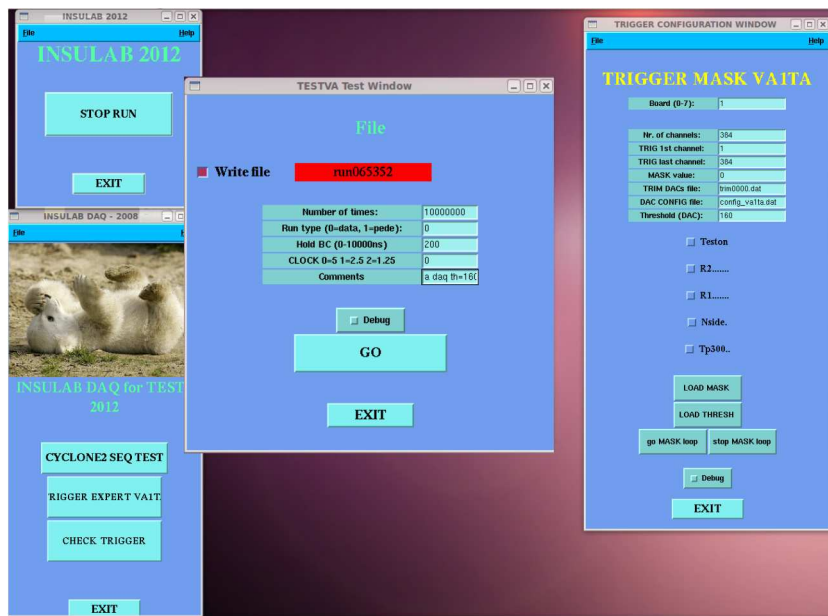


Figure 3.7: The DAQ user interface: several buttons are available and allow the setting of both the goniometer motors for the experiments with crystals (not shown in this picture) and the trigger configuration for the VATA ASICs (the *Trigger Mask VAITA* window).

The DAQ system philosophy is the following: the events are stored in dedicated memories during the spill³¹ and then transferred and written on the PC during the interspill period (that is when no particles are present) to reduce the dead time and increase the DAQ rate.

The DAQ system is divided into three main parts and it is based on custom ADC boards, dedicated VME readout/memory ones (the so-called *VME Readout Boards - VRBs*) and a custom trigger board [27]:

- each ADC board (figure 3.8(a)) is located close to the module and hosts up to 3 channels with an AD9220 12 bit ADC (Analog Devices) for the “*in situ*” signal digitization. The board is controlled by an Altera Cyclone II EP2C8³² FPGA (Field Programmable Gate Array) and the communication with the VRBs is performed with 16+16 I/O (Input/Output) LVDS (Low-Voltage Differential Signaling) lines. A Gigabit link either on optical fiber with the GOL Opto-Hybrid (GOH [110]) or on coaxial cables with a TLK1501 ASIC [111] (by TI³³) is available;
- the VRBs (INFN-Ts [112], figure 3.8(b)) are used to readout the ADC output signals and to store the data. Each VRB hosts an Altera EP2C50 FPGA with 50k cells and 581 kbit of internal RAM (Random Acces Memory) and 4 PLLs (Phase Locked Loops) for the clock generation. The board has 16+16 LVDS inputs/outputs, 2+2 TTL (Transistor-Transistor Logic) inputs/outputs, a TLK1501 Gigabit link and 4 Mword of 32 bit RAM. The FPGA is also in charge of the interface with the VME A32D32.

Each VRB can operate both in *normal* and in *zero suppression* mode:

- * in the first case the signal coming from the ADC board is de-multiplexed and the overall stream of data is stored in the RAM with a maximum of 4096 events with 384×2 strips each; this mode is used for the pedestal runs and the non zero suppressed ones;
- * in the second solution only the strips with a signal above a given threshold are stored in the RAM; the threshold is set considering the noise rms of each channel (see appendix A). A maximum of 65536 events with 16×2 strips each can be stored;
- the last part of the DAQ system is a dedicated trigger board (figure 3.8(c)) designed by INFN-Ts; it is responsible for the DAQ trigger generation (to

³¹Both at the SPS H4 and PS T9 beamlines, the particles are delivered to the users as particle bunches (the so-called *spills*) whose number and time structure depend on the beamline (see section 3.3 for more details).

³²Altera Corporation, <http://www.altera.com>.

³³Texas Instrument, <http://www.ti.com>.

start the readout sequence) that is the AND of the discriminated signals coming from a set of plastic scintillators (section 3.3) and the spill signal; the trigger generation is vetoed when the spill signal is not present. A random signal is used for the pedestal runs while several scalers are used to evaluate the particle and trigger rate.

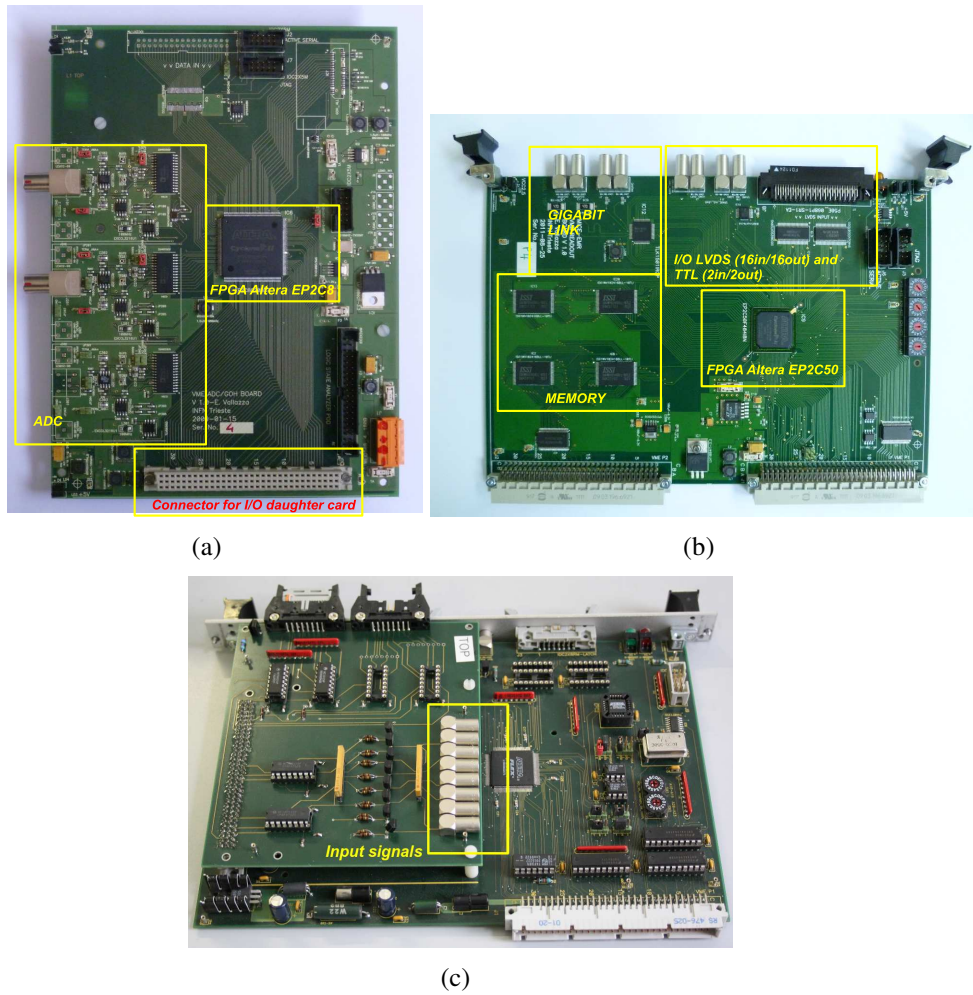


Figure 3.8: Photos of the readout electronics [27]: (a) the *ADC board*, (b) the *VRB* and (c) the *trigger board*; the main blocks performing the different tasks listed in the text are shown.

The present maximum DAQ rate is ~ 6 kHz: if 3 VRBs are used (that is 6 silicon sides are readout) the overall time to readout an event is $170 \mu\text{s}$ due to the irreducible multiplexing time ($\sim 80 \mu\text{s}$ with a 5 MHz readout clock) and to the initialization time of the boards themselves ($80 \mu\text{s}$); this latter has already been

reduced to $10 \mu\text{s}$. More details about the readout sequence and the data storage can be found in [86]. As will be discussed in chapter 5, a possible way to reduce the multiplexing time to one third (from ~ 80 to $\sim 27 \mu\text{s}$) is to read in parallel the three ASICs; in this case every ADC reads the output signals coming from one of the ASICs thus needing only 128 clock pulses for the complete signal shifting.

This DAQ system features a very high versatility; it could in fact operate with different tracking systems and frontend boards based on different ASICs (for example the MAROC3³⁴ one [113, 114]). As already mentioned the system has been used with larger silicon detectors (with a larger physical and readout pitch and the TA1 ASIC [115]), the SiBCs [105, 106], to test LYSO/PbWO₄ and shashlik calorimeters readout by SiPMs [74, 76, 104] for the FACTOR and TWICE experiments.

3.3 The experimental setup

The CSEM+VA2 reference modules have been tested both at the CERN SPS H4 beamline (with 150 GeV/c electrons) and at the PS T9 one (with muons and pions in the 1-10 GeV/c momentum range). Table 3.3 summarizes the main parameters of the two beamlines. As far as the time structure of the beam is concerned, the typical spill duration on the PS T9 line is 400 ms and the number of spills ranges from 1 to 3 in each 45 s cycle with a time distance which depends on the cycle type, while on the SPS H4 line the spill lasts 8 s with a cycle of 45 s.

The standard setup used at the SPS H4 beamline (figure 3.9(a)) consisted in:

- a $10 \times 10 \text{ cm}^2$ 1 cm thick plastic scintillator for the trigger generation (the so-called *large* trigger); the light produced by the interacting particles is readout by a PhotoMultiplier Tube (PMT) directly connected to the scintillator tile (figure 3.9(b)); the typical operational voltage is $\sim +1600 \text{ V}$;
- the INSULAB Telescope: the 4 modules were placed as close as possible to reduce the multiple scattering contribution; two external modules have been used as a high precision reference system (as in [1, 27]) while the module under test has been placed in the center;
- the DAQ system described in section 3.2 for the telescope readout; the signal used for the trigger generation (the one coming from the *large* plastic scintillator) is conditioned with a Nuclear Instrumentation Module (NIM)

³⁴Multi-Anode ReadOut Chip 3. This ASIC has been developed by the Laboratoire de l'Acélérateur Linéaire (LAL) of Orsay (<http://omega.in2p3.fr>) for the readout of the HAMAMATSU PMTs used by the ATLAS (A Toroidal LHC ApparatuS) Luminometer [113].

Beamlne	H4 SPS	T9 PS
Located at building	North Area 887	East Hall Area 157
Momentum range [GeV/c]	20-250	1-15
Particle type	e, μ , hadrons	e, μ , hadrons
Polarity	\pm	\pm
Intensity [particles/spill]	$4 \cdot 10^4$	10^3 - 10^4
Time structure		
# spills/cycle	1	1-3
spill time width	8 s	400 ms
spill cycle	45 s	45 s
spill distance	45 s	variable
Divergence [mrad] (in both directions)	0.1-0.2	0.5-5
Beam size [cm] (in both directions)	0.1-0.6	3-10

Table 3.3: The main technical parameters of the CERN SPS H4 and PS T9 beamlines; the beam divergence and size have been measured by the INSULAB Group during several beamtests and correspond to the FWHM of the corresponding distributions [1, 86, 116].

crate and standard NIM electronics; the discriminated signal is sent to the trigger board to generate the start of the readout sequence.

For the data taking at the PS T9 line some changes have been implemented given that:

- the beam energy is more than 10 times smaller than the SPS H4 line one; to limit the multiple scattering contribution only 3 modules have been set up and were placed closer than in the SPS H4 setup (the typical distance between each module was \sim 10-15 cm, blue values in figure 3.9(a));
- the beam size is \sim 100 times larger than that of the SPS H4 line and \sim 10 times larger than the detector sensitive area; an additional scintillator (figure 3.9(c) - the so-called *small* trigger) has been installed behind the last module; it consists in a 7 mm thick polystyrene tile with an active area of $2 \times 4 \text{ cm}^2$ [1] readout by a single anode 931-B PMT (HAMAMATSU [117]). The typical operational voltage is \sim -900 V and the scintillator has been directly coupled to the silicon module. Also in this case the signals coming from the two trigger systems (the *large* and the *small* one) were conditioned by standard NIM electronics, put in coincidence and vetoed with the spill signal.

Figure 3.9(d) shows a photo of the SPS H4 setup with the 150 GeV/c electron beam coming from the bottom.

3.3.1 The tests goals

The goal of the beamtests performed at the CERN beamlines was twofold:

- to study the behavior of the CSEM+VA2 reference modules with the new electronics both in the high and low momentum range. Each module has been characterized in terms of the following figures of merit:
 - * the pedestal and noise;
 - * the cluster³⁵ analysis; the number of clusters, the number of strips per cluster and the SNR distributions have been computed for each module;
- to evaluate the spatial resolution of one CSEM+VA2 reference module (chapter 4), *i.e.* to measure the precision with which the detector is able to reconstruct the hit position. As will be discussed in section 4.2.1, the high energy test allowed both to evaluate the Charge Sharing (CS) among the strips (section 3.5) and to compute the ultimate spatial resolution with the eta algorithm (section 4.3) for the junction side. On the other hand, given a strange behavior of the ohmic side of the third module (named *TELE 3-A*), it was not possible to evaluate the spatial resolution for this side. The problem has been ascribed to the high particle rate of the SPS H4 beam and to the damaged bondings (figure 3.10) found once the module has been dismounted at the end of the beamtest. For this reason the test has been repeated on the PS T9 beamline (section 4.2.2).

The analysis procedure used to select the set of the so-called *good events* is the same for all the beamtests and is presented in appendix A together with the module alignment procedure.

3.4 The commissioning phase @ SPS H4

3.4.1 Pedestal and noise

Figure 3.11(a) presents an example of the pedestal distribution both for the junction (top) and ohmic (bottom) side of one CSEM+VA2 reference module (named *TELE 4-E*). The three different regions in both pictures correspond to the three

³⁵See section 3.4.2 and appendix A for the definition of *cluster*.

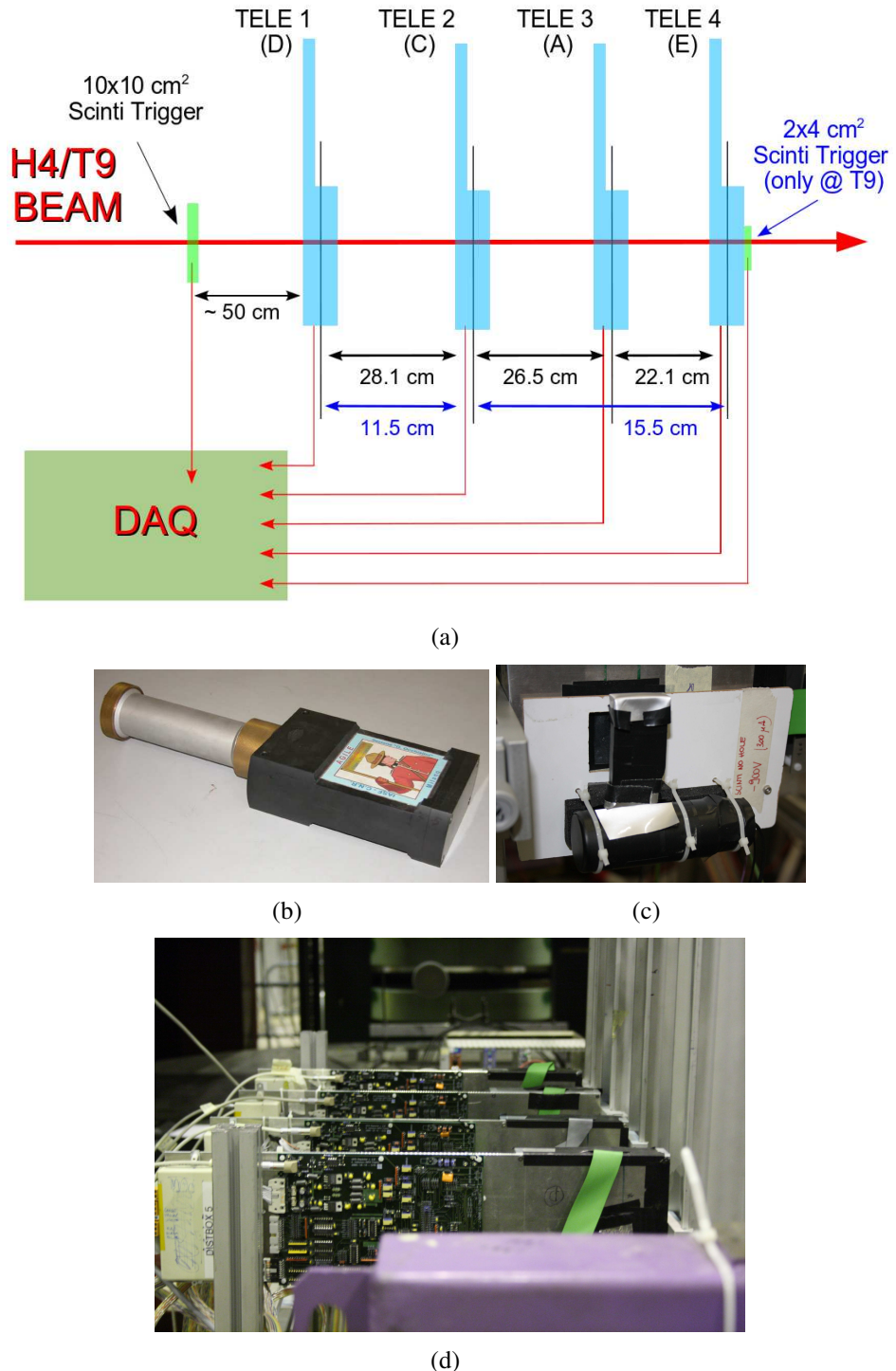


Figure 3.9: (a) Schematic view of the CERN SPS H4 setup (a similar one has been used at the PS T9 beamline with some changes described in the text). Photos of (b) the *large* $10 \times 10 \text{ cm}^2$ plastic scintillator and (c) the *small* $2 \times 4 \text{ cm}^2$ one; (d) photo of the INSULAB Telescope during the SPS H4 data taking [27]: the 150 GeV/c electron beam comes from the bottom.

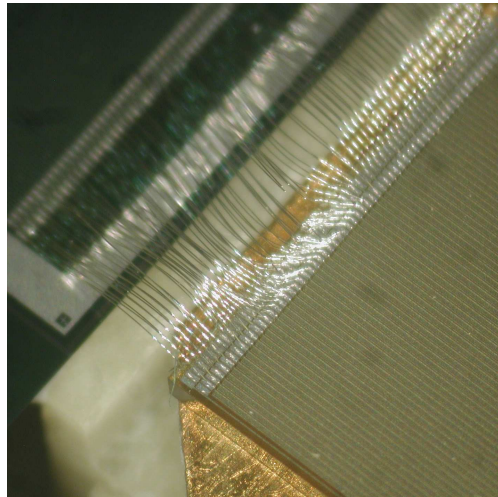


Figure 3.10: Photo of the damaged bondings of the *TELE 3-A* ohmic side.

readout ASICs (see section 3.1 for details). The global noise rms (black lines) and the noise rms after the common mode subtraction (red lines) distributions are presented in figure 3.11(b): the peaks correspond to the noisy channels which have been excluded in the analysis. The details about the pedestal and noise (global, common mode and intrinsic one) calculation can be found in appendix A while table 3.4 summarizes the values obtained for all the reference modules at the SPS H4 high energy beamtest together with the percentage of the unused (dead/noisy) strips. Similar values have been obtained during the PS T9 low energy beamtest while the ones for the *TELE 3-A* ohmic side are missing given the problem already mentioned above.

3.4.2 Cluster analysis: the modules behavior

All the reference modules have been characterized in terms of cluster SNR³⁶.

The first step of the analysis is the good event selection reconstructing the incoming particle impact position through the so-called *maximum pull* distribution. The pull is defined as the ratio between the Pulse Height (PH), in ADC counts, of the strip with the maximum signal in the event and its corresponding noise rms (see details in appendix A). Figure 3.12 shows an example of the pull distribution of one CSEM+VA2 reference module: the *two peak-shape* of the distribution in figure 3.12(a) is given by the one floating strip readout scheme adopted for the junction side. When the particle crosses the center of the floating strip, each of

³⁶The examples presented here refer to the test of the *TELE 4-E* module at the SPS H4 beamline; the other modules behave in a similar way and the obtained values are listed in table 3.5.

Module (TELE)	Pedestal range [ADC]	Global noise [ADC]	CM noise [ADC]	Intrinsic noise [ADC]	Unused ch [%]
3-A jun. ohm.	1940-2210 -	8.51±0.03 -	2.72±0.15 -	3.79±0.02 -	3.39 2.08
2-C jun. ohm.	1875-2115	4.44±0.02	2.51±0.09	3.27±0.02	4.95
	1810-2010	4.33±0.02	2.24±0.09	2.71±0.02	2.60
1-D jun. ohm.	1860-2170	6.28±0.03	1.81±0.06	6.03±0.02	1.83
	1815-1970	2.43±0.03	0.59±0.02	2.12±0.02	0.78
4-E jun. ohm.	1910-2220	5.52±0.02	1.82±0.06	5.21±0.02	1.30
	1870-2105	3.94±0.02	0.67±0.02	3.75±0.04	0.78

Table 3.4: Comparison of the pedestal, noise and number of unused (dead or noisy) channels of the CSEM+VA2 reference modules: the global, common mode and intrinsic noise values have been computed following the procedure in appendix A.

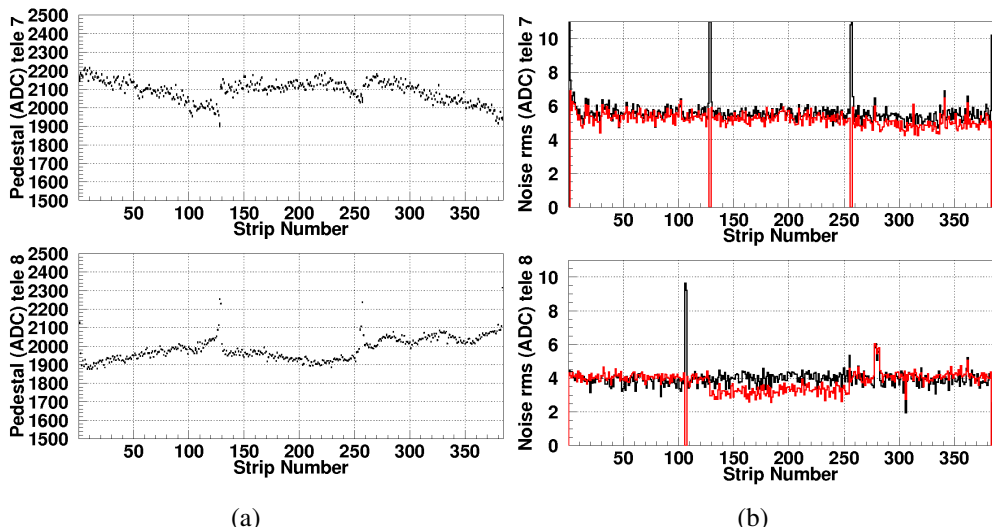


Figure 3.11: (a) The pedestal and (b) the noise distributions for the junction (top) and ohmic (bottom) side of a CSEM+VA2 reference module. The black lines represent the global noise rms while the red ones the intrinsic noise after the common mode subtraction.

the two neighbouring readout strips collects $\sim 39\%$ [27] of the total charge and the pulse height is smaller: this case corresponds to the first peak while the larger PH one is the one due to the particle crossing a readout strip.

The red solid lines in both figures indicate the threshold set to identify the hit strips: the pedestal has been subtracted from the raw data of each strip and the obtained value compared with the threshold (typically around $15-20\sigma$); the strip with the maximum is the one whose signal overcomes both the threshold and the signal of all the other channels.

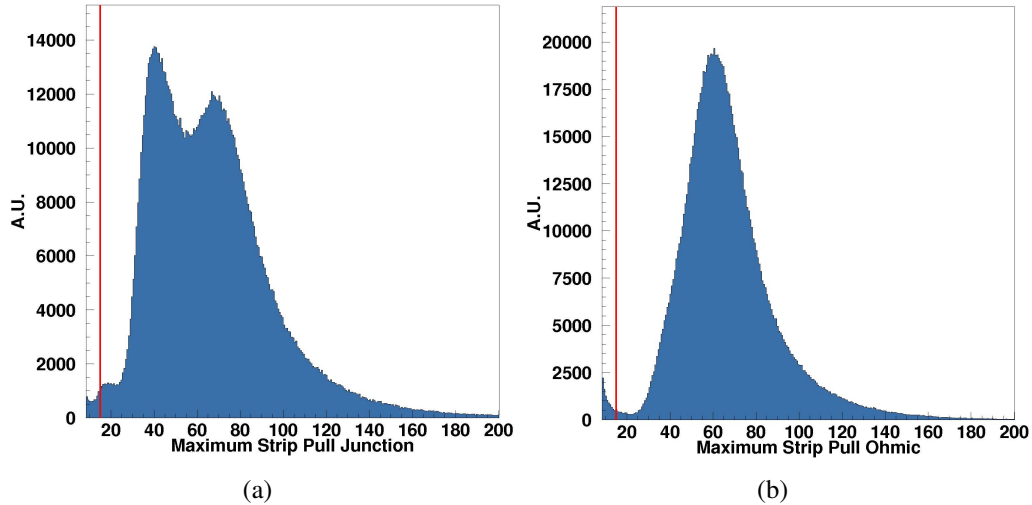


Figure 3.12: The maximum pull distributions of (a) the junction and (b) the ohmic side of one CSEM+VA2 reference module; the *two peak-shape* in (a) reflects the fact that a floating strip readout scheme is used.

Since the charge deposited by the particle can be shared among several strips (the so-called *cluster*), the hit position has been reconstructed using a *cluster-finding algorithm* based on the Center Of Gravity method (COG [118]). The analysis consists of the following steps:

- the number of clusters (figure 3.13(a)) and the number of strips composing the cluster (figure 3.13(b)) have been taken into account on an event by event basis. A strip has been considered as part of the cluster if its signal is larger than a given threshold set by the so-called *lateral pull distribution*³⁷, that is the pull distribution of the strips surrounding the one with the maximum signal in the event: typically the chosen threshold is smaller than the one for the strip with the maximum and is of the order of $5-10\sigma$. As expected, for both the junction (top) and ohmic (bottom) cases, more than 82% of

³⁷The complete definition and an example of the lateral pull distribution are given in appendix A.

the events are single cluster events³⁸ with more than 92% of the clusters typically composed of 1-2 strips. In the following analysis the good events are the ones with a single 1 or 2-contiguous strips cluster; for small incident angles, in fact, this is a reasonable approximation since only one or two strips collect the whole charge generated by the particle;

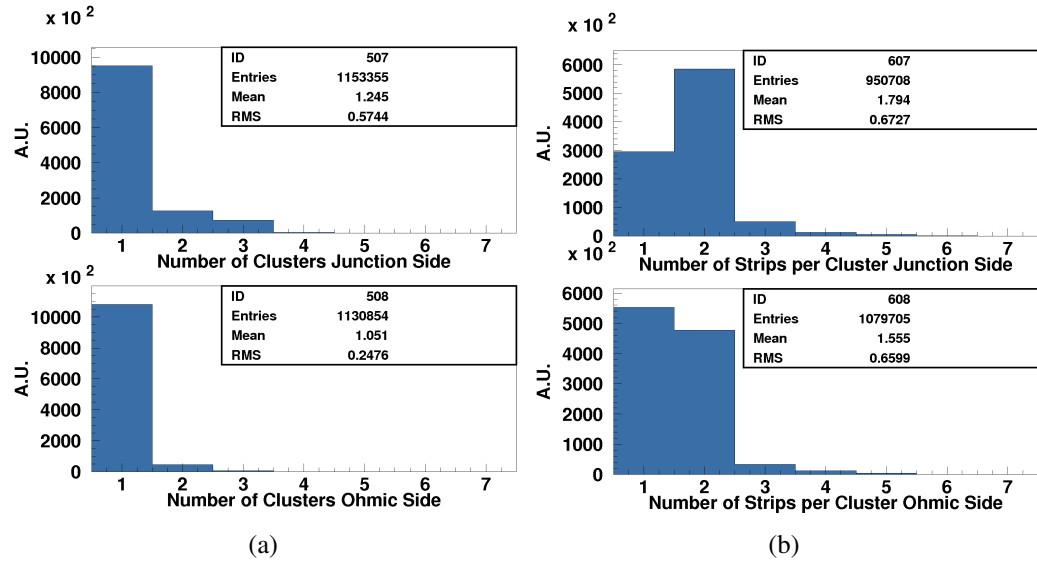


Figure 3.13: Distributions of (a) the number of clusters and (b) the number of strips per cluster of the junction (top) and ohmic (bottom) side of one CSEM+VA2 reference module: typically single 1-2 strips cluster events are present on both sides.

- the particle hit position has been computed as [118]

$$xp = \frac{\sum_i^N (PH_i \cdot STRIP_i)}{\sum_i^N PH_i} \quad (3.1)$$

where the i index runs over the number of strips composing the cluster and PH_i is the corresponding pulse height. An example of the SPS H4 beam profile measured by one CSEM+VA2 reference module (named *TELE 4-E*) considering only the set of good events is given in figure 3.14(a): both the horizontal (right) and vertical (left) direction have a Gaussian-like shape

³⁸Two clusters are considered as separated if there are at least five strips below threshold (set with the maximum pull distribution) between their respective *highest strips* i.e. the ones with the largest signal among the strips composing the clusters themselves.

while the regions with low statistics correspond to the dead/noisy channels. The same module together with the first one (named *TELE 1-D*) has been used to compute the beam divergence (figure 3.14(b)) that is less than $155 \mu\text{rad}$ in both directions³⁹. During the low energy beamtest at the PS T9 beamline, a parallel beam (that is a *top-hat* shape one) has been used in order to obtain a small enough divergence value;

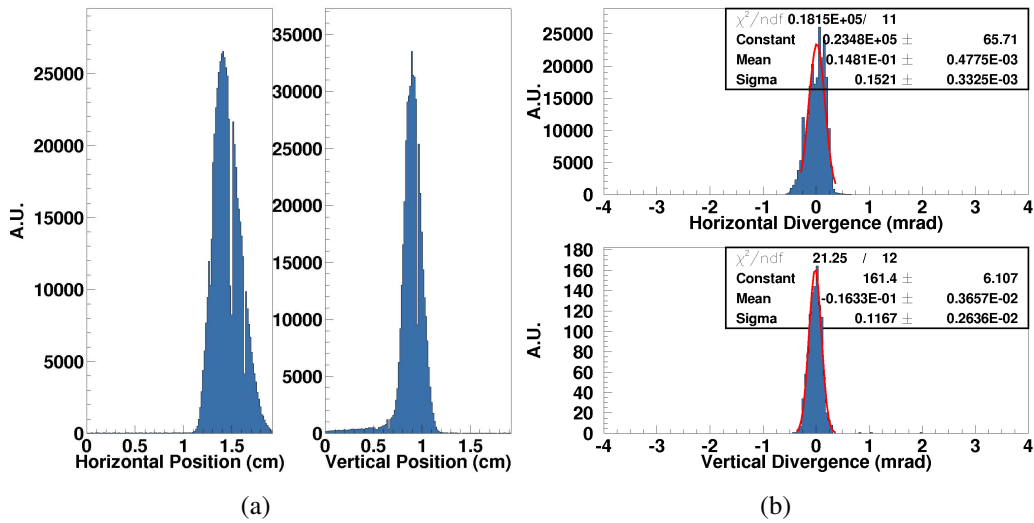


Figure 3.14: The SPS H4 (a) beam profile and (b) divergence measured by two CSEM+VA2 reference modules: the junction sides measure the horizontal direction while the ohmic sides the vertical one.

- to study the analog response of the detector in terms of the cluster pulse height and noise, and thus to compute its SNR, the following procedure has been applied:

³⁹It must be noted that for the *TELE 1-D* ohmic side the percentage of the 1-2 strips single cluster events was $\sim 10\%$ due to a non correct readout clock (see later on); for this reason the statistics used to compute the vertical divergence is much lower (\sim two orders of magnitude) than that for the horizontal one.

- * the cluster SNR has been defined as:

$$\begin{aligned}
 SNR_{clu} &= \frac{clu}{clunoise} \\
 clu &= \sum_i^N PH_i \\
 clunoise &= \sqrt{\frac{\sum_i^N \sigma_i^2}{N}}
 \end{aligned} \tag{3.2}$$

where clu is the total signal of the cluster, *i.e.* the sum of the pulse heights (PH_i) of all the strips (N) composing the cluster, and $clunoise$ is the noise rms of the cluster after the common mode subtraction (σ_i is the noise rms of each strip);

- * for each module the cluster pulse height distribution (clu) has been fitted with a Landau-like function (figure 3.15(a)), that can be parameterized as follows [119]:

$$\begin{aligned}
 F(\lambda) &= \frac{1}{\sqrt{2\pi}} \exp[-0.5(\lambda + \exp(-\lambda))] \\
 \lambda &= \frac{\Delta E - \Delta E_{MPV}}{\xi} \\
 \xi &= \text{FWHM}/4.02
 \end{aligned} \tag{3.3}$$

where ΔE_{MPV} is its Most Probable Value (MPV) [38]; the fit parameters represent, respectively, the normalization factor (P1), the FWHM (P2) and the MPV (P3). On the other hand, the cluster noise distribution ($clunoise$) has been fitted with a Gaussian-like function (figure 3.15(b)). The values obtained for all the CSEM+VA2 reference modules are listed in table 3.5;

- * the last step is the SNR calculation from equation 3.2; figure 3.16 shows an example of the junction side SNR distribution fitted with a Landau-like function: the MPV is 71.97 ± 0.07 . The values for the other modules are reported in table 3.5: typically the SNR values of the junction sides are larger than the ohmic sides ones, with the exception of the one for *TELE I-D* which has a smaller noise value. Nevertheless it must be noted that during the SPS H4 high energy beamtest the *delay* bit of the ohmic sides was turned ON causing an uncorrect analog

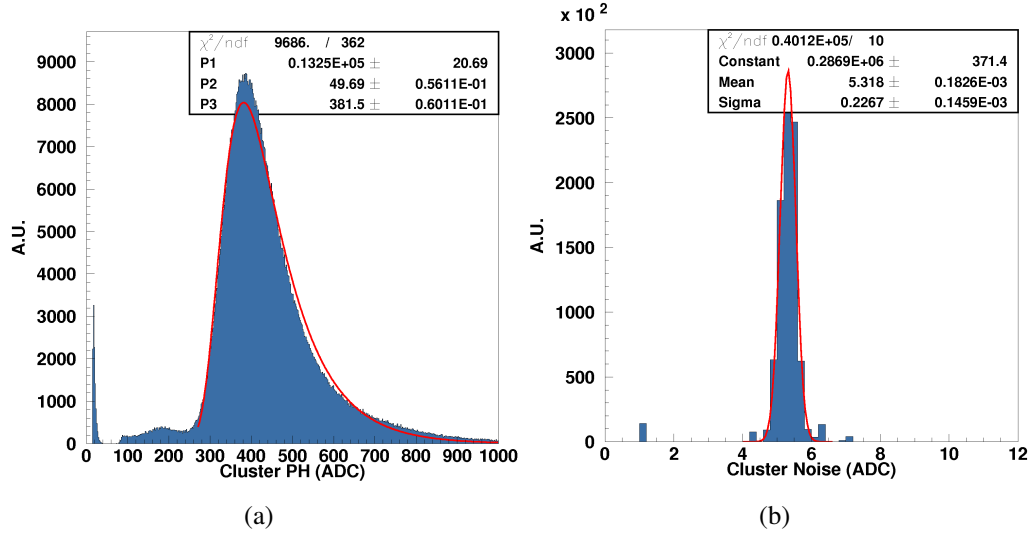


Figure 3.15: Fitted distributions of the cluster (a) pulse height and (b) noise of a CSEM+VA2 reference module; the pulse height distribution has been fitted with a Landau-like function while the noise one with a Gaussian.

Module (TELE)	Pulse Height [ADC]	Noise [ADC]	SNR
3-A jun. ohm.	390.52 ± 0.05	3.95 ± 0.01	108.46 ± 0.03
2-C jun. ohm.	250.07 ± 0.05 189.37 ± 0.22	3.43 ± 0.01 2.72 ± 1.00	85.37 ± 0.06 69.27 ± 0.08
1-D jun. ohm.	352.26 ± 0.06 168.10 ± 0.06	5.96 ± 0.01 1.83 ± 0.01	57.75 ± 0.01 91.95 ± 0.08
4-E jun. ohm.	381.50 ± 0.06 181.74 ± 0.02	5.32 ± 0.01 2.85 ± 0.01	71.60 ± 0.02 63.87 ± 0.01

Table 3.5: Comparison of the cluster pulse height, noise and Signal to Noise Ratio (SNR) values of the CSEM+VA2 reference modules.

signal sampling, *i.e.* the multiplexed output of the ASICs has not been sampled at its maximum (see section 3.1.2);

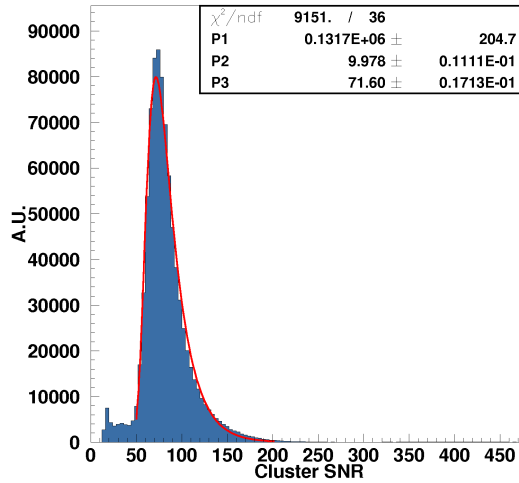


Figure 3.16: Fitted distribution of the cluster Signal to Noise Ratio of a CSEM+VA2 reference module; a Landau-like function has been used.

- * to better understand the large difference in the behavior of the *TELE 4-E* and *TELE 1-D* modules, the correlation between the charge collected by the junction and the ohmic side of both modules has also been considered (figure 3.17); the cluster SNR for both sides has been taken into account. The so-called *slicing method*⁴⁰ has been applied to evaluate the correlation value and the superimposed blue dots have been fitted with a linear function. A -0.15 ± 0.67 value for the intercept (P1) and a 0.96 ± 0.06 one for the slope (P2) have been found for the *TELE 4-E* module (figure 3.17(a)); the bisector (black line), corresponding to a 1:1 correlation, is also shown for comparison. Once again the two sides behave in a similar way and a similar amount of charge is collected by each one.

On the other hand the intercept and slope values for the *TELE 1-D* module (figure 3.17(b)) are -229.66 ± 3.39 and 6.17 ± 0.06 , respectively. In this case the correlation is completely lost: it has been ascribed to a non correct sampling of the ASIC output signal. For this module, in fact, it was not possible to adjust the so-called *clock jumper*

⁴⁰The basic idea of this analysis method (whose details will be presented in chapter 4) is to project the contour histograms in figure 3.17 into either vertical or horizontal slices and fit each of them with a given function; in this case a Landau-like function has been used.

placed on the ohmic side repeater board and in turn it was not possible to set a clock value to have a symmetric eta distribution; for this side the deposited charge is thus not equally shared among the strips. This fact has been confirmed considering and comparing the lateral and the maximum pull distributions (figure 3.18): the right strip pull (blue line) and the maximum strip one (black line) have a similar shape suggesting a certain amount of the charge has been shifted in the right strip while the left one (red line) collects a small amount of the signal (see [86] for more details).

3.5 The charge sharing distribution

As mentioned in section 2.2.2, in silicon detectors the capacitive coupling among the strips causes the charge deposited by a ionizing particle to be shared among neighbouring channels. The charge sharing for all the CSEM+VA2 reference modules has been studied with the same procedure described in [86].

The contour histograms in figure 3.19 show the signal collected by the strip with the maximum signal in the event as a function of the interstrip position⁴¹ computed with the standard COG method. In both cases 0 μm is the center of the first readout strip and 50 μm is the center of the nearby one; in figure 3.19(a) the center of the floating strip of the junction side is at 25 μm while for the ohmic side (figure 3.19(b)) the position at 25 μm corresponds to the border between the two readout strips.

As expected given the COG method does not take into account the dependence of the charge division from the particle hit position inside the strip itself, the distribution is not homogeneous and presents different regions that recall the shape of the eta distribution (figure A.3). The superimposed dots have been obtained with the slicing method presented in chapter 4: in this case the contour histograms in figure 3.19 have been projected in 50 vertical slices which have been fitted with a Landau-like function to obtain the MPV of the slice itself.

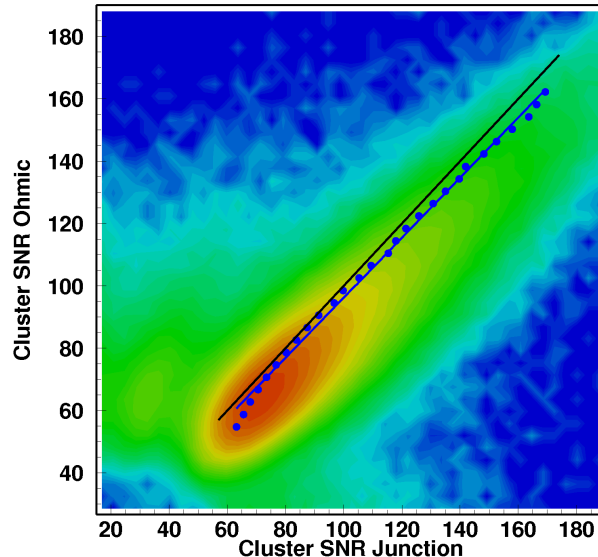
The charge sharing (CS) value has been computed as follows:

$$CS = \left(\left[\frac{(MPV_{25} + MPV_{26})/2}{(MPV_{sli\ start} + MPV_{sli\ stop})/2} \right] \cdot 100 \right) \cdot 2 \quad (3.4)$$

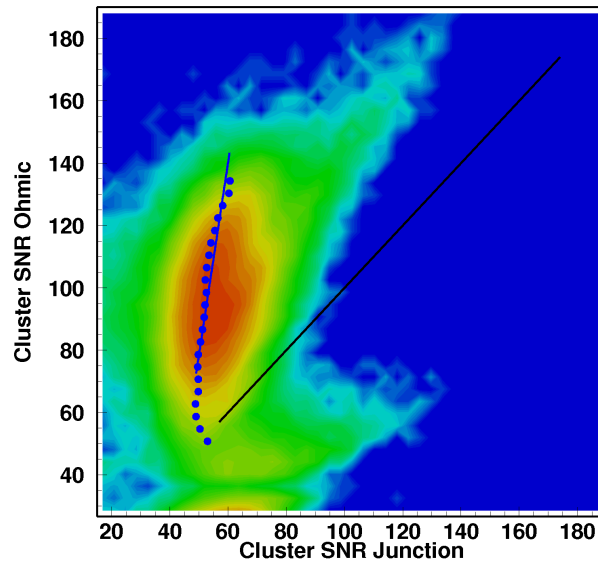
where *sli start* and *sli stop* correspond, respectively, to the first and the last fitted slices⁴². The charge sharing is thus defined as the ratio between the average of the

⁴¹The definition of the interstrip position ($xscal_j$) is given in section 4.3 (equation 4.7).

⁴²In both the examples presented in figure 3.19 only the slices from the 6th to the 45th have been considered given the statistics was too low for the others.



(a)



(b)

Figure 3.17: Correlation between the junction and ohmic cluster SNR of (a) the *TELE 4-E* module and (b) the *TELE 1-D* one; a slicing method (presented in chapter 4) has been applied to compute the blue dots while the black lines represent the bisectors.

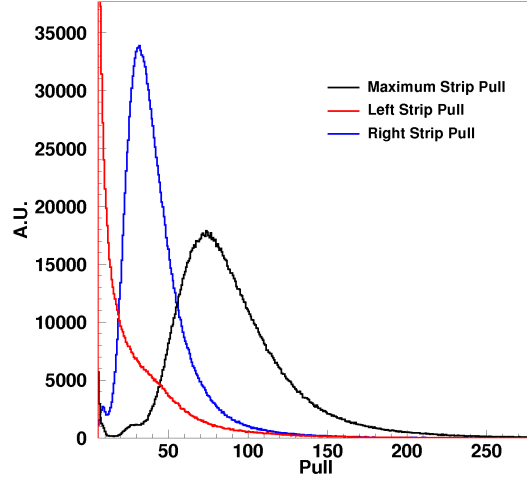


Figure 3.18: The maximum (black line), left (red line) and right (blue line) strip pull distributions of the ohmic side of the *TELE 1-D* module.

MPVs of the two central slices (yellow dots in figure 3.19) and the average of the MPVs of the first and last slice (red dots in figure 3.19) and the factor 2 reflects the fact that the signal is shared into the two neighbouring readout strips. Table 3.6 summarizes the values obtained from equation 3.4 for all the CSEM+VA2 reference modules; the values for the ohmic sides (with the exception of the *TELE 4-E* one) are missing given the used readout clock has not allowed to have a symmetric eta distribution which introduces a bias in the position reconstruction.

To evaluate the *real* charge sharing value the so-called *eta algorithm* has been applied following the procedure in [86, 108] to take into account the effective charge division between the strips and compute the *correct* particle hit. The details about this analysis method are given in section 4.3. Figure 3.20 presents the same contour histograms of figure 3.19 computed with the correct interstrip position (section 4.3): also in this case the superimposed dots have been obtained with the slicing method presented in chapter 4 and using a Landau-like function to identify the peak position⁴³. As expected both the junction (figure 3.20(a)) and the ohmic (figure 3.20(b)) distributions are more homogeneous compared to those in figure 3.19 and also the regions on the edges (*i.e.* the ones near 0 and 50 μm) are more populated.

The charge sharing value (table 3.6) has been computed with equation 3.4; also in this case the values for the ohmic sides (except the *TELE 4-D* one) are missing given that the eta algorithm cannot be applied if the eta distribution is

⁴³In this case for both the examples presented in figure 3.20 all the slices (from the 1st to the 50th) have been taken into account.

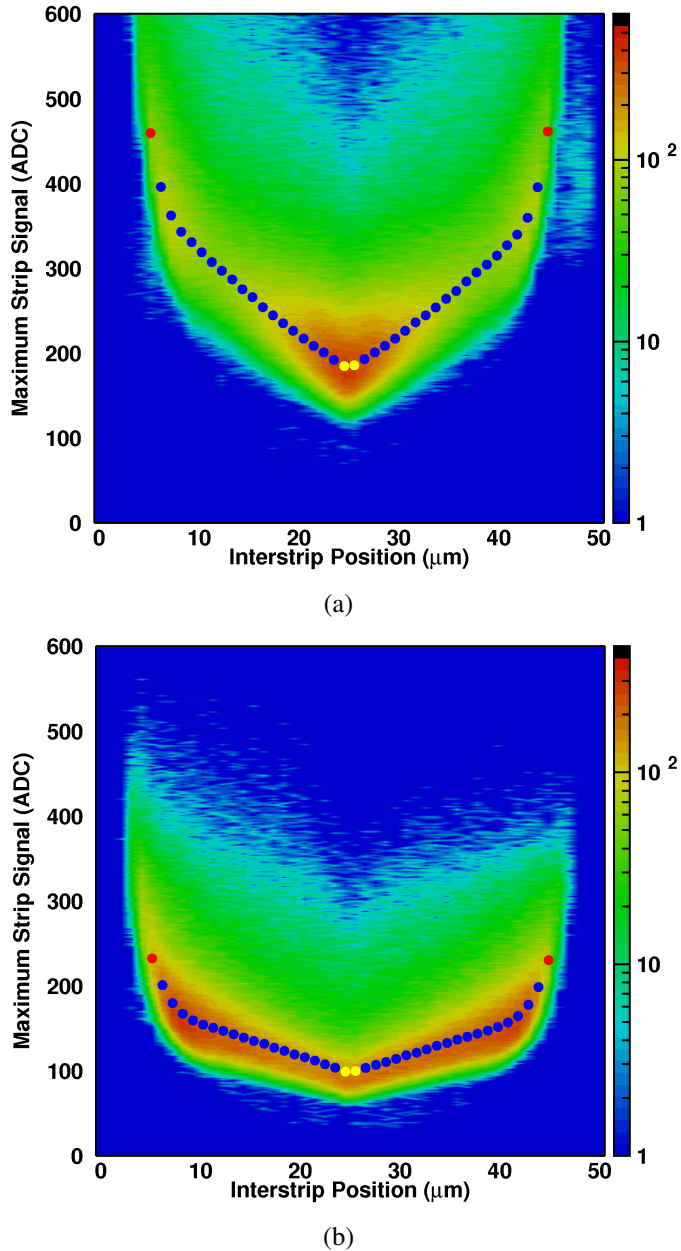


Figure 3.19: The charge sharing distributions of a CSEM+VA2 reference module: (a) junction and (b) ohmic side using the COG method for the particle position reconstruction; in both cases the blue dots have been computed with the slicing method presented in chapter 4 and using a Landau-like function.

Module (TELE)	Charge Sharing (COG) [%]	Charge Sharing (η) [%]
3-A jun. ohm.	96.39 -	92.33 -
2-C jun. ohm.	89.03 -	76.72 -
1-D jun. ohm.	73.89 -	76.20 -
4-E jun. ohm.	80.53 85.95	70.90 75.05
AVERAGE jun. ohm.	81.15 85.95	74.62 75.05

Table 3.6: Comparison of the charge sharing values of the CSEM+VA2 reference modules; the ones in the second column have been computed using the standard COG method while the ones in the third column with the eta algorithm (presented in chapter 4).

too asymmetric and the integration with equation 4.8 is not possible. The average between the junction side CS values (computed excluding the one for the *TELE 3-A*) is 74.62% and is similar to the one computed for the ohmic side of the *TELE 4-E* (75.05%). As mentioned in appendix A the capacitive coupling among the strips is similar for the two sides confirming they behave in a similar way in terms of charge sharing among the strips.

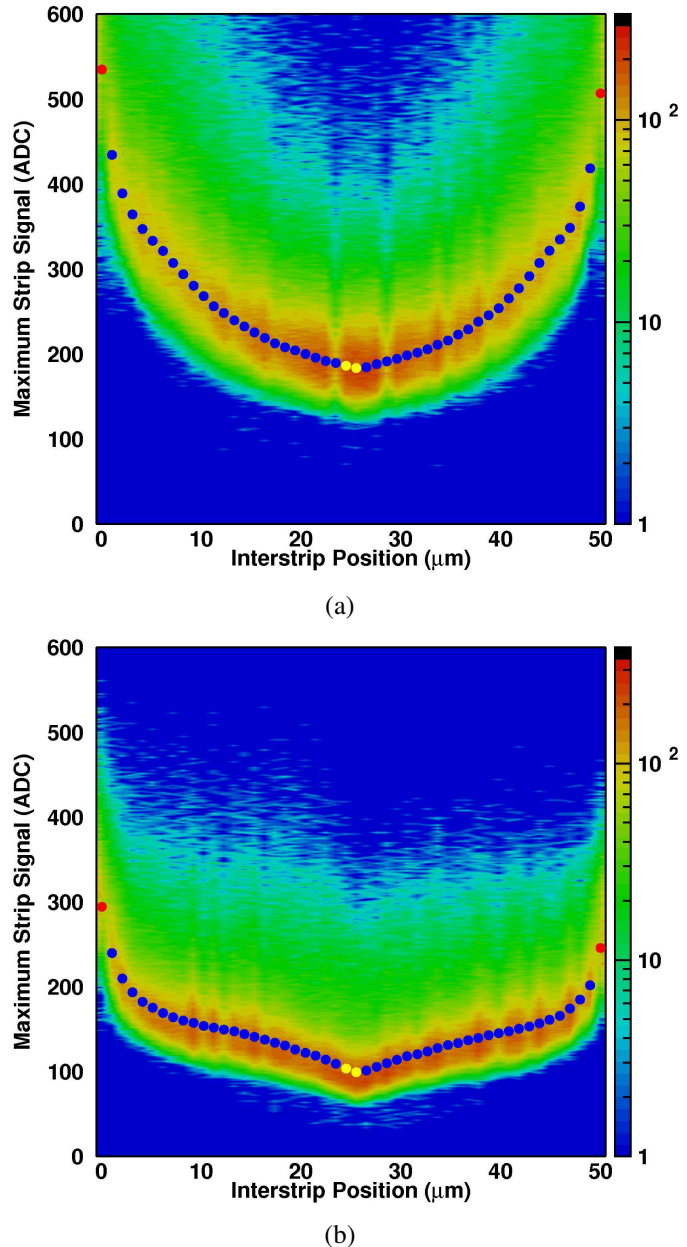


Figure 3.20: The charge sharing distributions of a CSEM+VA2 reference module: (a) junction and (b) ohmic side using the eta algorithm for the particle position reconstruction; in both cases the blue dots have been computed with the slicing method presented in chapter 4 and using a Landau-like function.

Chapter 4

The INSULAB reference detector: spatial resolution measurement

This chapter is devoted to the study of the spatial resolution of one *INSULAB Telescope* module as measured in dedicated beamtests at CERN; both 10 GeV e/μ and 150 GeV e beams have been used for the module characterization.

The so-called *residual method* has been adopted to measure the module performance and a dedicated analysis procedure has been applied to evaluate the Multiple Coulomb Scattering (MCS) contribution in the low energy case: the comparison between two different analysis algorithms, used for the particle position reconstruction, is given.

4.1 The spatial resolution measurement

The spatial resolution of a CSEM+VA2 reference module has been studied both with the 150 GeV electron beam at the SPS H4 beamline and the 10 GeV one at the PS T9 beamline. As already mentioned in chapter 2, the spatial resolution of a tracking system is defined as the capability to reconstruct the particle position in a given reference system. To measure this capability, the reference system should have a spatial resolution which is better or at worst similar to the one of the detector under test and at the same time should contribute as little as possible to the material budget not to perturb the particle trajectory.

Two different position finding algorithms have been used for the particle hit identification:

- the standard COG method [118] (section 4.2) where the particle position is defined as the weighted average given by equation 3.1;

- the so-called *eta algorithm* [108] (section 4.3) which takes into account the actual dependence of the charge division from the particle hit position.

In both cases the so-called *residual method* (section 4.1.1) has been used to compute the spatial resolution which is defined as the rms of the residual distribution.

4.1.1 The residual method

As shown in figure 4.1, the residual method consists in the following:

- the reference detectors (*i.e.* the *TELE 1-D* and *TELE 3-A* modules) have been placed at the $zsili_1$ and $zsili_3$ positions along the beamline and aligned with the method presented in section A.3;
- the position (in cm) computed with either the COG method or the eta algorithm for each module side has been taken into account (pink arrows);
- the particle trajectory (red arrow) has been reconstructed by the reference system and projected on the surface of the module under test (*i.e.* the *TELE 2-C* one) with the following formulae:

$$\begin{aligned} xproj_2 &= xtan_{31} * (zsili_2 - zsili_1) + xp_1 \\ xtan_{31} &= \frac{xp_3 - xp_1}{zsili_3 - zsili_1} \end{aligned} \quad (4.1)$$

where $xtan_{31}$ defines the tangent of the angle between the two reference silicon detectors (yellow triangle);

- the residual ($xres_2$) is defined as the difference between the particle position reconstructed by the reference system ($xproj_2$, blue arrow) and the one measured by the module under test itself (xp_2):

$$xres_2 = xproj_2 - xp_2 \quad (4.2)$$

- both the horizontal and the vertical directions have been considered; the obtained distributions have been fitted with a Gaussian-like function considering only the peak region to exclude the non Gaussian-like lateral tails (if present);
- the sigma value represents the spatial resolution including the Multiple Coulomb Scattering (MCS) contribution (equation 4.3). It must be noted that the MCS contribution is practically negligible for the energy used during

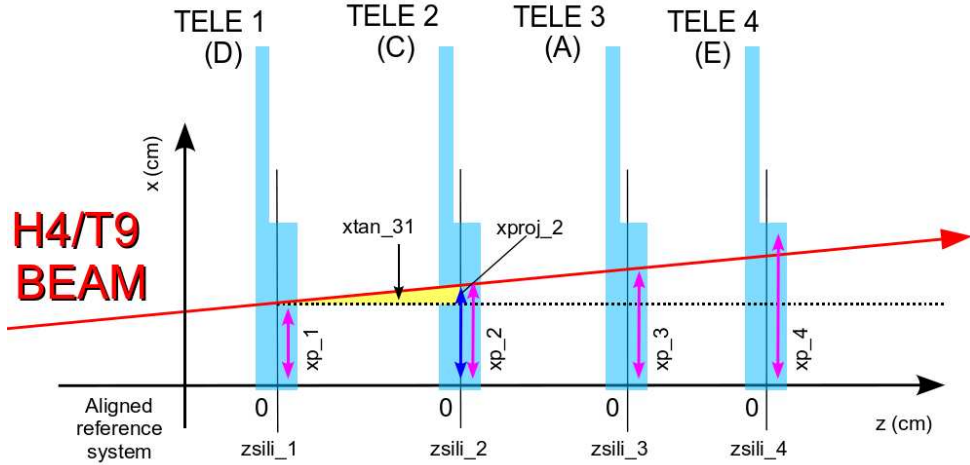


Figure 4.1: Schematic view of the residual method principle: the residual is defined as the difference between the trajectory reconstructed by the external reference modules (x_{proj_2}) and the one computed by the module under test (xp_2).

the SPS H4 high energy beamtest (150 GeV): in practice, the values obtained from the Gaussian fit correspond to the intrinsic resolution. On the other hand during the PS T9 low energy beamtest, given the working energy is ~ 10 times smaller than the H4 line one, the MCS contribution has been computed and subtracted following the procedure described in section 4.2.2.1;

- the obtained values have been compared with the so-called *theoretical* spatial resolution computed as follows:

* the measured spatial resolution can be parametrized with the following equation:

$$\sigma_{meas}^2 = \sigma_{MCS}^2 + \sigma_{det}^2 \quad (4.3)$$

where σ_{meas}^2 is the experimental spatial resolution obtained from a fit with a Gaussian-like function; σ_{MCS}^2 is the MCS contribution [37] and σ_{det}^2 is the spatial resolution of the module under test which in turn are given by

$$\begin{aligned} \sigma_{MCS}^2 &= \left(\frac{k}{E_{beam}} \right)^2 \\ \sigma_{det}^2 &= \sum_i \left[\sigma_i \cdot \frac{\partial f(x_i)}{\partial x_i} \right]^2 \end{aligned} \quad (4.4)$$

where k is the multiple scattering contribution factor, E_{beam} is the beam energy, $f(x_i)$ is given by equation 4.2 and σ_i and x_i are, respectively, the intrinsic resolution and the measured position of the i^{th} module (figure 4.2);

- * assuming all the modules have the same intrinsic resolution ($\sigma_{theo} = \sigma_i$) the measured spatial resolution σ_{meas} is given by

$$\sigma_{meas} = \sqrt{\left(2 - \frac{2 \cdot A \cdot B}{(A+B)^2}\right) \cdot \sigma_{theo}^2 + \left(\frac{k}{E_{beam}}\right)^2} \quad (4.5)$$

where A and B are the distances between the module under test and the ones used as reference¹ as shown in figure 4.2;

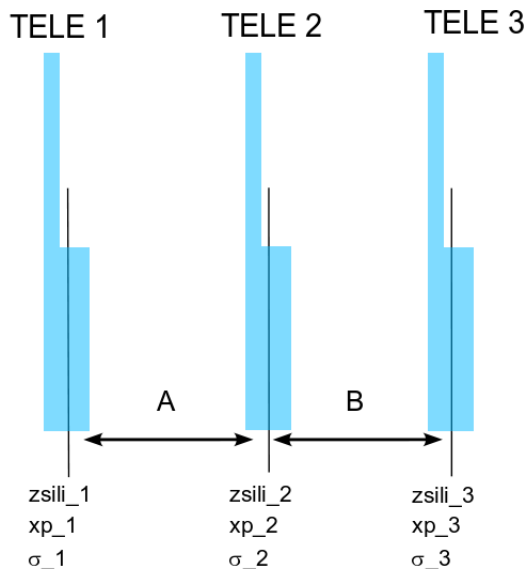


Figure 4.2: Schematic view of the elements considered for the theoretical (intrinsic) spatial resolution calculation (σ_{theo} in equation 4.5).

- * neglecting the MCS term and taking as σ_{meas} the so-called *digital* spatial resolution (computed as $p/\sqrt{12}$ where p is the strip pitch), one obtains the theoretical values listed in table 4.1 and used for the comparison with the measured ones.

¹See figure 3.9 for the exact value of the distances between the modules both at the SPS H4 and the PS T9 beamline.

4.2 Results with the standard COG method

4.2.1 The SPS H4 high energy beamtest

The residual distributions computed with both the junction and ohmic side of the *TELE* 2-C module are shown in figures 4.3(a) and 4.3(b) while table 4.1 summarizes the values obtained from the Gaussian fit (fourth column):

- a $4.90 \pm 0.01 \mu\text{m}$ value has been obtained for the junction side (figure 4.3(a)) fitting the $\pm 13 \mu\text{m}$ peak region; as expected, given the high SNR, the correct setting of all the ASICs parameters and the *one floating strip* scheme used for the readout, this value is smaller than the theoretical one (*i.e.* $5.89 \mu\text{m}$);

Module (<i>TELE</i>)	σ_{digi} [μm]	σ_{theo} [μm]	σ_{meas} (COG) [μm]
2-C			
jun.	7.22	5.89	4.90 ± 0.01
ohm.	14.45	11.65	17.28 ± 0.29

Table 4.1: The spatial resolution of the *TELE* 2-C CSEM+VA2 reference module measured during the SPS H4 high energy beamtest; also the *digital* and the *theoretical* ones are listed for both sides (see text for details).

- on the other hand a $17.28 \pm 0.29 \mu\text{m}$ value has been found for the ohmic side (figure 4.3(b)) fitting the $\pm 50 \mu\text{m}$ interval; in this case the measured value is much larger than the theoretical one (*i.e.* $11.65 \mu\text{m}$) given that:
 - * the *TELE* 3-A ohmic side could not be used to compute the residual given the bonding problem already presented in section 3.3. The position reconstructed by the *TELE* 4-E ohmic side has thus been considered and in turn the MCS contribution has slightly been increased; the theoretical value reported in table 4.1 for the ohmic side already takes into account this fact;
 - * as already discussed in section 3.4.2, the ohmic side SNR is smaller than the junction side one given the uncorrect settings of the ASICs parameters (the *delay* bit was turned ON);
 - * the readout clock was not the ideal one for the ohmic side of all the modules causing an unbalanced charge sharing among the strips (figure 3.18): the resolution gets worse since it is like having doubled the readout pitch (*i.e.* it is like having a $100 \mu\text{m}$ readout pitch detector).

This fact has been studied using the *TELE 08-2 FBK-irst+VA1_prime2* UA9 module (appendix B) and considering the behavior of the junction side spatial resolution as a function of three different readout clocks (figure 4.3(c)): as expected, the resolution increases of $\sim 36\%$ when using a 5 MHz clock. A similar worsening in the spatial resolution value could be in principle foreseen for the ohmic side: the real ohmic side spatial resolution could be thus around $11 \mu\text{m}$; the validation of this *predicted* value is presented in section 4.2.2.

4.2.2 The PS T9 low energy beamtest

The spatial resolution measurement has been repeated during the PS T9 low energy beamtest for the reasons mentioned in section 3.3 and listed above and, in particular, to validate the value obtained for the ohmic side. The same modules used at the SPS H4 beamline have been tested (with the exception of the *TELE 3-A* one) and the residual method (section 4.1.1) has been applied to compute the spatial resolution. The results are presented in figures 4.4(a) (junction side) and 4.4(b) (ohmic side): in both cases the rms value² is much larger than the expected one and the residual distributions themselves show a non Gaussian *top-hat* shape which has been ascribed to a rotational tilt angle introduced by the Newport supports³ (the so-called *knight*s) used to fix the modules along the beamline.

This fact has been confirmed and corrected in the offline analysis:

- the horizontal (vertical) residual value has been plotted as a function of the position along the vertical (horizontal) coordinate as shown in figure 4.5(a) for the junction side and in figure 4.5(b) for the ohmic one. The linear dependence is represented by the slopes of the blue histograms in figure 4.5 (A1 red values) and reflects the fact that the two coordinates are not uncorrelated but are *joined* by the presence of a rotational angle in the *x-y* plane;
- in both cases a p1-polynomial function fit (red lines in figure 4.5) has been performed excluding the regions with a poor statistics and the obtained parameters (red values in figure 4.5) have been used to compute the *correct* residual as follows:

$$\begin{aligned} x_{res2new} &= x_{res2} - (A0 + A1 \cdot y_{p2}) \\ y_{res2new} &= y_{res2} - (A0 + A1 \cdot x_{p2}) \end{aligned} \quad (4.6)$$

²In this case the Gaussian-like fit is meaningless (since the distributions are not Gaussian-like) and only the statistical parameters given by the analysis program (PAW) have been reported.

³Newport Corporation. <http://www.newport.com>.

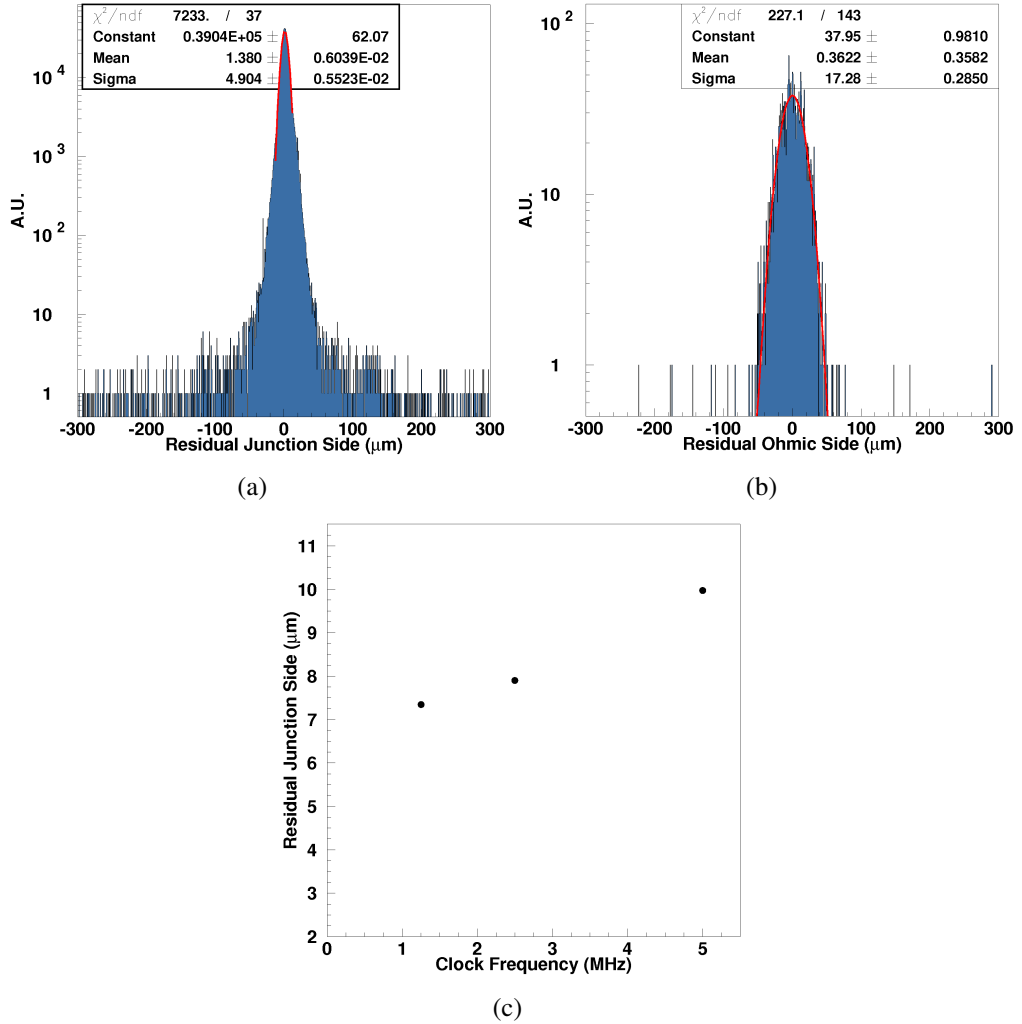


Figure 4.3: The residual distributions of (a) the junction and (b) the ohmic side of the *TELE 2-C CSEM+VA2* reference module: in both cases the standard COG method has been used for the particle hit identification. (c) The junction side residual of the *TELE 08-2 FBK-irst+VA1_prime2 UA9* module (appendix B) as a function of three different readout clock values.

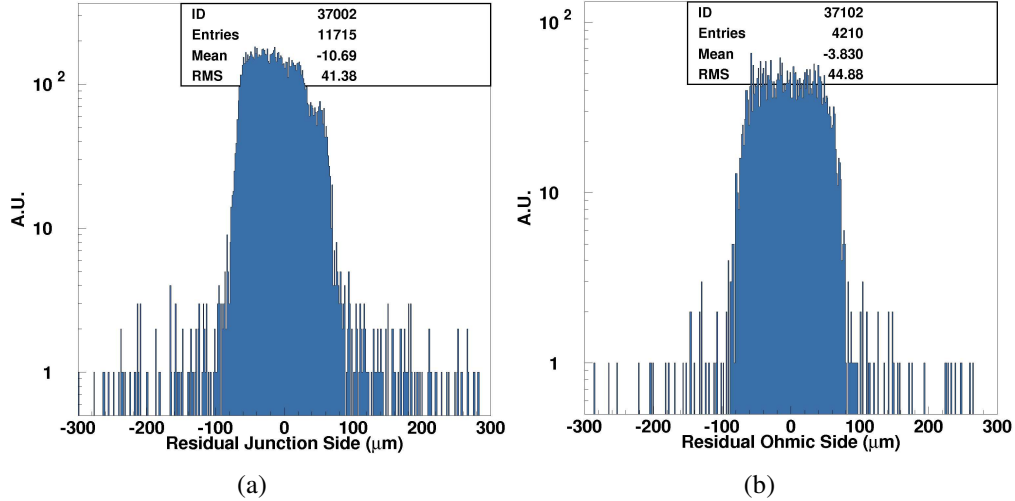


Figure 4.4: The residual distributions of the *TELE 2-C CSEM+VA2* reference module: (a) junction and (b) ohmic side computed with equation 4.2.

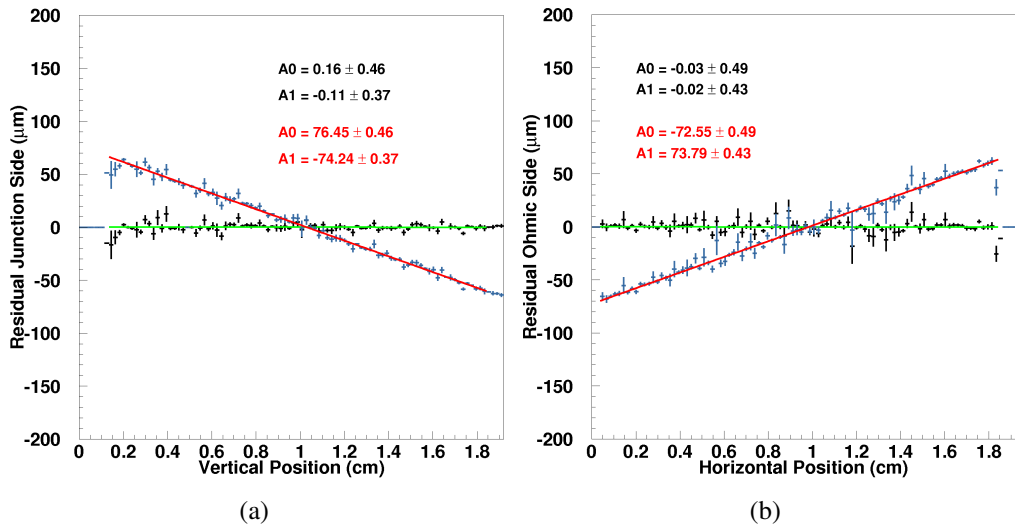


Figure 4.5: (a) The horizontal and (b) the vertical residual as a function of (a) the vertical and (b) the horizontal position (see text for details).

- the slopes in figure 4.5 have been *straightened* adding the correction factors given by equation 4.6 (A_0 and A_1 parameters): the results for both sides are represented by the black histograms in figure 4.5 where the dependence of the horizontal (vertical) residual from the vertical (horizontal) coordinate has been completely removed. Fitting the new distributions with a p1-polynomial function (green lines in figure 4.5) one obtains the new slope and intercept values (black values in figure 4.5) which are practically 0;
- the residual distribution has been then recomputed and the central peak region has been fitted with a Gaussian-like function obtaining (figure 4.6) a $5.59 \pm 0.05 \mu\text{m}$ value for the junction side and a $11.62 \pm 0.18 \mu\text{m}$ one for the ohmic side which is very similar to the one *predicted* during the SPS H4 high energy beamtest (see tables 4.1 and 4.2).

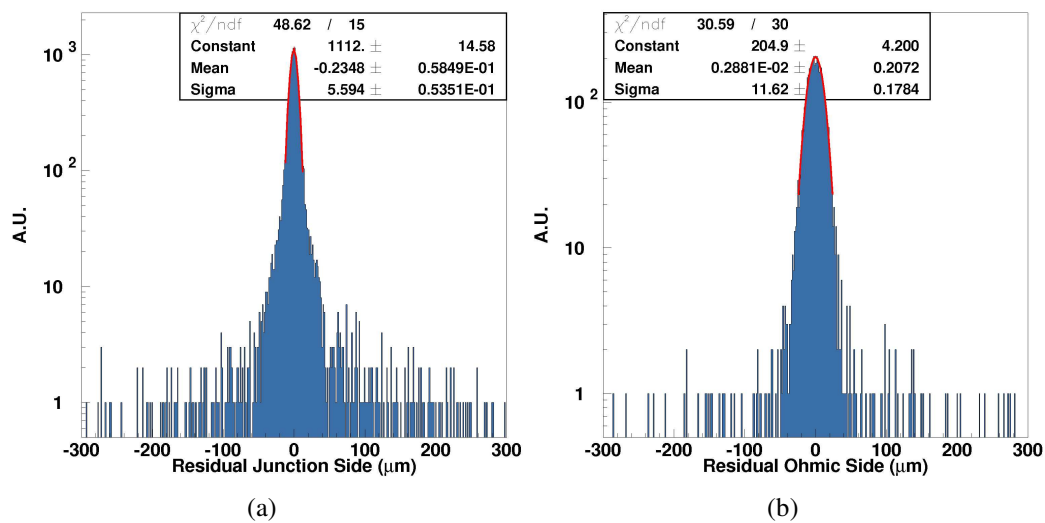


Figure 4.6: The residual distributions of the *TELE 2-C CSEM+VA2* reference module: (a) the junction and (b) the ohmic side after the position has been corrected with equation 4.6.

4.2.2.1 The MCS subtraction

Since the maximum available energy at the PS T9 beamline is 10 GeV, a dedicated study of the MCS contribution affecting the spatial resolution has been performed in the 1-10 GeV energy range. Figure 4.7 shows both the junction and ohmic residuals (computed with the method presented in section 4.1.1) as a function of the beam energy: the standard COG weighted average has been used to reconstruct

Module (TELE)	σ_{digi} [μm]	σ_{theo} [μm]	σ_{meas} (COG) [μm]	σ_{int} [μm]
2-C				
jun.	7.22	5.87	5.59 ± 0.05	4.54 ± 0.58
ohm.	14.45	11.74	11.62 ± 0.18	8.61 ± 0.44

Table 4.2: The spatial resolution of the *TELE* 2-C CSEM+VA2 reference module measured during the PS T9 low energy beamtest; also the *digital* and the *theoretical* ones are listed.

the particle hit position which has been corrected with equation 4.6 to remove the dependence from the rotational tilt angle introduced by the mechanical supports.

Both the distributions have been fitted with equation 4.5 to evaluate the σ_{int} intrinsic spatial resolution (table 4.2) and the k MCS contribution factor, corresponding, respectively, to the P1 and P2 parameters in the fit boxes. The following considerations hold:

- the intrinsic resolution is $4.54 \pm 0.58 \mu\text{m}$ for the junction side which is smaller than the theoretical one (*i.e* $5.87 \mu\text{m}$); moreover this value is also better than the one found during the SPS H4 high energy beamtest since the MCS contribution has been properly subtracted;
- the intrinsic resolution is $8.61 \pm 0.44 \mu\text{m}$ for the ohmic side and also in this case it is smaller than the theoretical one (*i.e* $11.74 \mu\text{m}$); this fact confirms the good quality (in terms of particle reconstruction capability) of the design used for the CSEM+VA2 reference module ohmic side;
- as far as the k MCS factor is concerned, they are very similar and the average is 38.65 ± 0.32 : this value will be used to compute the intrinsic resolution of the VISION modules (section 5.2.5).

4.3 Results with the eta algorithm

The standard COG method [118], presented in section 3.4.2 and used to estimate the spatial resolution of the *TELE* 2-C CSEM+VA2 reference module (section 4.2), is the most widespread and used pattern recognition algorithm. However, as mentioned in [80], it is a good approximation for a uniform charge distribution while it becomes inadequate for a Gaussian-like one. The standard COG method, in fact, does not take into account the real shape of the charge distribution causing the spatial resolution measurement to be affected by a wrong particle

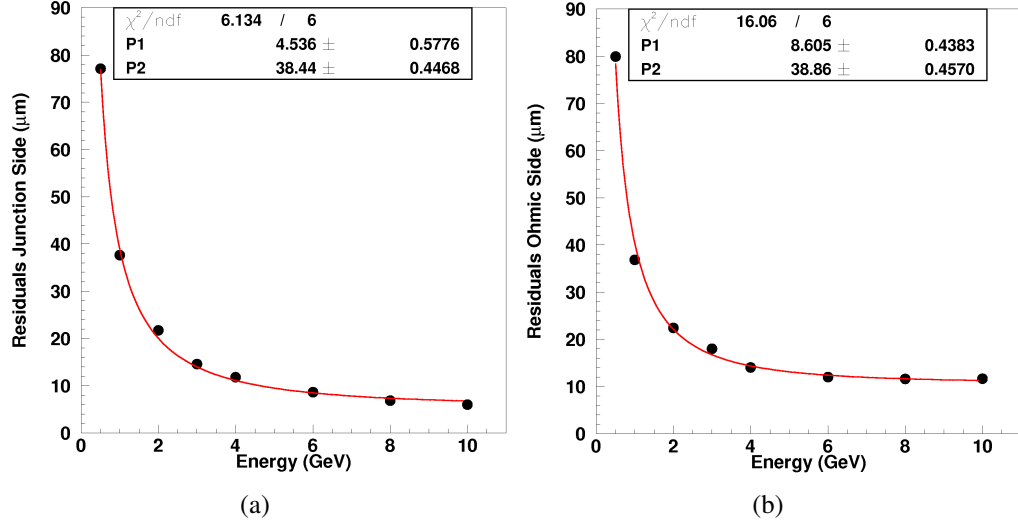


Figure 4.7: The *TELE 2-C CSEM+VA2* reference module residuals as a function of the beam energy: (a) the horizontal and (b) the vertical direction; in both cases equation 4.5 has been used for the fit.

position reconstruction. This fact is schematically shown in figure 4.8: a particle crossing the detector between two strips at $3/4$ of their distance (corresponding to the readout pitch p_{RO}) deposits in each strip a certain amount of charge which in turn depends on the shape of the charge distribution [80]:

- if the charge is uniformly distributed (figure 4.8(a)) the left and right strips collect, respectively, $1/4$ and $3/4$ of the total deposited charge: applying the standard COG method for the hit position reconstruction one obtains the correct position of the track at $x = 3/4 p_{RO}$ (yellow star in figure 4.8(a));
- on the other hand, for a Gaussian-like charge distribution (figure 4.8(b)) the signal collected by the left strip is less than $1/4$ and, in turn, the right strip collects more than $3/4$ of the total deposited charge: the position computed with the standard COG method is thus shifted towards the right strip (at $x > 3/4 p_{RO}$, yellow star in figure 4.8(b)) and, similarly, tracks passing closer to the left strip will be shifted to the left (at $x < 1/4 p_{RO}$). This effect introduces a bias in the position reconstruction and is clearly highlighted by the experimental eta distribution (figure 4.9): its non flat shape indicates that the hit position reconstruction inside the strip depends on the hit position itself.

The use of a non-linear method which takes into account the effective charge division between the strips could improve the spatial resolution [80] and allow

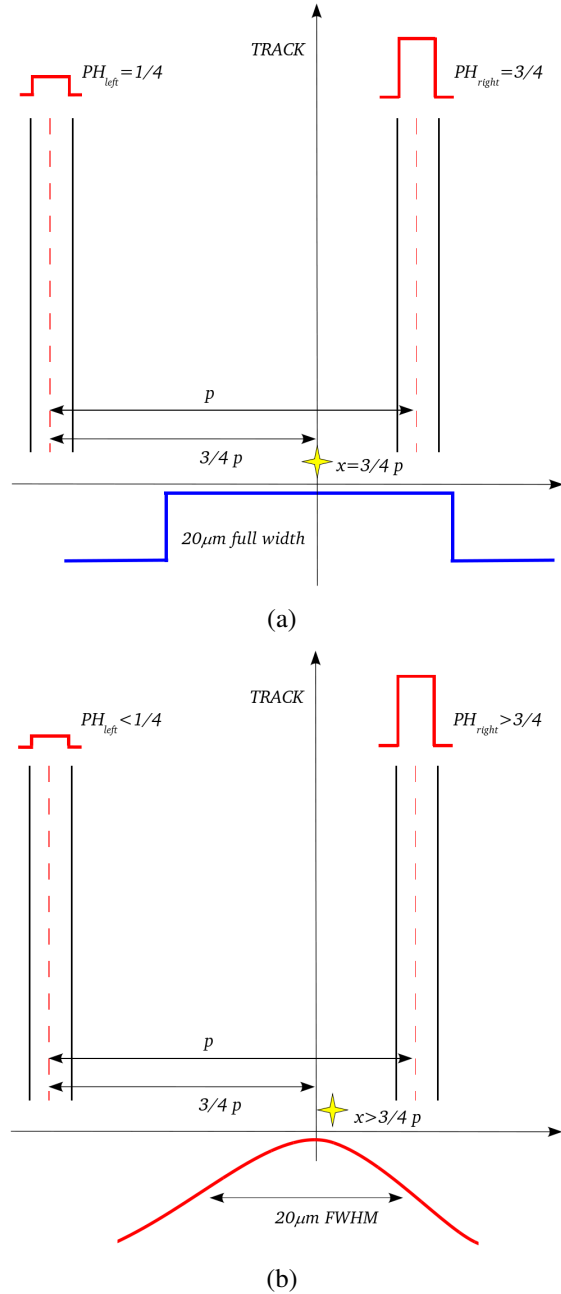


Figure 4.8: Schematic view of a particle crossing the detector at $3/4$ of the readout pitch (p_{RO}): (a) a uniform charge distribution and (b) a Gaussian-like one are considered.

to compute its ultimate value. Among several non-linear position reconstruction methods [91], the so-called *eta algorithm* has been chosen for the analysis presented in this thesis work. It has been applied following the procedure described in [86, 108] and consists in the following analysis steps:

- only the events with a single 2-*contiguous-strip* cluster have been considered and the eta distribution for both the sides of the *TELE 2-C CSEM+VA2* reference module has been computed (figure 4.9). The one for the junction side (figure 4.9(a)) is symmetric enough given the correct sampling of the signal. On the other hand, as already mentioned in sections 3.4.2 and 3.5, for the ohmic sides it was not possible to properly adjust the clock value to have a symmetric eta distribution (figure 4.9(b)); for this reason the eta algorithm has been applied to the junction side only;

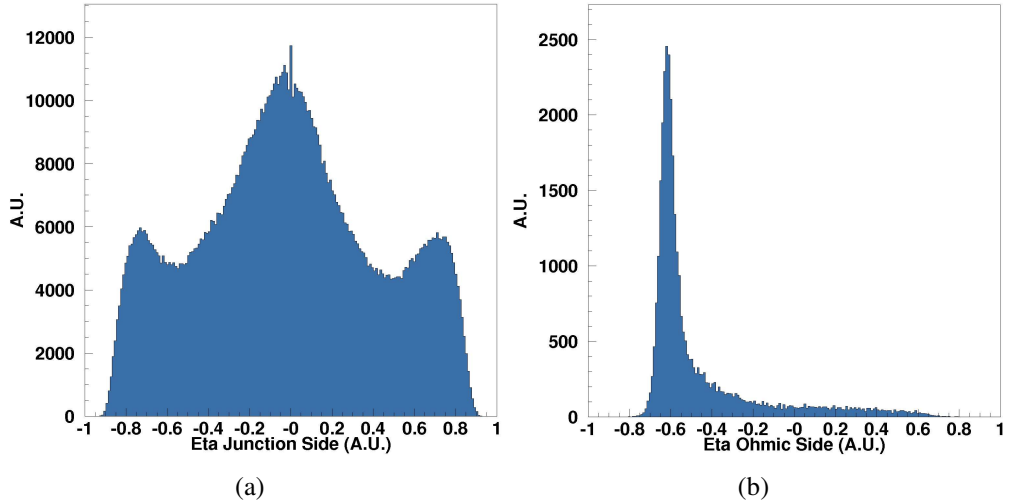


Figure 4.9: The eta distribution of the *TELE 2-C CSEM+VA2* reference module: (a) the junction side and (b) the ohmic one.

- the so-called *interstrip position*, defined as the particle hit position rescaled to the strip dimension (*i.e.* in the interval $[0,50]$ μm), has been computed both for the modules used as a reference system and the under test one; the following equation has been used:

$$xscal_j = xp_j - \text{int} \left(\frac{xp_j}{p_{RO}} \right) \cdot p_{RO} \quad (4.7)$$

where xp_j is the particle position computed with the standard COG method (equation 3.1), p_{RO} is the readout pitch and int is the integer part of the argument in the brackets and gives the number of the hit channel (which

is a number in the strip interval [1,384]). The interstrip position for the *TELE 2-C* junction side is presented in figure 4.10(a): 0 μm is the center of the first readout strip and 50 μm is the center of the nearby one while the position at 25 μm is the center of the floating strip. As expected, given the aforesaid considerations on the COG method, the distribution is not flat and resembles the eta one (figure 4.9(a));

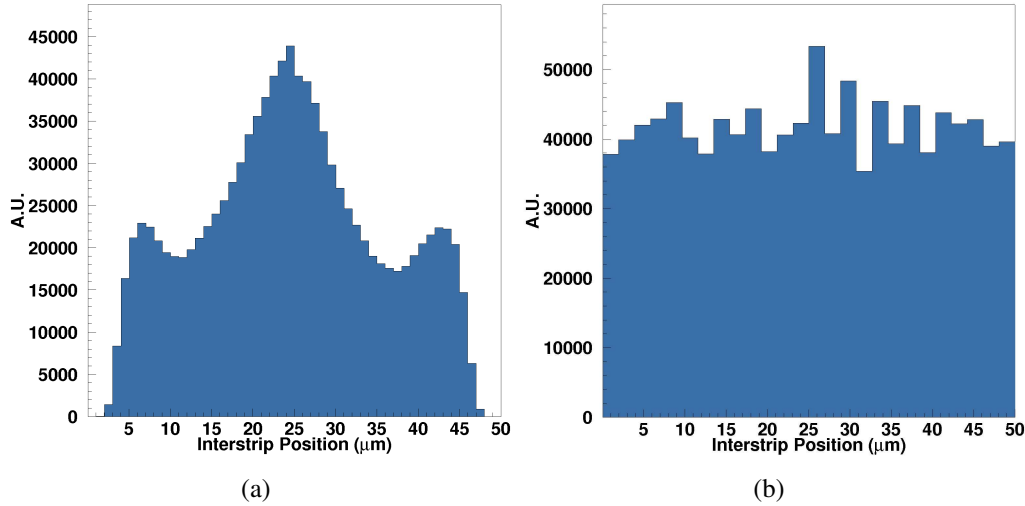


Figure 4.10: The interstrip position (a) before and (b) after the eta algorithm correction.

- the correct particle position on each module has been computed with the following formulas [108]:

$$x_{\text{petaj}} = x_{\text{left}} + f(\eta) \cdot p_{\text{RO}}$$

$$f(\eta) = \frac{\int_{-1}^{\eta} (\text{d}N/\text{d}\eta') \text{ d}\eta'}{\int_{-1}^{1} (\text{d}N/\text{d}\eta') \text{ d}\eta'} \quad (4.8)$$

where, as shown in figure 4.11, x_{left} is the position of the left strip in the pair composing the cluster⁴ and $f(\eta)$ is the eta cumulative probability distribution function [108]. It is defined as the integral of the experimental eta distribution $\text{d}N/\text{d}\eta'$ (figure 4.9(a)) in a given range (-1, η) normalized to the integral over the whole range (-1, 1);

⁴In this case the position of the left strip has been computed as $x_{\text{left}} = ch_{\text{left}} \cdot p$ where ch_{left} indicates the first channel composing the 2-strip cluster of the j^{th} module.

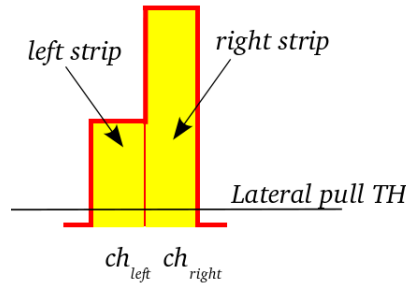


Figure 4.11: Cluster elements as used in the eta algorithm (adapted from [86]).

- the corrected interstrip position has been recomputed using x_{peta_j} in equation 4.7 obtaining the result presented in figure 4.10(b): as expected, the distribution is flat if compared to the one shown in figure 4.10(a) and the dependence of the reconstructed position from the impact position inside the strip has been removed;
- the new residual distribution (figure 4.12(a)) has been recomputed using x_{peta_j} in equations 4.1 and 4.2: a $5.78 \pm 0.01 \mu\text{m}$ value has been found which is worse than the one obtained with the standard COG method (*i.e.* $4.90 \pm 0.01 \mu\text{m}$). Nevertheless, the lateral non Gaussian-like tails are slightly less populated and present a smaller asymmetry;
- the increase in the spatial resolution value has been ascribed to the eta algorithm itself which introduces a further dependence on the position; this fact has been studied considering the residual as a function of the corrected interstrip position (figure 4.12(b)) and applying the so-called *slicing method*:
 - * the contour histogram in figure 4.12(b) has been projected into vertical slices: in total 50 slices of $1 \mu\text{m}$ of width have been considered;
 - * in order to compute the exact position of the slice peak, a Gaussian-like function fit has been performed for each slice obtaining a set of values for the mean and the sigma, respectively. Figure 4.12(c) shows an example of the central slice fit: the range for the fit has been chosen by hand in order to exclude the lateral regions with a poor statistics and to fit the interval $\pm 13 \mu\text{m}$ with respect to the peak position of each slice;
- the sets of mean and sigma values have been used to *straight* the contour histogram in figure 4.12(b) (with the same phylosophy applied for the tilt

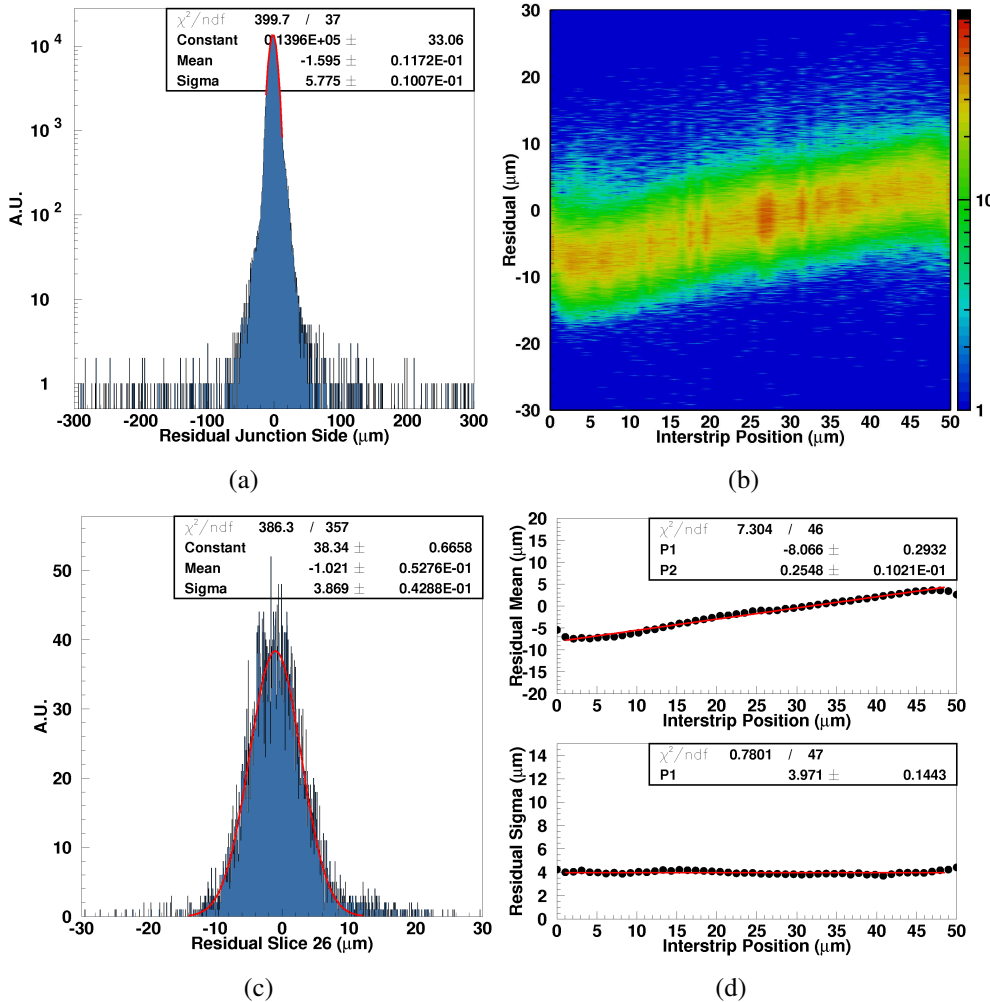


Figure 4.12: (a) The residual distribution of the *TELE 2-C* junction side after the eta correction. (b) The residual as a function of the corrected interstrip position. (c) Example of the Gaussian-like fit of the central slice: only the interval $\pm 13 \mu\text{m}$ with respect to the peak position has been taken into account. (d) The sets of mean (top) and sigma (bottom) values obtained from the slicing method and fitted with a p1- and a p0-polynomial function, respectively.

angle correction presented in section 4.2.2) and to find the ultimate spatial resolution value. Both the sets of data have been plotted as a function of the corrected interstrip position (figure 4.12(d)) and fitted with a given function:

- * the set of mean values (figure 4.12(d) top) has been fitted with a p1-polynomial function to evaluate the slope which has been in turn used to remove the dependence of the residual on the position as follows:

$$xres_{2corr} = xres_{2eta} - (P0 + P1 \cdot xscal_{2eta}) \quad (4.9)$$

where both $xres_{2eta}$ and $xscal_{2eta}$ have been computed using the definition of $xpeta_j$ (equation 4.8) in equations 4.1, 4.2 and 4.7, respectively. The obtained results are presented in figure 4.13(a) and in the top of figure 4.13(b): fitting with a p1-polynomial function the new set of mean values, obtained applying again the slicing method on figure 4.13(a), one gets a slope value which is practically 0;

- * as far as the set of sigma values is concerned, it has been fitted with a p0-polynomial function (figure 4.12(d) bottom) which shows that the sigma of the residuals remains practically constant at $3.97 \pm 0.14 \mu\text{m}$; the behavior remains practically the same also after the additional correction with equation 4.9 (figure 4.13(b) bottom).

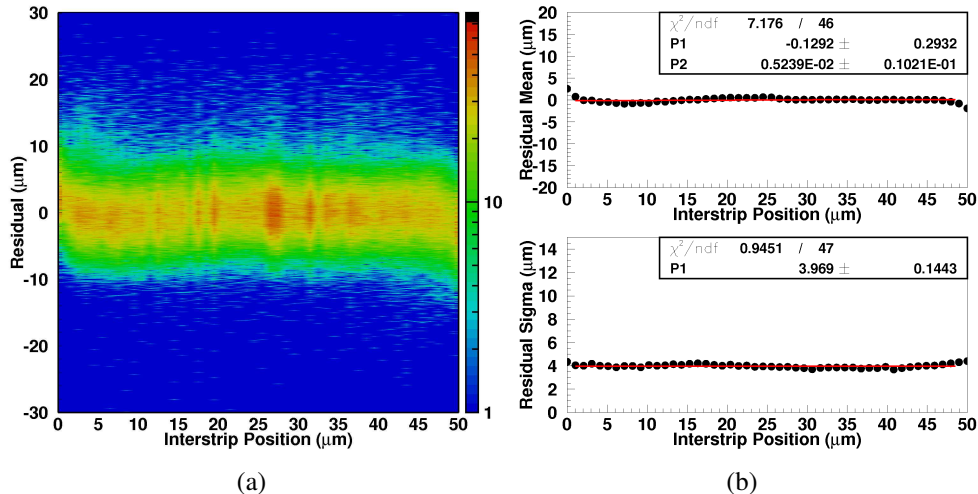


Figure 4.13: (a) The residual distribution of the TELE 2-C junction side after the eta and slope correction as a function of the interstrip position. (b) The new sets of mean (top) and sigma (bottom) values obtained from the slicing method and fitted with a p1- and a p0-polynomial function, respectively.

- the ultimate residual distribution obtained after the eta and the slope correction is presented in figure 4.14(a): fitting the distribution with a Gaussian-like function the measured value is $4.22 \pm 0.01 \mu\text{m}$. It must be noted that the asymmetric non Gaussian-like tails are much smaller than the ones in figures 4.3(a) and 4.12(a) even if they have not been completely removed due to the non 100% symmetry of the starting eta distribution (figure 4.9(a)) and, in particular, of the one measured for the *TELE 3-A* reference module (figure 4.14(b)) used as a reference. Further tightening the range for the fit to better exclude the lateral tails, considering the $(-10, 9.5) \mu\text{m}$ interval only, a $4.11 \pm 0.01 \mu\text{m}$ value (figure 4.14(c)) has been obtained.

Table 4.3 summarizes the comparison between the two different analysis method used for the residual calculation: as expected, given the aforesaid considerations on the COG method, an improvement up to $\sim 0.90 \mu\text{m}$ has been obtained applying the eta algorithm.

Module (TELE)	$\sigma_{\text{meas}} (\text{COG})$ [μm]	$\sigma_{\text{meas}} (\eta)$ [μm]	$\sigma_{\text{meas}} (\eta \pm 13)$ [μm]	$\sigma_{\text{meas}} (\eta \text{ ultim})$ [μm]
2-C jun.	4.90 ± 0.01	5.78 ± 0.01	4.22 ± 0.01	4.11 ± 0.01

Table 4.3: The ultimate spatial resolution of the *TELE 2-C CSEM+VA2* reference module junction side; the one computed with the standard COG method is also listed for comparison. The red and blue values refer, respectively, to the Gaussian fit of the histograms in figures 4.14(a) and 4.14(c).

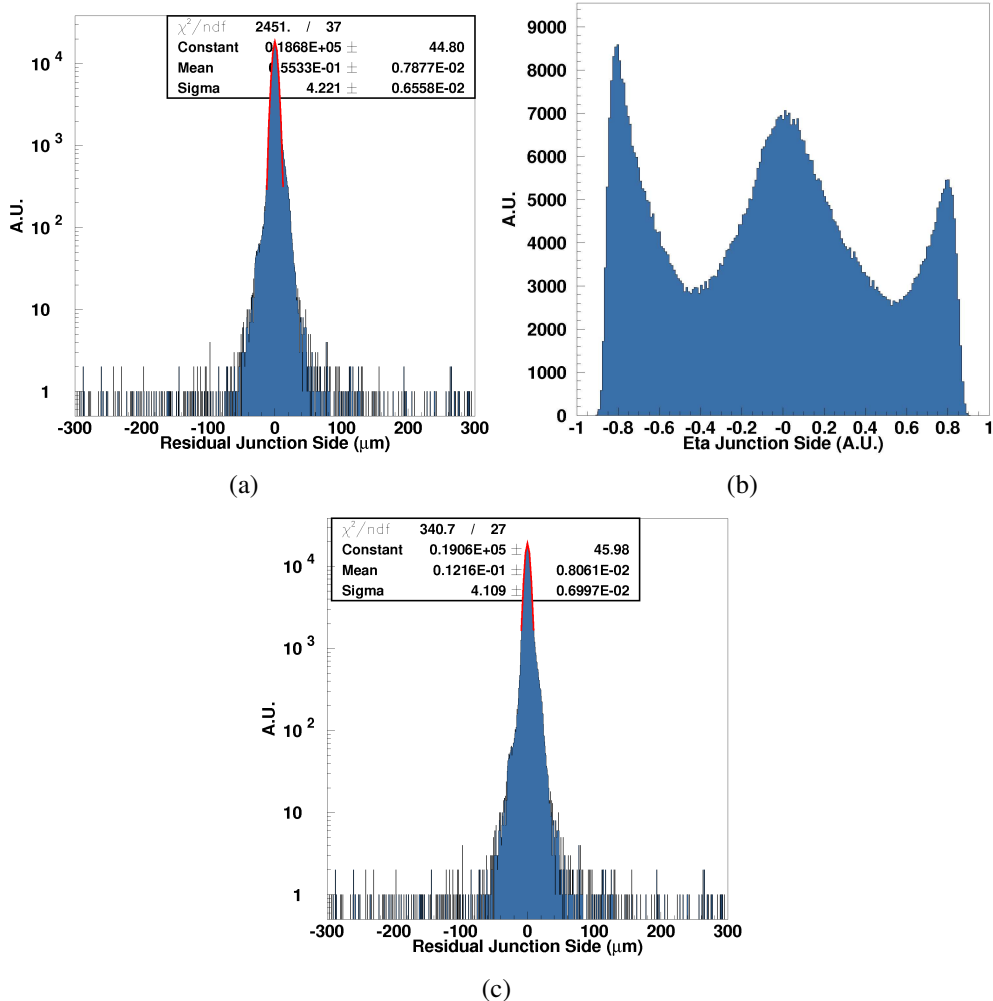


Figure 4.14: The ultimate spatial resolution of the *TELE 2-C* junction side after the eta and slope correction fitting (a) the $\pm 13 \mu\text{m}$ peak region and (c) the interval between -10 and $+9.5 \mu\text{m}$. (b) The *TELE 3-A* eta distribution: its not perfect symmetry is the reason why the lateral tails in the residuals ((a) and (c)) are not perfectly removed even with the eta algorithm.

Chapter 5

The VISION tracking system: moving to a high performance system

As already described in section 3.2 the new electronics chain developed and tested with the INSULAB Telescope (chapter 3) allowed to double the DAQ rate with respect to the standard electronics used until 2011 [103]. A 6 kHz DAQ rate value has been obtained in dedicated beamtests at the CERN SPS and PS beamlines maintaining the particle position reconstruction capability of the system; in the best case the intrinsic spatial resolution is $\sim 4.11 \mu\text{m}$, if a floating strip scheme is adopted (section 4.3), and $\sim 8.61 \mu\text{m}$ in the no floating strip configuration (section 4.2.2).

To further increase the DAQ rate value and in parallel to develop a more compact and general purpose readout system, a new version of the telescope has been assembled in the last 3 years. The so-called *VISION Telescope*, Versatile and Innovative SilicON Telescope, consists in several modules featuring both single and double side silicon tiles from HAMAMATSU and FBK-irst, the VA1TA ASIC by IDEAS and the same electronics chain used with the CSEM+VA2 reference modules (section 3.2).

The complete description of the VISION telescope modules (in terms of silicon tiles, ASICs, assembly and mechanics) is given in the first part of this chapter. In particular the attention will be focused on the VA1TA working principle and its possibility to generate a trigger signal for the readout sequence, and on the slow control system developed to remotely monitor the whole system. The second part of the chapter presents the results in terms of noise, SNR, spatial resolution and charge sharing obtained in a dedicated commissioning phase at INSULAB and during the PS T9 low energy beamtest. The last part of the chapter deals with the results obtained by the ICE-RAD experiment at the Mainzer

Mikrotron¹ (MAMI [120]) where one of the VISION modules is installed since January 2013 and used to reconstruct the electron beam after the interaction with bent and straight crystals [24, 60, 66]. The description of the new data transmission system based on Gigabit link connections (through standard LEMO² cables or optical fibers) or on a Universal Serial Bus 2 (USB2) interface is also presented.

5.1 The VISION modules

The so-called *VISION Telescope* [27, 66] consists in several modules equipped with the FBK-irst and the HAMAMATSU silicon tiles coupled to the self-triggering VA1TA ASICs [94] and the same frontend and readout electronics used with the CSEM+VA2 reference modules (section 3.2). All the modules have been designed and produced by INFN-Ts starting from the design described in [121] and used by the UA9 experiment³ for the modules presented in appendix B:

- only one module (named in the following FBK-irst- Ω) has been assembled with the FBK-irst tile (the same used in [121]);
- three modules with the HAMAMATSU tiles have been mounted; two modules house a pair of silicon tiles, assembled one close to each other on the same support, while in the third module only one tile is present. A total of five HAMAMATSU silicon tiles (named in the following *SN01-05*) have been tested.

The following sections describe the silicon detectors, the characteristics and the working principle of the VA1TA ASIC and the modifications implemented on the electronics chain for the conditioning of the self-triggering part of the ASICs. The description of the so-called *Slow Control (SC)* system (to remotely monitor the whole telescope) is also given.

5.1.1 The silicon detectors

Figure 5.1 presents a photo of the VISION modules whose technical features are summarized in table 5.1. The design for both the FBK-irst and the HAMAMATSU modules is very similar:

- the FBK-irst- Ω module (figure 5.1(a)) consists in a double side silicon microstrip detector with a sensitive area of $1.92 \times 1.92 \text{ cm}^2$ (as the CSEM+VA2 reference modules one);

¹<http://www.kph.uni-mainz.de/eng/108.php>.

²LEon MOuttet, <http://www.lemo.com>.

³UA9 Official Website, <http://home.web.cern.ch/about/experiments/ua9>

- the HAMAMATSU SN01-05 tiles (figures 5.1(b) and 5.1(c)) have a slightly larger sensitive area ($2.10 \times 2.10 \text{ cm}^2$) and house single side silicon microstrip detectors.

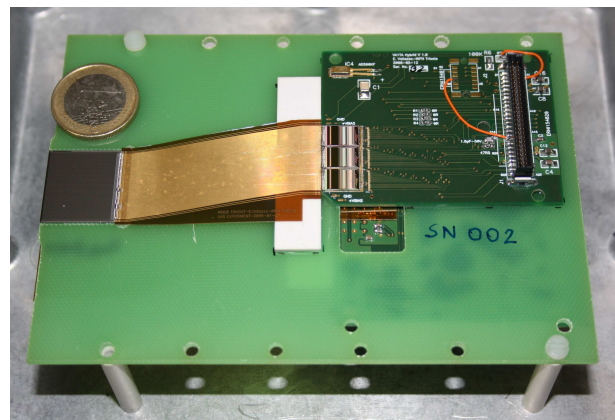
In both cases the detectors are high resistivity $300 \mu\text{m}$ thick silicon tiles and have a total of 384 readout channels; no floating strip scheme has been adopted for the readout. In the FBK-irst- Ω module the strips are oriented perpendicularly; only the ohmic side of the tile has been bonded to the readout ASICs while the junction side is connected only for biasing. The silicon tiles are fully depleted with a bias voltage in the 36-54 V range and the average leakage current is of the order of 1.5-2.0 nA per strip.

Detector	Double (only Ω)	Single
Produced by	FBK-irst	HAMAMATSU
ASIC	VA1TA	VA1TA
Detector dimensions [cm 2]	1.92×1.92	2.10×2.10
Number of readout channels	384	384
Bulk thickness [μm]	300	300
Resistivity [k $\Omega\cdot\text{cm}$]	> 4	> 4
Leakage current [nA/strip]	1.5-2.0	1.5-2.0
Full depletion bias voltage [V]	36-54	36-54
AC coupling	yes	yes
p-side - <i>junction</i>		
physical pitch [μm]	not bonded	50
readout pitch [μm]	-	50
floating scheme	-	no
n-side - <i>ohmic</i>		
physical pitch [μm]	50	-
readout pitch [μm]	50	-
floating scheme	no	-
Fiberglass support		
shape	L-shape	rectangular
dimensions [cm 2]	13.5×13.5	13.5×9.5
thickness [cm]	0.5	0.35
ASIC connection	direct bonding	upilex fanout

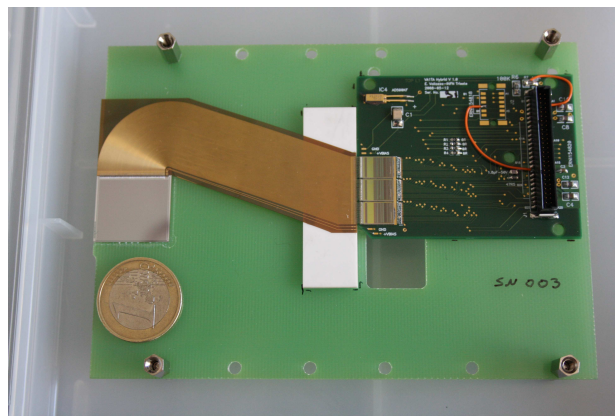
Table 5.1: General features of the VISION modules.



(a)



(b)



(c)

Figure 5.1: Photos of the VISION microstrip silicon detectors assembled on a fiberglass support together with the readout ASICs [27, 66]: (a) the FBK-irst- Ω module; the HAMAMATSU modules with (b) the *straight* and (c) the *bent* flexible upilex fanout.

5.1.2 The VA1TA ASIC

The readout of the whole detector (or detector side in the FBK-irst- Ω case) is accomplished by three VA1TA ASICs. The technical features of this ASIC are listed in table 5.2: it is a 128 channel radiation tolerant integrated circuit built with the $0.35\text{ }\mu\text{m}$ N-well CMOS technology.

ASIC name	VA1TA
Process (N-well CMOS)	$0.35\text{ }\mu\text{m}$
Die surface [mm^2]	9.28×6.12
Die thickness [μm]	~ 725
Number of channels	128
Input pad size [μm^2]	50×90
Output pad size [μm^2]	90×90
ENC at $1\text{ }\mu\text{s}$ of peaking time [e^- rms]	$180 + 7.5 \cdot C_d$
Power consumption [mW]	195
Slow shaper peaking time [μs]	0.3-1
Fast shaper peaking time [μs]	0.075 or 0.3
Dynamic range [# MIPs]	± 10
Current gain [$\mu\text{A}/\text{fC}$]	~ 10

Table 5.2: Technical features of the VA1TA ASIC [94].

The ASIC has the same architecture of the VA2 one for the analog sampling (the so-called *VA-part*) while the self-trigger signal generation is performed by the so-called *TA-part*. Figure 5.2(a) presents the ASIC working principle:

- the two parts share the same charge preamplifiers (located in the VA-part) and the inputs of the TA-part are directly coupled to the corresponding outputs of the preamplifiers;
- each channel of the VA-part includes the same components of the VA2 ASIC one (described in section 3.1.2); in the VA1TA case also a pole zero cancellation has been implemented for the CR-RC shaper;
- each channel of the TA-part (figure 5.2(b)) consists in
 - * a charge sensitive preamplifier (shared with the VA-part);
 - * a CR-RC fast shaper with a peaking time of either 0.075 or $0.3\text{ }\mu\text{s}$;
 - * a level-sensitive discriminator with a tunable threshold and a monostable to generate fixed width trigger signals; both positive and negative

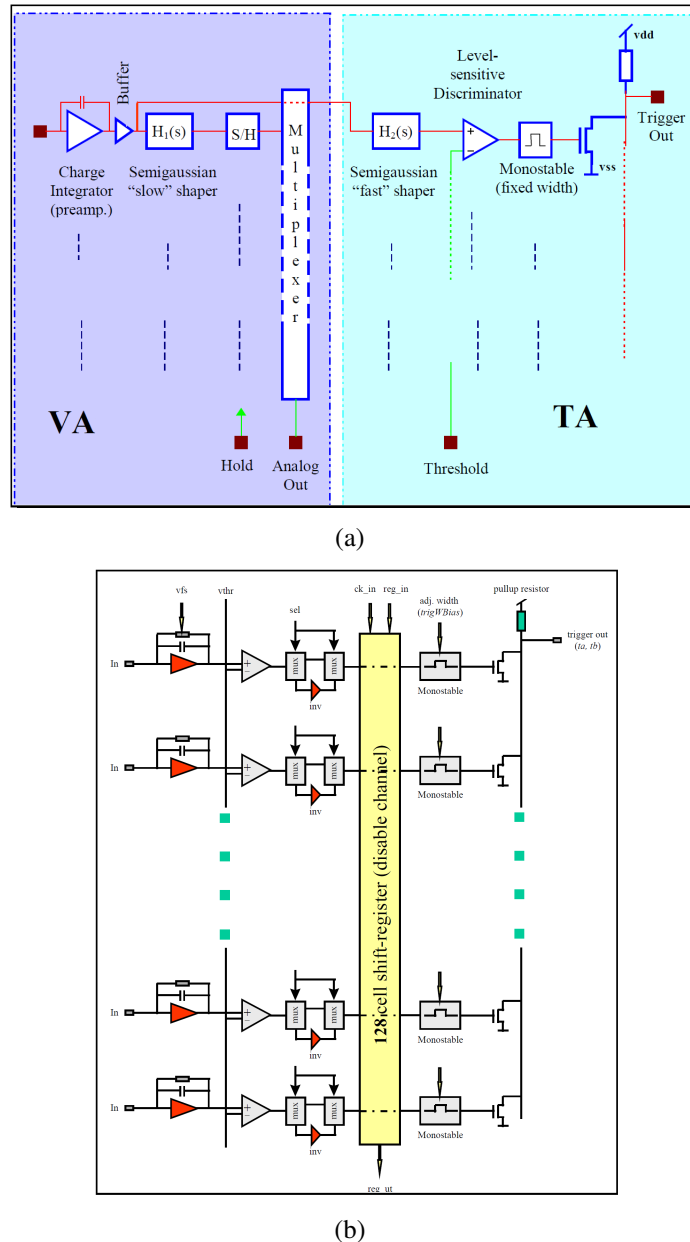


Figure 5.2: (a) The VATA working principle [94]: the first part (the VA one) has the same architecture of the VA2 ASIC; (b) the TA architecture is responsible of the self-trigger generation [94].

input signals can be used to generate the ASIC trigger. A high-pass filter (not shown in figure 5.2(b)) with a very low cut-off frequency is also present before the discriminator to reduce the offset spread across the whole ASIC;

- * a 4 bit Digital to Analog Converter (DAC) to trim the *local* (*i.e.* on a channel by channel basis) and in turn the *global* threshold values.

The ASIC trigger output is the OR of all the discriminators outputs: whenever a signal in any of the channels rises above the discriminator threshold, a global ASIC trigger is generated. The readout is a multiplexed one with a maximum clock frequency of 10 MHz (as for the CSEM+VA2 reference modules, the chosen readout clock was 1.25, 2.5 or 5 MHz).

The so-called *configuration mask* has to be loaded serially to properly operate the VA1TA ASIC; thanks to this sequence of bits (mask), it is possible to set and adjust all the main ASIC parameters as the CR-RC slow/fast shaper peaking time, the gain of the preamplifier, the trigger width, the DAC threshold, etc. The 680 bit shift register performing this task is presented in figure 5.3: the sequence numbers are shown at the top of each box; bit 0 is the first one to be loaded. More details about the serial data shift-in register can be found in [94].

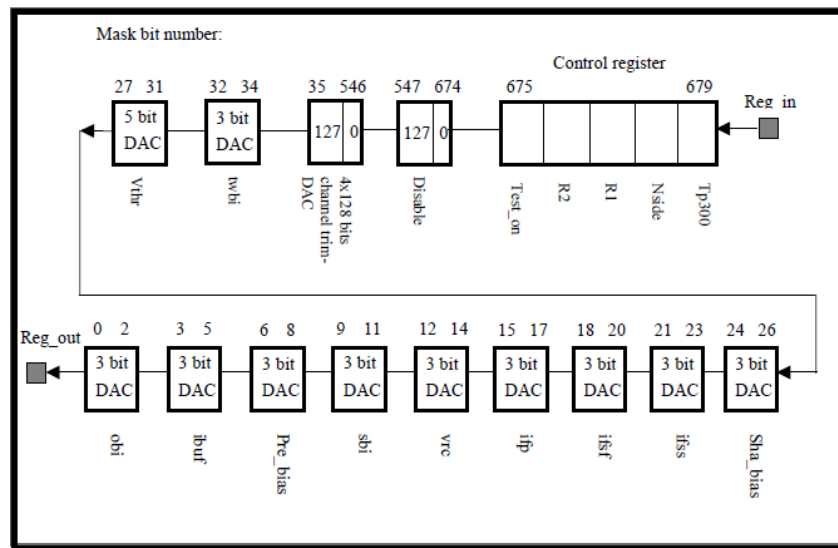


Figure 5.3: The sequence of the serial shift register mask for the VA1TA ASIC [94]; the mask loading starts from bit 0.

5.1.3 The mechanical assembly

Depending on the used detector (the FBK-irst or the HAMAMATSU ones), different solutions have been adopted for the module assembly (see table 5.1 for details). In the FBK-irst- Ω case the silicon tile is assembled on a L-shape fiberglass support, $13.5 \times 13.5 \text{ cm}^2$ wide and 0.5 cm thick (figure 5.1(a)), and directly connected to the readout ASICs which are in turn hosted on a custom PCB inserted in the support itself. On the other hand, for the HAMAMATSU SN01-05 tiles the connection between the detector and the readout ASICs is performed through a flexible 50 μm thick upilex⁴ fanout with 5 μm copper lines where about 1 μm of galvanic gold is deposited for the bonding. Two different fanout types have been manufactured: in the first case (figure 5.1(b)) the so-called *straight* design has been adopted *i.e.* the fanout directly connects the strips to the ASICs; in the second solution, the so-called *bent* fanout (figure 5.1(c)), the copper lines are bent of a 90° angle. The silicon tiles, the ASICs PCB and the fanouts are mounted on a $13.5 \times 9.5 \text{ cm}^2$ 0.35 cm thick rectangular fiberglass frame.

In both the FBK-irst- Ω and HAMAMATSU SN01-05 cases the ASICs have been glued with the Epotek H20E epoxy glue and the control and output pads are bonded with 17 μm diameter Al wires; the detectors are AC coupled. $18 \times 45 \text{ cm}^2$ 4 cm thick aluminum boxes have been used to house the fiberglass frame and the first part of the readout electronics.

5.1.4 The electronics chain

The same electronics chain described in section 3.2 has been used for the readout of the VISION modules; the following modifications, introduced to fulfill the conditioning and the generation of the self-trigger signal, have been implemented:

- the ASICs configuration part of the repeater boards has been enabled via software and controlled by a *piggy-back* daughter board directly plugged onto the master VRB; it allows to load the VA1TA shift-in register (figure 5.3) and to read back the mask to check the correct settings of all the parameters; the connection between the VRB daughter and the repeater boards is made via two 17 pins twisted cables and scotchflex connectors;
- the self-triggering TA-part of the ASICs generates the trigger signal which in this case is not vetoed with the spill one; it means that when the particles arrive on the detector the readout sequence is immediately started by the detector itself.

⁴It is the material commonly used to fabricate the fanouts: it is a heat resistant polyimide film made of biphenyl tetracarboxylic dianhydride (BPDA) monomers and has been developed by UBE industries (<http://www.ube-ind.co.jp/english/>).

5.1.5 The Slow Control system

In the present version of the electronics chain the biasing of the VISION Telescope silicon tiles is provided by dedicated battery boxes placed near the detectors (as for the CSEM+VA2 reference modules case, section 3.2.1). On the other hand the electronics chain voltages (both the ones for the repeater and the ADC boards) are generated by standard power supplies, the Agilent 3631A voltage generator or the QL335TP one (by TTI⁵).

During the beamtest the power supplies for the electronics should be placed in a low radiation zone which typically is not accessible when the beam is running; moreover the detectors could be placed in vacuum chambers (as in the ICE-RAD experiment presented in section 5.3). For these reasons a slow control system has been developed to continuously monitor the behaviour of the whole detector and to turn OFF/ON the power supplies. Moreover the possibility of biasing the silicon tiles themselves with a dedicated power supply (such as the Agilent E3647A one) has pushed the INSULAB Group to implement the SC system.

The SC design (figure 5.4(a)) starts from the one of the UA9 experiment [122, 123] and consists in:

- a GPIB⁶/Ethernet controller (GPIB-ENET/1000 by NI⁷) placed near the power supplies and connected through GPIB cables to the voltage generators themselves (red square in figure 5.4(b));
- a standard net cable connecting the GPIB/Ethernet controller to the DAQ PC (red arrow in figure 5.4(a)); both the input and output signals are managed by the same cable.

The SC software is written in C with a Tcl/Tk user interface; it performs the following tasks:

- it allows to turn OFF and ON the tracking modules and their whole electronics;
- it continuously measures the voltages and the currents of the power supplies; an alert signal is sent to the DAQ PC in case of a too high current and the SC system turns OFF all the supplies in the case of latch up events;
- it stores on a dedicated log file the interesting ASICs and detectors parameters such as the analog and digital currents, the bias current (to check the correct working of the silicon tiles) and the DAC threshold values for the trigger;

⁵TTI Global Distribution, <http://www.tti.com/>.

⁶General Purpose Interface Bus.

⁷National Instruments S.r.l., <http://italy.ni.com/>.

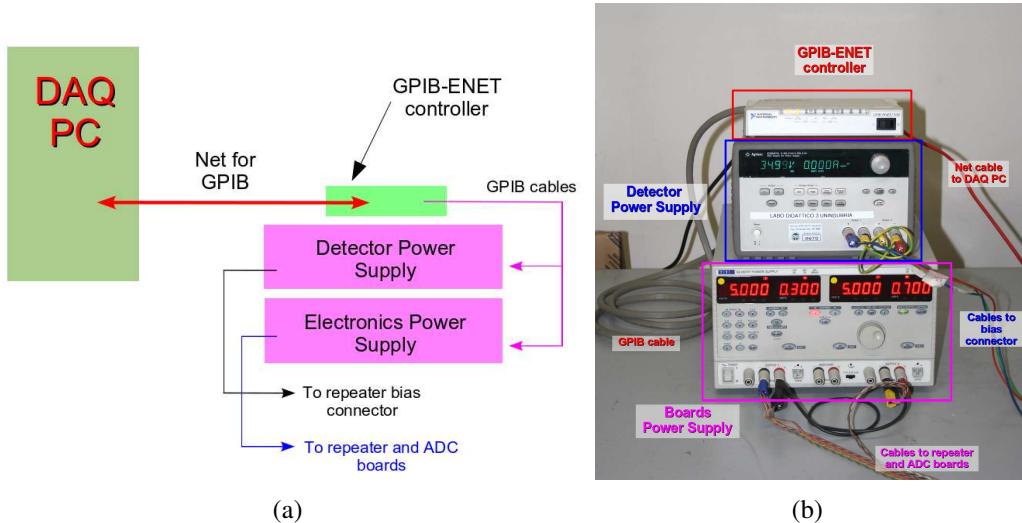


Figure 5.4: (a) Schematic view and (b) photo of the Slow Control system.

- dedicated temperature, pressure and dose probes would be also installed (on the ASICs PCBs) in case the detector is placed in a vacuum system to monitor the chamber environment.

As far as the present thesis work is concerned, the SC system has not been used either during the commissioning phases at INSULAB and the PS T9 line or during the beamtest at MAMI. The final version of the SC system will be implemented and manufactured in the next months and further tests are foreseen at the CERN SPS, at MAMI and at the Beam Test Facility (BTF) of Frascati (LNF⁸).

5.2 The commissioning phases

5.2.1 The tests setup and goals

The VISION modules have been tested both with a standard ^{90}Sr β^- source (SPECTECH⁹) at INSULAB and at the PS T9 beamline at CERN. In particular:

- all the HAMAMATSU SN01-05 modules have been tested with the ^{90}Sr source; the pedestal, the noise and the SNR have been used as figures of merit to select the best modules to be used for the spatial resolution evaluation at CERN (section 5.2.5) and the test with bent crystals at MAMI (section 5.3). During this phase the SN04-05 module has also been used

⁸Laboratori Nazionali di Frascati, <http://w3.lnf.infn.it/>.

⁹Spectrum Techniques, <http://www.spectrumtechniques.com>.

to optimize the signal sampling (in terms of the *hold* value) as will be discussed in section 5.2.3;

- both the FBK-irst- Ω module and the HAMAMATSU *SN04-05* one have been characterized in terms of spatial resolution and charge sharing at the PS T9 beamline (section 5.2.5); during the data taking only two of the three readout ASICs have been sampled given the strips connected to the first ASIC were not inside the incoming beam acceptance (section 5.2.5): thus only 256 channels out of the 384 strips measuring the horizontal direction have been considered.

Figure 5.5(a) shows a schematic view of the setup used for the test at Como consisting in:

- the module under test housed in its aluminum box together with the frontend electronics and placed on a table;
- the ^{90}Sr placed above the module; the Al box is cut and covered with a thin Al window (a $\sim 17\ \mu\text{m}$ thick foil) in the position corresponding to the silicon tile both to limit the absorption of the β^- particles and the MCS contribution due to the box material budget;
- the DAQ system described in section 3.2.2.

In figures 5.5(b) and 5.5(c) a photo of the used β^- source and its decay scheme are presented: the ^{90}Sr isotope undergoes a β^- decay with a 28.79 years half-life and a 0.55 MeV decay energy shared among an electron, an anti-neutrino and the ^{90}Y daughter; in turn the ^{90}Y undergoes a β^- decay with a 64 hours half-life and a 2.28 MeV decay energy distributed among an electron, an anti-neutrino and the stable ^{90}Zr isotope¹⁰. The electrons are isotropically emitted with a 2.28 MeV end point energy and an emission rate of ~ 5000 particles/s.

As far as the CERN PS T9 setup is concerned, as already mentioned in section 3.3, only three modules have been assembled with either the HAMAMATSU *SN04-05* module or the FBK-irst- Ω one placed in the center and characterized by means of two CSEM+VA2 reference modules. In the following sections both the results obtained at Como and at CERN are presented.

5.2.2 Pedestal and noise

Figure 5.6 presents the pedestal and rms noise distributions of a few VISION modules while table 5.3 summarizes the values (both for the pedestal and global,

¹⁰The $^{90}\text{Sr}/\text{Y}$ source is almost a pure β^- particle source; the γ emission from ^{90}Y is in fact so rare that can normally be ignored; <http://atom.kaeri.re.kr/ton/nuc6.html>.

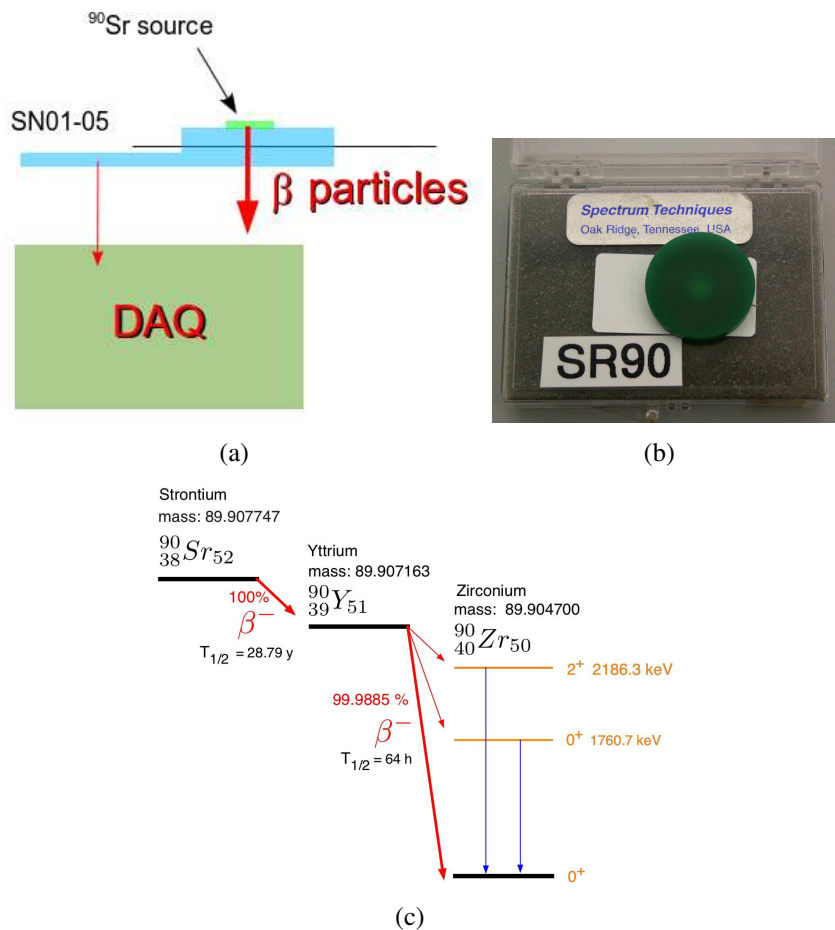


Figure 5.5: (a) Schematic view of the setup used for the ^{90}Sr source test; (b) the used source with (c) its decay scheme.

common mode and intrinsic noise) obtained with all the modules. The ones reported for the FBK-irst- Ω refer to the PS T9 low energy beamtest while all the others (*i.e.* the ones for the HAMAMATSU SN01-05 modules) refer to the test with the ^{90}Sr source. Figure 5.6(a) shows the distributions of only the channels which are readout; in all the cases the peaks in the rms noise distribution correspond to the noisy channels and have not been taken into account in the pedestal and noise calculation. The analysis procedure presented in appendix A has been applied.

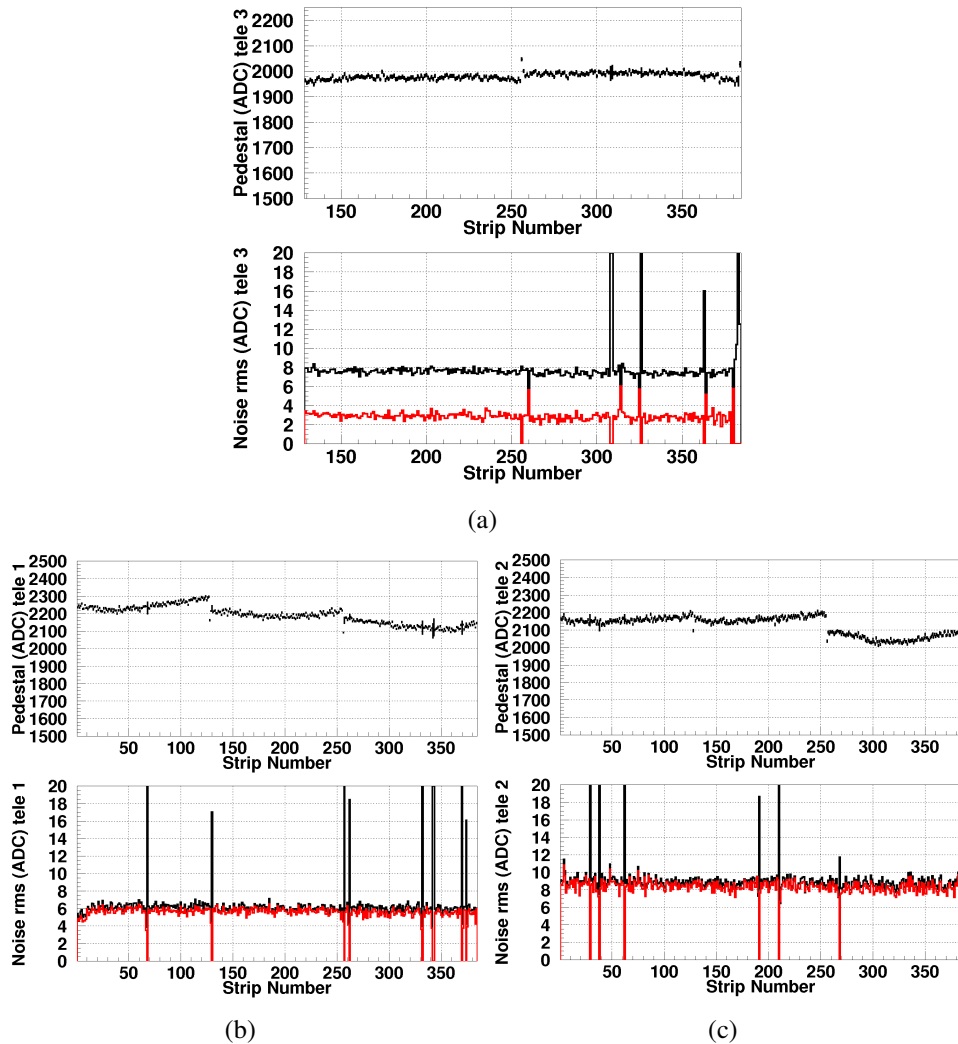


Figure 5.6: Pedestal and noise rms distributions of the VISION modules. (a) The FBK-irst- Ω one measured during the PS T9 data taking: only the 256 readout channels are shown. The HAMAMATSU (b) SN05 and (c) SN04 distributions as obtained at INSULAB.

Module (SN)	Pedestal range [ADC]	Global noise [ADC]	CM noise [ADC]	Intrinsic noise [ADC]	Unused ch [%]
01	2000-2200	7.06±0.03	2.03±0.07	6.76±0.03	8.85
02	2100-2250	6.04±0.02	1.85±0.06	5.67±0.02	3.38
03	2050-2150	5.03±0.02	1.26±0.04	5.14±0.02	2.08
04	2000-2200	8.83±0.03	2.37±0.08	8.37±0.03	1.56
05	2100-2300	6.08±0.02	1.49±0.04	5.70±0.02	2.35
FBK-irst	1950-2050	7.53±0.02	6.88±0.36	2.86±0.02	3.9

Table 5.3: Comparison of the pedestal, noise and number of unused (dead or noisy) channels of the VISION modules; the values in blue refer to the PS T9 low energy beamtest. The global, common mode and intrinsic noise values have been computed following the procedure in appendix A.

5.2.3 Hold scan

As mentioned in section 5.1.2, the VA1TA slow shaper peaking time can be varied in the 0.3-1 μ s range. Given the signal sampling plays an important role for the module characterization, the so-called *hold scan* has been performed to study the analog shape of the ASIC output signal and to select the hold value that corresponds to the maximum of the signal itself. The knowledge of the signal shape helps in fact to understand the degree of freedom one has during a beamtest where the choice of the *correct* hold value could be affected not only by the experimental area conditions (*e.g.* by the time structure of the beam itself) but also by the length of the cables.

The hold is defined as the interval between the trigger signal, which in this case is generated by the TA-part of the ASIC, and the sampling of the slow shaper output signal. Figure 5.7(a) presents the hold scan working principle:

- after a particle crosses the silicon detector at t=0, the deposited charge is amplified by the ASIC preamplifier (top blue line); as already mentioned in section 5.1.2, the VA1TA ASIC is equipped with a fast CR-RC shaper which has been used for the trigger generation and a slow shaper which is the one performing the analog signal sampling;
- the trigger signal (pink line) is generated by the TA-part of the ASIC and sent to and processed by the master VRB (section 3.2.2) which at this point generates the hold delay (cyan line);
- the rising edge of the hold signal is the one sampling the slow shaper output

(black line) and the sampled value is stored to be sent to the ADC board during the readout sequence;

- since the hold value must be set in order to sample the peak of the signal, the shape of the analog output signal can be obtained varying the hold time width thus sampling the signal in different places. Referring to figure 5.7(a), a Δt_1 hold value (black) allows to sample the signal peak while a Δt_2 one (red) causes the signal to be sampled after its peak.

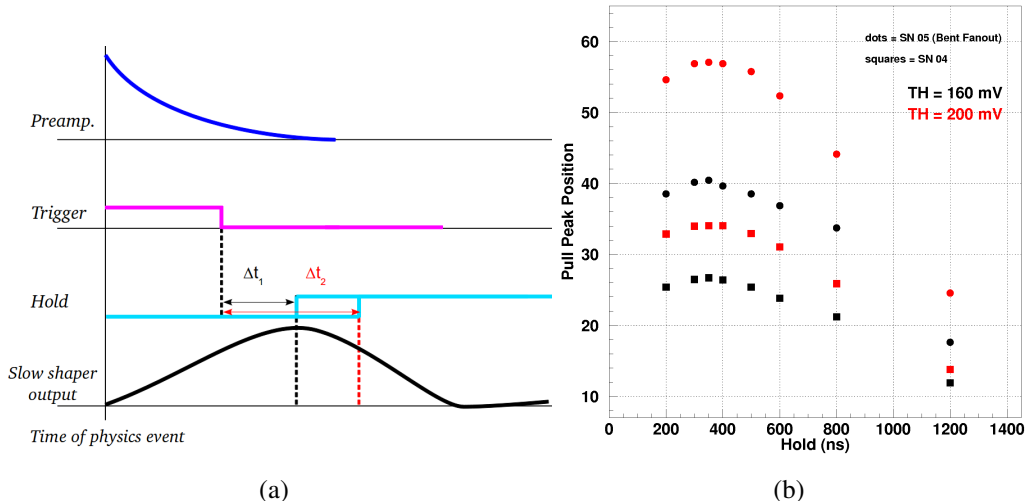


Figure 5.7: (a) The hold scan principle: the charge deposited by the particle is amplified by the preamplifier and the master VRB generates the trigger signal; the hold signal is generated by the DAQ to sample the shaper output. (b) The hold scans performed with the HAMAMATSU SN05 (dots) and SN04 (squares) tiles with different DAC threshold values: in all the cases the peaking time is ~ 350 ns.

To perform the scan the hold value has been varied in the 200-1200 ns range with steps of variable time width (50, 100, 200 or 400 ns). The pull of the strip with the maximum signal in the event has been taken into account and fitted with a Landau-like function (equation 3.3) to evaluate the peak position (*i.e.* the MPV of the distribution). Figure 5.7(b) shows the obtained MPVs as a function of the hold values for both the HAMAMATSU SN05 (dots) and SN04 (squares) tiles. Two different DAC threshold values have been used: the peaking time in all the cases is ~ 350 ns while the difference in the signal amplitude of the two tiles is given by a different gain of the entire electronics chain.

5.2.4 Cluster analysis

All the VISION modules have been characterized in terms of Signal to Noise Ratio with the same procedure for the good event selection and the SNR calculation presented in section 3.4.2 for the CSEM+VA2 reference modules. Figure 5.8(a) shows the SNR distribution obtained for the FBK-irst- Ω module during the PS T9 low energy beamtest: the MPV obtained with a Landau-like function fit is 50.36 ± 0.11 . The SNR distributions for the HAMAMATSU *SN05* and *SN04* tiles are presented in figures 5.8(b) and 5.8(c), respectively: also in this case the distributions have been fitted with a Landau-like function obtaining 48.04 ± 0.30 for the *SN05* tile and 31.93 ± 0.27 for the *SN04* one; the values obtained for the other modules are summarized in table 5.4. The *SN04* and *SN05* tiles are not the ones with the highest SNR but they have a very low percentage of unused channels; for this reason they have been selected both for the PS T9 low energy beamtest at CERN and for the crystals tests at MAMI. The *SN03* tile has the highest SNR value but it has been excluded since it allows to measure only one coordinate at a time; finally the *SN01* and *SN02* tiles have a larger percentage of dead/noisy strips.

Module (SN)	Pulse Height [ADC]	Noise [ADC]	SNR
01	282.10 ± 2.19	6.54 ± 0.01	41.76 ± 0.33
02	290.41 ± 1.44	5.22 ± 0.01	55.35 ± 0.45
03	341.88 ± 1.99	4.40 ± 0.01	76.41 ± 0.57
04	259.36 ± 2.91	8.15 ± 0.01	31.93 ± 0.27
05	257.77 ± 1.31	5.36 ± 0.01	48.04 ± 0.30
FBK-irst	119.55 ± 0.22	2.34 ± 0.01	50.36 ± 0.11

Table 5.4: Comparison of the cluster pulse height, noise and Signal to Noise Ratio of the VISION modules; the values in blue refer to the PS T9 low energy beamtest.

5.2.5 The spatial resolution and charge sharing measurement @ PS T9

The spatial resolution for the VISION modules has been measured at the PS T9 beamline considering the 2-strip single cluster events; the *eta algorithm* has not been applied given the low statistics after the event selection. Figure 5.9 presents the distributions obtained for both the FBK-irst- Ω tile and the HAMAMATSU *SN05* one: in both cases the rms value is much larger than the theoretical spatial

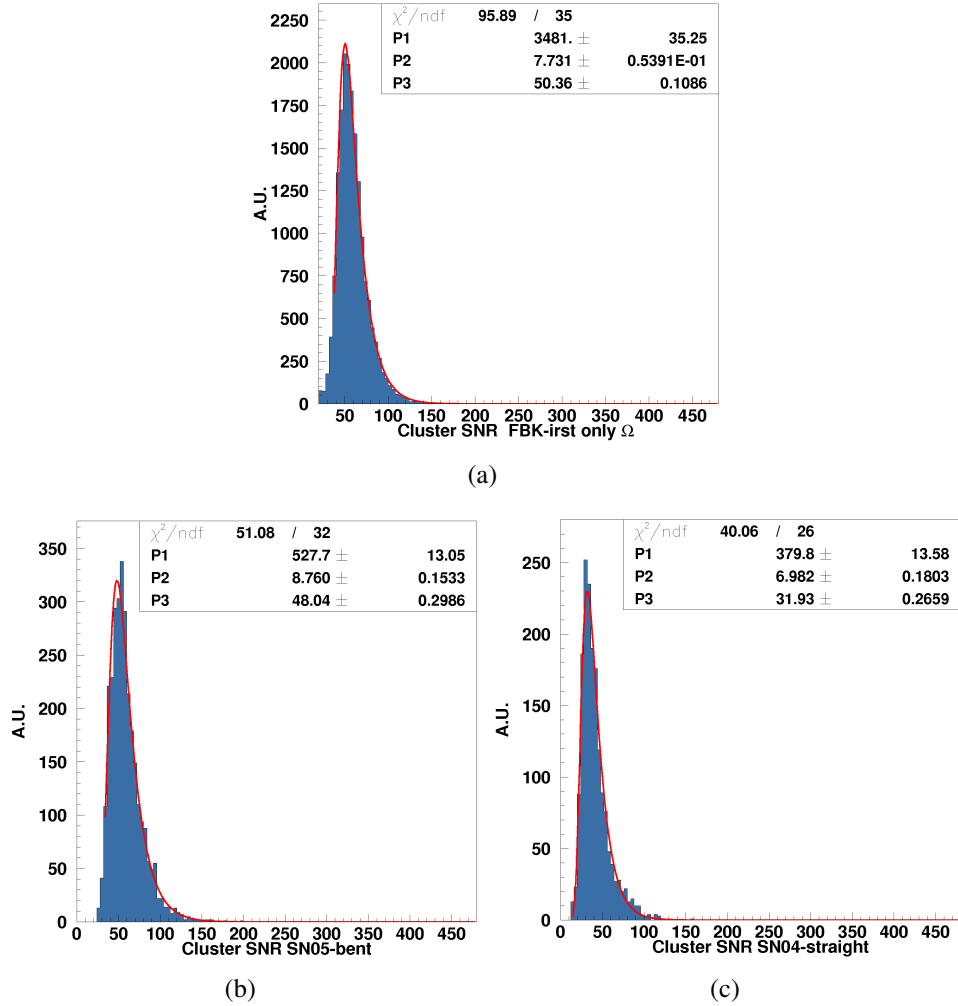


Figure 5.8: The Signal to Noise Ratio distributions fitted with a Landau-like function of (a) the FBK-irst- Ω tile (measured at the PS T9 line), (b) the HAMA-MATSU SN05 and (c) the SN04 ones (measured during the ^{90}Sr source test).

resolution value (*i.e.* $11.76 \mu\text{m}$) and the distributions have not a Gaussian-like shape; for this reason the fit is missing.

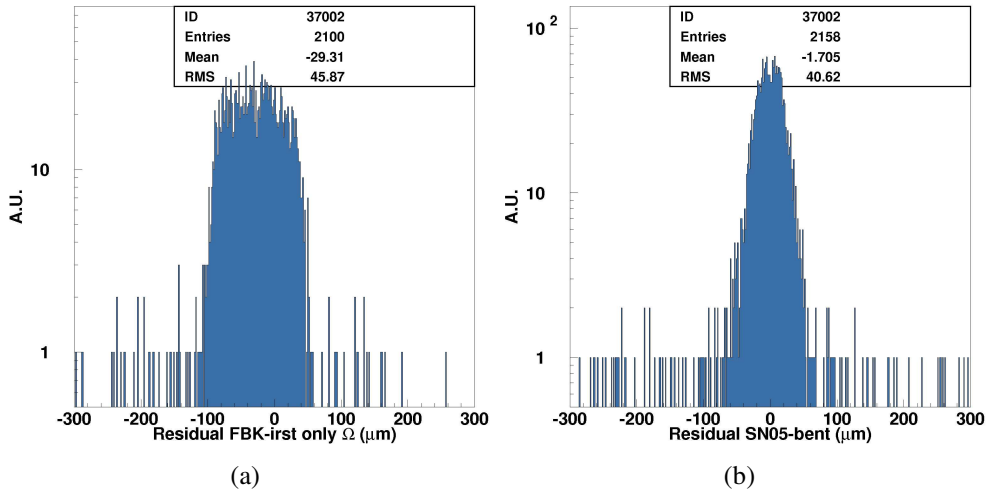


Figure 5.9: The residual distributions of (a) the FBK-irst- Ω tile and (b) the HAMAMATSU SN05 one.

As in the CSEM+VA2 reference module case (section 4.2.2), a rotational tilt angle has been introduced by the mechanical supports: in this case the effect on the residual distribution is much more evident given a custom mechanical support has been used instead of the standard Newport knights (figure 5.10). The same procedure described in section 4.2.2 has been used to compute the *correct* particle position (equation 4.6): the ultimate spatial resolution values after the MCS contribution subtraction¹¹ are listed in table 5.5 together with the *digital* and the *theoretical* ones (computed with equation 4.5).

Module	σ_{digi} [μm]	σ_{theo} [μm]	σ_{meas} [μm]	σ_{int} [μm]
FBK-irst	14.45	11.76	9.12 ± 0.41	6.72 ± 0.38
SN05	14.45	11.76	11.74 ± 0.92	9.02 ± 0.79

Table 5.5: The measured spatial resolution of the FBK-irst- Ω tile and the HAMA-MATSU *SN05* one; also the *digital* and the *theoretical* ones are listed.

Figure 5.11(a) for the FBK-irst- Ω tile and figure 5.11(c) for the HAMA-MATSU SN05 one show the obtained distributions (after the position correction) fitted with a Gaussian-like function; the correlations between the residual

¹¹The procedure described in section 4.2.2.1 has been applied to compute and subtract the MCS contribution.

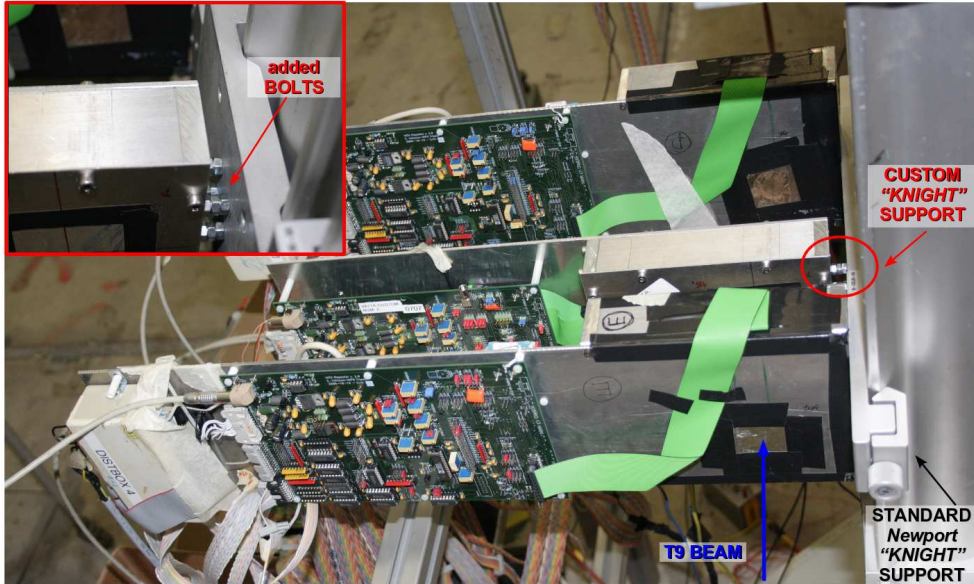


Figure 5.10: Photo of the mechanical supports used during the PS T9 low energy beamtest: the red insert shows the *custom* support used to fix the VISION module under test.

itself and the vertical projected position $yproj$ ¹² are presented in figures 5.11(b) and 5.11(d), respectively. The blue histograms with the red fit lines are the ones computed without the tilt angle correction while the black histograms with the green fit lines refer to the residuals obtained after the correction given by equation 4.6; the red and black values refer, respectively, to the red and green fit results. In both cases the initial *flat region* ($yproj \leq 0.6$ cm) corresponds to the first readout ASIC which has not been readout since it was out of the incoming beam acceptance.

A $6.72 \pm 0.38 \mu\text{m}$ value and a $9.02 \pm 0.79 \mu\text{m}$ one have been obtained fitting the central peak region for the FBK-irst- Ω module and the HAMAMATSU SN05 tile, respectively; in both cases the spatial resolution values are smaller than the theoretical ones (table 5.5). Moreover, the poorer spatial resolution with respect to the CSEM+VA2 reference module junction side one (*i.e.* $4.54 \pm 0.58 \mu\text{m}$ measured at the PS T9 line in the same experimental conditions) reflects the larger physical pitch ($50 \mu\text{m}$) scheme adopted for these modules with respect to the smaller one ($25 \mu\text{m}$) used in the CSEM+VA2 case. On the other hand, comparing the obtained

¹²It must be remembered that for the VISION modules only the horizontal direction has been taken into account during the PS T9 low energy beamtest: the junction side is not bonded in the FBK-irst- Ω module while the HAMAMATSU SN04 tile has not been readout.

values with the CSEM+VA2 reference module ohmic side (*i.e.* $8.61 \pm 0.44 \mu\text{m}$), a similar spatial resolution value has been found for both the tested VISION modules.

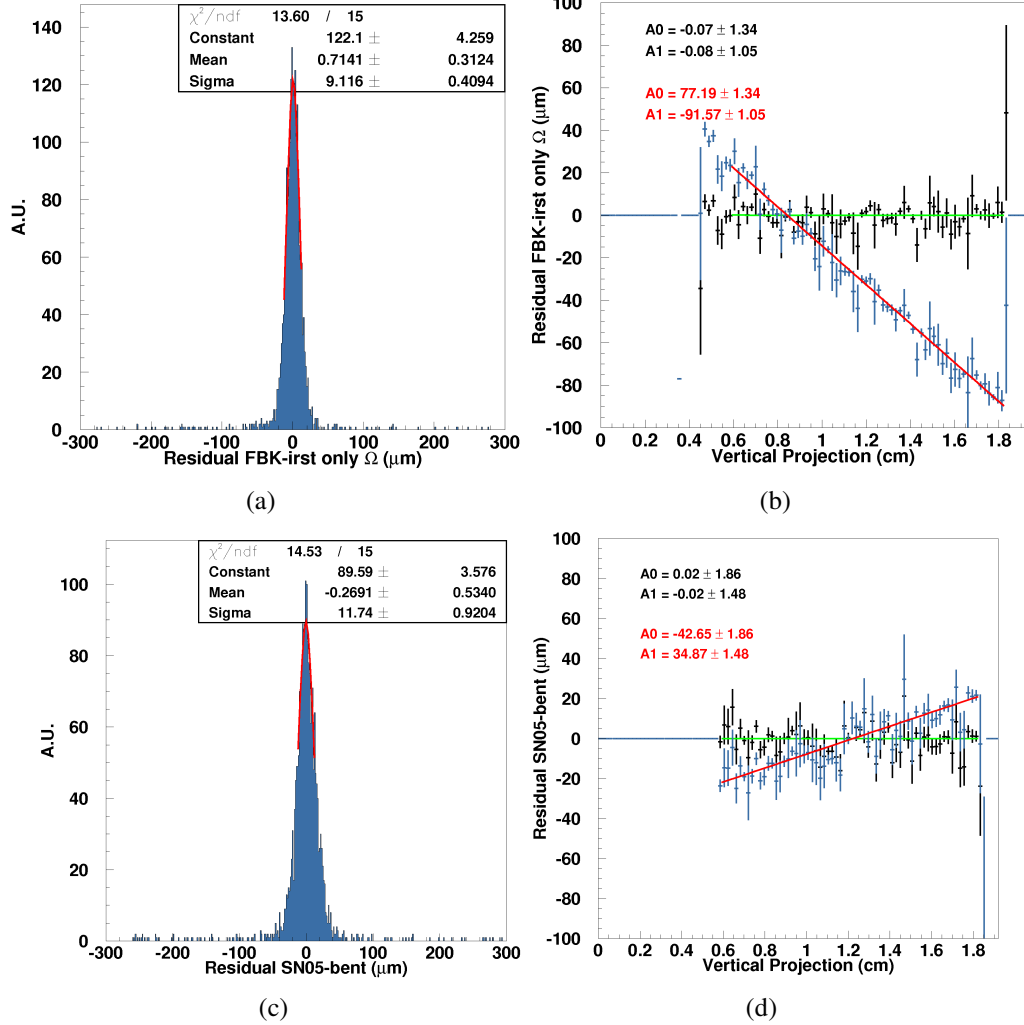


Figure 5.11: The residual distribution after the tilt angle correction of (a) the FBK-irst- Ω tile and (c) the HAMAMATSU SN05 one [66]; the residuals as a function of the projected vertical position ((b) and (d)): before (blue histograms with red fit lines) and after (black histograms with green fit lines) the position has been corrected with equation 4.6.

As far as the charge sharing is concerned, even if the readout clock was set to the slowest available value (*i.e.* 1.25 MHz), for the FBK-irst- Ω module the signal sampling was not performed in the correct way and the eta distribution was not symmetric (figure 5.12(a)); on the other hand the one for the HAMAMATSU

SN05 tile presents a much more symmetric shape (figure 5.12(b)). For this reason the charge sharing has been studied with the procedure described in section 3.5 with the HAMAMATSU *SN05* tile only.

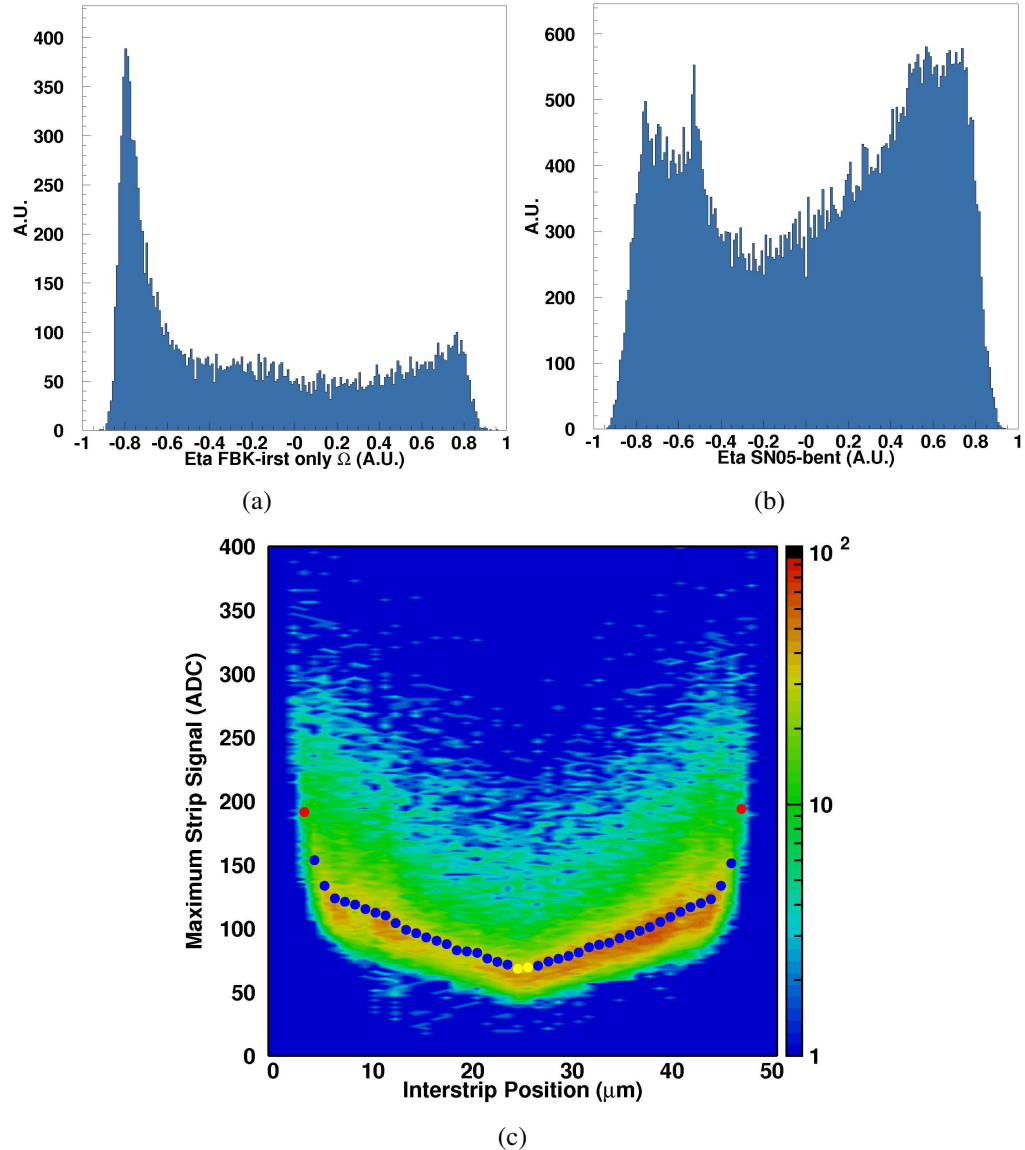


Figure 5.12: The eta distribution of (a) the FBK-irst- Ω and (b) the HAMAMATSU *SN05* tile; (c) the charge sharing distribution of the HAMAMATSU *SN05* tile using the COG method for the particle position reconstruction [66].

As already mentioned above, given the low statistics after the good event selection, the eta algorithm has not been applied and the particle position has been

computed with the standard COG method only. The maximum strip signal as a function of the interstrip position is presented in figure 5.12(c): 0 μm is the center of the first readout strip and 50 μm is the center of the nearby one while the position at 25 μm corresponds to the border between the two strips. Equation 3.4 has been used to find a CS value of 71.43% (table 5.6), which is slightly less than the one found for both the CSEM+VA2 reference modules (table 3.6) and the FBK-irst+VA1_prime2 UA9 ones (table B.3).

Module	Charge Sharing (COG) [%]
FBK-irst	-
SN05	71.43

Table 5.6: Charge sharing of the VISION modules: the value for the FBK-irst- Ω tile is missing given the reason explained in the text.

Both the spatial resolution and the charge sharing will be measured again in the next beamtests at CERN and at BTF for both the FBK-irst- Ω and the HAMA-MATSU *SN05* tile. A large enough statistics will be acquired to evaluate the tiles performance with the eta algorithm and to test all the VISION modules as a whole tracking system.

5.3 The detector at work: beamtest @ MAMI

5.3.1 The Mainzer Mikrotron

The Mainzer Mikrotron (MAMI [120]) is a normal conducting Continuous Wave (CW) 4-stage electron accelerator located at the Institute for Nuclear Physics (Institut für Kernphysik - IKPh¹³) at the University of Mainz (Germany). It was started in 1975 [124] and since 1991 delivers a high quality 100 μA electron beam with a maximum energy which was 180 MeV in the first two stages (MAMI-A, 1983), 855 MeV in the third stage (MAMI-B, 1990) and now is 1.5 GeV, as provided by the innovative Harmonic Double Sided Microtron (HDSM) system completed in 2006 [125].

Figure 5.13(a) shows the MAMI acceleration complex consisting in a pre-accelerator (a RF-Linac up to 3.7 MeV) and a 4-stage cascade based on three RaceTrack Microtrons (RTM1, RTM2 and RTM3) and the HDSM [126]. The

¹³<http://www.kph.uni-mainz.de/eng/index.php>.

RTM working principle is presented in figure 5.13(b)¹⁴ while table 5.7 summarizes the main parameters of each stage (SYTRACE¹⁵ simulated values are reported in red) while figure 5.13(c) shows a photo of the RTM3 stage at MAMI.

Stage	Injector	RTM1	RTM2	RTM3	HDSM
Starting operation year	1990	1983	1983	1990	2006
Injection energy [MeV]	0.511	3.5	14.86	180	855
Extraction energy [MeV]	3.5	14.86	180	855	1500
Number of turns	-	18	51	90	43
Frequency [GHz]	2.45	2.45	2.45	2.45	2.45 / 4.90
Magnetic field [T]	-	0.10	0.55	1.28	0.95 - 1.53
Energy spread [keV]	1.2	1.2	2.8	13	110
Normalized emittance					
horizontal [$\pi \cdot 10^{-6}$ m]	0.05	0.07	0.25	13	27
vertical [$\pi \cdot 10^{-6}$ m]	0.04	0.07	0.13	0.84	1.2
Delivered energy [MeV]	-	-	180	195 - 855	855 - 1500

Table 5.7: Technical parameters of the MAMI accelerator stages [120, 125, 126]. The values simulated with SYTRACE are shown in red while the energy range delivered by the third and fourth stages are indicated in blue: in both cases a 15 MeV stepping is possible.

The MAMI accelerator supplies electron beams to the 4 experimental sites where 4 different collaborations perform several research activities¹⁶:

- the A1 Collaboration (A1 hall) studies hadrons with electromagnetic probes for high precision tests of the structure of matter and the so-called *kaons*

¹⁴The RaceTrack Microtron (RTM [127]) is a type of particle accelerator consisting in a couple of 180° bending magnets facing each other and separated by a field free zone in which a LINear ACcelerator (LINAC) stage is placed [127]. The particles acceleration takes place in a recirculating way *i.e.* the beam is turning around in the magnets and passes several times through the LINAC stage until the final energy is reached; the particle beam is then deflected into a further acceleration stage or to an experimental area. The ΔE energy gained at each turn is proportional to the magnetic field intensity (B) and the RF-system wavelength (λ_{RF}) through the following expression [125, 127]:

$$\Delta E = \frac{ecB}{2\pi} \cdot n \cdot \lambda_{RF} \quad (5.1)$$

where n is an integer, e is the electron charge and c the speed of light.

¹⁵SYTRACE is a particle tracking program including effects of stochastic emission of synchrotron radiation photons [125].

¹⁶“20 Years of Physics at the Mainz Microtron MAMI” Symposium, October 20-22 2005 held at the IKPh of the Mainz University; <http://www1.kph.uni-mainz.de/Symposium/> and IKPh website.

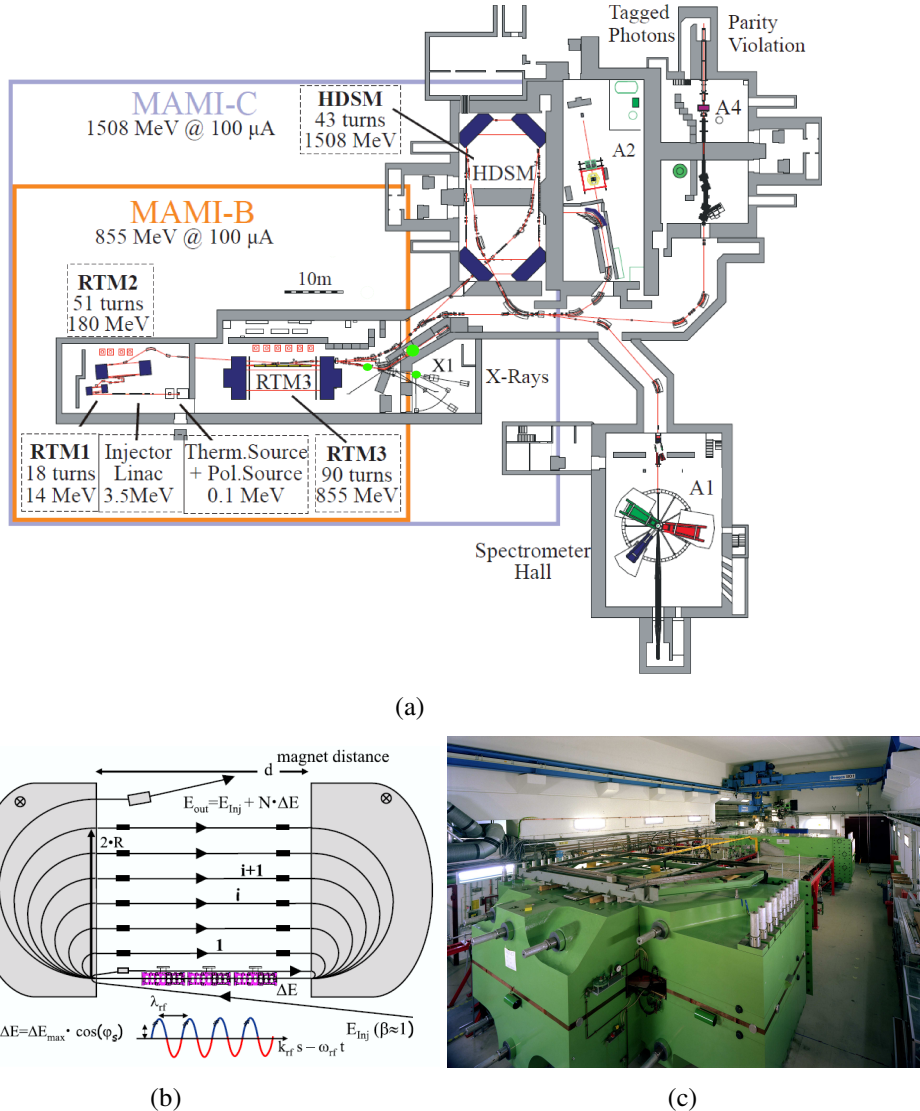


Figure 5.13: (a) The MAMI accelerator floor plan [126]: the acceleration stages together with the 4 main experimental areas are shown with the maximum extraction energy for each stage. (b) Basic setup scheme for a RaceTrack Microtron [125]. (c) Photo of the RTM3 stage at MAMI [courtesy of the MAMI Group].

electroproduction;

- the reactions induced by circularly and linearly polarized high energy photons incident on nucleons or nuclei are measured by the A2 Collaboration (A2 hall);
- the A4 Collaboration (A4 hall) investigates the nucleon form factor through the polarized electron scattering off unpolarized protons;
- the X1 Experiment (X1 hall) is dealing with the production of a high brilliance X-ray source (both in the soft and hard region) for applications in several fields of physics, material science, biology and medicine.

5.3.2 The experimental setup: detectors & crystals

The experimental setup used at MAMI in the INFN ICE-RAD project framework has been installed near the X1 hall (green circles in figure 5.13(a)); it allows to characterize the crystals in terms of both their deflection and radiation emission properties¹⁷. The schematic view of the used setup is shown in figure 5.14; two functional parts can be identified: the so-called *deflection part* is dedicated to the beam monitoring and to the study of the crystals deflection properties while the so-called *radiation part* is in charge of the crystals radiated energy measurements.

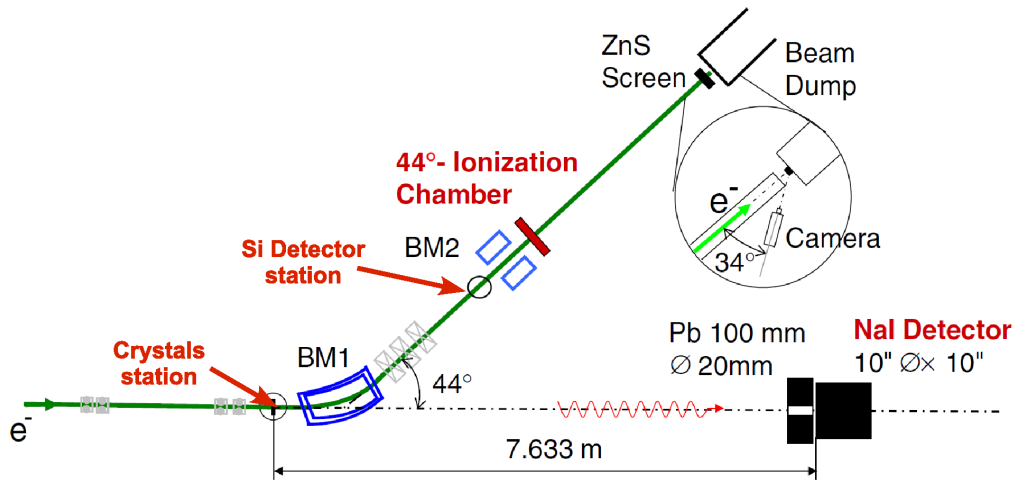


Figure 5.14: Schematic view of the experimental setup used at MAMI with the electron beam coming from the left [66]: both the *deflection* and the *radiation part* are shown.

¹⁷More details on the experimental setup can be found in [66]

The setup working principle can be described as follows:

- the 855 MeV electron beam¹⁸ comes from the left (from the RTM3 acceleration stage) and encounters a first vacuum chamber where the crystals are installed on the same mechanical holder and mounted on a goniometric system¹⁹. Several different crystal samples, produced by INFN-Fe²⁰ and LNL²¹, have been tested. Figures 5.15(a) and 5.15(b) present the photos of some of the used samples whose technical parameters are summarized in table 5.8. Several germanium samples and silicon membranes of different thickness have been tested to study their properties as a function of the thickness itself and to find the best thickness value to be used for deflection at low energy. Figure 5.15(a) also shows a single wire detector (purple square) used to check the beam profile in the first vacuum chamber (*i.e.* at the crystals z position along the beam direction);
- the charged beam is deflected by the BM1 magnet (with a 44° horizontal angle and a 7.2° vertical one) to the silicon detector station (figure 5.16(a)): the HAMAMATSU SN04-05 module has been used as a profilometer. It has been mounted on a couple of remotely controlled motors (figure 5.16(b)), to adjust its position with respect to the incoming beam, and placed in a vacuum chamber, a 593 mm inner diameter cylinder 675 mm high (red insert in figure 5.16(a)) placed before the BM2 magnet. The connection with the “*outside*” world (the repeater and ADC boards) is made via two 50 pin 1.2 m long ERNI cables (one per tile) glued in one of the chamber flange (figure 5.16(b)); the frontend and the readout electronics have been placed near the vacuum chamber on a dedicated table. The SN05 tile and the SN04 one have been used to measure, respectively, the horizontal and the vertical direction. A 40 mm diameter fluorescence screen placed about 2.5 cm beside the profilometer has been also installed to monitor the beam spot;
- before the beam dump there is a ZnS luminescent screen with a professional 1/3” Sony black/white CCD (Charge Coupled Device) camera (400 TV lines resolution) that allows to monitor the electron beam when the detec-

¹⁸At this energy the typical emittance of the beam is $\epsilon_h=0.01 \text{ mm}\cdot\text{mrad}$ and $\epsilon_v=0.001 \text{ mm}\cdot\text{mrad}$ in the horizontal and vertical direction, respectively. The beam has been focused with dedicated quadrupole lenses: the resulting dimension and divergence are, respectively, less than $\sim 230 \mu\text{m}$ and $\sim 50 \mu\text{rad}$ in both the directions.

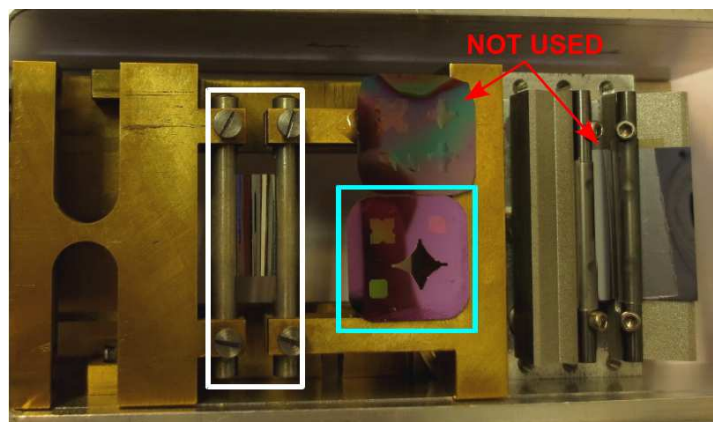
¹⁹The relevant stages (three rotational ones, with a $10^{-3} - 10^{-4}$ deg repeatability [66], and two linear ones) are from Physik Instrumente (PI, <http://www.physikinstrumente.com>) and controlled by the PI Mercury C863.11 DC motor controller.

²⁰INFN Sezione di Ferrara, <http://www.fe.infn.it/>.

²¹Laboratori Nazionali di Legnaro, <http://www.lnl.infn.it/>.

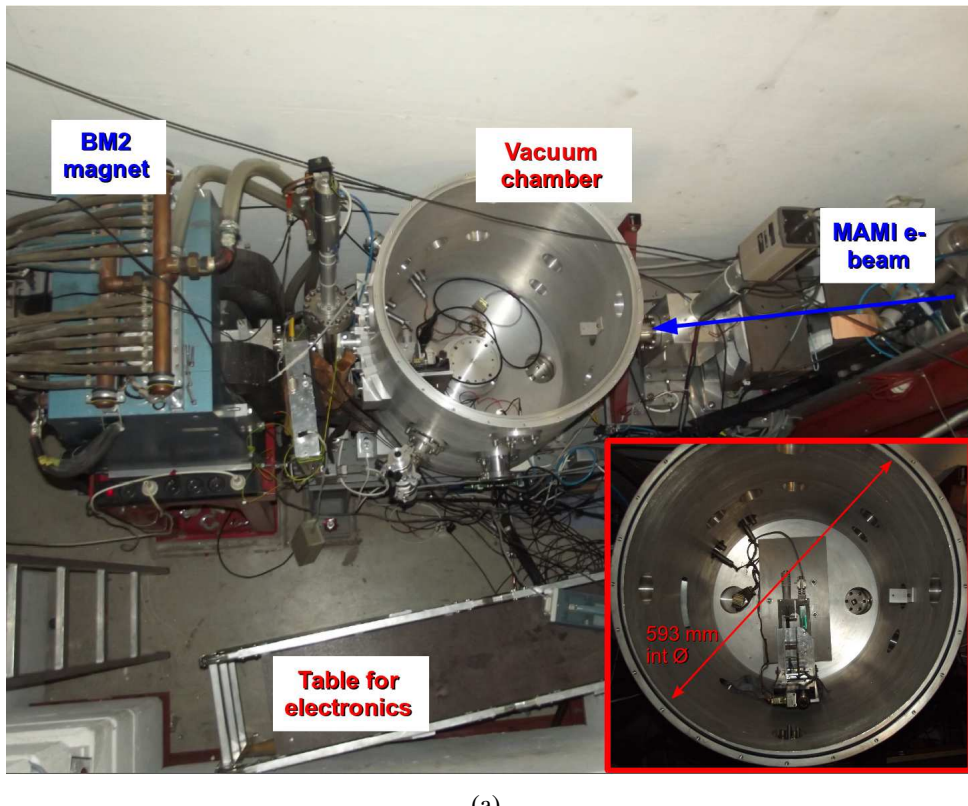


(a)

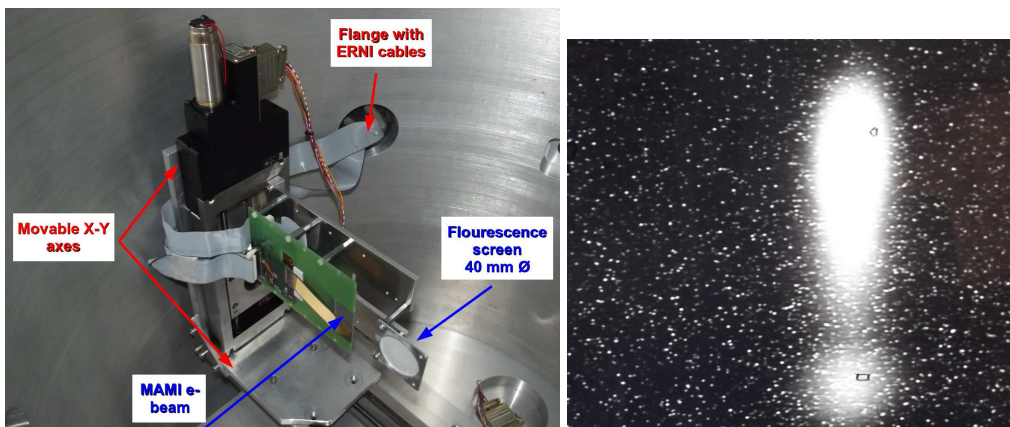


(b)

Figure 5.15: Photos of the crystals tested at the MAMI accelerator: (a) the first set of samples has been tested in the first 3 months of 2013 [66] while (b) the second one has been characterized in January 2014.



(a)



(b)



(c)

Figure 5.16: (a) The *deflection* profilometer station; the electron beam comes from the right while the red insert shows a top view photo of the vacuum chamber with the detector installed inside. Photos of (b) the profilometer support and the flange with the ERNI cables connecting the VA1TA ASIC PCBs to the repeater boards and (c) the beam spot recorded by the ZnS-CCD camera with the SiB crystal in channeling regime [courtesy of the MAMI Group].

Crystal	SiB	SiF1	GeB	GeF1	GeF2	SiM1	SiM2
Produced by	Fe	Fe	LNL	LNL	LNL	Fe	Fe
Material	Si	Si	Ge	Ge	Ge	Si	Si
Type	bent	flat	bent	flat	flat	memb.	memb.
Figure color	blue	green	white	pink	-	yellow	cyan
Dimensions [mm ²]	20×14	4×4	13×15	13×15	13×15	1×1	1×1
Thickness [μm]	30.5	30	13	20.5	27.2	1	0.2
Curvature radius [mm]	33.5	-	15.5	-	-	-	-
Deflecting planes	(111)	(110)	(110) (112)	(110) (112)	(110) (112)	(110)	(110)
Deflection angle [μrad]	905	-	840	-	-	-	-

Table 5.8: Technical parameters of the crystals used at MAMI in the 2013 and 2014 beamtests.

tor is in the so-called *safe position*²² (*i.e.*, it is outside the incoming beam acceptance): figure 5.16(c) shows an example of the beam spot recorded by the CCD camera with the bent silicon crystal (named *SiB*) in channeling regime;

- as far as the neutral particle beam is concerned, the photons produced by the interaction with the crystals follow a straight line of ~8 m and are detected by a 10" diameter 10" length NaI detector shielded by a 100 mm thick lead wall with a 20 mm diameter aperture [128]. The signal is readout by three standard PMTs whose signals are summed together and conditioned by two parallel lines with a different gain²³. Each line consists in a 2025 Automatic Fine Tuning (AFT [129]) Research Amplifier module (Canberra Industries²⁴) and a Multiport-II MultiChannel Analyzer (MCA [130], Canberra Industries) connected via the USB interface to the PC [131]. In addition the photon beam can be collimated with a movable rod of Densimet

²²During the radiation measurement phases the beam voltage (that in turn acts on the beam intensity) has been raised from -25 up to -11.8 V. Given a very high beam intensity could damage the silicon tiles, the profilometer was placed out of the beam acceptance and the deflected electron beam has been reconstructed by the forward ZnS screen only.

²³In this way the system is *sensitive* at the same time to different regions of the radiation spectrum.

²⁴Canberra Industries Inc., <http://www.canberra.com>.

D176 (from PLANSEE²⁵, density 17.6 g/cm³, 92.5% tungsten, 5% nickel and 2.48% iron) which has a 4 mm diameter 261 mm long hole [66].

Some results in terms of deflection capabilities obtained with the bent silicon crystal are given in section 5.3.4; the complete characterization of the crystal, both in terms of deflection and radiation emission properties, can be found in [24, 60].

5.3.3 Performance of the HAMAMATSU profilometer

5.3.3.1 Pedestal and noise

Figure 5.17 shows the pedestal and noise distributions of the HAMAMATSU SN04-05 profilometer used at MAMI. The study of the pedestal has been repeated for two reasons:

- the noise condition of the experimental area at MAMI could in principle be different from the one either at Como or at CERN; the knowledge of the noise induced on the detector cables is fundamental to set the correct bit configuration (mask) for the self-trigger generation of the VA1TA ASICs²⁶; in particular a possible contribution of electromagnetic noise due to the presence of pumps for the beamline vacuum could negatively affect the detector performance (limiting its capabilities) and must be eventually reduced;
- the ERNI cables (connecting the ASIC PCBs and the repeater boards) have been mounted once the detector has been brought at MAMI; an increase of the number of dead/noisy channels was thus in principle possible.

Comparing the distributions measured at Como (figures 5.6(b) and 5.6(c)) and the ones obtained at MAMI (figure 5.17) it is clear that the number of unused channels remains unchanged; moreover both the HAMAMATSU SN04-05 tiles have a lower noise value (\sim 3-4 ADC) and no particular care has been required to reduce the noise further.

5.3.3.2 Hold and DAC threshold scans

Since a different length of the ERNI cables connecting the ASICs and the frontend boards could modify the output signal timing (especially the peaking time when

²⁵PLANSEE SE Group, <http://www.plansee.com/>.

²⁶If in fact the noise value is large and the threshold is too low, the system is always triggered and most of the events are noise ones; on the other hand a too high threshold value to avoid the noise events means no counts (see figure 5.19(a) for details).

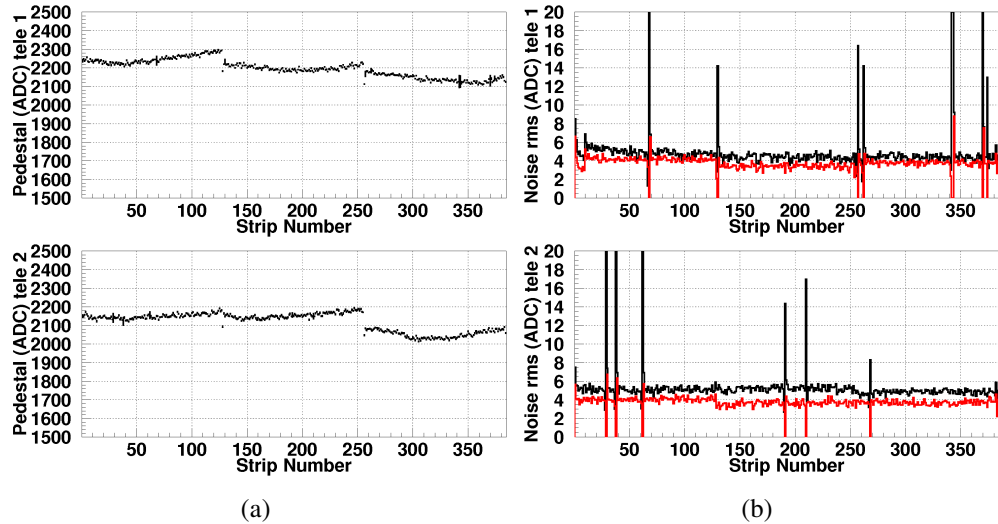


Figure 5.17: Pedestal and noise distributions of the HAMAMATSU *SN05* (top) and *SN04* (bottom) tiles measured at MAMI.

the signal should be sampled), the hold scan has been repeated; the same procedure described in section 5.2.3 for the test with the ^{90}Sr source has been applied. A data run has been acquired for each of the hold values in the 100-1200 ns range (with 100 or 200 ns steps); the maximum pull distribution has been fitted with a Landau-like function (equation 3.3) to evaluate the peak position.

Figure 5.18 shows the obtained MPVs as a function of the hold ones for both the HAMAMATSU *SN05* (black dots) and *SN04* (black squares) tiles; in this case the DAC threshold was set to 170 mV²⁷. The peaking time in both cases is \sim 300 ns and is slightly smaller than the one computed with the ^{90}Sr source (figure 5.7(b)) because of the different length of the used ERNI cables. As far as the signal amplitude is concerned, the difference with respect to the ^{90}Sr source test is given by the low noise value measured at MAMI (especially for the *SN04* tile whose noise decreased from \sim 8-9 down to 3-4 ADC).

Once the exact hold value was selected, it was also possible to study the output signal shape as a function of the different DAC threshold settings of the ASIC TA-part; only the global DAC threshold has been changed (see section 5.1.2 for details). In figure 5.18 the hold scans performed with 3 different DAC threshold values (170, 180 and 200 mV) are shown: for both the HAMAMATSU *SN05* (dots) and *SN04* (squares) tiles, the larger is the DAC threshold value, the larger is the pull peak position. As expected, given the DAC threshold value does not affect the time structure of the output signal, the peaking time remains \sim 300 ns in

²⁷See later on to understand the meaning of the other coloured points.

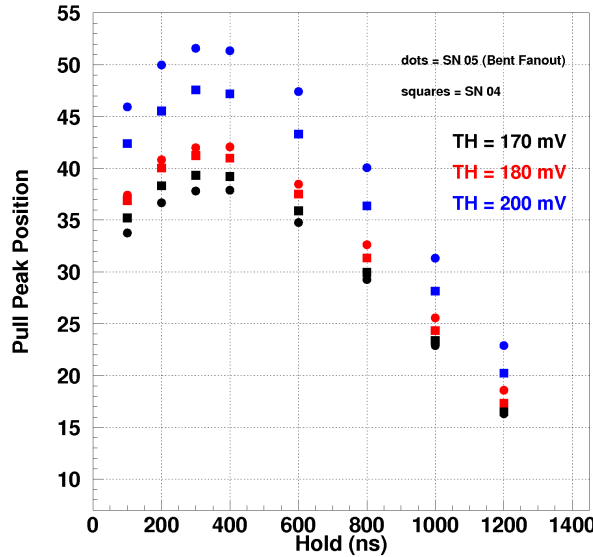


Figure 5.18: The hold scans performed with the HAMAMATSU SN05 (dots) and SN04 (squares) tiles with different DAC threshold values [66]: in all the cases the peaking time is ~ 300 ns.

all the cases.

A scan varying the DAC threshold value in the 130-240 mV range has also been performed with a fixed hold value of 300 ns (Δt_{Hold}). Referring to figure 5.19(a), the working principle of the threshold scan is the following:

- when the threshold value is very small (blue line - TH_0) the system is always triggered given the input signal is always higher than the discriminator threshold in the ASIC TA-part. The value set for the threshold is thus very similar to the noise signal amplitude: a large number of events are noise ones and the DAQ rate is very high;
- increasing the threshold, only the signals actually given by a particle event are recorded; moreover, since the signal is sampled after a time interval (Δt_{Hold}) due to the hold delay, a further increase of the threshold value means sampling the signal in a different place as indicated by the yellow stars in figure 5.19(a): for TH_1 (red line) the output signal amplitude is PH_1 while for a higher threshold TH_2 (black line) the output is $PH_2 \gg PH_1$;
- when the threshold is too high (*i.e.* it reaches the value indicated by the pink line in figure 5.19(a)), the shaper signal never crosses the threshold and the system does not count²⁸.

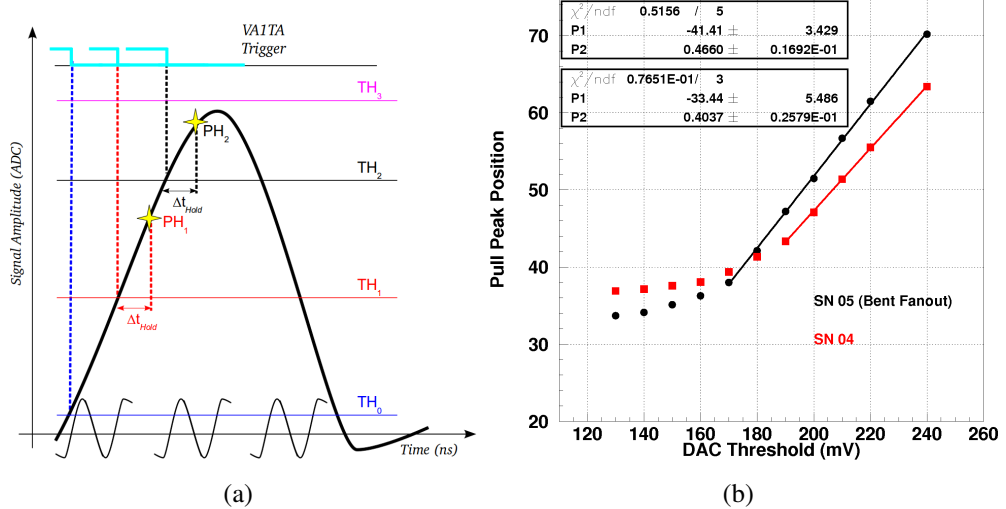


Figure 5.19: (a) The threshold scan principle. (b) The DAC threshold scan of the HAMAMATSU SN05 (black dots) and SN04 (red squares) tiles [66]; in both cases the linear fit is also shown.

The same procedure used for the hold scans presented above and in section 5.2.3 has been applied to evaluate the position of the maximum pull distribution; the results for both the HAMAMATSU SN05 (black dots) and SN04 (red squares) tiles are presented in figure 5.19(b). In both cases, after a flat-like trend at threshold values from 130 mV up to ~ 170 -190 mV (which correspond to the blue line case in figure 5.19(a)), the behavior becomes linear and has been fitted with a p1-polynomial function. The values of the linear fit slopes (P2 parameters) are very similar for both the tiles confirming they behave in a similar way and the two complete chains (tile+ASIC+electronics) are similar in terms of gain and settings.

To better understand which is the best DAC threshold value, both the pull of the strip with the maximum signal in the event (figure 5.20(a)) and the DAQ rate²⁹ (figure 5.20(b)) as a function of the threshold itself have been taken into account.

As expected, the larger the DAC threshold, the smaller the number of noise events in the pull distribution: the peak near 0 in figure 5.20(a) decreases increasing the threshold. On the other hand, the larger the DAC threshold, the smaller the DAQ rate: a reduction of $\sim 40\%$ has been measured going from a threshold value

²⁸For the VA1TA ASIC the maximum available DAC threshold value is 255 mV which at MAMI implied a DAQ rate smaller than 10 Hz.

²⁹The DAQ rate has been directly computed by the DAQ software and is strictly related to the trigger rate of the VA1TA ASIC. The DAQ rate is defined as the number of coincidence events, *i.e.* the ones in which the signal of at least one channel of both tiles is larger than the cut set with the maximum pull distribution; in other words it means that both the tiles have *seen* at least one particle.

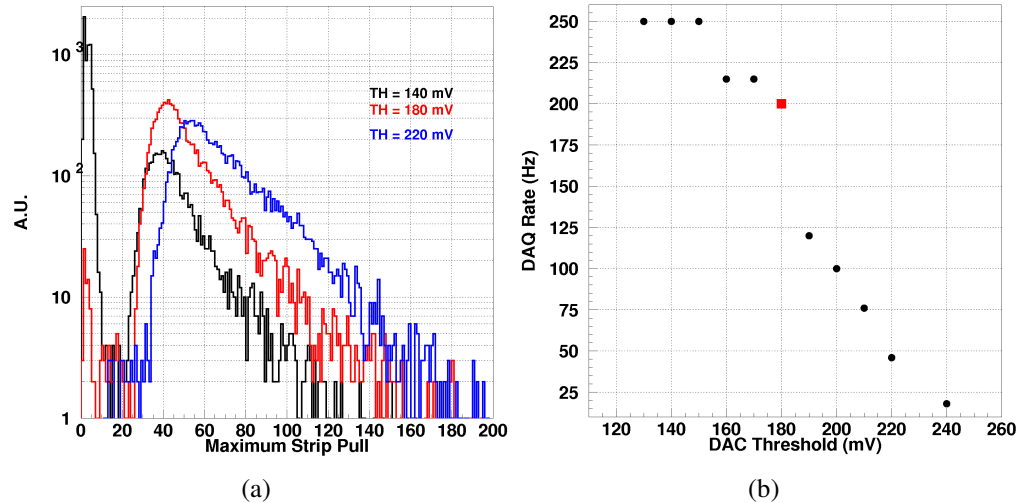


Figure 5.20: (a) The HAMAMATSU SN04 maximum pull distribution and (b) the DAQ rate as a function of different DAC threshold values: the red line and the red square indicate the chosen value (used for the tests with the crystals).

of 180 mV to a 190 mV one and a decrease of more than 90% has been found with a DAC threshold of 240 mV. The chosen value for the following tests with the INFN-Fe and LNL crystals was the one that allows both to maintain an adequate DAQ rate (~ 200 Hz, red square in figure 5.20(b)) and to limit the number of noise events in the pull distribution (red line in figure 5.20(a)).

5.3.3.3 Analog response

Once the exact hold and threshold values have been selected (300 ns and 180 mV, respectively) the analog response of each tile has been analysed. The cluster SNR distributions (equation 3.2) of the HAMAMATSU module are shown in figure 5.21 and have been fitted with a Landau-like function (equation 3.3) to evaluate the MPVs. A 75.49 ± 0.21 and 76.48 ± 0.19 value have been found for the SN05 (figure 5.21(a)) and the SN04 tile (figure 5.21(b)), respectively: once again, the behavior of the two tiles is very similar and the higher SNR values, compared to the one measured in the ⁹⁰Sr source test (figures 5.8(b) and 5.8(c)), are given by the lower noise present at MAMI.

5.3.3.4 Beam profile analysis

Figures 5.22(a) and 5.22(b) show, respectively, the electron beam profile and the number of strips per cluster measured at MAMI with the HAMAMATSU silicon profilometer. The following considerations hold:

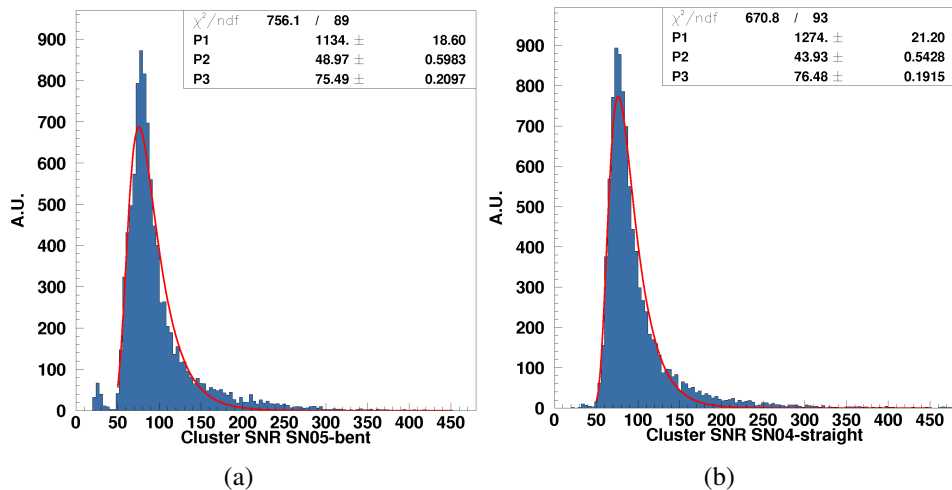


Figure 5.21: The SNR fitted with a Landau-like function of the HAMAMATSU (a) SN05 and (b) SN04 tile.

- as expected, the MAMI electron beam has a Gaussian-like shape with a very small size: both the horizontal direction (figure 5.22(a) top) and the vertical one (figure 5.22(a) bottom) have a σ smaller than $\sim 265 \mu\text{m}$. The beam divergence has been estimated by the MAMI Group (with a custom beam optic program taking into account the beamline magnets current and the distance between the two vacuum chamber stations) to be $70 \mu\text{rad}$ and $30 \mu\text{rad}$, respectively, for the horizontal and vertical directions [60];
 - in both the tiles the clusters are typically composed of 2 or 3 strips; moreover, considering the histograms in figure 5.22(b) refer to the single cluster events only and the fact that a total of 66000 events had been acquired, $\sim 98\%$ of the events are single cluster ones.

5.3.4 Some results with a Si crystal

As mentioned in section 5.3.2, during the last two years several crystal samples have been tested with the MAMI electron beam in the 195-855 MeV energy range. This section briefly describes some of the results obtained with the SiB bent silicon crystal tested in 2013 with a 855 MeV beam [60]. Only the single cluster events (selected with the procedure described in appendix A) have been considered.

Figure 5.23(a) shows a schematic view of the orientation of the SiB crystal planes with respect to the incoming electron beam: the so-called *quasi mosaic* effect [1] has been exploited in order to obtain a bending of the (111) planes

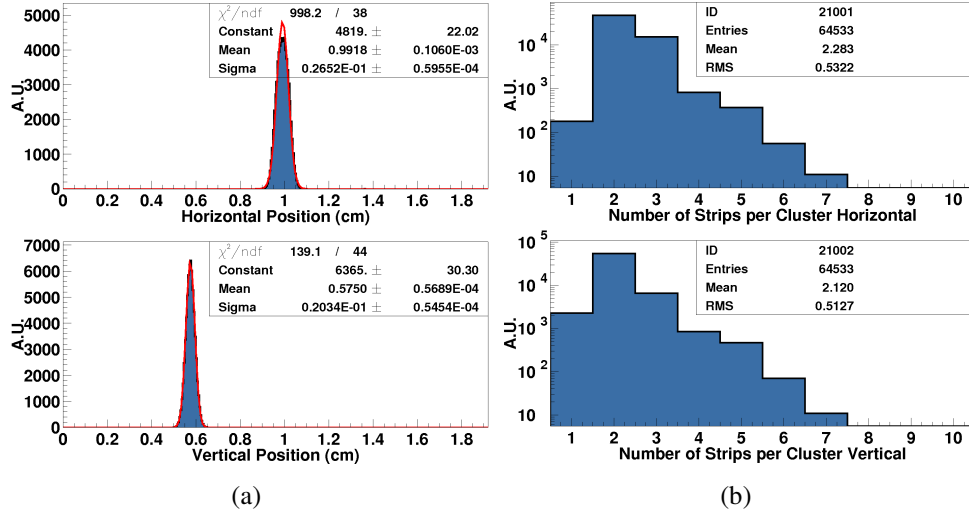


Figure 5.22: (a) The electron beam profile [66]: (top) horizontal and (bottom) vertical direction; both the distributions have been fitted with a Gaussian-like function. (b) The number of strips per cluster measured by both the tiles.

resulting in a deflection of the incoming beam along the vertical coordinate (*i.e.* up or down referring to figure 5.23(a)). The gold arrows correspond to the channeled particles while the pink ones to the over barrier particles.

Figure 5.23(b) shows the beam profile measured by the HAMAMATSU SN04 tile with the SiB crystal oriented in different regimes³⁰:

- the black histogram refers to the amorphous condition: with respect to the one presented in figure 5.22(a)-bottom the presence of the crystal is clearly visible given that the vertical distribution is ∼3.8 times larger; a σ of ∼990 μm has been found fitting the distribution with a Gaussian-like function (not shown in figure 5.23(b) for simplicity);
- the blue histogram refers to the volume reflection condition: the peak on the left corresponds to the portion of the beam which has been reflected while the smaller one on the right refers to the particles in volume capture; the Gaussian-like fit of the VR peak gives a x_{mean} of 4.56 ± 0.01 mm *i.e.* a displacement of more than 1 mm (corresponding to a deflection angle³¹ of ∼190 μrad [60]) has been imparted by the crystal to the incoming electron beam;

³⁰See section 1.1 and figure 1.2 for the details about the bent crystal working principle and the definition of the different regimes.

³¹The lever arm used for the deflection angle calculation is given by the distance between the crystal and the detector stations which is 5973 mm [60].

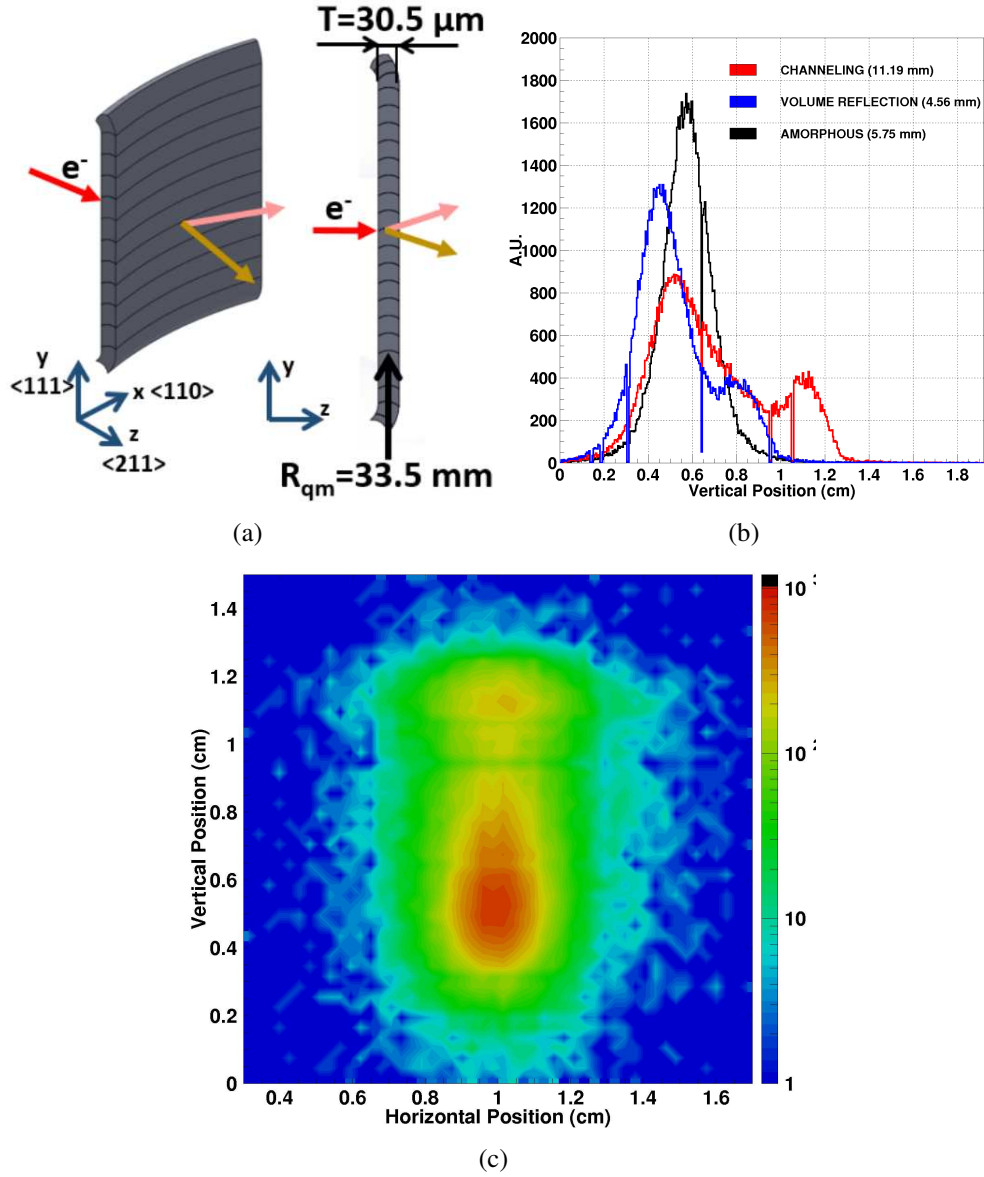


Figure 5.23: (a) Scheme of the SiB bending and planes orientation with respect to the incoming beam [60]; (b) the vertical beam profile recorded by the HAMAMATSU SN04 tile with the crystal aligned in different orientations (see text for details): the values in the brackets give the position of the main peak of each histogram. (c) The scatter plot measured with the crystal in channeling regime: it resembles the one presented in figure 5.16(c).

- finally, the red histogram corresponds to the channeling condition; the peak on the right corresponds to the channeled particles while the one on the left to the over barrier particles which are slightly deflected in the opposite side with respect to the channeling ones ($x_{mean} = 5.28 \pm 0.01$ mm). Also in this case a Gaussian-like fit has been used to estimate the channeling peak position which is $\sim 11.19 \pm 0.01$ mm (corresponding to a deflection angle of $\sim 910 \mu\text{rad}$ [60]).

As can be seen from figure 5.23(b) (and described more quantitatively in [60]), the channeling efficiency is much smaller ($\sim 20\%$) with respect to the volume reflection one ($\sim 76\%$)³²; this latter is in turn smaller than the one measured at higher energy, which for 13 GeV negative particles is $\sim 88\%$ [1]. On the other hand, thanks to the high spatial resolution of the HAMAMATSU SN04-05 module, the different regimes depending on the crystal orientation have been identified: the *channeling beam spot* in figure 5.23(c) (which shows the 2D beam profile measured with the profilometer) is clearly separated by the one in the bottom part of the plot which corresponds to the non-channelled particles.

5.4 Faster and general purpose: the new data transmission

As already mentioned in section 3.2.2, a way to increase the DAQ rate up to ~ 20 kHz is to read in parallel the output signals of each of the three VA1TA ASICs of each silicon tile or side (in the double side detector case); moreover, the possibility to use a limited number of cables for the ASICs configuration/readout or to move to optical fiber connections has pushed the INSULAB Group to design and develop a new data transmission system.

Figure 5.24 presents the new concept for the data transmission system developed and produced up to now; the following considerations hold:

- the mask configuration operation is performed one time at the beginning of each data/pedestal run; for this purpose it is not necessary to work with very high speed connections and both the ADC and VA1TA ASICs signals can be sent on LVDS lines travelling on two standard LEMO cables ($2 \pm$ inputs); the *piggy back* daughter board used at the PS T9 low energy beamtest (section 5.1.4) and plugged onto the master VRB performs this task;

³²Both the channeling and the volume reflection efficiencies are defined as the number of particles in the CH or VR regime over the total number of particles impinging on the crystal (section 1.1).

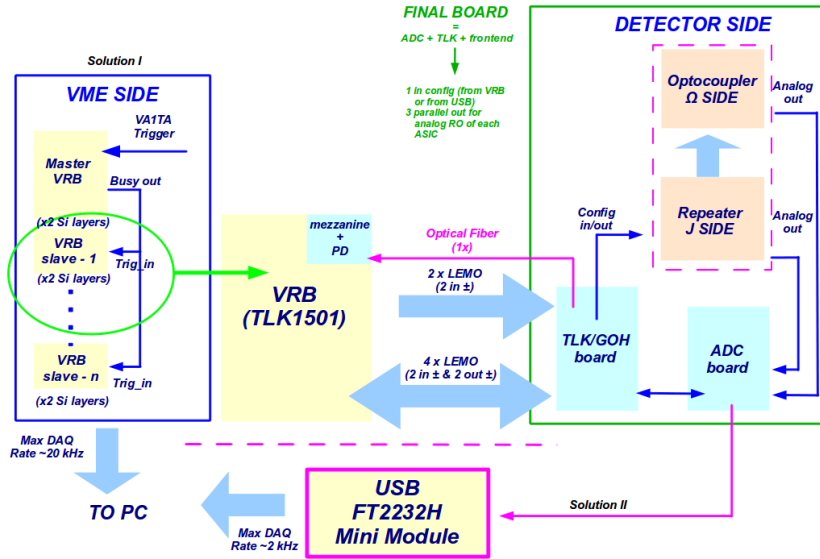


Figure 5.24: Schematic view of the new data transmission based on the TLK+Fiber+VME (top left part) or on the USB2 interface (bottom pink part); the solid green box indicates the final version of the detector side electronics (see text for details).

- on the other hand, the readout operation should be as fast as possible to increase the overall DAQ rate: a gigabit link with LEMO cables or dedicated optical fiber connections could represent a valid option for this purpose. At the same time the electronics should be as compact and as simple as possible: a USB2 interface could be the easiest way to achieve this goal.

Following the phylosophy explained above, two separate strategies (whose pros and cons are summarized in table 5.9) have been adopted:

- the so-called *solution I* (top left part of figure 5.24) is based either on the TLK1501 ASIC [111] or on the GOL (Gigabit Optical Link) one coupled, respectively, to standard LEMO cables or optical fibers (figure 5.25(a) top) and readout by the INSULAB Telescope VME electronics (section 3.2.2) with some minor modifications; in both cases the data transmission system has been designed starting from the one developed for the UA9 experiment [121–123]. A VRB for each module is responsible of the data readout, performing the zero suppression (if needed) and identifying the good events (thanks to the characteristic pattern of the time stamp) before sending the data to the PC. The so-called *TLK/GOH* driver board is in charge of the output data transmission; depending on the used connections (LEMO cables or

fibers), the board contains a different electronics:

- * in the first case (LEMO cables), the clever part of the board is represented by the TLK1501 ASIC which provides a very high-speed I/O bidirectional data transmission (with a 1.5 Gbps maximum speed). The two input lines of the ASIC are used for the configuration signals, coming from the master VRB and sent to both the ADC and repeater boards. On the other hand, the two ASIC outputs are used for the readout and directly connected with two standard LEMO cables to the input LEMO connectors of the VRB of each module;
- * in the second case (optical fibers), the GOH (GOL Opto-Hybrid) part is used. It is in charge of the electrical-to-light signal conversion and consists in the GOL ASIC [110] and a laser diode (figure 5.25(a) bottom). The GOH acts as a SERializer-DESerializer (SERDES) with a 40 MHz maximum clock frequency: in other words it takes the stream of 16 bit words from the ADC boards and serializes the bits at 640 Mbit/s. A small *mezzanine* adapter, plugged onto each VRB, contains a PhotoDiode (PD) for the reception of the fiber signals and the lighth-to-electrical signal conversion. Figure 5.25(b) shows the mezzanine used by the UA9 experiment: a simpler new version, hosting a PD whose pins are directly soldered onto the VRB LEMO inputs, will be integrated in the existing VRBs. The TLK1501 ASIC installed on each VRB acts as a deserializer and performs the data readout;
- the so-called *solution II* consisting in a USB2 interface (bottom part of figure 5.24); it is based on the FT2232H Mini Module [132] by FTDI³³ (figure 5.26(a)). The clever part of the module is the FT2232H ASIC [133] which handles all the USB signalling and protocols and performs the data transmission with a maximum speed of 480 Mbit/s which correspond to a maximum DAQ rate of ~ 2 kHz in the VISION Telescope case. More details about the FT2232H functionalities can be found in [133] while figure 5.26(b) shows the module plugged onto one of the ADC boards through a custom DIN41612 connector (RS³⁴) adapter. The same USB2 interface has been already successfully used by the INSULAB Group for the readout of the MICE (Muon Ionization Cooling Experiment) EMR (Electron Muon Ranger) detector [116, 134].

In both the solutions the electronics for the silicon detector readout (right part in figure 5.24) is the same and is very similar to the one presented in sections 3.2.1

³³Future Technology Devices International Ltd, <http://www.ftdichip.com/>.

³⁴RS Components S.p.A., <http://it.rs-online.com/web/>.

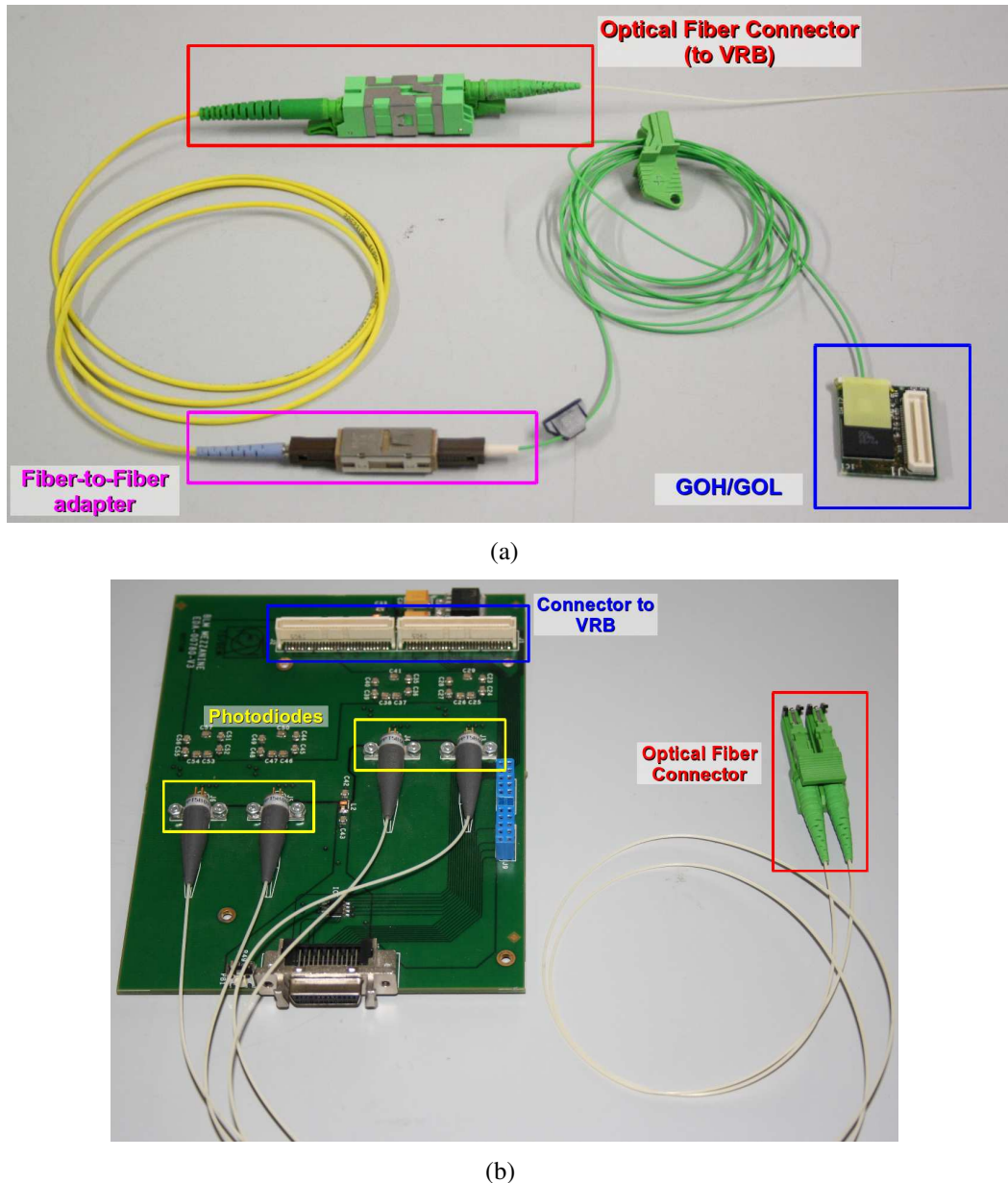


Figure 5.25: Photos of the TLK/GOH data transmission system: (a) the optical fiber and the GOH/GOL (blue square); (b) the UA9 mezzanine where the PDs are installed; a smaller one will be designed for the VISION Telescope (see text for details).

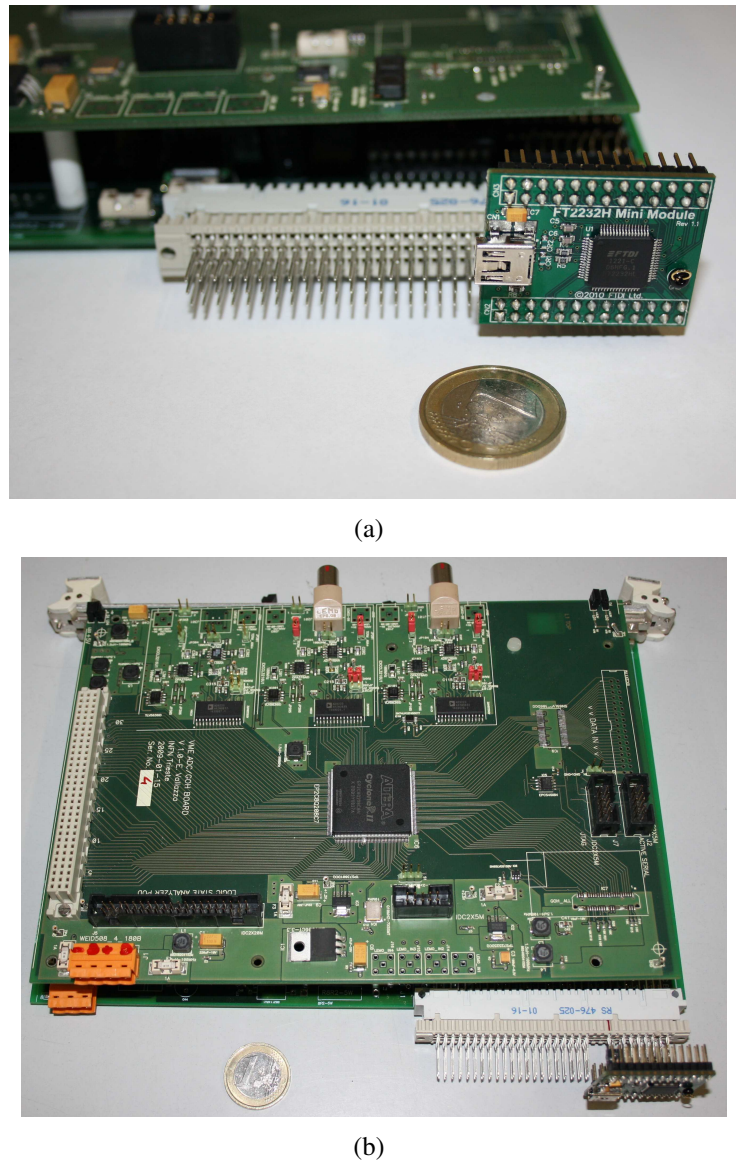


Figure 5.26: The prototype of the USB2 interface: (a) the detail of the USB FT2232H Mini Module connection: the FT2232H ASIC is also visible on the Mini Module itself; (b) the ADC board with the module plugged through a custom DIN connector.

and 3.2.2 for the INSULAB Telescope; also in this case the DAQ software is written in C and the graphical user interface is based on the Tcl/Tk toolkit.

The *INSULAB Telescope* (chapter 3) will be used as a test bench for the commissioning of the new data transmission system based on the TLK/GOH ASICs (*solution I*); its performance, in particular in terms of DAQ rate and speed, will be studied in dedicated beamtests both at the CERN beamlines (PS T9 and SPS H4 and H8) and at the BTF of Frascati.

On the other hand, the system based on the USB2 interface (*solution II*) will be used with the HAMAMATSU modules; the space available at the MAMI experimental areas is in fact limited (the setup shown in figure 5.16(a) is $\sim 2 \times 3 \times 3 \text{ m}^3$) and a more compact and easy to handle system is needed. A commissioning phase with cosmic rays and with the ^{90}Sr source is foreseen for the next months. Moreover, the whole system should be brought at SLAC³⁵) to study the crystals properties in an intermediate energy range between the MAMI and the CERN ones³⁶.

System	Pros	Cons
TLK/GOH	Faster (up to $\sim 20 \text{ kHz}$)	Expensive More complicated
USB2	Compact & Simple Cheap User friendly Rapid integration into existing electronics	Slower (up to $\sim 2 \text{ kHz}$)

Table 5.9: Comparative table between the two data transmission systems.

As far as the final version of the electronics is concerned, a single more compact board (solid green box in figure 5.24) will integrate the TLK/GOH + ADC + frontend parts performing all the tasks of the present three boards at once: a single input for the ASICs mask configuration and three parallel output lines for the analog readout will be necessary for the signal conditioning of 384 channels (which means for the complete configuration/readout of a single silicon tile of the HAMAMTSU modules or a single side of the FBK-irst ones).

³⁵Stanford Linear Accelerator Center, <https://www6.slac.stanford.edu/>.

³⁶A proposal, the CHanneling of NEgative Leptons (CHANEL) project aimed to the study of the flat/bent crystals deflection and radiation properties in the 100 MeV - 400 GeV energy range, has been submitted by the INSULAB Group, the INFN-Fe group and the LNL one to the INFN Commissione Scientifica Nazionale V (CSNV - <http://www.infn.it/csn5/>). The project has been approved for the 2015-2016 biennium.

Chapter 6

Conclusions & Outlooks

This thesis work has dealt with the commissioning and the characterization of two tracking and beam profiling systems (the so-called *INSULAB* and *VISION Telescopes*), both developed and tested in the framework of the NTA-HCCC, COHERENT, ICE-RAD and CHANNEL INFN experiments, all dedicated to the study, in terms of deflection and electromagnetic radiation emission capability, of straight/bent crystals in the 0.5-200 GeV energy range.

As shown in the first chapter (which is dedicated to the crystals physics and its main applications in high energy particle experiments), to study and characterize the crystals with a good enough accuracy, a very high precision (in the 5-10 μm range) in the particle position reconstruction is required.

The last 30 years were characterized by a strong effort to develop very high spatial resolution systems: from the first Drift Chambers, through the Nuclear Emulsions to arrive to the modern tracking systems based on semiconductor detectors which combine a very high spatial resolution with fast response.

The working principle and the peculiarities of this kind of devices (in particular the ones based on silicon microstrips) have been illustrated in the second chapter listing the figures of merit, such as the noise response and the Signal to Noise Ratio (SNR), used to study the performance of the modules under test. Moreover, since the focus of this thesis work was the measurement of the particle position reconstruction capability, a detailed discussion on the parameters affecting the final value of the intrinsic spatial resolution (σ_{int}) and the Charge Sharing (CS) among the strips has been given; in particular different design solutions, such as the choice of both the physical (p) and readout (p_{RO}) pitch or the use of a floating strip scheme, have been taken into account and compared.

As shown in chapters 3 and 5, two very high spatial resolution telescopes have been developed and assembled: several modules, equipped with different silicon tiles and readout ASICs sharing the same very fast readout electronics have been tested in the last three years with high and low energy particle beams (from 10

to 150 GeV) at the CERN SPS H4 and PS T9 beamlines and used at the MAMI accelerator to characterize a set of new generation crystals. The readout chain, upgraded in 2012 to comply with high particle rate minimizing the dead time and to be at the same time as compact as possible, is based on custom ADC and memory/readout boards and allows a Data AcQuisition (DAQ) rate up to 6 kHz.

The results obtained with the offline analyses and algorithms presented in chapters 3, 4 and 5, are listed in table 6.1 (the general features of each module are also shown for comparison). All the values in the second column refer to the INSULAB *TELE 2-C* module (except the one indicated by the (*) which has been computed with the *TELE 4-E* one) while the ones in the third and fifth columns are, respectively, from the UA9 *TELE 08-2* and the HAMAMATSU *SN-05* ones. The red values refer to the SPS H4 high energy beamtest where the so-called *eta algorithm* has been used to calculate σ_{int} while the blue ones refer to the PS T9 low energy data taking where the standard COG method, together with the correction of the tilt angle introduced by the module supports and the subtraction of the MCS contribution (both presented in chapter 4), has been adopted.

The following considerations hold:

- as far as the SNR is concerned, for all the tested modules the SNR is around or larger than 40 which ensures that the noise of the whole readout electronics is low enough;
- as a consequence the measured spatial resolution is very high; in particular, considering the so-called *residual distribution* (chapter 4), it follows that:
 - * in the best case σ_{int} is $\sim 4.1 \mu\text{m}$, if a floating strip scheme is adopted, and $\sim 6.7 \mu\text{m}$ in the no floating strip configuration;
 - * the values obtained with all the modules with a readout and physical pitch of $50 \mu\text{m}$ are very similar except the one for the HAMAMATSU *SN-05* one which could be ascribed to a slightly smaller capacitive coupling among the strips; as shown in chapter 2, in fact, the number of events with a cluster composed by more than one strip is reduced and the spatial resolution worsens;
 - * finally, even if the improvement on the spatial resolution using the *eta algorithm* is not so critical, $\sim 1-1.4 \mu\text{m}$ (*i.e.* $\sim 18-24\%$ less, see also table 4.3 and B.3), both the non Gaussian lateral tails and the asymmetry in the residual distribution have been reduced;
- as far as the CS is concerned, it is larger than 70% in all the cases; the largest value obtained with the UA9 *TELE 08-2* has been ascribed to a different width of the strip implant.

Detector Produced by ASIC	Double CSEM VA2	Double FBK-irst VA1_prime2	Double (only Ω) FBK-irst VA1TA	Single HAMAMATSU VA1TA
Detector dimensions [cm ²]	1.92×1.92	1.92×1.92	1.92×1.92	2.10×2.10
Number of readout channels	384	384	384	384
Bulk thickness [μm]	300	300	300	300
Resistivity [k Ω ·cm]	> 4	> 4	> 4	> 4
Leakage current [nA/strip]	1.5-2.0	1.5-2.0	1.5-2.0	1.5-2.0
Full depletion bias voltage [V]	36-54	36-54	36-54	36-54
AC coupling p-side - <i>junction</i>	no	yes	yes	yes
physical pitch [μm]	25	25	not bonded	50
readout pitch [μm]	50	50	-	50
floating scheme	yes	yes	-	no
n-side - <i>ohmic</i>				
physical pitch [μm]	50	50	50	-
readout pitch [μm]	50	50	50	-
floating scheme	no	no	no	-
Fiberglass support shape	square	L-shape	L-shape	rectangular
dimensions [cm ²]	12.5×12.5	13.5×13.5	13.5×13.5	13.5×9.5
thickness [cm]	1.0	0.5	0.5	0.35
ASIC connection	direct bonding	direct bonding	direct bonding	upilex fanout
SNR				
<i>junction</i>	85.37±0.06	39.99±0.01	-	48.05±0.30
<i>ohmic</i>	69.27±0.08	-	50.36±0.11	-
σ_{int} [μm]				
<i>junction</i>	4.11±0.01	4.49±0.01	-	9.02±0.79
<i>ohmic</i>	8.61±0.44	-	6.72±0.38	-
CS [%]				
<i>junction</i>	76.72	81.29	-	71.43
<i>ohmic</i>	75.05 (*)	-	-	-

Table 6.1: Comparison of the SNR, σ_{int} and CS values of the INSULAB and VISION modules; the general features of the silicon detectors and modules are also indicated (see text for details on the colors).

As far as the future steps are concerned, the following actions are foreseen:

- as mentioned in chapter 5, from the hardware and electronics points of view, a new faster and general purpose DAQ system is being developed; in particular:
 - * the telescopes will now be equipped with a new data transmission system based on a Gigabit link;
 - * the parallel readout of the 3 VA1TA ASICs will be implemented on the repeater board allowing to reduce the overall readout cycle and increase the DAQ rate up to ~ 20 kHz;
 - * the slow control of the overall frontend electronics (based on the existing parts used in the UA9 experiment framework) will be also integrated in the present DAQ to remotely monitor the whole telescopes;
 - * the more compact electronics based on the USB2 interface will be tested to limit the complexity of the whole system maintaining at the same time an adequate DAQ rate (up to ~ 2 kHz).

Dedicated beamtests are thus foreseen both to characterize the new parts of the electronics and to measure again the spatial resolution and the charge sharing, in particular with the VISION Telescope, acquiring a large enough statistics to evaluate the tiles performance with the eta algorithm;

- from the software (analysis and simulation) point of view:

- * a detailed analysis of the multicluster events, based on the correlation between the signals recorded by each detector side, is foreseen for the INSULAB Telescope modules;
- * a complete simulation of both the INSULAB and VISION telescopes will be implemented to better understand the effect on the spatial resolution of a wrong detector positioning along the line (such as the tilt given by the supports); part of the simulation work has been already done by some members of the INSULAB Research Group;
- * an offline algorithm to *remove* the zone corresponding to the noisy/dead channels is under study; a possible solution should be, after a dedicated equalization of the response of all the strips in a tile, to assign to a dead channel a signal equal to the average of the ones recorded by the two neighbour strips.

This thesis work has been developed in the framework of the straight and bent crystals physics: the two tracking systems developed in the last years (the

INSULAB and the VISION Telescopes) have demonstrated to be a fundamental part of the system for the crystals characterization. Both of them allow a very precise particle position reconstruction (up to $\sim 4 \mu\text{m}$) in a very short time (the DAQ rate is 6 kHz) which are two primary tasks when working with straight/bent crystals.

On the other hand both the telescopes proved to be general purpose tracking systems that have been used in the test of SiliconPhotoMultiplier (SiPM) readout calorimeters and in the characterization of other tracking systems (such as the prototype of the GAMMA-400 Silicon detector): they are compact, easy to handle and mount, fast and with a very good particle reconstruction capability and, at last, extremely versatile. They have been already used, in fact, in several different experimental environments (for instance, with the continuous low energy electron beam at MAMI or the pulsed high energy ones at CERN) for testing new detectors (and detector components) and characterize them in terms of efficiency, signal and time response and linearity.

Appendix A

Analysis procedure

The same data taking/analysis procedure has been applied to all the data collected in the data taking periods presented in chapters 3, 4 and 5 in order to select the set of the so-called *good events*. The examples discussed in the following sections refer to the high and low energy beamtest at the CERN SPS H4 and PS T9 beamlines with the CSEM+VA2 INSULAB reference modules. The procedure has been divided in different steps:

- acquisition and analysis of the so-called *pedestal run* (section A.1); the baseline of the electronics chain and its noise behavior have been studied to evaluate a threshold for each channel to identify the strips in which the particle has deposited its energy. This threshold value has also been used to operate the VRBs in the zero suppression mode (see section 3.2.2 for details);
- data acquisition and selection of the good events (section A.2); for each event, the charge deposited by a particle can be shared among several strips, defining the so-called *cluster*; a *position finding algorithm* based on the Center Of Gravity method (COG [118]) has been applied to reconstruct the exact hit position on each module; moreover the study of the eta distribution as a function of the readout clock has been performed in order to optimize the signal sampling;
- detector alignment (section A.3); an offline procedure has been applied to align all the detectors with respect to the same reference system;
- offline data analysis; to evaluate the ultimate spatial resolution the particle impact position has been reconstructed using the so-called *eta algorithm* (section 4.3) instead of the COG one. In this case also the information of the charge deposit in each strip must be known to perform the correct analysis.

The output data are saved in binary files (PAW ntuples) and the data storage for the physics analysis is performed by a dedicated *stripping program* which automatically generates an ASCII (American Standard Code for Information Interchange) DST (Data Summary Tape) output file containing the relevant information for all the detectors:

- the hit position on each module (in cm);
- the number of clusters and/or the number of strips per cluster (to monitor the beam intensity);
- if present, as in the COHERENT experiment at CERN, both the energy released by the particles in a calorimeter (as in [20]) and the values of the goniometric system (2 rotational stages and 2 translation ones);
- the event number.

The analysis software is written in FORTRAN (FORmula TRANslator) [135].

A.1 Pedestal analysis

When a particle crosses a silicon detector, it deposits a certain amount of charge which is then amplified and sampled by the readout ASICs and sent to the ADC boards for the digitization. When no signal is present, the baseline level digitized by the ADC boards (due to the complete detector+electronics chain) is called *pedestal*. To evaluate the electronics baseline and the *noise* of each channel a pedestal run is acquired with a random trigger: 200 triggers are randomly generated and the mean value of each channel of the ASICs represents the pedestal while the rms corresponds to the noise.

The results obtained for one of the CSEM+VA2 reference modules have been already shown in section 3.4.1. The presented noise distributions (figure 3.11(b)) have been also used to identify the noisy or dead channels which have been excluded in the analysis.

As mentioned in section 3.4.1, the pedestal run also allows to evaluate the so-called *Common Mode (CM) noise* which is defined as the noise contribution due to the external noise on the detector bias line (for example the electromagnetic noise). In other words, the common mode noise corresponds to a common variation of the baseline of all the channels of the electronics chain. The following procedure has been performed in order to compute the pedestal and the intrinsic noise rms (that is without the common mode contribution):

- calculation of the pedestal and noise rms values of each strip (figure 3.11);

- calculation of the common mode for each ASIC:

$$CM_j = \frac{\sum_i^N (raw_i - pede_i)}{N} \quad (A.1)$$

$j \rightarrow$ number of ASIC $i \rightarrow$ number of channel per ASIC
 $j = 1, 2, 3$ and $i = 1, \dots, 128$

i.e., on an event by event basis, the pedestal value of each channel ($pede_i$) has been subtracted from the raw data (raw_i) and the mean value CM_j has been computed ASIC by ASIC excluding the dead/noisy channels (N indicates the number of *good* channels); the rms value associated to this number (*i.e.* the rms of CM_j) represents the common mode noise of a single ASIC;

- subtraction of the mean value of the common mode on an event by event basis from the raw data

$$pedecm_i = raw_i - pede_i - CM_j \quad (A.2)$$

- re-calculation of the pedestal and noise rms distributions.

The common mode noise is a detector feature as can be seen in figure A.1(a), that presents the correlation of the common mode of two different ASICs connected to the same silicon side.

Figure A.1(b) shows an example of the common mode noise of one of the CSEM+VA2 reference modules; both the junction (top) and ohmic (bottom) distributions have been fitted with a Gaussian function. The mean value is ~ 0 for both cases while the σ one is ~ 1.82 ADC for the junction side and ~ 0.67 ADC for the ohmic one. Considering the distribution of the global noise (figure A.1(c) top) and subtracting in quadrature the common mode noise value (given by the Gaussian fit in figure A.1(b)) one obtains, for the junction side, a 5.2 ADC value for the intrinsic noise¹ that is perfectly in agreement with the value obtained through the Gaussian fit in figure A.1(c) bottom. The same procedure may be applied to the ohmic side obtaining a 4.1 ADC intrinsic noise value. The value of the common mode for both sides is clearly negligible with respect to the intrinsic noise which means the VRBs can work in a zero suppression mode (see section 3.2.2 for details). If in fact the common mode noise is large, the threshold used for the zero suppression should be increased reducing the detector efficiency. On the other

¹The following equation has been used for the intrinsic noise calculation:

$$\sigma_{int} = \sqrt{\sigma_{global}^2 - \sigma_{CM}^2} \quad (A.3)$$

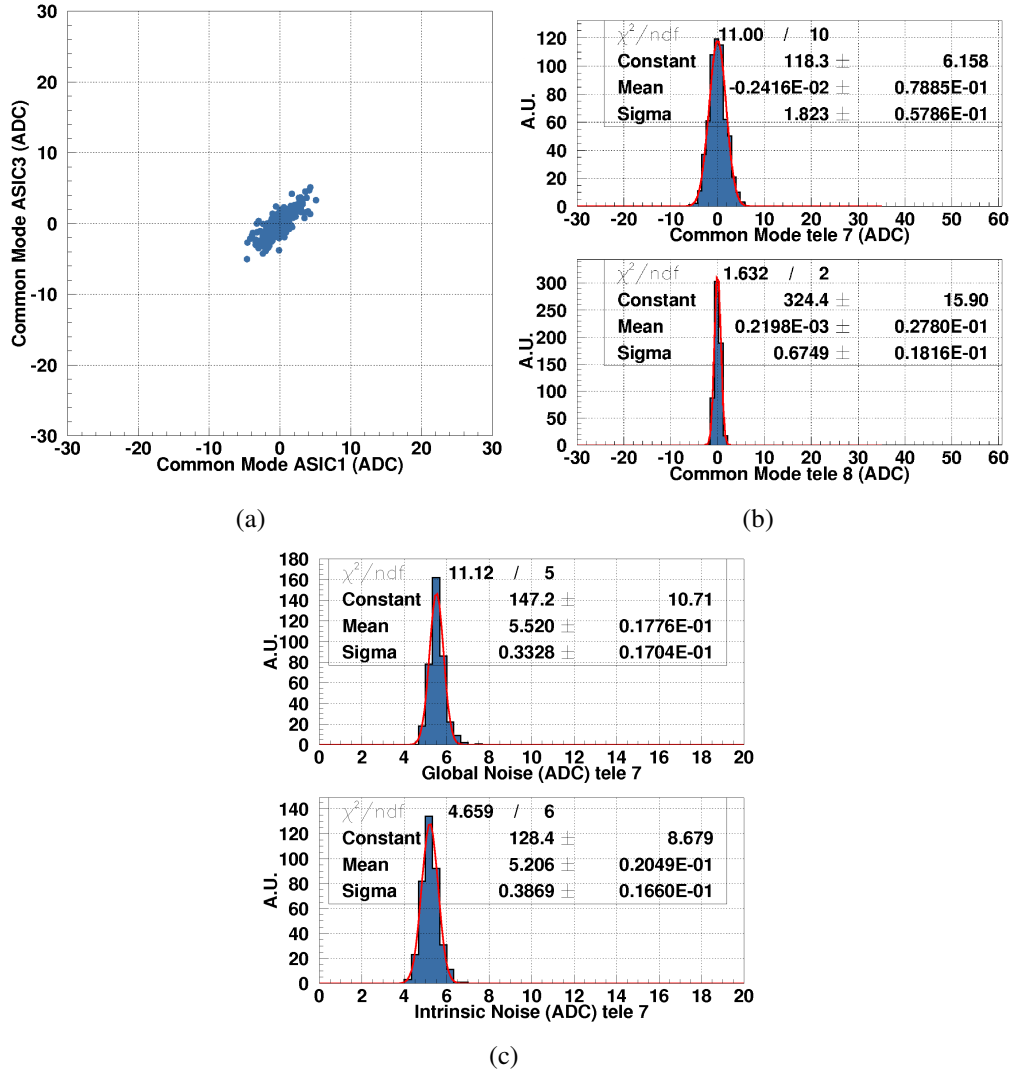


Figure A.1: (a) The common mode correlation of two readout ASICs connected to the same silicon side. (b) The common mode noise distribution of a single tile fitted with a Gaussian function: junction (top) and ohmic (bottom) side. (c) Gaussian fit of the global noise (top) and intrinsic noise (bottom) distribution of the junction side.

hand, large noise and standard threshold means a larger number of strips to read per module (since they are over threshold) and thus a smaller DAQ rate. The typical threshold value used with the INSULAB reference modules and the VISION ones was set to 3-5 times the overall noise rms (that means $\sim 15\text{--}25$ ADC). A study of the number of strips above the threshold as a function of the considered threshold value for the INSULAB reference modules can be found in [86].

A.2 Particle position finding algorithm

As mentioned in section 3.4.2, the reconstruction of the hit position on each module has been performed considering the maximum pull distribution, defined as the ratio between the pulse height of the channel with the maximum signal in the event and its corresponding noise rms: in practice the signal is expressed in terms of its noise rms (figure 3.12). Moreover, given the capacitive coupling and the fact that the tracks incidence angle is not 90° with respect to the strip, the charge deposited by the particle is shared among several neighbouring strips: as already mentioned in section 3.4.2, this group of contiguous strips is called *cluster*.

To select the set of good events, the cluster-finding algorithm based on the COG method [118] (equation 3.1) has been applied to identify the exact position of the particle in the detector. The lateral pull distributions, defined as

$$\begin{aligned} pull_{left} &= pull_{max-1} = \frac{PH_{max-1}}{rmscm_{max-1}} \\ pull_{right} &= pull_{max+1} = \frac{PH_{max+1}}{rmscm_{max+1}} \end{aligned} \quad (\text{A.4})$$

where PH indicates the pulse height and $rmscm$ is the noise rms after the common mode subtraction, have been studied for both sides to choose the threshold value for the strips that surround the one with the maximum. Figure A.2 presents an example of the *left* (a) and *right* (b) pull distributions for the junction side of one of the CSEM+VA2 reference modules; the other side behaves in a similar way. The typical lateral threshold values used with the INSULAB and VISION modules (red lines in figure A.2) are $5\text{--}10\sigma$.

Two sets of good events have been selected depending on the data taking period:

- @ CERN (SPS H4 and PS T9) with the CSEM+VA2 reference modules, only the events with a single 1 or 2-contiguous strips cluster on each module have been considered;
- @ MAMI with the HAMAMATSU VISION module, only the events with a single cluster in both the module sides have been included in the analysis.

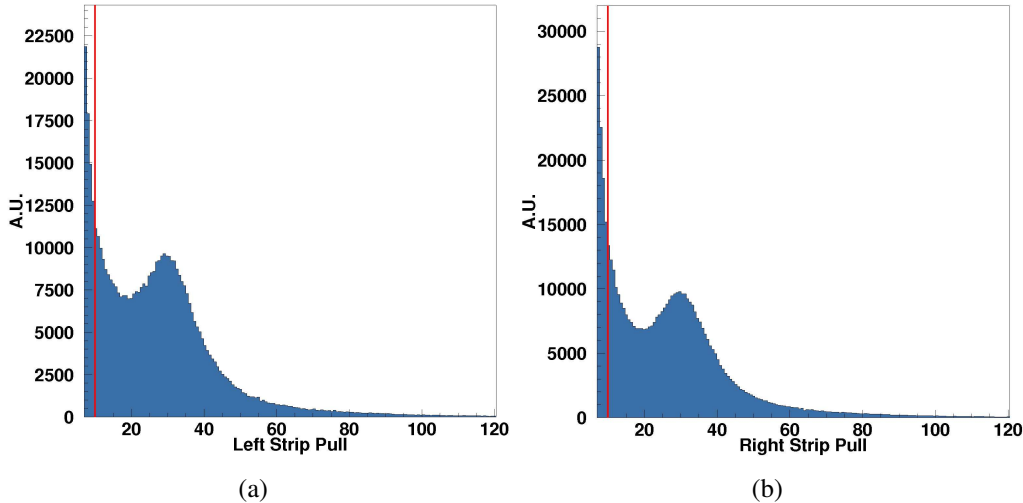


Figure A.2: (a) The *left* and (b) the *right* lateral pull distributions of the junction side of one CSEM+VA2 reference module.

As mentioned in section 3.1.2, the clock sampling the multiplexed analog information of the readout ASIC can be set to 1.25, 2.5, 5 and 10 MHz. The so-called *eta distribution*² (figure A.3) helps to identify the best clock value to be used. Figures A.3(a) and A.3(b) report the distributions measured with a readout clock value of 2.5 MHz (the typical one used during the SPS H4 and PS T9 beamtests): as expected, given the correct sampling of the output signals, both the distributions are symmetric. The large central peak in figure A.3(a) is due to the floating strip while the lateral ones around ± 0.75 in both figures reflect the fact that the capacitive coupling among the strips is similar for the two sides. Figures A.3(c) and A.3(d) show the same distributions for a 5 MHz readout clock: in this case the distributions are completely asymmetric given the signal sampling is not the correct one. Details about the asymmetries introduced by a readout clock that causes a non correct sampling of the signal itself can be found in [86].

A.3 Module alignment

During all the beamtests presented in chapters 3, 4 and 5 the silicon detectors have not been installed with absolute precision (figure A.4 left). For this reason an alignment procedure has been applied as follows (the data presented in this section refer to the PS T9 low energy beamtest where only 3 modules were installed):

- only the alignment in the x - y plane (the one perpendicular to the incoming

²The definition of the eta is given in chapter 2.

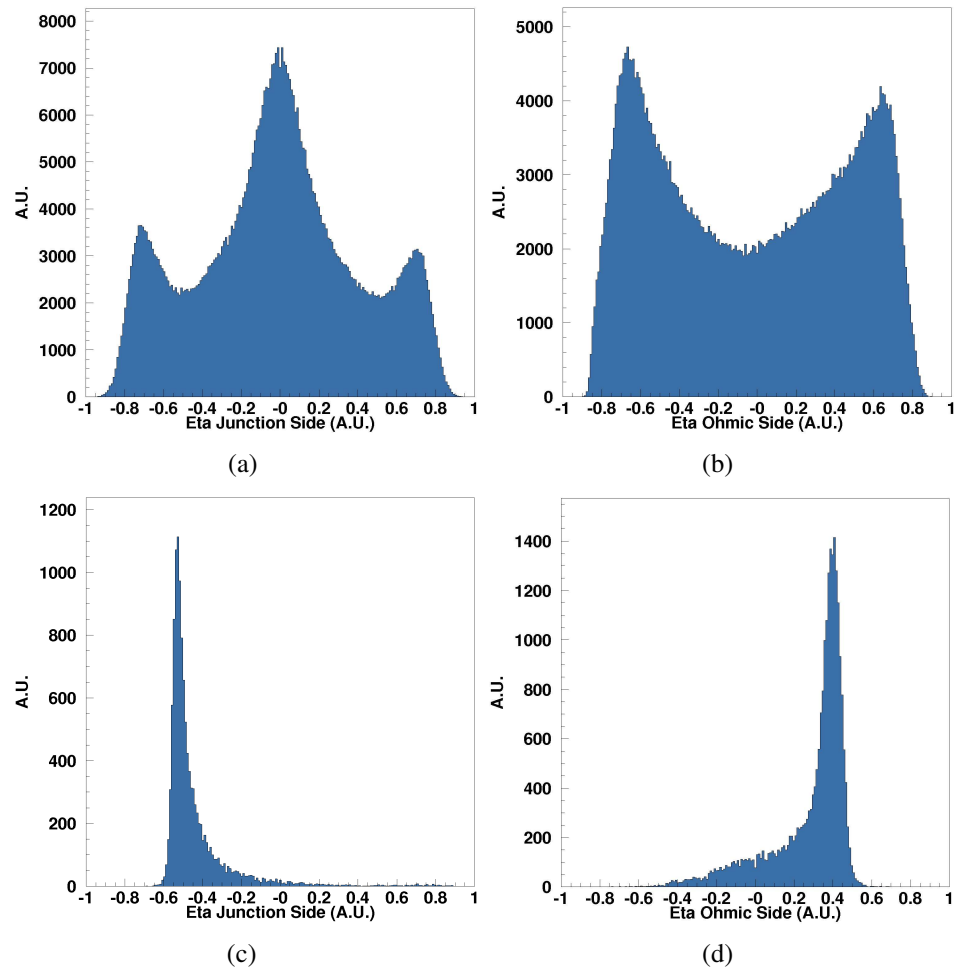


Figure A.3: The junction (a) and ohmic (b) eta distributions with a 2.5 MHz readout clock and a 5 MHz one ((c) and (d)): the symmetry of the distributions is lost when the sampling is not performed in the correct way.

beam direction) has been considered;

- the first step, the so-called *coarse alignment*, consists in acquiring scout data runs (with low statistics, ~ 2000 events) and moving the modules until each of them is inside the incoming beam acceptance: figure A.5(a) shows an example of correctly aligned modules while in figure A.5(b) the last module is slightly out of the beam (left tail) and misaligned with respect to the others;
- an additional offline detector alignment, the so-called *fine alignment*, based on the translation of the coordinate system of the module themselves (figure A.4 right) is also needed. The main steps are the following:
 - * the distribution of the difference of the particle position reconstructed by the external modules is computed for each direction:

$$\begin{aligned} x_4 - x_1 &= a \\ y_4 - y_1 &= b \end{aligned} \tag{A.5}$$

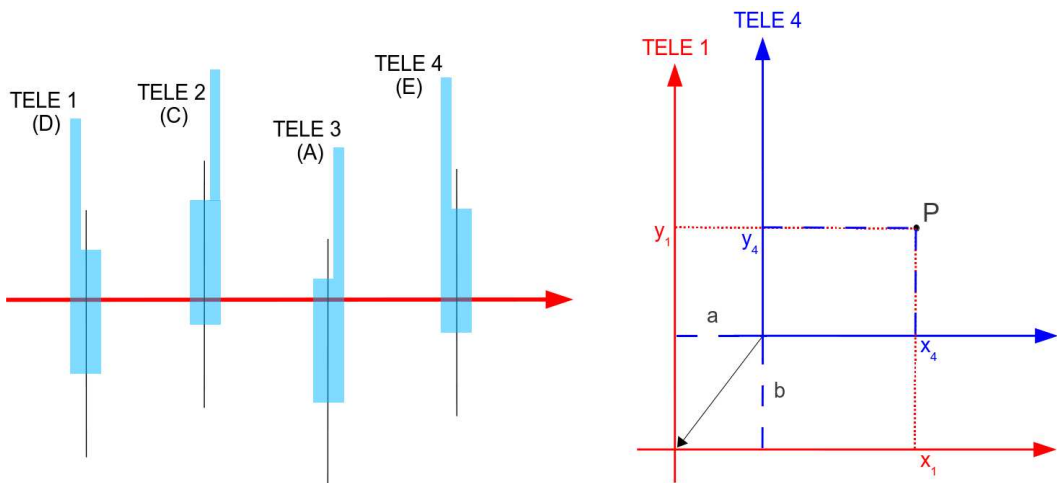


Figure A.4: The silicon detector alignment procedure is based on a translation of the coordinate system of the detectors themselves.

- * if the detectors are perfectly aligned, the distribution is centered on 0 (red histogram in figure A.5(c)); on the other hand, if the detectors are misaligned (blue histogram in figure A.5(c)) the values computed with equation A.5 are used to translate the axes of the last module to obtain the red histogram;

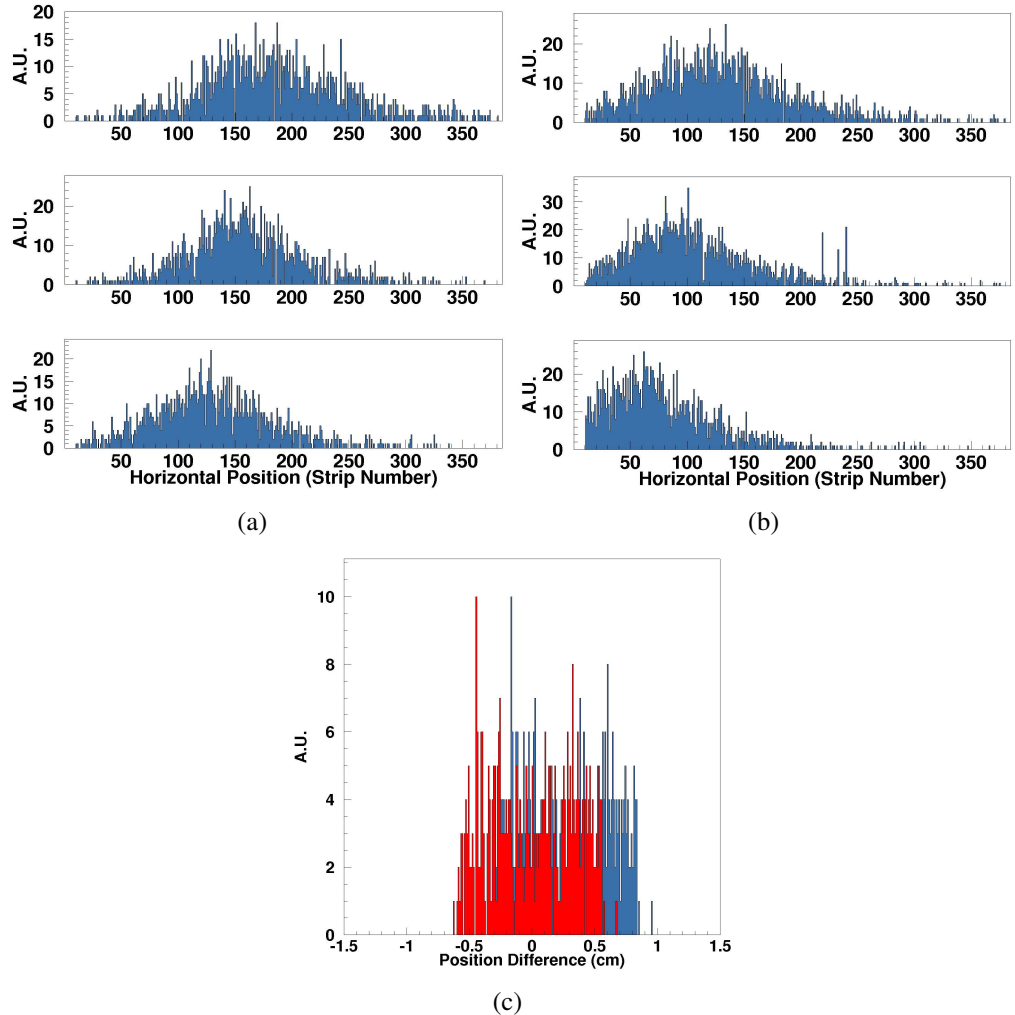


Figure A.5: The *coarse alignment* of the modules: (a) all the detectors are aligned while (b) the last module is slightly misaligned; (c) the *fine alignment*: the distributions of the difference of the particle position reconstructed by the two external modules; the one calculated after the alignment is shown in red.

- * to align the central module the residual distribution (section 4.1) is computed and fitted with a Gaussian-like function: the mean value is used to shift the residual distribution itself to 0 (with the same phylosophy applied for the external modules);
- as presented in section 4.2.2 an additional rotational tilt angle of the modules themselves could be introduced by the supports used to fix them along the beamline; moreover during the PS T9 low energy beamtest custom supports have been used to mount the VISION modules (section 5.2.5). The procedure described in sections 4.2.2 and 5.2.5, based on the study of the residual in one direction (*e.g.* the horizontal one) as a function of the position along the other coordinate (*i.e.* the vertical one), has been applied to compute the correct residual (equation 4.6).

Appendix B

The FBK-irst+VA1_prime2 UA9 modules

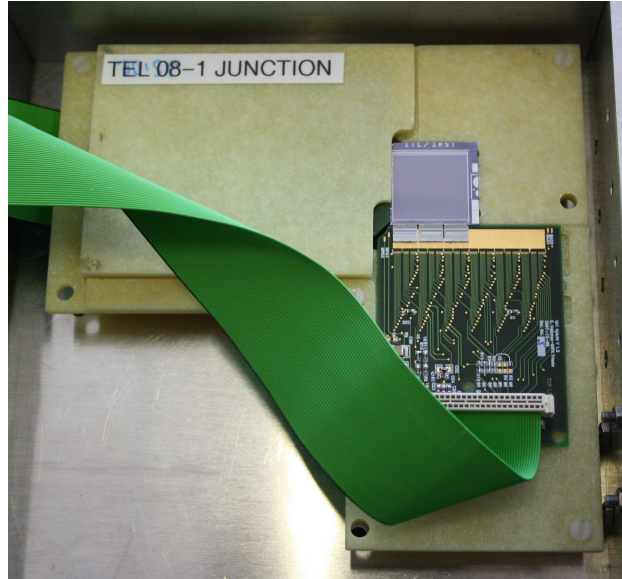
The following sections present the design and the SPS H4 high energy beamtest results of the two FBK-irst+VA1_prime2 UA9 modules. They have been designed and produced as prototypes for the UA9 experiment [121] and in parallel as a test bench for the development and test of the final electronics chain presented in section 3.2 and to study the performance of the VA1TA ASIC.

B.1 Module description

B.1.1 The silicon tiles and the mechanical assembly

Both the FBK-irst+VA1_prime2 UA9 modules (figure B.1) house the same $300\text{ }\mu\text{m}$ thick high resistivity double side silicon microstrip detector used in [121] whose technical features are summarised in table B.1. The silicon tile has a $1.92 \times 1.92\text{ cm}^2$ sensitive area for a total of 384 channels on both sides. The physical strip pitch is $25\text{ }\mu\text{m}$ on the junction side and $50\text{ }\mu\text{m}$ on the ohmic one while the readout pitch is $50\text{ }\mu\text{m}$ for both sides: a one floating strip scheme has been adopted for the junction side readout. The silicon tile is fully depleted with a bias voltage in the 36-54 V range and the average leakage current is of the order of 1.5-2.0 nA per strip.

The silicon tiles are assembled on a $13.5 \times 13.5\text{ cm}^2$ 0.5 cm thick L-shape fiberglass support while the ASICs have been glued with the Epotek H20E epoxy glue on dedicated PCBs inserted in the fiberglass frame. The detectors are AC coupled and the connection between the ASICs control and output pads is made via $17\text{ }\mu\text{m}$ diameter Al wires. The same Al boxes used with the VISION modules (section 5.1.3) have been used to handle and protect the silicon tiles and the first part of the electronics.



(a)



(b)

Figure B.1: Photo of (a) the junction and (b) the ohmic side of one FBK-irst+VA1_prime2 UA9 module assembled on the fiberglass frame together with the ASICs PCBs.

Detector	Double
Produced by	FBK-irst
ASIC	VA1_prime2
Detector dimensions [cm ²]	1.92×1.92
Number of readout channels	384
Bulk thickness [μm]	300
Resistivity [k $\Omega\cdot\text{cm}$]	> 4
Leakage current [nA/strip]	1.5-2.0
Full depletion bias voltage [V]	36-54
AC coupling	yes
p-side - <i>junction</i>	
physical pitch [μm]	25
readout pitch [μm]	50
floating scheme	yes
n-side - <i>ohmic</i>	
physical pitch [μm]	50
readout pitch [μm]	50
floating scheme	no
Fiberglass support	
shape	L-shape
dimensions [cm ²]	13.5×13.5
thickness [cm]	0.5
ASIC connection	direct bonding

Table B.1: General features of the FBK-irst+VA1_prime2 UA9 modules.

B.1.2 The readout ASIC and electronics

Three VA1_prime2 ASICs [93] per side have been used to readout the whole detector. This ASIC, whose technical features are listed in table B.2, is a 128 channel radiation tolerant integrated circuit build with the $0.35\text{ }\mu\text{m}$ N-well CMOS technology. It has the same architecture of the VA2 ASIC for the analog output signal conditioning (section 3.1.2) and has been developed and optimized to work with larger overall capacitance C_d (the one *seen* by the ASIC inputs). The ENC noise term which depends on the input capacitance is in fact the half with respect to the VA2 one (tables 3.2 and B.2): assuming a $\sim 10\text{ pF}$ value for the overall capacitance of the silicon tiles typically used in this thesis work, one obtains $80 + 15 \cdot C_d = 230$ and $180 + 7.5 \cdot C_d = 255$ for the VA2 and the VA1_prime ASIC, respectively.

ASIC name	VA1_prime2
Process (N-well CMOS)	$0.35\text{ }\mu\text{m}$
Die surface [mm^2]	4.95×6.12
Die thickness [μm]	~ 725
Number of channels	128
Input pad size [μm^2]	50×90
Output pad size [μm^2]	90×90
ENC at $1\text{ }\mu\text{s}$ of peaking time [e^- rms]	$180 + 7.5 \cdot C_d$
Power consumption [mW]	235
Slow shaper peaking time [μs]	0.3-1
Fast shaper peaking time [μs]	not present
Dynamic range [# MIPs]	± 10
Current gain [$\mu\text{A/fC}$]	~ 10

Table B.2: Technical features of the VA1_prime2 ASIC [93].

As far as the readout chain is concerned, the same version of both the frontend and readout electronics used with the CSEM+VA2 reference modules (section 3.2) has been used.

B.2 The SPS H4 beamtest results

The FBK-irst+VA1_prime2 UA9 modules have been tested during the SPS H4 high energy beamtest; the same setup described in section 3.3 has been used and both the modules have been characterized by means of two CSEM+VA2 reference modules in terms of Signal to Noise Ratio, charge sharing among the strips and

spatial resolution (section B.2.1). The same analysis procedures described in sections 3.4.2, 3.5 and 4.3 to study, respectively, the SNR, the charge sharing and the spatial resolution have been adopted.

B.2.1 The modules behavior

Figure B.2(a) presents the Signal to Noise Ratio of one FBK-irst+VA1_prime2 UA9 module; equation 3.2 has been used to compute the SNR and the distribution has been fitted with a Landau-like function (equation 3.3). The values obtained for both the FBK-irst+VA1_prime2 UA9 modules are listed in the second column of table B.3: a slightly larger value has been found for the *TELE 08-1* junction side and in both cases, as expected given the different used ASICs and silicon tiles, the SNR is smaller than the one of the CSEM+VA2 reference modules (table 3.5).

Module (TELE)	SNR	Charge Sharing (η) [%]	σ_{meas} (COG) [μm]	σ_{meas} (η) [μm]
08-1 jun. ohm.	47.48 ± 0.02	85.68	-	-
08-2 jun. ohm.	39.99 ± 0.01	81.29	5.81 ± 0.01	4.43 ± 0.01

Table B.3: Comparison of the cluster SNR, the charge sharing and the spatial resolution values of the FBK-irst+VA1_prime2 UA9 modules.

The charge sharing distribution of one FBK-irst+VA1_prime2 UA9 module is presented in figure B.2(b). The interstrip position has been computed with the eta algorithm (section 4.3); $0 \mu\text{m}$ and $50 \mu\text{m}$ are the center of the two readout strips while $25 \mu\text{m}$ is the center of the floating one. Equation 3.4 has been used to find the charge sharing value (third column of table B.3): in both cases when the particle crosses the center of the floating strip, each of the two neighbouring readout strips collects $\sim 42\%$ of the total charge deposited by the particle. The charge sharing among the strips is thus slightly larger than the one of the CSEM+VA2 reference modules; it has been ascribed to a different width of the strip implant.

Figure B.2(c) shows the residual distribution of the junction side of one FBK-irst+VA1_prime2 UA9 module; also in this case the residual method presented in section 4.1 has been applied. The spatial resolution (table B.3) decreases from $5.81 \pm 0.01 \mu\text{m}$ using the standard COG method to $4.43 \pm 0.01 \mu\text{m}$ applying the eta algorithm; as in the CSEM+VA2 reference module case the improvement in

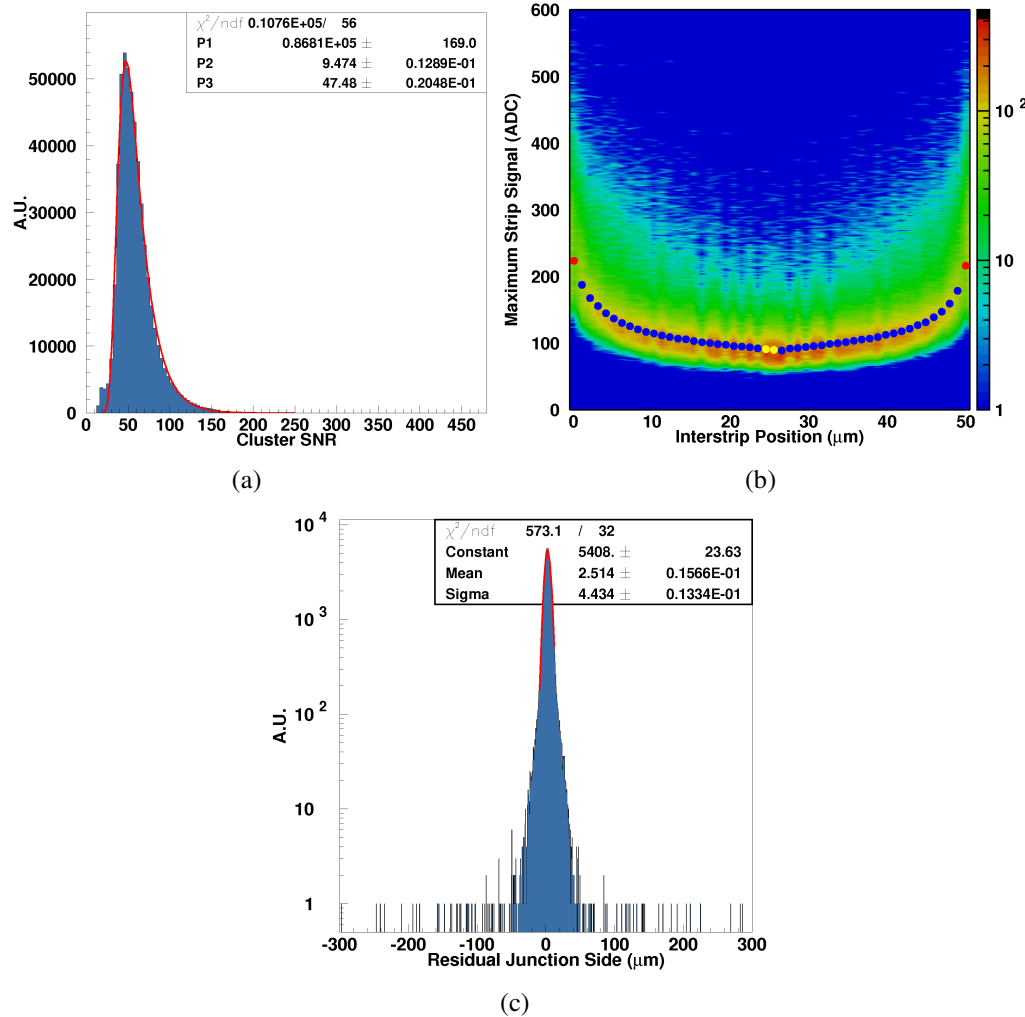


Figure B.2: (a) The cluster SNR, (b) the charge sharing and (c) the residuals distributions of the junction side of one FBK-irst+VA1_prime2 UA9 module; the interstrip position and the residuals have been computed applying the eta algorithm (section 4.3).

the spatial resolution is not so critical ($\sim 1.38 \mu\text{m}$ *i.e.* $\sim 24\%$ less) but the non Gaussian-like lateral tails in the residual distribution are much smaller.

List of acronyms

ACH	Axial CHanneling (regime)
ADC	Analog to Digital Converter
AFT	Automatic Fine Tuning
AGILE	Astro-rivelatore Gamma a Immagini LEggero
ALICE	A Large Ion Collider Experiment
AMO	AMOrphous (regime)
APV25	Analogue Pipeline Voltage (mode) 25
ASCII	American Standard Code for Information Interchange
ASIC	Application Specific Integrated Circuit
ATLAS	A Toroidal LHC ApparatuS
BaBar	B/B-bar system of mesons produced at SLAC PEP-II collider
BM	Bending Magnet
BNL	Brookhaven National Laboratory (USA)
BPDA	biphenyl tetracarboxylic dianhydride
BTF	Beam Test Facility
CAEN	Costruzioni Apparecchiature Elettroniche Nucleari
CCD	Charge Coupled Device
CERN	Conseil Europeen pour la Recherche Nucleaire - European Organization for Nuclear Research (Swiss)
CH	CHanneling (regime)
CHANNEL	CHanneling of NEgative Leptons
CM	Common Mode (noise)
CMOS	Complementary Metal Oxide Semiconductor
CMS	Compact Muon Solenoid
COHERENT	COHERENT effects in crystals for the physics of accelerators
COG	Center Of Gravity
CS	Charge Sharing
CSA	Charge Sensitive Amplifier

CSEM	Centre Suisse d'Electronique et Microtechnique (Swiss)
CSNV	Commissione Scientifica Nazionale V
CU	Crystalline Undulator
CW	Continuous Wave
DAC	Digital to Analog Converter
DAQ	Data AcQuisition
DC	Drift Chamber
DCH	DeCHanneling (regime)
DELPHI	DEtector with Lepton, Photon and Hadron Identification
DIN	Deutsches Institut fr Normung - German Institute for Standardization
DST	Data Summary Tape
DYNECHARM++	DYNamic ECHARM++
ECHARM	Electrical CHARacteristics of Monocrystals
EMR	Electron Muon Ranger
ENC	Equivalent Noise Charge
ERNI	ERNI Electronics Inc. (USA)
FACTOR	Fiber Apparatus for Calorimetry and Tracking with Optoelectronic Read-out
FBK-irst	Fondazione Bruno Kessler (Italy)
FNAL	Fermi National Accelerator Laboratory (USA)
FORTRAN	FORmula TRANslator
FPGA	Field Programmable Gate Array
FWHM	Full Width Half Maximum
FTDI	Future Technology Devices International Ltd (UK)
GAMMA-400	Gamma Astronomical Multifunctional Modular Apparatus
GeB	Germanium Bent (crystal)
GeV	Germanium Flat (crystal)
GOH	GOL Opto-Hybrid
GOL	Gigabit Optical Link
GPIB	General Purpose Interface Bus
HAMAMATSU	HAMAMATSU Photonics (Japan)
HDSM	Harmonic Double Sided Microtron
HEP	High Energy Physics
IC	Integrated Circuit
ICE-RAD	Interaction in Crystals for Emission of RADiation

IDEAS	Integrated Detector & Electronics AS (Norway)
IHEP	Institute for High Energy Physics (Russia)
IKPh	Institut für Kernphysik - University of Mainz (Germany)
ILC	International Linear Collider
INFN	Istituto Nazionale di Fisica Nucleare
INFN-Fe	INFN Sezione di Ferrara
INFN-Ts	INFN Sezione di Trieste
INSULAB	INSUBria LABoratory Research Group
I/O	Input/Output
IUPAC	International Union of Pure and Applied Chemistry
 JINR	Joint Institute for Nuclear Research (Russia)
 KEK	Kō Enerugi Kasokuki Kenkyū Kikō - High Energy Accelerator Research Organization (Japan)
 LAL	Laboratoire de L'Acelerateur Lineaire
LEMO	LEon MOuttet Inc. (USA)
LHC	Large Hadron Collider
LHCb	Large Hadron Collider beauty
LINAC	LINear ACcelerator
LINP	Leningrad Institue of Nuclear Physics (Russia)
LNF	Laboratori Nazionali di Frascati (Italy)
LNL	Laboratori Nazionali di Legnaro (Italy)
LSI	Large Scale Integration
LYSO	Lutetium Yttrium Orthosilicate
LVDS	Low Voltage Differential Signaling
LvL1T	LeveL 1 Trigger
 MAMI	MAinzer MIkrotron
MAROC	Multi-Anode ReadOut Chip
MAV	Mean Average Value
MCA	MultiChannel Analyzer
MCS	Multiple Coulomb Scattering
MOS	Metal Oxide Semiconductor
MICE	Muon Ionization Cooling Experiment
MIP	Minimun Ionizing Particle
MPV	Most Probable Value
MSE	Multiple Coulomb Scattering on Electrons
MSN	Multiple Coulomb Scattering on Nuclei
MVD	Micro Vertex Detector (in CMS)

MVR	Multi Volume Reflection (in a sequence of crystals)
MVROC	Multi Volume Reflection in One Crystal
NTA-HCCC	INFN experiment dedicated to the crystal physics
NI	National Instruments S.r.l. (Italy)
NIM	Nuclear Instrumentation Module
NE	Nuclear Emulsion
OS	O-Shaped (crystal)
PAW	Physics Analysis Workstation
PbWO₄	lead tungstate
PC	Personal Computer
PCB	Printed Circuit Board
PD	PhotoDiode
PEP-II	Positron Electron Project-II (SLAC B Factory)
PH	Pulse Height
PI	Physik Instrumente (Germany)
PICH	Particle Identification with CHanneling radiation
PID	Particle IDentification
PIXE	Particle Induced X-ray Emission
PLANSEE	PLANSEE SE Group (Austria)
PLL	Phase Locked Loop
PMT	PhotoMultiplier Tube
PNPI	Petersburg Nuclear Physics Institute (Russia)
PS	Proton Synchrotron
QM	QuasiMosaic (crystal)
R&D	Research & Development
RAM	Random Access Memory
RF	Radio Frequency
rms	Root Mean Square
RTM	RaceTrack Microtron
RWTH	Rheinisch-Westflische Technische Hochschule (Germany)
S&H	Sample & Hold
SALT	Silicon ASIC for LHCb Tracker
SBS	SBS Technologies Inc. (now GE Intelligent Platforms, USA)
SC	Slow Control
SCT	Semiconductor Tracker (in ATLAS)

SERDES	SERializer-DESerializer
SiB	Silicon Bent (crystal)
SiBC	Silicon Beam Chamber
SiD	Silicon Detector
SiF	Silicon Flat (crystal)
SiM	Silicon Membrane (crystal)
SiPM	Silicon PhotoMultiplier
SLAC	Stanford Linear Accelerator Center (USA)
SNR	Signal to Noise Ratio
SPECTECH	SPECtrum TECHniques (USA)
SPS	Super Proton Synchrotron
SSD	Silicon Strip Detector (in ALICE)
SST	Silicon Strip Tracker (in CMS)
ST	STrip-like (crystal)
SVT	Silicon Vertex Tracker (in BaBar)
TAL	Target Aperture Limitation
Tcl/Tk	Tool Command Language/Toolkit
TI	Texas Instruments Inc. (USA)
TRD	Transition Radiation Detector
TTI	TTI Global Distribution (USA)
TTL	Transistor-Transistor Logic
TWICE	Techniques for Wide-range Instrumentation in Calorimetry Experiments
UA9	Underground Area 9
USB	Universal Serial Bus
USB2	Universal Serial Bus 2
UT	Upstream Tracker (in LHCb)
VC	Volume Capture (regime)
VELO	VErtex LOcator (in LHCb)
VISION	Versatile and Innovative SilicON tracking system
VLSI	Very Large Scale Integration
VME	Versa Module Eurocard
VR	Volume Reflection (regime)
VRB	VME Readout Board

List of Figures

1.1	Stark's idea.	6
1.2	Bent crystals working principle.	8
1.3	Scheme of the particle motion in a bent crystal.	12
1.4	Potential wells and trajectories for positive and negative particles inside a crystal.	14
1.5	Scheme of the interplanar potential.	16
1.6	Effective potential for different crystal curvature radii.	18
1.7	Scheme of the DeCHanneling process in a bent crystal.	19
1.8	Scheme of the Volume Capture process in a bent crystal.	20
1.9	Scheme of the Volume Reflection process in a bent crystal.	21
1.10	Volume Reflection angle and rms versus the crystal curvature radius.	23
1.11	Volume Reflection inefficiency versus the crystal curvature radius.	23
1.12	Scheme and photo of the Multi Volume Reflection in a series of bent crystals.	24
1.13	Schemes of the bent crystal advanced effects.	26
1.14	Schemes of the crystal-based beam splitting and focusing.	28
1.15	Schemes of the crystal-based extraction/collimation systems. . . .	30
1.16	Schemes and photos of the new generation bent crystals.	34
1.17	Trajectories of channeled and volume reflected particles in a bent crystal.	35
1.18	Crystalline e^+ source used at KEKB compared with a standard one.	36
1.19	Experimental results of the PICH program.	37
1.20	Crystalline Undulator working principle.	37
1.21	Profile of the IHEP proton beam measured with a nuclear emulsion.	39
1.22	Schemes of two setups for crystal channeling experiments.	41
2.1	Scheme of the energy bands structure.	44
2.2	Impurities and Fermi levels in a doped semiconductor.	47
2.3	Scheme of a p-n junction.	48
2.4	Scheme and photo of an AC coupled double side silicon microstrip detector.	52

2.5	Cross section of an AC coupled microstrip detector.	53
2.6	Simulated n-side isolation configurations.	55
2.7	Scheme of the floating strip readout method.	56
2.8	Capacitive connections and the capacitance as a function of the bias voltage in a microstrip silicon detector.	58
2.9	Bias voltage as a function of the bulk material resistivity.	59
2.10	Radiation damage in standard silicon detector.	60
2.11	Scheme of the drift and diffusion processes.	61
2.12	Pion energy loss in silicon.	62
2.13	Scheme of a cluster composed of one or two strips.	63
2.14	Schemes of the detector frontend and its equivalent circuit.	65
2.15	ENC as a function of the amplifier shaping time.	67
2.16	Eta distributions of a double side silicon microstrip detector.	68
2.17	Different regions close to a couple of readout strips.	69
2.18	η distribution for a detector with a different number floating strips.	70
2.19	Main components of a silicon microstrip detector electronics chain.	71
2.20	Scheme of the APV25 ASIC.	73
3.1	Photo of a CSEM+VA2 reference module.	78
3.2	The VA2 ASIC.	78
3.3	The VA2 analog outputs.	81
3.4	Details of the CSEM+VA2 reference module assembly.	83
3.5	Schematic view of the complete electronics chain.	84
3.6	Photos of the frontend electronics.	86
3.7	DAQ user interface.	87
3.8	Photos of the readout electronics.	89
3.9	Scheme and photos of the SPS H4 setup.	93
3.10	Photo of the <i>TELE 3-A</i> damaged bondings.	94
3.11	Pedestal and noise distributions of a CSEM+VA2 reference module.	95
3.12	Maximum pull distributions of a CSEM+VA2 reference module.	96
3.13	Number of clusters and of strips per cluster of a CSEM+VA2 reference module.	97
3.14	SPS H4 beam profile and divergence measured by a CSEM+VA2 reference module.	98
3.15	Cluster pulse height and noise of a CSEM+VA2 reference module.	100
3.16	Cluster SNR of a CSEM+VA2 reference module.	101
3.17	Correlation between the junction and ohmic cluster SNR of two CSEM+VA2 reference modules.	103
3.18	Maximum and lateral strip pull of a CSEM+VA2 reference module.	104
3.19	Charge sharing of a CSEM+VA2 reference module with the position computed with the COG method.	105

3.20 Charge sharing of a CSEM+VA2 reference module with the position computed with the eta algorithm.	108
4.1 Scheme of the residual method principle.	111
4.2 Elements used for the intrinsic resolution calculation.	112
4.3 Residual distributions of a CSEM+VA2 reference module measured at the SPS H4 line.	115
4.4 Residual distributions of a CSEM+VA2 reference module measured at the PS T9 line.	116
4.5 Residual distributions of a CSEM+VA2 reference module as a function of the position.	116
4.6 Residual distributions of a CSEM+VA2 reference module after the tilt angle correction.	117
4.7 Energy scans for the MCS contribution study.	119
4.8 Signal deposited in 2 silicon strips in case of a uniform and a Gaussian-like charge distribution.	120
4.9 Eta distributions of the <i>TELE</i> 2-C CSEM+VA2 reference module. .	121
4.10 Interstrip position of the <i>TELE</i> 2-C CSEM+VA2 reference module. .	122
4.11 Eta algorithm cluster elements.	123
4.12 Residual distribution of the <i>TELE</i> 2-C junction side after the eta correction and the residual as a function of the corrected interstrip position.	124
4.13 Residual distribution of the <i>TELE</i> 2-C junction side after the eta and slope correction as a function of the interstrip position. . . .	125
4.14 Ultimate spatial resolution of the <i>TELE</i> 2-C CSEM+VA2 reference module after the eta and slope correction.	127
5.1 Photos of the VISION modules.	132
5.2 The VA1TA working principle and architecture.	134
5.3 The VA1TA serial shift register.	135
5.4 Scheme and photo of the Slow Control system.	138
5.5 Scheme and photos of the ^{90}Sr source test setup.	140
5.6 Pedestal and noise distributions of the VISION modules.	141
5.7 Hold scan principle and scans performed with a HAMAMATSU module during the ^{90}Sr source tests.	143
5.8 Cluster SNR of the VISION modules.	145
5.9 Residual distributions of the VISION modules measured at the PS T9 line.	146
5.10 Photo of the mechanical supports used at the PS T9 line.	147
5.11 Residual distributions of the VISION modules after the tilt angle correction.	148

5.12	Eta and charge sharing of a VISION module.	149
5.13	MAMI floor plan and photos.	152
5.14	Scheme of the MAMI setup.	153
5.15	Photos of the crystals used at MAMI.	155
5.16	Photos of the MAMI setup.	156
5.17	Pedestal and noise distributions of a HAMAMATSU module measured at MAMI.	159
5.18	Hold scans of a HAMAMATSU module measured at MAMI.	160
5.19	Threshold scan principle and scan performed with the HAMAMATSU module at MAMI.	161
5.20	Pull and DAQ rate measured at MAMI with different DAC thresholds.	162
5.21	SNR of the HAMAMATSU module at MAMI.	163
5.22	Beam profile and number of strips per cluster measured at MAMI.	164
5.23	Results of the SiB crystal tested at MAMI.	165
5.24	Scheme of the new data transmission.	167
5.25	Photos of the TLK/GOH data transmission system.	169
5.26	Photos of the USB2 data transmission system.	170
A.1	Noise distributions of a CSEM+VA2 reference module.	182
A.2	Lateral pull distributions of a CSEM+VA2 reference module.	184
A.3	Eta distributions with different readout clocks of a CSEM+VA2 reference module.	185
A.4	Scheme of the module alignment procedure.	186
A.5	Module alignment example.	187
B.1	Photo of a FBK-irst+VA1_prime2 UA9 module.	190
B.2	Cluster SNR, charge sharing and residuals of a FBK-irst+VA1_prime2 UA9 module.	194

List of Tables

1.1	Crystal channel parameters for Si, Ge and W.	13
1.2	Extraction/collimation experiments in the last 30 years.	31
1.3	Comparison of the track reconstruction systems used in crystals physics.	40
2.1	General features of Si, Ge, GaAs and diamond.	45
2.2	Intrinsic spatial resolution for different physical pitch values. . . .	64
3.1	General features of the CSEM+VA2 reference modules.	79
3.2	VA2 ASIC technical features.	80
3.3	CERN SPS H4 and PS T9 beamlines technical parameters.	91
3.4	Pedestal, noise and unused channels of the CSEM+VA2 reference modules.	95
3.5	Cluster pulse height, noise and SNR of the CSEM+VA2 reference modules.	100
3.6	Charge sharing of the CSEM+VA2 reference modules.	106
4.1	Spatial resolution of a CSEM+VA2 reference module measured at the SPS H4 line.	113
4.2	Spatial resolution of a CSEM+VA2 reference module measured at the PS T9 line.	118
4.3	Ultimate spatial resolution of a CSEM+VA2 reference module junction side.	126
5.1	General features of the VISION modules.	131
5.2	VA1TA ASIC technical features.	133
5.3	Pedestal, noise and unused channels of the VISION modules. . . .	142
5.4	Cluster pulse height, noise and SNR of the VISION modules. . . .	144
5.5	Spatial resolution of the VISION modules.	146
5.6	Charge sharing of the VISION modules.	150
5.7	Technical parameters of the MAMI accelerator.	151
5.8	Characteristics of the crystals used at MAMI.	157

5.9	Comparison of the new data transmission systems.	171
6.1	SNR, σ_{int} and CS of the INSULAB and VISION modules.	175
B.1	General features of the FBK-irst+VA1_prime2 UA9 modules.	191
B.2	VA1_prime2 ASIC technical features.	192
B.3	Cluster SNR, charge sharing and spatial resolution of the FBK- irst+VA1_prime2 UA9 modules.	193

Bibliography

- [1] S. Hasan. “*Experimental Techniques for Deflection and Radiation Studies with Bent Crystals*”. PhD thesis. Università degli Studi dell’Insubria, 2011.
- [2] V. M. Biryukov *et al.* *Crystal Channeling and its Application at High-Energy Accelerators*. Ed. by Springer. 1996. ISBN: 978-3-540-60769-2.
- [3] P. Forman. “*Discovery of the Diffraction of X-Rays by Crystals; A Critique of the Myths*”. In: Archive for History of Exact Sciences 6 (1969), p. 38.
- [4] J. Stark. “*Bemerkung fiber Zerstreuung und Absorption von Strahlen und Röntgenstrahlen in Kristallen*”. In: Physic Zeitschrift 13 (1912), p. 973.
- [5] G. R. Piercy *et al.* “*Experimental Evidence for the Increase of Heavy Ion Ranges by Channeling in Crystalline Structure*”. In: Physical Review Letters 10 (1963), p. 399.
- [6] M. T. Robinson *et al.* “*Computer Studies of the Slowing Down of Energetic Atoms in Crystals*”. In: Physical Review 132 (1963), p. 2385.
- [7] J. Lindhard. “*Motion of swift charged particles, as influenced by strings of atoms in crystals*”. In: Physics Letters 12 (1964), p. 126.
- [8] J. Lindhard. “*Influence of Crystal Lattice on Motion of Energetic Charged Particles*”. In: Det Kongelige Danske Videnskabernes Selskab 34 (1965), p. 1.
- [9] E. N. Tsyganov. “*Some Aspects of the Mechanism of a Charge Particle Penetration Through a Monocrystal*”. In: Fermilab Reports TM-682 (1976), p. 1.
- [10] A. F. Elishev. “*Steering of Charged Particle Trajectories by a Bent Crystal*”. In: Physics Letters 88 B (1979), p. 387.
- [11] A. M. Taratin *et al.* ““*Volume Reflection*” of High-Energy Charged Particles in Quasi-Channeling States in Bent Crystals”. In: Physics Letters A 119 (1987), p. 425.

- [12] Y. M. Ivanov *et al.* “*Volume Reflection of a Proton Beam in a Bent Crystal*”. In: Physical Review Letters 97 (2006), p. 144801.
- [13] W. Scandale *et al.* “*High-Efficiency Volume Reflection of an Ultrarelativistic Proton Beam with a Bent Silicon Crystal*”. In: Physical Review Letters 98 (2007), p. 154081.
- [14] B. Ferretti. “*Sulla “Bremsstrahlung” nei cristalli*”. In: Il Nuovo Cimento 7 (1950), p. 118.
- [15] M. L. Ter Mikaelian. “*Scatter of high energy electrons in crystals*”. In: Journal of Experimental and Theoretical Physics 25 (1953), p. 289.
- [16] F. H. Dyson *et al.* “*Anisotropy of Bremsstrahlung and Pair Production in Single Crystals*”. In: Physical Review 99 (1955), p. 604.
- [17] G. Diambrini Palazzi. “*High-Energy Bremsstrahlung and Electron Pair Production in Thin Crystals*”. In: Reviews of Modern Physics 40 (1968), p. 611.
- [18] V. G. Baryshevsky *et al.* “*Generation of γ -quanta by channeled particles in the presence of a variable external field*”. In: Physical Review Letters A 77 (1980), p. 61.
- [19] W. Scandale *et al.* “*Experimental study of the radiation emitted by 180-GeV/c electrons and positrons volume-reflected in a bent crystal*”. In: Physical Review A 79 (2009), p. 012903.
- [20] D. Lietti *et al.* “*Radiation emission phenomena in bent silicon crystals: Theoretical and experimental studies with 120 GeV positrons*”. In: Nuclear Instruments and Methods in Physics Research B 283 (2012), p. 84.
- [21] L. Bandiera *et al.* “*On the radiation accompanying volume reflection*”. In: Nuclear Instruments and Methods in Physics Research B 309 (2013), p. 135.
- [22] L. Bandiera *et al.* “*Broad and Intense Radiation Accompanying Multiple Volume Reflection of Ultrarelativistic Electrons in a Bent Crystal*”. In: Physical Review Letters 111 (2013), p. 255502.
- [23] L. Bandiera *et al.* “*Single and Multiple Volume Reflections of Ultra-Relativistic Electrons in a Bent Crystal as Tools for Intense Production of Electromagnetic Radiation*”. In: Journal of Physics: Conference Series 517 (2014), p. 012043.
- [24] L. Bandiera *et al.* “*Investigation on the electromagnetic radiation emitted by sub-GeV electrons in a bent crystal*”. submitted to Physical Review Letters. 2015.

- [25] W. Scandale *et al.* “Apparatus to study crystal channeling and volume reflection phenomena at the SPS H8 beamline”. In: Review of Scientific Instruments 79 (2008), p. 023303.
- [26] E. Bagli. “Innovative Approaches for Monte Carlo Simulations of Orientational Effects in Crystals and their Experimental Verification”. PhD thesis. Università degli Studi di Ferrara, 2014.
- [27] D. Lietti *et al.* “A microstrip silicon telescope for high performance particle tracking”. In: Nuclear Instruments and Methods in Physics Research A 729 (2013), p. 527.
- [28] S. Hasan. “Bent Silicon Crystals for the LHC Collimation: Studies with an Ultrarelativistic Proton Beam”. MA thesis. Università degli Studi dell’Insibria, 2007.
- [29] V. M. Biryukov *et al.* “Crystal collimation as an option for the large hadron colliders”. In: Nuclear Instruments and Methods in Physics Research B 234 (2005), p. 23.
- [30] V. Guidi *et al.* “Shaping of silicon crystals for channeling experiments through anisotropic chemical etching”. In: Journal of Physics D Applied Physics 41 (2008), p. 245501.
- [31] Y. M. Ivanov *et al.* “Observation of the Elastic Quasi-Mosaicity Effect in Bent Silicon Single Crystals”. In: Letters to Journal of Experimental and Theoretical Physics 81 (2005), p. 99.
- [32] S. Hasan *et al.* “Volume reflection observations in bent crystals with 13 GeV particles”. In: Nuclear Instruments and Methods in Physics Research B 269 (2011), p. 612.
- [33] A. M. Taratin *et al.* “Volume reflection of high-energy protons in short bent crystals”. In: Nuclear Instruments and Methods in Physics Research B 262 (2007), p. 340.
- [34] E. Bagli *et al.* “Calculation of the potential for interaction of particles with complex atomic structures”. In: Physical Review E 81 (2010), p. 026708.
- [35] W. Scandale *et al.* “Measurement of the dechanneling length for high-energy negative pions”. In: Physics Letters B 719 (2013), p. 70.
- [36] E. Bagli *et al.* “DYNECHARM++: a toolkit to simulate coherent interactions of high-energy charged particles in complex structures”. In: Nuclear Instruments and Methods in Physics Research B 309 (2013), p. 124.
- [37] J. Beringer *et al.* (PDG Collaboration). “Review of Particle Physics”. In: Physical Review D 86 (2012), p. 010001.

- [38] W. R. Leo. *Techniques for Nuclear and Particle Physics Experiments: A How-To Approach*. Ed. by Springer. 1994. ISBN: 0-387-57280-5.
- [39] Yu. A. Chesnokov *et al.* “*70 GeV proton volume capture into channeling mode with a bent Si single crystal*”. In: Nuclear Instruments and Methods in Physics Research B 69 (1992), p. 247.
- [40] W. Scandale *et al.* “*Volume Reflection Dependence of 400 GeV/c Protons on the Bent Crystal Curvature*”. In: Physical Review Letters 101 (2008), p. 234801.
- [41] W. Scandale *et al.* “*Double volume reflection of a proton beam by a sequence of two bent crystals*”. In: Physics Letters B 658 (2008), p. 109.
- [42] W. Scandale *et al.* “*High-Efficiency Deflection of High-Energy Protons through Axial Channeling in a Bent Crystal*”. In: Physical Review Letters 101 (2008), p. 164801.
- [43] V. Tikhomirov *et al.* “*Multiple Volume Reflection from Different Planes Inside One Bent Crystal*”. In: Physics Letters B 655 (2007), p. 217.
- [44] W. Scandale *et al.* “*First observation of multiple volume reflection by different planes in one bent silicon crystal for high-energy protons*”. In: Physics Letters B 682 (2009), p. 274.
- [45] A. G. Afonin *et al.* “*High-Efficiency Beam Extraction and Collimation Using Channeling in Very Short Bent Crystals*”. In: Physical Review Letters 87 (2001), p. 094802.
- [46] A. G. Afonin *et al.* “*The schemes of proton extraction from IHEP accelerator using bent crystals*”. In: Nuclear Instruments and Methods in Physics Research B 234 (2005), p. 14.
- [47] V. A. Andreev *et al.* “*Spatial focusing of 1-GeV protons by a curved single crystal*”. In: Pis’ma v Zhurnal Eksperimental’noi i Teoreticheskoi Fiziki 41 (1985), p. 408.
- [48] V. M. Biryukov. “*Crystal Channeling in Accelerators*”. Proceedings of the 10th European Particle Accelerator Conference, Edinburgh (Scotland) 2006.
- [49] V. V. Avdeichikov *et al.* “*Accelerated Beam Extraction by Means of a Bent Single Crystal at the JINR Synchrophasotron*”. In: Fermilab Note 429 (1984), p. 1.
- [50] S. I. Baker *et al.* “*First operation with a crystal septum to replace a magnet in a charged particle beam*”. In: Nuclear Instruments and Methods in Physics Research A 234 (1985), p. 602.

- [51] R. A. Carrigan *et al.* “*First observation of luminosity-driven extraction using channeling with a bent crystal*”. In: Physical Review Special Topics - Accelerators and Beams 1 (1998), p. 022801.
- [52] V. Zvoda *et al.* “*Advanced Bent Crystal Collimation Studies at the Tevatron (T-980)*”. In: Fermilab Conf 11-127-APC (2011), p. 1.
- [53] A. A. Asseev *et al.* “*Extraction of 50 GeV protons from the IHEP accelerator by the bent crystal*”. In: Nuclear Instruments and Methods in Physics Research A 334 (1993), p. 283.
- [54] G. Arduini *et al.* “*Deflection and Extraction of Pb Ions up to 33 TeV/c by a Bent Silicon Crystal*”. In: Physical Review Letters 79 (1997), p. 4182.
- [55] G. Arduini *et al.* “*On the energy dependence of proton beam extraction with a bent crystal*”. In: Physics Letters B 422 (1998), p. 325.
- [56] A. Baurichter *et al.* “*Channeling of high-energy particles in bent crystals - Experiments at the CERN SPS*”. In: Nuclear Instruments and Methods in Physics Research B 164-165 (2000), p. 27.
- [57] W. Scandale *et al.* “*First results on the SPS beam collimation with bent crystals*”. In: Physics Letters B 692 (2010), p. 78.
- [58] W. Scandale *et al.* “*Comparative results on collimation of the SPS beam of protons and Pb ions with bent crystals*”. In: Physics Letters B 703 (2011), p. 547.
- [59] R. P. Fliller III *et al.* “*Results of bent crystal channeling and collimation at the Relativistic Heavy Ion Collider*”. In: Physical Review Special Topics - Accelerators and Beams 9 (2006), p. 013501.
- [60] A. Mazzolari *et al.* “*Steering of a Sub-GeV Electron Beam through Planar Channeling Enhanced by Rechanneling*”. In: Physical Review Letters 112 (2014), p. 135503.
- [61] A. Baurichter *et al.* “*New results from the CERN-SPS beam deflection experiments with bent crystals*”. In: Nuclear Instruments and Methods in Physics Research B 119 (1996), p. 172.
- [62] V. N. Baier *et al.* *Electromagnetic Processes at High Energies in Oriented single Crystals*. Ed. by World Scientific Publishing Co. Pte. Ltd. 1998. ISBN: 978-981-02-1603-3.
- [63] T. Suwada *et al.* “*First application of a tungsten single-crystal positron source at the KEK B factory*”. In: Physical Review Special Topics - Accelerators and Beams 10 (2007), p. 073501.

- [64] C. Favuzzi *et al.* “*Particle identification by means of channeling radiation in high collimated beams*”. In: Nuclear Instruments and Methods in Physics Research A 617 (2010), p. 402.
- [65] E. Bagli *et al.* “*Experimental evidence of planar channeling in a periodically bent crystal*”. In: The European Physical Journal C 74 (2014), p. 3114.
- [66] D. Lietti *et al.* “*The experimental setup of the Interaction in Crystals for Emission of RADiation collaboration at Mainzer Mikrotron: Design, commissioning, and tests*”. In: Review of Scientific Instruments 86 (2015), p. 045102.
- [67] D. S. Gemmell *et al.* “*An Apparatus for “Channeling” Experiments*”. In: Nuclear Instruments and Methods 91 (1971), p. 15.
- [68] H. Esbensen *et al.* “*Random and channeled energy loss in thin germanium and silicon crystals for positive and negative 2-15-GeV/c pions, kaons, and protons*”. In: Physical Review B 18 (1978), p. 1039.
- [69] S. M. Sze. *Physics of Semiconductor Devices*. Ed. by Wiley & Sons. 1969. ISBN: 0-471-87424-8.
- [70] G. Lutz. *Semiconductor Radiation Detectors - Device Physics*. Ed. by Springer. 1999. ISBN: 978-3-540-71678-5.
- [71] J. Kemmer. “*Fabrication of a low-noise silicon radiation detector by the planar process*”. In: Nuclear Instruments and Methods in Physics Research A 169 (1980), p. 499.
- [72] G. Dissertori. *LHC Detectors and Early Physics*. Lecture given at the 65th Scottish Universities Summer School in Physics, arXiv:1003.2222. 2009.
- [73] C. L. Gómez. “*Study of Silicon Microstrip Detector Properties for the LHCb Silicon Tracker*”. PhD thesis. Universidade de Santiago de Compostela, 2006.
- [74] A. Berra. “*Silicon Photomultipliers in High Energy and Space Applications*”. PhD thesis. Università degli Studi dell’Insubria, 2012.
- [75] A. Berra *et al.* “*LYSO crystal calorimeter readout with silicon photomultipliers*”. In: Nuclear Instruments and Methods in Physics Research A 763 (2014), p. 248.
- [76] A. Berra *et al.* “*A SiPM based readout system for lead tungstate crystals*”. In: Nuclear Instruments and Methods in Physics Research A 732 (2013), p. 380.
- [77] H. Spieler. *Semiconductor Detector Systems*. Ed. by Oxford University Press. 2005. ISBN: 978-0-19-852784-8.

- [78] F. Djama *et al.* “A submicron precision silicon telescope for beam test purposes”. In: Nuclear Instruments and Methods in Physics Research A 372 (1996), p. 379.
- [79] J. P. B. Valenzuela. “Development of innovative silicon radiation detectors”. PhD thesis. Universitat Autònoma da Barcelona, 2012.
- [80] A. Peisert *et al.* “Silicon Microstrip Detector”. In: Instrumentation in High-Energy Physics World Scientific Publishing (1992).
- [81] M. Friedl. “Diamond Detectors for Ionizing Radiation”. MA thesis. University of Technology Vienna, 1999.
- [82] M. Gabrysich. “Electronics Properties of Diamond”. PhD thesis. Uppsala Universitet, 2008.
- [83] J.R. Woodyard. Nonlinear circuit device utilizing germanium. US Patent 2,530,110. 1950.
- [84] C. J. S. Damerell. *Vertex Detector: The State of the Art and Future Prospects*. Ed. by Rutherford Appleton Laboratory. 1995.
- [85] G. Casse. “Overview of the recent activities of the RD50 collaboration on radiation hardening of semiconductor detectors for the sLHC”. In: Nuclear Instruments and Methods in Physics Research A 598 (2009), p. 54.
- [86] S. Bonfanti. “The High resolution Silicon Telescope of the INSULAB Group”. MA thesis. Università degli Studi dell’Insubria, 2012.
- [87] I. Abt. *Silicon Detectors: Technology and Applications*. Ed. by Max-Planck-Institut für Physik. 1998.
- [88] S. Chatterji *et al.* “Optimization of various isolation techniques to develop low noise, radiation hard double-sided silicon strip detectors for the CBM Silicon Tracking System”. In: IEEE Transactions on Nuclear Science 60 (2013), p. 2254.
- [89] Z. Drásal. “Simulation of Charge Collection in Semiconductor Microstrip Detectors”. MA thesis. Charles University of Prague, 2006.
- [90] G. Lindstrom *et al.* “Radiation damage in silicon detectors”. In: Nuclear Instruments and Methods in Physics Research A 512 (2003), p. 30.
- [91] R. Turchetta. “Spatial resolution of silicon microstrip detectors”. In: Nuclear Instruments and Methods in Physics Research A 335 (1993), p. 44.
- [92] IDEAS. *The VA2, Specifications*. <http://www.ideas.no>; the datasheet is provided directly by the firm.
- [93] IDEAS. *The VA1_prime2, preliminary version*. <http://www.ideas.no>; the datasheet is provided directly by the firm.

- [94] IDEAS. *The VAITA, Version 0.9*. <http://www.ideas.no>; the datasheet is provided directly by the firm.
- [95] M. J. French *et al.* “*Design and Results from the APV25, a Deep Sub-micron CMOS Front-End Chip for the CMS Tracker*”. In: Nuclear Instruments and Methods in Physics Research A 534 (2001), p. 359.
- [96] The LHCb Collaboration. *LHCb Tracker TDR Upgrade*. CERN/LHCC 2014-001. 2014.
- [97] H. Guo *et al.* *The HAL25 Front-end chip for the ALICE Silicon Strip Detectors*. Proceeding of 7th Workshop on Electronics for LHC Experiments, Stockholm (Sweden). 2001.
- [98] The ATLAS Collaboration. “*Operation and performance of the ATLAS semiconductor tracker*”. In: Journal of Instrumentation 9 (214), P08009.
- [99] E. Bagli *et al.* “*Coherent Effects of High-Energy Particles in a Graded Si_{1-x}Ge_x Crystal*”. In: Physical Review Letters 110 (2013), p. 175502.
- [100] D. De Salvador *et al.* “*Highly bent (110) Ge crystals for efficient steering of ultrarelativistic beams*”. In: Journal of Applied Physics 114 (2013), p. 154902.
- [101] E. Bagli *et al.* “*A topologically connected multistrip crystal for efficient steering of high-energy beam*”. In: Journal of Instrumentation 7 (2012), P04002.
- [102] A. Mazzolari *et al.* “*Fabrication of large area silicon nanothickness membranes for channeling experiments*”. In: Nuclear Instruments and Methods in Physics Research B 309 (2013), p. 130.
- [103] D. Bolognini. “*Study of Channeling Phenomena in Bent Crystals: the New Frontiers*”. MA thesis. Università degli Studi dell’Insubria, 2008.
- [104] D. Guffanti *et al.* *Test of a LYSO calorimeter prototype readout by large-area Silicon PhotoMultipliers*. Proceedings of 13th ICATPP Conference on Astroparticle, Particle, Space Physics and Detectors for Physics Applications, Como (Italy). 2013.
- [105] G. Barbiellini *et al.* “*The AGILE silicon tracker: testbeam results of the prototype silicon detector*”. In: Nuclear Instruments and Methods in Physics Research A 490 (2002), p. 146.
- [106] M. Prest *et al.* “*The AGILE silicon tracker: an innovative γ-ray instrument for space*”. In: Nuclear Instruments and Methods in Physics Research A 501 (2003), p. 280.

- [107] M. de Palma *et al.* “*A high resolution beam telescope built with double sided silicon strip detectors*”. In: Nuclear Instruments and Methods in Physics Research A 381 (1996), p. 49.
- [108] M. Bari *et al.* “*Results from the BaBar Silicon Vertex Tracker test beam*”. In: BaBar Note 278 (1996).
- [109] E. Bagli *et al.* “*Steering efficiency of a ultrarelativistic proton beam in a thin bent crystal*”. In: The European Physical Journal C 74 (2014), p. 2740.
- [110] Minnesota group at CERN. *CMS ECAL Optical Links*. <http://cms-ecal-optical-links.web.cern.ch/cms-ecal-optical-links/>.
- [111] Texas Instruments. *TLK1501 0.6 to 1.5 Gbps Transceiver*. <http://www.ti.com/lit/ds/symlink/tlk1501.pdf>.
- [112] D. Bolognini. “*The MICE Electron Muon Ranger: a Fundamental Step Towards a Neutrino Factory*”. PhD thesis. Università degli Studi dell’Insubria, 2012.
- [113] S. Franz *et al.* “*ATLAS ALFA-measuring absolute luminosity with scintillating fibres*”. In: Nuclear Instruments and Methods in Physics Research A 610 (2009), p. 35.
- [114] Omega Group. *MAROC Datasheet*. <http://omega.in2p3.fr>; the datasheet is provided directly by the firm.
- [115] IDEAS. *The TA1, Specifications*. <http://www.ideas.no>; the datasheet is provided directly by the firm.
- [116] D. Lietti. “*The Electron Muon Ranger for the MICE Experiment*”. MA thesis. Università degli Studi dell’Insubria, 2010.
- [117] HAMAMATSU Photonics. *The 931-B Technical Datasheet*. <http://www.hamamatsu.com>; the datasheet is provided directly by the firm.
- [118] G. Landi. “*Properties of the center of gravity as an algorithm for position measurements*”. In: Nuclear Instruments and Methods in Physics Research A 485 (2002), p. 698.
- [119] L. Landau *et al.* “*On the energy loss of fast particles by ionization*”. In: 8 (1944), p. 201.
- [120] K. H. Kaiser *et al.* “*The 1.5 GeV harmonic double-sided microtron at Mainz University*”. In: Nuclear Instruments and Methods in Physics Research A 593 (2008), p. 159.

- [121] D. Bolognini *et al.* “*The high performance microstrip silicon detector tracking system for an innovative crystal based collimation experiment*”. In: Nuclear Instruments and Methods in Physics Research A 617 (2010), p. 439.
- [122] M. Prest. “*The UA9 Silicon DAQ and Data Organization*”. In: UA9 Experiment Internal Report (2009). <http://insulab.dfm.uninsubria.it>.
- [123] M. Prest. “*Report on the First Tracking Module in the SPS*”. In: UA9 Experiment Internal Report (2009). <http://insulab.dfm.uninsubria.it>.
- [124] H. Herminghaus *et al.* “*The Design of a Cascade 800 MeV Normal conducting C.W. Race Track Microtron*”. In: Nuclear Instruments and Methods 138 (1976), p. 1.
- [125] A. Jankowiak. “*The Mainz Microtron MAMI - Past and future*”. In: The European Physical Journal A 28 (2006), p. 149.
- [126] H. J. Kreidel *et al.* Sustaining the Reliability of the MAMI-C Accelerator. Proceedings of International Particle Accelerator Conference 2012, New Orleans (USA). 2012.
- [127] Y. M. Tsipenyuk. The Microtron. Development and Applications. Ed. by Taylor & Francis. 2002. ISBN: 0-415-27238-6.
- [128] H. Backe *et al.* “*Planar channeling experiments with electrons at the 855 MeV Mainz Mikrotron MAMI*”. In: Nuclear Instruments and Methods in Physics Research B 226 (2008), p. 3835.
- [129] CANBERRA Industries. *2025 Automatic Fine Tuning Research Amplifier*. http://www.canberra.com/products/radiochemistry_lab/pdf/Model-2025-SS-CSP0161.pdf.
- [130] CANBERRA Industries. *Multiport-II Multichannel Analyzer*. http://www.-canberra.com/products/radiochemistry_lab/pdf/Multiport-II-SS-C10142.pdf.
- [131] W. Lauth. *The NaI Detector Readout System*. ICE-RAD Experiment Internal Communication. 2014.
- [132] FTDI. *FT2232H Mini Module - USB Hi-speed FT2231H Evaluation Module Version 1.7*. http://www.ftdichip.com/Support/Documents/DataSheets/Modules/DS_FT2232H_Mini_Module.pdf.
- [133] FTDI. *FT2232H Dual High Speed USB to Multipurpose UART/FIFO IC Datasheet*. http://www.ftdichip.com/Support/Documents/DataSheets/ICs/DS_FT2232H.pdf.
- [134] S. Rabaioli. “*Cosmic Rays, a tool for didactics in Physics*”. MA thesis. Università degli Studi dell’Insubria, 2014.

-
- [135] SunSoft. *FORTRAN 77 4.0 Reference Manual.*

Acknowledgement

CERN

INFN ICE-RAD/CHANEL

Werner + MAMI

Mazzolari - Bandiera - De Salvador (Bagli) G.G. (GiGi) -ζ per tutte le volte che ci
hai procurato la cena mentre eravamo in Tb a Mainz! Sei proprio un damerino!!!
Michela + Erik

Prof. Berra

Simon

Nico

Guff il mio *texnico* di fiducia (**consigli latex** + correlatrice) Labo HEP (Fede - Sil-
ver)

il *Club della Corsa* + Anna e Kasper

Elena Grandi - Valeryia - Mara - Despoina - Lucia

Prof.ssa Marina Lozej e famiglia

Pamy - Ricky - Ferry - Laura - Mario - Pitteo

Paolo + famiglia

Mamma - Papà - Elisa - Davide - Elena - Pujo - Gabriele

Vally - zio Tullio

*How wonderful life is while you're in the world
Your Song - Elton John*

